
Probing hadronic medium produced in relativistic heavy-ion collision

A Thesis

*Submitted In Partial Fulfillment Of The Requirements For
The Award Of Degree Of*

DOCTOR OF PHILOSOPHY

Submitted by

Aswini Kumar Sahoo
(Enrollment No. 1920502)



DEPARTMENT OF PHYSICAL SCIENCES
INDIAN INSTITUTE OF SCIENCE EDUCATION AND RESEARCH
BERHAMPUR 760010, INDIA

December, 2024

CERTIFICATE

The undersigned have examined the Ph.D. thesis entitled:

Probing hadronic medium produced in relativistic heavy-ion collision presented by **Aswini Kumar Sahoo**, a candidate for the degree of Doctor of Philosophy in **department of physical sciences**, and hereby certify that it is worthy of acceptance.

Thesis Supervisor: Dr. Md. Nasim

Signature: Md. Nasim 09.05.25

Chairperson: Dr. Santanu Bhattacharyya

Signature: ~~XX~~ 09/5/25

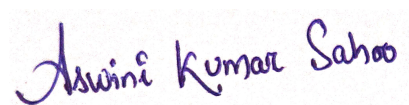
Thesis Examiner: Prof. Sadhana Dash

Signature: Sadhana Dash

ACADEMIC INTEGRITY AND COPYRIGHT DISCLAIMER

I hereby declare that this thesis is my own work and, to the best of my knowledge, it contains no materials previously published or written by any other person, or substantial proportions of material which have been accepted for the award of any other degree or diploma at IISER Berhampur or any other educational institution, except where due acknowledgment is made in the thesis.

I certify that all copyrighted material incorporated into this thesis is in compliance with the Indian Copyright (Amendment) Act, 2012 and that I have received written permission from the copyright owners for my use of their work, which is beyond the scope of the law. I agree to indemnify and save harmless IISER Berhampur from any and all claims that may be asserted or that may arise from any copyright violation.



Date: 9th May 2025
IISER Berhampur, Odisha, India

Aswini Kumar Sahoo

List of Publications

Published (As a primary author):

(Publications marked (*) are included in the thesis)

- [1] K^{*0} production in Au+Au collisions at $\sqrt{s_{NN}} = 7.7, 11.5, 14.5, 19.6, 27,$ and 39 GeV from the RHIC beam energy scan. [STAR Collaboration] *
Primary Contributors : **Aswini Kumar Sahoo**, Md. Nasim, Subhash Singha
Phys. Rev. C. 107. 034907 (2023)
- [2] K^{*0} meson production using a transport and a statistical hadronization model at energies covered by the RHIC beam energy scan. *
Aswini Kumar Sahoo, Md. Nasim, Subhash Singha
Phys. Rev. C. 108. 044904 (2023)
- [3] Examining the influence of hadronic interactions on the directed flow of identified particles in RHIC Beam Energy Scan energies using UrQMD model. *
Aswini Kumar Sahoo, Prabhupada Dixit, Md. Nasim, Subhash Singha
Modern Physics Letters A Vol. 39, No. 07, 2450015 (2024)
- [4] The study of hadronic rescattering on K^{*0} resonance yield in baryon-rich QCD matter. *
Aswini Kumar Sahoo, Subhash Singha, Md. Nasim
J. Phys. G: Nucl. Part. Phys. 52, 015101 (2025)
- [5] Study of bulk properties of the system formed in U+U collisions at $\sqrt{s_{NN}} = 2.12$ GeV using JAM model.
Aswini Kumar Sahoo, Xionghong He, Yasushi Nara, Subhash Singha
Phys.Rev.C 109. 054902 (2024)

STAR internal analysis notes:

- [1] K^{*0} production in RHIC beam energy scan Au+Au collisions at $\sqrt{s_{NN}} = 7.7 - 39$ GeV
Primary Contributors : **Aswini Kumar Sahoo**, Md. Nasim, Subhash Singha
- [2] Precise measurement of K^{*0} meson production using BES-II data in STAR
Primary Contributors : **Aswini Kumar Sahoo**, Md. Nasim, Subhash Singha

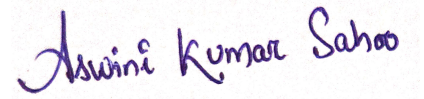
Conference proceedings

- [1] Production Yield and Azimuthal Anisotropy Measurements of Strange Hadrons from BES at STAR
Aswini Kumar Sahoo (for the STAR Collaboration)
In Proceedings of : *XXIXth International Conference on Ultra-relativistic Nucleus-Nucleus Collisions (QM-2022), Krakow, Poland*
[Acta Phys. Pol. B Proc. Suppl. 16, 1-A132 \(2023\)](#)
- [2] Production of K^{*0} in Au+Au collisions at $\sqrt{s_{NN}} = 19.6$ GeV from RHIC BES-II
Aswini Kumar Sahoo (for the STAR Collaboration)
In Proceedings of : *The XXth International Conference on Strangeness in Quark Matter (SQM 2022), Busan, South Korea*
[EPJ Web of Conferences 276, 03007 \(2023\)](#)
- [3] Production of K^{*0} in Au+Au collisions at $\sqrt{s_{NN}} = 19.6$ GeV in BES-II from STAR
Aswini Kumar Sahoo (for the STAR Collaboration)
In Proceedings of : *XXV DAE-BRNS High Energy Physics (HEP) Symposium 2022, 12–16 December, Mohali, India*
[Springer Nature Singapore, 2024, pp. 286–289](#)

Conference/Workshop presentations

- [1] Production Yield and Azimuthal Anisotropy Measurements of Strange Hadrons from BES at STAR
XXIXth International Conference on Ultra-relativistic Nucleus-Nucleus Collisions (QM-2022), 4-10 April 2022, Krakow, Poland
- [2] Production of K^{*0} in Au+Au collisions at $\sqrt{s_{NN}} = 19.6$ GeV from RHIC BES-II
XXth International Conference on Strangeness in Quark Matter (SQM 2022), 13 - 17 June 2022, Busan, South Korea
- [3] Probing the hadronic phase via the measurement of resonances in Au+Au collisions at $\sqrt{s_{NN}} = 19.6$ GeV from STAR BES-II
Workshop on Critical Point and Onset of Deconfinement (CPOD-2022), online
- [4] Production of K^{*0} in Au+Au collisions at $\sqrt{s_{NN}} = 19.6$ GeV in BES-II from STAR
XXVth DAE-BRNS High Energy Physics (HEP) Symposium, 12–16 December 2022, Mohali, India

- [5] Probing hadronic rescattering via resonance production in Au+Au collisions at $\sqrt{s_{NN}} = 19.6$ GeV from STAR BES-II
VIIIth International Conference on Physics and Astrophysics of Quark Gluon Plasma (ICPAQGP-2023), 7-10 February 2023, Puri, Odisha, India
- [6] Strange resonance production in heavy-ion collisions (invited talk)
STAR eTOF and BES-II workshop, 3-6 Dec 2024, BNL, USA (online)
- [7] Probing hadronic rescattering via K^{*0} resonance production at RHIC
Xth Asian Triangle Heavy-Ion Conference - ATHIC 2025, 13–16 January 2025, Berhampur, OdishaIndia



(Aswini Kumar Sahoo)

Acknowledgements

This thesis is the result of unwavering support, inspiration and guidance from many incredible individuals, to whom I wish to convey my sincere gratitude.

First, I owe my sincere thanks to my supervisor, Dr. Md. Nasim, for his unwavering support and motivation throughout my Ph.D. journey. I am truly thankful for the opportunity he gave me to become a part of his research group and granting me the invaluable opportunity to work with the STAR collaboration. As someone new to the field with minimal prior exposure, I deeply appreciate his patience in addressing my mistakes and offering constructive criticism and feedback, which greatly contributed to my growth as a researcher. His profound understanding of the subject, expertise in data analysis techniques, and approach to tackle the challenges in analysis have been a constant source of inspiration. I have immensely benefited from his valuable insights and the stimulating discussions we shared. I will always be grateful for Dr. Nasim's support, due to which I could attend my first international conference, Quark Matter 2022, in person—an experience I will always cherish. I am also thankful for the opportunities he provided to participate in several national and international conferences and to visit research groups both in India and abroad. These experiences enhanced my understanding of contemporary research and helped me communicate effectively with fellow researchers in the scientific community.

I express my gratitude to Dr. Subhash Singha for his kind support and mentorship since the early days of starting my thesis work. I am grateful to him and Dr. Hao Qiu for welcoming me to QMRC, IMPCAS Lanzhou, as a visiting fellow and allowing me to engage in discussions with their group. I am also thankful to Dr. Singha and his family for their care and support during my stay at IMPCAS, Lanzhou.

I would like to thank my RPC members, Dr. Chitrasen Jena, and Dr. Sandeep Chatterjee, for continuously reviewing my work and providing valuable suggestions. I also thank the Director of IISER, Berhampur, for providing the necessary resources throughout my Ph.D. I would like to thank the faculty members of the Department of Physical Sciences of IISER Berhampur for teaching me during the Ph.D. course work. I would also like to thank my collaborators, Dr. Xionghong He and Dr. Yasushi Nara, for their support in working with the JAM model. My sincere thanks go to the conveners of the LFS-UPC PWG group, my GPC members, and the members of the STAR collaboration for providing valuable insights and helpful feedback to improve my analysis. Additionally, I appreciate the feedback I received during the collaboration meetings from the ALICE-STAR India collaborators.

I am deeply thankful to Mr. Prabhupada Dixit and Mr. Pranjal Barik for being such kind and supportive lab mates. A special thanks to Mr. Prabhupada Dixit. We both started our Ph.D. together and he was always there to assist me with the STAR analysis framework or to engage in discussions regarding data analysis.

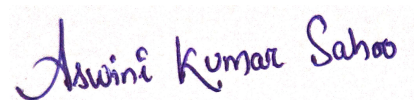
I would like to thank Dr. Sandeep Chatterjee and his group for the insightful physics discussions. I am especially grateful to my senior, Mr. Tribhuban Parida, for his constant support and encouragement from the very first day of my Ph.D. He has greatly helped me understand complex physics concepts and always motivated me to become a better researcher. He stood by me throughout my journey, and without his guidance, I would not have been able to complete my doctoral studies. I also extend my heartfelt thanks to Mr. Kaiser Shafi for being a good friend who was always willing to help, whether it

was with coding or understanding theoretical concepts. I deeply appreciate Mr. Nimish Kumar Mahapatra, for the care and support over these years. Starting from preparing delicious food to all those moments filled with fun and laughter these memories will always remain unforgettable.

I extend my heartfelt appreciation to Dr. Ashutosh Dash for his valuable advice and engaging discussions. He has been a great source of inspiration for me throughout my Ph.D., and I will always remember his support during my stay in Krakow for Quark Matter 2022. I am also deeply grateful to Dr. Dukhishyam Mallick for his constant availability and willingness to help, no matter how trivial the issue. He never looked at the clock when I sought his assistance, whether it was with analysis or physics discussions. I would also like to mention Dr. Kasinath Das, one of the most humble person, I have ever seen. His humble nature, jovial personality, and love for physics have always been a source of inspiration. I feel truly fortunate to have had elder brothers like them guiding and supporting me throughout my doctoral journey.

I would like to thank Nimish Bhai, Tribhuban Bhai and Prabhupada Bhai for being wonderful friends and making my time at IISER truly enjoyable. The moments we shared and the trips we took together will remain some of my most treasured memories. I also want to thank my friends, Mr. Raju Sharma and Ms. Aisa Mohanty, for their understanding and support. They were always there for me, making my time at IISER memorable. I feel lucky to have had the company of friends like Jagbir Bhai, Krishan Bhai, Rishabh, Ishu, Arushi, Sharang, Navneet, Satabdi, Sururchee Didi, Amiya Bhai, and Bhagyashree Didi during these days, who brought laughter and joy to my Ph.D. life.

Lastly, I reserve a special place in my heart for my beloved parents and elder sisters for their love, support, and belief in my abilities throughout my life. I thank the Supreme One for being kind and bestowing His blessings upon me, enabling me to successfully complete my research.



(Aswini Kumar Sahoo)

Abstract

Till the date quarks and gluons are understood to be the fundamental building blocks of nucleons within the atomic nucleus. The theory that governs the strong interaction between the quark and gluons is called quantum chromodynamics (QCD). According to the QCD prediction, when the temperature and/or density reach extreme high levels, the quark and gluons escape their confinement within hadrons and create an exotic state of matter called Quark-Gluon Plasma (QGP). After the big-bang, the micro-second old universe is believed to exist in such a state, where quarks and gluons are the primary degrees of freedom. Modern day heavy-ion collider facilities like those at LHC and RHIC, strive to recreate such a primordial state of the early universe in laboratory and study its properties. Over the past two decades, high-energy heavy-ion collisions at the top RHIC and LHC energies have focused on exploring the characteristics of the medium produced at zero baryon chemical potential ($\mu_B = 0$).

However, since 2010, with the initiation of the RHIC Beam Energy Scan (BES) program, the focus has shifted to lower collision energies to investigate the medium produced at finite μ_B , enabling exploration of the QCD phase diagram in the $T - \mu_B$ plane. With the decrease in collision energy, the baryon chemical potential (μ_B) of the system increases, leading to a mid-rapidity region dominated by baryons at RHIC-BES energies.

Due to such change in the chemical composition of the system produced at low and high collision energies, distinct difference in the particle interaction can be expected. The focus of the thesis is to explore the late-stage interactions of QCD matter produced at RHIC Beam Energy Scan (BES) energies by analyzing the production of hadronic resonances, utilizing the data collected by the STAR detector at RHIC.

Resonances are short-lived particles that decay via strong interactions, with lifetimes, in the order of 10^{-23} seconds, or a few fm/c. Their lifetimes are comparable to the lifespan of the fireball created in heavy-ion collisions. In this thesis, the K^{*0} resonance (lifetime ≈ 4.16 fm/c) is studied. Due to its short lifetime, the K^{*0} meson decays within the fireball. During the hadronic phase, its decay products primarily undergo two simultaneous processes: rescattering and regeneration, through elastic or pseudo-elastic interactions. Consequently, the properties of the K^{*0} meson such as mass, width, momentum, and yield are likely to be modified due to these in-medium interactions.

In the current work the production of K^{*0} meson has been studied in Au+Au collisions at center of mass energies ranging from 7.7-39 GeV. The analysis includes measurements of transverse momentum spectra, p_T integrated yield (dN/dy), mean transverse momentum ($\langle p_T \rangle$), nuclear modification factor (R_{cp}) and resonance to stable particle ratios. Additionally the resonance to non resonance ratio for K^{*0} meson has been utilized to estimate a lower limit on the hadronic phase lifetime using a simple toy model approach. Simultaneous comparison with various model studies helps to get insight about the change in type of hadronic interactions in both lower and high energy collisions.

From these explanations, it can be concluded that hadronic interactions can have a significant impact on the yield of short-lived resonances. To extend this study, motivation has arisen to explore the effect of hadronic interactions on flow observables. Recent studies have indicated that the flow of resonance particles can be influenced by such interactions.

In this thesis, the UrQMD transport model has been implemented to estimate the effect of prolonged hadronic interactions on the flow coefficients of identified hadrons.

Specifically, the rapidity-odd first-order anisotropic flow (known as the directed flow coefficient or v_1) has been studied. With an increase in the hadronic cascade duration, a significant difference in the v_1 slope has been observed between oppositely charged particles in central and mid-central collisions. This effect has been most prominent for protons. These observations have suggested that the charge-dependent v_1 splitting recently reported by STAR may also have contributions from hadronic interactions.

Contents

Certificate	ii
List of publications	iv
Acknowledgements	vii
Abstract	ix
Contents	xi
List of Figures	xvi
List of Tables	xxiv
1 Introduction	1
1.1 Insights into Quantum Chromodynamics	2
1.2 QCD phase transition and Quark Gluon Plasma	4
1.2.1 QCD phase diagram	5
1.3 Relativistic Heavy-Ion collisions : The Experimental realisation	7
1.3.1 Space-time evolution	7
1.3.2 Glossary of kinematic variables	10
A. Center of mass energy	11
B. Transverse momentum (p_T)	11
C. Azimuthal angle (ϕ)	11
D. Rapidity (y)	12
E. Pseudo-rapidity (η)	12
F. Particle Multiplicity	13
1.3.3 Natural units	15
1.4 Experimental signatures of Quark Gluon Plasma	15
1.4.1 Strangeness enhancement	15
1.4.2 Suppression of high p_T particle yield	17
1.4.3 Quarkonia suppression	19
1.4.4 Collectivity in the medium	20
1.5 Investigating freeze-out dynamics through resonance production	21
1.5.1 Resonances	22
1.6 Thesis motivation	24
2 The STAR Detector Setup at RHIC	25
2.1 Introduction	25
2.2 The STAR Experiment	29
2.2.1 The Time Projection Chamber: TPC	31
2.2.2 The Time Of Flight Detector set up	34
A. The Vertex Position Detector: VPD	34
B. The Time Of Flight Detector: TOF	34
2.2.3 Particle identification (PID): Using both TPC and TOF	35

2.2.4	Trigger detectors	37
A.	Zero Degree Calorimeter: ZDC	38
B.	Beam Beam Counters: BBC	39
C.	Vertex Position Detectors: VPD	39
D.	Electro Magnetic Calorimeters: EMC	39
2.3	Summary	39
3	K^{*0} production in Au+Au collisions from RHIC beam energy scan phase-I	40
3.1	Introduction	40
3.2	Data sets, events and track selection cuts	41
3.2.1	Data set	41
3.2.2	Event cuts	41
3.2.3	Centrality determination	43
3.2.4	Track cuts	45
3.3	Particle Identification (PID)	46
3.3.1	Particle Identification from TPC	46
3.3.2	Particle Identification from TOF	46
3.4	Signal Extraction	48
3.4.1	Track rotation method	48
3.4.2	Mixed event method	48
3.4.3	Raw Yield extraction	50
3.5	Correction factors	50
3.5.1	Detector tracking efficiency and acceptance	50
3.5.2	Efficiency re-weighting	52
3.5.3	PID efficiency calculation	53
A.	TPC PID efficiency	54
B.	TOF PID efficiency	54
C.	PID efficiency for K^{*0}	55
3.6	Systematic Uncertainties	56
3.6.1	Uncertainty from signal extraction method:	56
3.6.2	Uncertainty from yield extraction method:	56
3.6.3	Uncertainty from PID, Event and Track selection cuts:	57
3.6.4	Uncertainty due to low p_T extrapolation:	57
3.6.5	Uncertainty due to global tracking efficiency	57
3.6.6	Total systematic uncertainty:	58
3.7	Results	58
3.7.1	Mass and Width of K^{*0} meson:	58
3.7.2	Transverse momentum (p_T) spectra:	59
3.7.3	K^{*0} meson yield per unit rapidity:	61
3.7.4	Mean transverse momentum ($\langle p_T \rangle$) of K^{*0} meson:	61
3.7.5	Particle ratios:	63
3.7.6	Estimation of lower limit of hadronic phase lifetime:	66
3.7.7	Summary:	68
3.8	Appendix	69
3.8.1	K^{*0} invariant mass distribution for 0-20% centrality in Au+Au collisions at $\sqrt{s_{NN}} = 7.7$ GeV	69
3.8.2	K^{*0} invariant mass distribution for 20-40% centrality in Au+Au collisions at $\sqrt{s_{NN}} = 7.7$ GeV	69
3.8.3	K^{*0} invariant mass distribution for 40-60% centrality in Au+Au collisions at $\sqrt{s_{NN}} = 7.7$ GeV	70

3.8.4	K^{*0} invariant mass distribution for 60-80% centrality in Au+Au collisions at $\sqrt{s_{NN}} = 7.7$ GeV	70
3.8.5	K^{*0} invariant mass distribution for 0-10% centrality in Au+Au collisions at $\sqrt{s_{NN}} = 11.5$ GeV	71
3.8.6	K^{*0} invariant mass distribution for 10-20% centrality in Au+Au collisions at $\sqrt{s_{NN}} = 11.5$ GeV	71
3.8.7	K^{*0} invariant mass distribution for 20-30% centrality in Au+Au collisions at $\sqrt{s_{NN}} = 11.5$ GeV	72
3.8.8	K^{*0} invariant mass distribution for 30-40% centrality in Au+Au collisions at $\sqrt{s_{NN}} = 11.5$ GeV	72
3.8.9	K^{*0} invariant mass distribution for 40-60% centrality in Au+Au collisions at $\sqrt{s_{NN}} = 11.5$ GeV	73
3.8.10	K^{*0} invariant mass distribution for 60-80% centrality in Au+Au collisions at $\sqrt{s_{NN}} = 11.5$ GeV	73
3.8.11	K^{*0} invariant mass distribution for 0-10% centrality in Au+Au collisions at $\sqrt{s_{NN}} = 14.5$ GeV	74
3.8.12	K^{*0} invariant mass distribution for 10-20% centrality in Au+Au collisions at $\sqrt{s_{NN}} = 14.5$ GeV	74
3.8.13	K^{*0} invariant mass distribution for 20-30% centrality in Au+Au collisions at $\sqrt{s_{NN}} = 14.5$ GeV	75
3.8.14	K^{*0} invariant mass distribution for 30-40% centrality in Au+Au collisions at $\sqrt{s_{NN}} = 14.5$ GeV	75
3.8.15	K^{*0} invariant mass distribution for 40-60% centrality in Au+Au collisions at $\sqrt{s_{NN}} = 14.5$ GeV	76
3.8.16	K^{*0} invariant mass distribution for 60-80% centrality in Au+Au collisions at $\sqrt{s_{NN}} = 14.5$ GeV	76
3.8.17	K^{*0} invariant mass distribution for 0-10% centrality in Au+Au collisions at $\sqrt{s_{NN}} = 19.6$ GeV	77
3.8.18	K^{*0} invariant mass distribution for 10-20% centrality in Au+Au collisions at $\sqrt{s_{NN}} = 19.6$ GeV	77
3.8.19	K^{*0} invariant mass distribution for 20-30% centrality in Au+Au collisions at $\sqrt{s_{NN}} = 19.6$ GeV	78
3.8.20	K^{*0} invariant mass distribution for 30-40% centrality in Au+Au collisions at $\sqrt{s_{NN}} = 19.6$ GeV	78
3.8.21	K^{*0} invariant mass distribution for 40-60% centrality in Au+Au collisions at $\sqrt{s_{NN}} = 19.6$ GeV	79
3.8.22	K^{*0} invariant mass distribution for 60-80% centrality in Au+Au collisions at $\sqrt{s_{NN}} = 19.6$ GeV	79
3.8.23	K^{*0} invariant mass distribution for 0-10% centrality in Au+Au collisions at $\sqrt{s_{NN}} = 27$ GeV	80
3.8.24	K^{*0} invariant mass distribution for 10-20% centrality in Au+Au collisions at $\sqrt{s_{NN}} = 27$ GeV	80
3.8.25	K^{*0} invariant mass distribution for 20-30% centrality in Au+Au collisions at $\sqrt{s_{NN}} = 27$ GeV	81
3.8.26	K^{*0} invariant mass distribution for 30-40% centrality in Au+Au collisions at $\sqrt{s_{NN}} = 27$ GeV	81
3.8.27	K^{*0} invariant mass distribution for 40-60% centrality in Au+Au collisions at $\sqrt{s_{NN}} = 27$ GeV	82
3.8.28	K^{*0} invariant mass distribution for 60-80% centrality in Au+Au collisions at $\sqrt{s_{NN}} = 27$ GeV	82

3.8.29	K^{*0} invariant mass distribution for 0-10% centrality in Au+Au collisions at $\sqrt{s_{NN}} = 39$ GeV	83
3.8.30	K^{*0} invariant mass distribution for 10-20% centrality in Au+Au collisions at $\sqrt{s_{NN}} = 39$ GeV	83
3.8.31	K^{*0} invariant mass distribution for 20-30% centrality in Au+Au collisions at $\sqrt{s_{NN}} = 39$ GeV	84
3.8.32	K^{*0} invariant mass distribution for 30-40% centrality in Au+Au collisions at $\sqrt{s_{NN}} = 39$ GeV	84
3.8.33	K^{*0} invariant mass distribution for 40-60% centrality in Au+Au collisions at $\sqrt{s_{NN}} = 39$ GeV	85
3.8.34	K^{*0} invariant mass distribution for 60-80% centrality in Au+Au collisions at $\sqrt{s_{NN}} = 39$ GeV	85
3.8.35	Reference multiplicity, $\langle N_{part} \rangle$ and $\langle N_{coll} \rangle$	86
3.8.36	Comparison between yield extracted from simple and relativistic breit-wigner function:	87
3.8.37	Lorentz factor (γ):	87
3.8.38	Particle yield and mean transverse momentum:	88
3.8.39	Particle ratios:	89
4	Understanding K^{*0} production using hadronic transport and statistical thermal model	92
4.1	Model description:	92
4.1.1	The thermal model	92
4.1.2	The UrQMD Model	93
4.2	Signal Reconstruction	95
4.3	Results and Discussions:	96
4.3.1	Effect of hadronic cascade time on K^{*0} meson	96
A.	Yield of K^{*0} and charged kaons (K^{\pm})	96
B.	Resonance to non-resonance ratio	97
C.	Rapidity dependent K^{*0} production from UrQMD model	99
4.3.2	Hadronic rescattering in high baryon density region.	100
A.	Multiplicity dependent particle yields	100
B.	K^{*0}/K ratio	102
4.4	Summary	102
5	K^{*0} production in Au+Au collisions from RHIC beam energy scan phase-II	104
5.1	Introduction	104
5.2	Data sets, events and track selection	105
5.2.1	Data set	105
5.3	Track cuts and Particle identification	105
5.4	Signal extraction	106
5.4.1	Combinatorial background estimation	106
5.4.2	Raw yield extraction	106
5.5	Efficiency correction	107
5.6	Systematic uncertainties	109
5.7	Results	111
5.7.1	Transverse momentum spectra	111
5.7.2	Mid-rapidity particle yield	112
5.7.3	K^{*0}/K ratio	114
5.7.4	Nuclear modification factor (R_{cp})	116
5.7.5	Rapidity dependent K^{*0} yield	117

5.8	Summary	117
5.9	Appendix	119
5.9.1	K^{*0} p_T spectra comparison between BES-I and BES-II	119
5.9.2	Significance of K^{*0}/K suppression	119
5.9.3	Efficiency \times Acceptance	120
5.9.4	Corrected p_T spectra for different rapidity bins	121
A.	Au+Au, $\sqrt{s_{NN}} = 7.7$ GeV	121
B.	Au+Au, $\sqrt{s_{NN}} = 11.5$ GeV	121
C.	Au+Au, $\sqrt{s_{NN}} = 14.6$ GeV	122
D.	Au+Au, $\sqrt{s_{NN}} = 19.6$ GeV	122
E.	Au+Au, $\sqrt{s_{NN}} = 27$ GeV	123
5.9.5	Reference multiplicity, Average multiplicity $((dN_{ch}/dy)^{1/3})$, $\langle N_{part} \rangle$ and $\langle N_{coll} \rangle$ for BES-II data sets	123
6	Studying effect of hadronic rescattering on flow observables using a trans- port based model	125
6.1	Introduction	125
6.2	Analysis details	127
6.3	Results and Discussion	127
6.3.1	Directed flow (v_1) vs rapidity from UrQMD model	127
6.3.2	Collision energy and centrality dependence of dv_1/dy	129
6.3.3	Model to experimental data comparison	130
6.4	Summary	131
7	Thesis Summary	132
7.1	Future Prospectives	134
8	Appendix	135
8.1	Branching ratios	135
	References	137

List of Figures

1.1	The visual representation of the standard model, with three generations of elementary particles, along with force-carrying gauge bosons and Higgs boson. The figure has been sourced from [1].	2
1.2	The observed variation of the running coupling constant $\alpha_s(Q)$ with respect to the energy scale Q . The figure has been sourced from [2].	3
1.3	The variation of energy density, pressure density and entropy density as a function of temperature from (2+1) flavor lattice QCD calculations represented by coloured bands. The results from hadron resonance gas (HRG) model is presented by the solid lines at the lower temperature side. The dashed lines at the higher temperature side denotes, the non-interacting HRG or the Stefan-Boltzmann ideal gas limit. The figure has been sourced from [3].	5
1.4	The conjectured QCD phase diagram depicts various phases of strongly interacting matter. It illustrates a transition from a hadron gas to a deconfined quark-gluon plasma (QGP) phase through smooth crossover transition (represented by the dashed line) at the transition temperature, and first-order phase transition (indicated by the solid black line), that is theorized to terminate at the possible QCD critical point (marked by a solid-square). The chemical freeze-out curve is indicated by the red-yellow dotted line, obtained through thermal model fits to particle yield data. The semi-circular marker at $T \approx 0$ and $\mu_B \approx 925$ MeV represents ground-state nuclear matter. Different regions of the phase diagram are accessible through various experimental facilities, as indicated in the upper section of the figure. The figure has been sourced from [4].	6
1.5	Left side: A schematic picture of a relativistic nuclear collision along z-direction, where the nucleons denoted by red colour are participant nucleons and those in blue colours are the spectator nucleons. Right side : The same collision picture in the transverse plane (xy-plane) for a central and peripheral collision.	7
1.6	Schematic illustration of the space-time evolution of a relativistic heavy ion collision. The figure has been sourced from [5].	8
1.7	The mid-rapidity p_T -integrated particle yield ratios for central Au+Au collisions at $\sqrt{s_{NN}} = 200$ GeV. Fitting of experimental data to the statistical thermal model is shown by blue horizontal lines. The figure has been sourced from [6].	9
1.8	The χ^2 contours of kinetic freezeout temperature (T_{fo}) and mean radial velocity $\langle\beta\rangle$, extracted from thermal+radial flow fits (Blast-wave function fits) to the light (π, K, p) and multi-strange (ϕ, Ω) hadron p_T -spectra for Au+Au collisions at 200 GeV. The figure has been sourced from [6].	10
1.9	The pseudo-rapidity distribution of the produced particles ($\frac{dN_{ch}}{d\eta}$) of different p_T and mass, which is converted from a flat rapidity distribution ($\frac{dN_{ch}}{dy} = 1$), using equation 1.3.26.	14
1.10	Strangeness enhancement factor (ϵ), for $K(s=1)$, $\phi(s=0)$, $\Lambda(s=1)$ and $\Xi(s=2)$ as a function of $\langle N_{part} \rangle$ for Au+Au and Cu+Cu collisions at 200 and 62.4 GeV. The figure has been sourced from [7].	16
1.11	Schematic representation of jet formation in $p + p$ and A+A collisions.	17
1.12	Systematic measurement of di-jet azimuthal correlation at $\sqrt{s_{NN}} = 200$ GeV by the STAR experiment. The figure has been sourced from [6].	18

1.13	The measurement nuclear modification factor (R_{AA}) from STAR experiment for different centrality classes, for center of mass energy of 200 GeV. The figure has been sourced from [8].	18
1.14	The measurement nuclear modification factor (R_{AA}) from STAR experiment for different centrality classes, for center of mass energy of 200 GeV. The figure has been sourced from [9].	19
1.15	The measurement of elliptic flow coefficient (v_2) for identified hadrons in Au+Au collisions at $\sqrt{s_{NN}} = 200$ GeV by STAR and PHENIX experiment. The flow parameter for different particles predicted by hydrodynamic model has been shown by solid and dashed lines. The figure has been sourced from [10]. . . .	20
1.16	The elliptic flow coefficient (v_2) scaled by no. of constituent quarks (ncq) for identified hadrons in Au+Au collisions at $\sqrt{s_{NN}} = 200$ GeV with ncq scaled transverse kinetic energy ($(m_T - m_0)/n_q$). The figure has been sourced from [11].	21
1.17	Pictorial representation of in-medium interactions for the K^{*0} decay daughters.	22
1.18	Naive expectation of the centrality dependence of the K^{*0}/K ratio in a context of re-scattering/regeneration dominant picture.	23
1.19	Previous experimental measurement of resonance to no-resonance ratio ($K^{*0}/K, \phi/K$) from STAR and ALICE. The figure has been sourced from [12–14].	23
1.20	The collision energy dependence of kinetic and chemical freezeout temperature. The figure has been sourced from [15].	24
2.1	Overview of RHIC experimental facility at Brookhaven National Laboratory taken from the Ref [16].	26
2.2	Schematic diagram of ion-beam injection into the RHIC ring.	26
2.3	The schematic picture of the Solenoidal Tracker at RHIC (STAR) detector illustrating the layout and arrangement of its various sub-detector systems. The figure has been sourced from Chi Yang’s presentation in ICNFP-2017 (STAR Collaboration).	29
2.4	The first collision event recorded by the STAR TPC detector for Au+Au collisions at $\sqrt{s_{NN}} = 200$ GeV, in 2001. The colored lines show the tracks of different charged particles. The figure has been sourced from [17].	29
2.5	Arrangement of sub detector systems along with the co-ordinates in STAR. The figure has been sourced from [18].	30
2.6	Upgraded sub detector in BES-II program. The figure has been sourced from [19].	30
2.7	Three dimensional technical layout of the STAR-TPC, indicating major structural elements. The figure has been sourced from [20].	31
2.8	The layout of the TPC anode sector showing the outer and inner sub-sectors, located on the left and right, respectively. The figure has been sourced from [20]. This design corresponds to the BES-I data-taking period.	32
2.9	(a) A detailed view of the STAR iTPC sector with its components, that includes a supporting aluminum strongback, pad plane and three layers of wires supported on the corresponding wire mounts. (b) The final lay-out of the iTPC sector. The picture has been sourced from ref [21].	33
2.10	The top and bottom figure shows the longitudinal and side wise cut view of Multi Resistive Plate Chambers module of the STAR TOF. The plots have been scaled arbitrarily. The figure has been sourced from [22].	34

2.11	Left Panel: The ionisation energy loss (dE/dx) as a function of rigidity (p/q) for different charged particles for minimum bias Au+Au collisions at $\sqrt{s_{NN}} = 19.6$ GeV. Different colored lines represent the Bichsel function expectations for different particles Right panel: The $Mass^2$ as a function of rigidity (p/q) for different charged particles for minimum-bias Au+Au collisions at $\sqrt{s_{NN}} = 19.6$ GeV. The dashed line represents the PDG values for different particles.	36
2.12	The diagram showing the arrangement of different trigger detectors in STAR experiment. The figure has been sourced from [23]. Currently, central trigger barrel (CTB) has been replaced by the TOF detector system and Forward Pion Detector (FPD) has been replaced by the Forward Meson Spectrometer (FMS).	38
3.1	The distribution of the z-component of the primary vertex from Au+Au collisions after applying cuts at six different center-of-mass energies.	42
3.2	The distribution of V_x vs. V_y from Au+Au collisions after applying cuts at six different center-of-mass energies.	42
3.3	The uncorrected charged particle multiplicity (Refmult) distribution of reconstructed per unit pseudo-rapidity interval at mid-rapidity at six different centre-of-mass energies for minimum bias Au+Au collisions.	44
3.4	Ionization energy loss(dE/dx) deposited by various charged particles in TPC for Au+Au collisions at $\sqrt{s_{NN}} = 19.6$ GeV vs. Rigidity ($p \times q$). The dashed curves represent the theoretical expectation of mean ionisation energy loss (dE/dx) values for each corresponding particle, calculated using the Bichsel function [24].	47
3.5	Mass-squared ($mass^2$) of various charged particles measured by TOF for Au+Au collisions at $\sqrt{s_{NN}} = 19.6$ GeV as a function of Rigidity (p/q). The dashed lines represent the PDG $mass^2$ values for each corresponding particle.	47
3.6	Left panel: The invariant mass distribution of πK pairs reconstructed using unlike-charge pairs from the same event, unlike-charge pairs from mixed events, and rotated track pairs from the same event in 60-80% Au+Au collisions at $\sqrt{s_{NN}} = 39$ GeV. Right panel: The πK pair invariant mass distribution after subtracting the normalized background pair distributions, measured using different methods, from the unlike-charge same event distribution.	49
3.7	The track-rotation combinatorial background-subtracted $K\pi$ invariant mass distribution for $1.2 < p_T < 1.6$ GeV/c (at 14.5 and 39 GeV) is shown for central (0-10%) and peripheral (60-80%) centralities. The data are fitted with a Breit-Wigner function combined with a first-order polynomial (as described in equation 3.4.2), represented by the solid line and the dashed line represents the residual background. The uncertainties on the data points are statistical and are indicated by error bars.	50
3.8	The Distribution of DCA and TPC hit points, of pions (top panel) and kaons (Bottom panel) from embedding (solid red line) and real data (solid blue line) for $0.2 < p_T < 0.6$ GeV/c in Au+Au collisions at $\sqrt{s_{NN}} = 11.5$ GeV. The distributions have been normalized to unit area.	51
3.9	Flow chart of efficiency calculation for K^{*0} meson.	52
3.10	The detector tracking efficiency for K^{*0} meson as a function of p_T at various collision centralities in Au+Au collisions at $\sqrt{s_{NN}} = 7.7-39$ GeV. The statistical uncertainties are within the marker size.	53
3.11	Test of re-weighting of efficiency using 19.6 GeV data and simulation.	53

3.12	TPC $N\sigma$ distribution for pion and kaon in $0.1 < p_T(\text{GeV}/c) < 0.2$ for 19.6 GeV.	54
3.13	Variation of $N\sigma_{TPC}$ efficiency with p_T for 19.6 GeV.	54
3.14	$mass^2$ distribution for pion and kaon in different p_T ranges for 19.6 GeV. . .	55
3.15	Variation of TOF PID efficiency with p_T for 19.6 GeV.	55
3.16	Variation of TOF match efficiency with p_T for 19.6 GeV.	55
3.17	Variation of K^{*0} PID efficiency with p_T for 19.6 GeV.	56
3.18	Upper Panel: K^{*0} mass and width as a function of p_T for Au+Au collisions at 11.5 GeV compared with the results for $p + p$ and Au+Au at 200 GeV [25]. Lower Panel: K^{*0} mass and width as a function of p_T for Au+Au collisions at 11.5 GeV for different centralities.	59
3.19	The K^{*0} meson transverse momentum (p_T) spectra at mid-rapidity ($ y < 1$) are shown for various collision centrality intervals in Au+Au collisions at $\sqrt{s_{NN}} = 7.7, 11.5, 14.5, 19.6, 27,$ and 39 GeV. The solid lines depict the Levy-Tsallis fit to the measured data, while the dashed lines represent the extrapolation to the unmeasured low p_T region. Both statistical and systematic uncertainties are smaller than the marker size.	60
3.20	The mid-rapidity yield of K^{*0} meson as a function of the average number of participating nucleons ($\langle N_{part} \rangle$) in Au+Au collisions at $\sqrt{s_{NN}} = 7.7, 11.5, 14.5, 19.6, 27,$ and 39 GeV is shown. The vertical bars represent the statistical uncertainties, while the open boxes indicate the systematic uncertainties.	61
3.21	The mid-rapidity yield per average number of participating nucleons for $K^{*0}, K^\pm, p,$ and \bar{p} as a function of $\langle N_{part} \rangle$ in Au+Au collisions at $\sqrt{s_{NN}} = 7.7, 11.5, 14.5, 19.6, 27,$ and 39 GeV is presented. The $K^\pm, p,$ and \bar{p} yield has been taken from ref [15, 26]. The vertical bars indicate statistical uncertainties, while the open boxes represent systematic uncertainties.	62
3.22	The mean transverse momentum of K^{*0} meson as a function of the average number of participating nucleons ($\langle N_{part} \rangle$) in Au+Au collisions at $\sqrt{s_{NN}} = 7.7, 11.5, 14.5, 19.6, 27,$ and 39 GeV is shown. The vertical bars represent the statistical uncertainties, while the open boxes indicate the systematic uncertainties.	63
3.23	The mean transverse momentum for $K^{*0}, \pi^\pm, K^\pm, p(\bar{p})$ as a function of $\langle N_{part} \rangle$ in Au+Au collisions at $\sqrt{s_{NN}} = 7.7, 11.5, 14.5, 19.6, 27,$ and 39 GeV is presented. The $\pi^\pm, K^\pm, p(\bar{p})$ results has been taken from ref. [15, 26] The vertical bars indicate statistical uncertainties, while the open boxes represent systematic uncertainties.	63
3.24	p_T - integrated yield ratios of resonances to their ground state particles (eg. K^{*0}/K and ϕ/K [27]) at midrapidity as a function of the average number of participating nucleons in Au+Au collisions at $\sqrt{s_{NN}} = 7.7, 11.5, 14.5, 19.6, 27,$ and 39 GeV is shown. Vertical bars represent statistical uncertainties, while boxes indicate systematic uncertainties. Since error bars are large in the measurement, the dashed lines are included to guide the reader.	64
3.25	The K^{*0}/K ratio at mid-rapidity as a function of $(dN_{ch}/dy)^{1/3}$ in Au+Au collisions at $\sqrt{s_{NN}} = 7.7, 11.5, 14.5, 19.6, 27,$ and 39 GeV is presented. Vertical bars denote statistical uncertainties, and boxes represent systematic uncertainties. The results are compared with previously published measurements from STAR [12, 25] and ALICE [14, 28].	64

3.26	The beam energy dependence of K^{*0}/K ratio in e+e [29–32], p+p [25,33–35], d+Au [13], p+Pb [36,37] and most-central C+C [38], Si+Si [38], Au+Au [12], Cu+Cu [12] and Pb+Pb [14,28] collisions. For e+e and p+p collisions, the bars denote the quadratic sum of statistical and systematic uncertainties. For p+A and A+A data, the bars denote the statistical uncertainties and the boxes denote the systematic uncertainties.	65
3.27	The ϕ/K^{*0} ratio at midrapidity as a function of the average number of participating nucleons in Au+Au collisions at $\sqrt{s_{NN}} = 7.7, 11.5, 14.5, 19.6, 27$, and 39 GeV is shown. Vertical bars represent statistical uncertainties, while boxes indicate systematic uncertainties.	66
3.28	The lower bound on the time difference (Δt) between chemical and kinetic freeze-out is presented as a function of the average number of participating nucleons. These results are compared with prior measurements from STAR and ALICE. The error bars represent the combined statistical and systematic uncertainties, propagated from the uncertainties in the K^{*0}/K ratio.	67
3.29	$K\pi$ invariant mass for 0-20 % centrality at $\sqrt{s_{NN}} = 7.7$ GeV.	69
3.30	$K\pi$ invariant mass for 20-40 % centrality at $\sqrt{s_{NN}} = 7.7$ GeV.	69
3.31	$K\pi$ invariant mass for 40-60 % centrality at $\sqrt{s_{NN}} = 7.7$ GeV.	70
3.32	$K\pi$ invariant mass for 60-80 % centrality at $\sqrt{s_{NN}} = 7.7$ GeV.	70
3.33	$K\pi$ invariant mass for 0-10 % centrality at $\sqrt{s_{NN}} = 11.5$ GeV.	71
3.34	$K\pi$ invariant mass for 10-20 % centrality at $\sqrt{s_{NN}} = 11.5$ GeV.	71
3.35	$K\pi$ invariant mass for 20-30 % centrality at $\sqrt{s_{NN}} = 11.5$ GeV.	72
3.36	$K\pi$ invariant mass for 30-40 % centrality at $\sqrt{s_{NN}} = 11.5$ GeV.	72
3.37	$K\pi$ invariant mass for 40-60 % centrality at $\sqrt{s_{NN}} = 11.5$ GeV.	73
3.38	$K\pi$ invariant mass for 60-80 % centrality at $\sqrt{s_{NN}} = 11.5$ GeV.	73
3.39	$K\pi$ invariant mass for 0-10 % centrality at $\sqrt{s_{NN}} = 14.5$ GeV.	74
3.40	$K\pi$ invariant mass for 10-20 % centrality at $\sqrt{s_{NN}} = 14.5$ GeV.	74
3.41	$K\pi$ invariant mass for 20-30 % centrality at $\sqrt{s_{NN}} = 14.5$ GeV.	75
3.42	$K\pi$ invariant mass for 30-40 % centrality at $\sqrt{s_{NN}} = 14.5$ GeV.	75
3.43	$K\pi$ invariant mass for 40-60 % centrality at $\sqrt{s_{NN}} = 14.5$ GeV.	76
3.44	$K\pi$ invariant mass for 60-80 % centrality at $\sqrt{s_{NN}} = 14.5$ GeV.	76
3.45	$K\pi$ invariant mass for 0-10 % centrality at $\sqrt{s_{NN}} = 19.6$ GeV.	77
3.46	$K\pi$ invariant mass for 10-20 % centrality at $\sqrt{s_{NN}} = 19.6$ GeV.	77
3.47	$K\pi$ invariant mass for 20-30 % centrality at $\sqrt{s_{NN}} = 19.6$ GeV.	78
3.48	$K\pi$ invariant mass for 30-40 % centrality at $\sqrt{s_{NN}} = 19.6$ GeV.	78
3.49	$K\pi$ invariant mass for 40-60 % centrality at $\sqrt{s_{NN}} = 19.6$ GeV.	79
3.50	$K\pi$ invariant mass for 60-80 % centrality at $\sqrt{s_{NN}} = 19.6$ GeV.	79
3.51	$K\pi$ invariant mass for 0-10 % centrality at $\sqrt{s_{NN}} = 27$ GeV.	80
3.52	$K\pi$ invariant mass for 10-20 % centrality at $\sqrt{s_{NN}} = 27$ GeV.	80
3.53	$K\pi$ invariant mass for 20-30 % centrality at $\sqrt{s_{NN}} = 27$ GeV.	81
3.54	$K\pi$ invariant mass for 30-40 % centrality at $\sqrt{s_{NN}} = 27$ GeV.	81
3.55	$K\pi$ invariant mass for 40-60 % centrality at $\sqrt{s_{NN}} = 27$ GeV.	82
3.56	$K\pi$ invariant mass for 60-80 % centrality at $\sqrt{s_{NN}} = 27$ GeV.	82
3.57	$K\pi$ invariant mass for 0-10 % centrality at $\sqrt{s_{NN}} = 39$ GeV.	83
3.58	$K\pi$ invariant mass for 10-20 % centrality at $\sqrt{s_{NN}} = 39$ GeV.	83
3.59	$K\pi$ invariant mass for 20-30 % centrality at $\sqrt{s_{NN}} = 39$ GeV.	84
3.60	$K\pi$ invariant mass for 30-40 % centrality at $\sqrt{s_{NN}} = 39$ GeV.	84
3.61	$K\pi$ invariant mass for 40-60 % centrality at $\sqrt{s_{NN}} = 39$ GeV.	85
3.62	$K\pi$ invariant mass for 60-80 % centrality at $\sqrt{s_{NN}} = 39$ GeV.	85
3.63	p_T -spectra comparison for yield extraction using simple and relativistic breittwigner function.	87

4.1	The evolution of hadronic interactions for meson-meson (M+M) and meson-baryon (M+B) pairs at $\sqrt{s_{NN}} = 7.7$ and 200 GeV (for Au+Au and Cu+Cu collisions) with hadronic cascade time based on the UrQMD model.	94
4.2	Invariant mass distribution of K^{*0} meson (blue line) and reconstructed $K\pi$ pairs (red dots) for (a) 0-10% and (b) 60-80% Au+Au collisions at 7.7 GeV from UrQMD model.	95
4.3	The p_T integrated yield of K^{*0} and charged kaons vs $\langle N_{part} \rangle$ in Au+Au collisions at 11.5 GeV (upper panel) and 39 GeV (lower panel), measured using the UrQMD model.	96
4.4	The resonance to non-resonance ratios (K^{*0}/K and ϕ/K) vs $\langle N_{part} \rangle$ measured at mid-rapidity from the STAR experiment [39] compared with corresponding thermal model and UrQMD model results at $\sqrt{s_{NN}} = 11.5$ and 39 GeV. The systematic and statistical uncertainties on the experimental data are shown by the caps and boxes respectively.	97
4.5	The K^{*0}/K ratio as a function of $\sqrt{s_{NN}}$ for central (0-10%) and peripheral (60-80%) Au+Au collisions at midrapidity [39] is shown alongside corresponding measurements from thermal and UrQMD models.	98
4.6	The p_T -integrated yield (dN/dy) for K^{*0} mesons as a function of rapidity is shown for 0-10% and 60-80% centralities at $\sqrt{s_{NN}} = 11.5$ GeV (upper panel) and 19.6 GeV (lower panel), respectively.	99
4.7	The p_T -integrated yield (dN/dy) for K^{*0} mesons with $\tau = 10$ and 20 fm/c, normalized by the dN/dy value at $\tau = 5$ fm/c, is plotted as a function of rapidity for both 0-10% and 60-80% centralities.	99
4.8	Left Panel: Multiplicity dependent p/π ratio (left panel) , Λ/π (right panel) ratio for $\sqrt{s_{NN}} = 7.7$ and 200 GeV at mid rapidity ($ y < 0.5$) from UrQMD model.	100
4.9	p_T -integrated K^{*0} and charged K yield in different collision systems and beam energies from UrQMD model.	101
4.10	The ratio of reconstructed to true resonance counts for K^{*0} (left panel) and ϕ (right panel) resonances, respectively, as a function of $(dN_{ch}/d\eta)^{1/3}$ from the UrQMD model in Au+Au collisions at $\sqrt{s_{NN}} = 7.7$ and 200 GeV.	101
4.11	The K^{*0}/K ratio calculated at mid-rapidity as a function of $(dN_{ch}/d\eta)^{1/3}$ for various collision systems and beam energies from the UrQMD calculation.	102
5.1	(Left panel) K^{*0} signal from unlike sign pair (red marker) and background estimated from track rotation method (black marker).(Right panel) Invariant mass distribution of $K\pi$ pairs after subtraction of background estimated from track rotation method. The blue line denotes the Breit Wigner fit and red line represents the fit for the residual background. The results are shown for $1.0 < p_T < 1.2$ GeV/c and 0 – 10% centrality at $\sqrt{s_{NN}} = 19.6$ (top panels) and 7.7 (bottom panels) GeV respectively. The error bars shown are statistical only.	107
5.2	The Significance of the K^{*0} signal as a function of p_T for different centralities at $\sqrt{s_{NN}} = 19.6$ GeV. The green and red shaded areas denote the same for BES-I and BES-II respectively.	108
5.3	The p_T dependent detector efficiency \times Acceptance for K^{*0} meson in Au+Au collisions at $\sqrt{s_{NN}} = 7.7$ -27 GeV. The statistical error bar shown here are within the marker size.	108
5.4	The tracking efficiency comparison for the K^{*0} meson in 0-10% (top panel) and 60-80% (bottom panel) centrality ranges is presented for both BES-I and BES-II. The statistical error bar shown here are within the marker size.	109

5.5	The K^{*0} meson transverse momentum (p_T) spectra at mid-rapidity ($ y < 1$) are shown for various collision centrality intervals in Au+Au collisions at $\sqrt{s_{NN}} = 7.7, 11.5, 14.5, 19.6, 27, \text{ and } 39$ GeV. Both statistical and systematic uncertainties are smaller than the marker size. These results are not published or approved as STAR preliminary and are currently under review within the collaboration.	111
5.6	Comparison between like sign and track rotation method of background estimation for K^{*0} meson at Au+Au 19.6 GeV. Error bars shown are statistical only and within marker size.	112
5.7	The mid-rapidity p_T -integrated yield of K^{*0} meson as a function of centrality for Au+Au collisions at $\sqrt{s_{NN}} = 7.7\text{-}27$ GeV. The BES-II results are shown with red markers and compared with that of BES-I presented by gray markers. The statistical and systematic uncertainties are denoted by vertical bars and caps respectively.	113
5.8	The mid-rapidity p_T -integrated yield of K^{*0} (left panel) and charged kaons (right panel) is shown as a function of multiplicity or $(dN_{ch}/dy)^{1/3}$ for different collision systems and center of mass energies [15, 26, 40, 41]. The error bars displayed represent the quadrature sum of statistical and systematic uncertainties. The BES-II K^{*0} results are not published or approved as STAR preliminary and are currently under review within the collaboration.	113
5.9	K^{*0}/K ratio as a function of multiplicity or $(dN_{ch}/dy)^{1/3}$ in Au+Au collisions at $\sqrt{s_{NN}} = 7.7\text{-}27$ GeV. The measurements are compared with previous experimental results [12, 14, 28]. The statistical and systematic uncertainties are shown by error bars and boxes respectively. The model calculation (blue solid line) has been taken from [42]. UrQMD results for $\sqrt{s_{NN}} = 7.7$ and 200 GeV Au+Au collisions are shown in colored bands and taken from [43]. The BES-II K^{*0} results are not published or approved as STAR preliminary and are currently under review within the collaboration.	114
5.10	Collision energy dependence of K^{*0}/K ratio in Au+Au collisions in most central (left panel) and most peripheral (right panel) collisions. The results are compared with thermal model (dashed line) and transport model (blue band), taken from ref [43, 44]. The BES-II K^{*0} results are not published or approved as STAR preliminary and are currently under review within the collaboration.	116
5.11	Nuclear modification factor (R_{cp}) of K^{*0} , K_s^0 , Λ and ϕ for Au+Au collisions at $\sqrt{s_{NN}} = 7.7, 11.5, 19.6$ and 27 GeV. The R_{cp} values for K_s^0 , Λ and ϕ are from BES-I measurements, taken from ref [27]. The results for K^{*0} meson is obtained within $ y < 1.0$ with for other particles the calculation is done within $ y < 0.5$. The vertical error bars represent statistical uncertainties, while caps indicate systematic uncertainties. On the left of each panel, the uncertainty in N_{coll} scaling for R_{cp} measurement in BES-I and BES-II is shown by gray and blue bands at unity. The BES-II K^{*0} results are not published or approved as STAR preliminary and are currently under review within the collaboration.	117
5.12	K^{*0} yield as a function of rapidity for different centralities and center of mass energies. The vertical error bars represent statistical uncertainties, while caps indicate systematic uncertainties. These results are not published or approved as STAR preliminary and are currently under review within the collaboration.	118
5.13	Comparison of The K^{*0} meson transverse momentum (p_T) spectra at mid-rapidity ($ y < 1.0$) for BES-I and BES-II data sets. The error bars shown here are statistical only and are within the marker size.	119

5.14	The tracking efficiency \times acceptance for the K^{*0} meson is presented across different centralities, rapidities, and collision energies, ranging from $\sqrt{s_{NN}} = 7.7$ -27 GeV for Au+Au collisions. The statistical errors are within the marker size.	120
5.15	The corrected p_T spectra for K^{*0} meson in diferent rapidity bins for Au+Au collisions, $\sqrt{s_{NN}} = 7.7$ GeV. The error bars shown here are statistical only. . .	121
5.16	The corrected p_T spectra for K^{*0} meson in diferent rapidity bins for Au+Au collisions, $\sqrt{s_{NN}} = 11.5$ GeV. The error bars shown here are statistical only. .	121
5.17	The corrected p_T spectra for K^{*0} meson in diferent rapidity bins for Au+Au collisions, $\sqrt{s_{NN}} = 14.6$ GeV. The error bars shown here are statistical only. .	122
5.18	The corrected p_T spectra for K^{*0} meson in diferent rapidity bins for Au+Au collisions, $\sqrt{s_{NN}} = 19.6$ GeV. The error bars shown here are statistical only. .	122
5.19	The corrected p_T spectra for K^{*0} meson in diferent rapidity bins for Au+Au collisions, $\sqrt{s_{NN}} = 27$ GeV. The error bars shown here are statistical only. . .	123
6.1	Directed flow (v_1) as a function rapidity (y) for identified hadrons (π^\pm , K^\pm , $p(\bar{p})$) in central (0-10%) Au+Au collisions at $\sqrt{s_{NN}} = 7.7, 11.5, 14.5, 19.6, 27$ and 39 GeV from UrQMD model. The results with different marker colors correspond to different hadronic cascade lifetime (τ) = 5, 10 and 20 fm/c. . . .	127
6.2	Directed flow (v_1) as a function rapidity (y) for identified hadrons (π^\pm , K^\pm , $p(\bar{p})$) in mid-central (10-40%) Au+Au collisions at $\sqrt{s_{NN}} = 7.7, 11.5, 14.5, 19.6, 27$ and 39 GeV from UrQMD model. The results with different marker colors correspond to different hadronic cascade lifetime (τ) = 5, 10 and 20 fm/c.	128
6.3	Directed flow (v_1) as a function rapidity (y) for identified hadrons (π^\pm , K^\pm , $p(\bar{p})$) in peripheral (40-80%) Au+Au collisions at $\sqrt{s_{NN}} = 7.7, 11.5, 14.5, 19.6, 27$ and 39 GeV from UrQMD model. The results with different marker colors correspond to different hadronic cascade lifetime (τ) = 5, 10 and 20 fm/c.	128
6.4	Slope of rapidity dependent v_1 (dv_1/y) as a function of collision energy ($\sqrt{s_{NN}}$) for identified hadrons (π^\pm , K^\pm , $p(\bar{p})$) with different hadronic cascade lifetime (τ) = 5, 10 and 20 fm/c.	129
6.5	Difference in rapidity differential directed flow slope ($\Delta dv_1/y$) of positively and negatively charged light flavored hadrons (π , K and p) as a function of collision centrality for Au+Au collisions at $\sqrt{s_{NN}} = 7.7, 11.5, 14.5, 19.6, 27$ and 39 GeV with different hadronic cascade lifetime (τ) = 5, 10 and 20 fm/c. .	130
6.6	Comparison of difference in rapidity differential directed flow slope ($\Delta dv_1/y$) of positively and negatively charged light flavored hadrons (π , K and p) at 27 GeV Au+Au collisions by STAR [45] with UrQMD calculations with $\tau = 20$ fm/c.	130

List of Tables

1.1	Conversion of some basic physical quantities in terms of natural units. . .	15
2.1	Beam parameters achieved during the phase-I of RHIC Beam Energy Scan (RHIC-BES) program, for different center of mass energies in Au+Au collisions. The data is collected from [46].	27
2.2	Beam parameters achieved during the phase-II of RHIC Beam Energy Scan (RHIC-BES) program for different center of mass energies in Au+Au collisions. The data is collected from [46].	28
2.3	The pseudo-rapidity coverage of various trigger detectors in STAR experiment. The data is collected from [47].	37
3.1	Collision energy, production year, production tag, and triggers used. . .	41
3.2	List of event cuts applied on primary vertex selection for each collision energy and number of minimum bias good events.	43
3.3	experimental values of σ_{NN}^{inel} and n_{pp}	44
3.4	List of track selection cuts applied for the analysis presented in this chapter. . .	45
3.5	Fractional systematic uncertainties (in %) for the p_T spectra, dN/dy and $\langle p_T \rangle$ of K^{*0} meson at $\sqrt{s_{NN}} = 7.7 - 39$ GeV.	58
3.6	Reference multiplicity or N_{ch}^{raw} values for different collision energies. . .	86
3.7	$\langle N_{part} \rangle$ values for different collision energies.	86
3.8	$\langle N_{coll} \rangle$ values for different collision energies.	86
3.9	Lorentz factor (γ) for Au+Au collisions at $\sqrt{s_{NN}} = 7.7-39$ GeV.	87
3.10	Mid rapidity dN/dy and $\langle p_T \rangle$ of K^{*0} meson in Au+Au collisions at $\sqrt{s_{NN}} = 7.7$ GeV.	88
3.11	Mid rapidity dN/dy and $\langle p_T \rangle$ of K^{*0} meson in Au+Au collisions at $\sqrt{s_{NN}} = 11.5$ GeV.	88
3.12	Mid rapidity dN/dy and $\langle p_T \rangle$ of K^{*0} meson in Au+Au collisions at $\sqrt{s_{NN}} = 14.5$ GeV.	88
3.13	Mid rapidity dN/dy and $\langle p_T \rangle$ of K^{*0} meson in Au+Au collisions at $\sqrt{s_{NN}} = 19.6$ GeV.	89
3.14	Mid rapidity dN/dy and $\langle p_T \rangle$ of K^{*0} meson in Au+Au collisions at $\sqrt{s_{NN}} = 27$ GeV.	89
3.15	Mid rapidity dN/dy and $\langle p_T \rangle$ of K^{*0} meson in Au+Au collisions at $\sqrt{s_{NN}} = 39$ GeV.	89
3.16	Mid rapidity particle ratios in Au+Au collisions at $\sqrt{s_{NN}} = 7.7$ GeV. . .	89
3.17	Mid rapidity particle ratios in Au+Au collisions at $\sqrt{s_{NN}} = 11.5$ GeV. . .	90
3.18	Mid rapidity particle ratios in Au+Au collisions at $\sqrt{s_{NN}} = 14.5$ GeV. . .	90
3.19	Mid rapidity particle ratios in Au+Au collisions at $\sqrt{s_{NN}} = 19.6$ GeV. . .	90
3.20	Mid rapidity particle ratios in Au+Au collisions at $\sqrt{s_{NN}} = 27$ GeV. . .	90
3.21	Mid rapidity particle ratios in Au+Au collisions at $\sqrt{s_{NN}} = 39$ GeV. . .	91
5.1	Event selection cuts for min-bias events.	105
5.2	Variation in selection criteria for systematic uncertainty estimation. . .	110
5.3	The contribution of various sources to the systematic uncertainties for K^{*0} yield at $ y < 1.0$ in Au+Au collisions at $\sqrt{s_{NN}} = 7.7-27$ GeV. . . .	111

5.4	Level of suppression of K^{*0}/K ratio in central collisions w.r.t peripheral collisions or thermal model predictions.	119
5.5	Average multiplicity $(dN_{ch}/dy)^{1/3}$ values for different collision energies.	123
5.6	Reference multiplicity or N_{ch}^{raw} values for different collision energies for BES-II data sets.	124
5.7	$\langle N_{part} \rangle$ values for different collision energies for BES-II data sets.	124
5.8	$\langle N_{coll} \rangle$ values for different collision energies for BES-II data sets.	124

Chapter 1

Introduction

”What is the smallest constituent of the matter ???”-this fundamental question has driven the curiosity of elementary particle physicists for generations. The foundation of elementary particle physics was laid in the 1897 with the discovery of the electron by J. J. Thomson [48]. However, the electrically neutral atom has a mass far greater than that of an electron. In 1911, E. Rutherford’s renowned α -particle scattering experiment revealed the existence of a heavy positively charged atomic nucleus [49]. This was followed by the discovery of the proton by Rutherford in 1919 [50] and the neutron by J. Chadwick in 1932 [51], which provided insight into the composition and properties of the atomic nucleus. Later, electron-proton scattering experiments, known as Deep-Inelastic Scattering, uncovered the internal structure of the proton, revealing fractional charge-carrying partons. Furthermore, the Deutsches Elektronen-Synchrotron (DESY) experiments in Germany confirmed the existence of gluons (the strong force carriers) through e^+e^- annihilation experiments, in the year 1979 [52].

As per the knowledge gained so far, protons and neutrons are not the fundamental constituents of matter. Atoms are composed of electrons and nucleons (protons and neutrons), with the nucleons held together within the atomic nucleus by the strong force, mediated by gluons. The Standard Model (SM), developed by Glashow [53], Salam [54], and Weinberg [55], encompasses all known elementary constituents of matter and the force carriers responsible for mediating the interactions among them. Furthermore, it provides a comprehensive description of three fundamental forces of nature—strong, electromagnetic and weak interactions—leaving gravitational force outside its framework. However, the model has evolved through a series of theoretical and experimental breakthroughs during the latter half of the 20th century [53–59]. The existence of force carriers such as the W^\pm and Z^0 bosons, predicted by the Standard Model, was

later experimentally confirmed [60]. The most recent addition to this framework was the experimental discovery of the Higgs boson at CERN, by the CMS [61] and ATLAS [62] collaboration in 2012, that was theoretically proposed by Peter Higgs in the year 1964 [63,64].

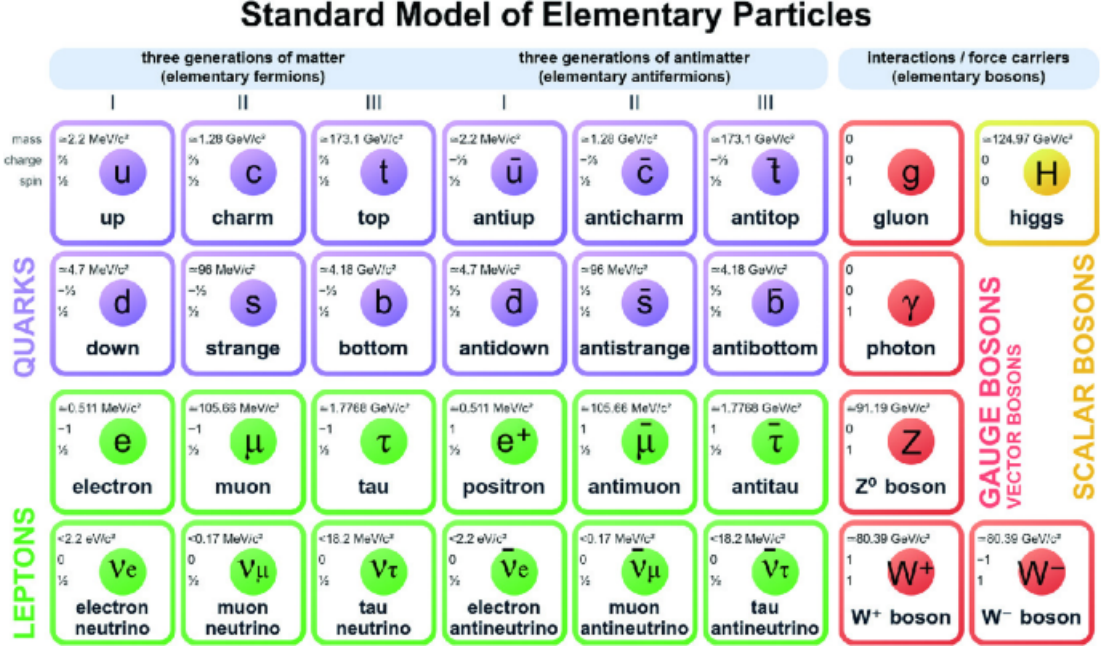


Figure 1.1: The visual representation of the standard model, with three generations of elementary particles, along with force-carrying gauge bosons and Higgs boson. The figure has been sourced from [1].

Figure 1.1 provides a pictorial representation of ultimate constituents of the standard model. It depicts 12 elementary fermions (6 leptons and 6 quarks) along with their corresponding antiparticles, which have identical masses but opposite quantum numbers. These particles are organized into three generations, each comprising two quarks and two leptons. Additionally, the figure includes the force carriers for three of the four fundamental forces of nature, known as gauge bosons: photons for electromagnetic interactions, gluons for strong interactions, and W^\pm and Z^0 bosons for weak interactions. The interaction of elementary particles with the Higgs field imparts mass to these particles and the quantum excitation of this field produces the Higgs boson. In the Standard Model, the Higgs boson is a scalar boson that have spin 0.

Hence, in total, the Standard Model comprises 12 leptons, 36 quarks, 8 gluons, 3 vector bosons (W^\pm , Z^0), 1 photon, and 1 Higgs boson, making a total of 61 constituents.

1.1 Insights into Quantum Chromodynamics

There are specific theories that describe the fundamental forces of nature. For example, Quantum Chromodynamics (QCD) [65] explains the strong interaction, while Quantum Electrodynamics (QED) [66] describes the electromagnetic interaction. Similar to how electric charge is used in QED, QCD involves three types of "color charges," commonly labeled as red, blue, and green, along with their corresponding anti-colors: anti-red, anti-blue, and anti-green. Quarks, the fundamental particles in QCD, carry color charges but are never found isolated in nature. Instead, they combine in ways that result in a net

”color-neutral” charge. For example, a meson is made up of a pair of quark and an antiquark (color + anti-color), whereas a baryon consists of three quarks (red + blue + green). This confinement ensures that observable particles always have a total zero color charge.

The QCD interaction potential takes the following form:

$$V(r) = \frac{-4}{3} \frac{\alpha_s}{r} + kr \quad (1.1.1)$$

Here α_s , is the running QCD coupling constant (as the coupling constant depends on energy, hence the term ”running”), that determines the strength of the strong interaction, r is the distance between the interacting particles and k is the color string tension constant.

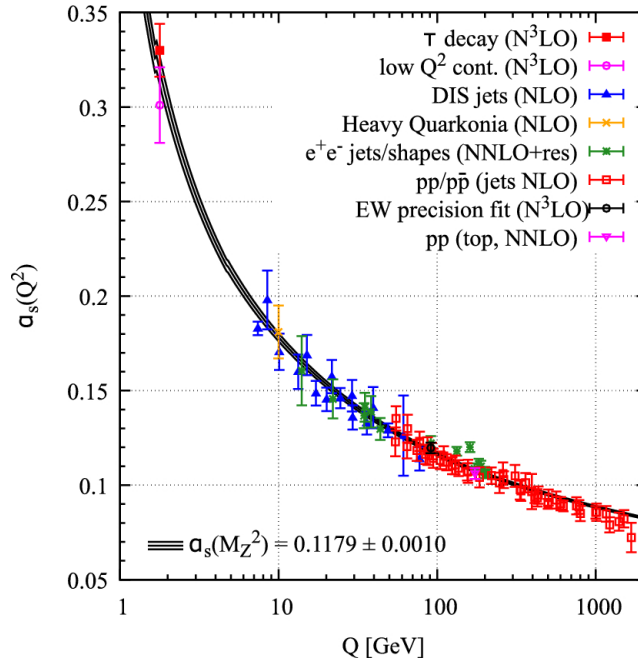


Figure 1.2: The observed variation of the running coupling constant $\alpha_s(Q)$ with respect to the energy scale Q . The figure has been sourced from [2].

The strong coupling constant, that depend on the momentum transfer, is defined as follows.

$$\alpha_s(Q^2) = \frac{12\pi}{(11n_c - 2n_f) \ln\left(\frac{Q^2}{\Lambda_{QCD}^2}\right)} \quad (1.1.2)$$

Where,

n_c = Number of color charges

n_f = Number of flavors

Q^2 = Momentum transfer

Λ_{QCD} = QCD scale parameter

It is challenging to precisely measure Λ_{QCD} experimentally. Hence, the theoretically predicted value of Λ_{QCD} is estimated to lie within the range of 0.1–0.5 GeV. Figure 1.2 illustrates the variation of the QCD coupling constant across a wide range of momentum

transfers. QCD predictions align quite well with experimental data [2]. The energy dependence of Λ_{QCD} leads to two important consequences in QCD. From the figure, it is evident that at large distance scales (low momentum transfer), the coupling constant is large. This results in a strong binding force between quarks, confining them within hadrons—a phenomenon known as "confinement". Conversely, at small distance scales (high momentum transfer), the coupling constant becomes very small, allowing quarks to behave as nearly free, non-interacting particles. In this state, quarks and gluons can exist freely in the vacuum, a phenomenon termed "asymptotic freedom".

The discovery of asymptotic freedom in 1973 led to the awarding of the 2004 Nobel Prize in Physics to David Gross, Frank Wilczek, and David Politzer [65, 67, 68]. As a direct consequence of asymptotic freedom, it is theorized that at extremely high temperatures or pressure QCD matter can exist as a state of free quarks and gluons.

1.2 QCD phase transition and Quark Gluon Plasma

The phase transition in the Quantum Electrodynamics (QED) sector is well understood, with order parameters serving as variables to distinguish between different phases. For instance, during the first-order phase transition of water, the order parameter is the density, which changes as water transitions between solid, liquid, and gaseous states. Similarly, in the transition from a ferromagnetic to a paramagnetic phase, the order parameter is magnetization. Ferromagnets exhibit rotational symmetry, but heating them beyond the Curie temperature leads to spontaneous symmetry breaking, causing the magnetization to change and the system to transition into the paramagnetic phase [69, 70].

In the Quantum Chromodynamics (QCD) sector, the phase of deconfined quarks and gluons is associated with "chiral symmetry". However, in nature, quarks and gluons are bound within hadrons, resulting in the breaking of chiral symmetry. This raises a compelling question: Whether the broken chiral symmetry be restored under certain conditions? In 1974, following the discovery of asymptotic freedom, T.D. Lee [71], and J.C. Collins and M.J. Perry [72] predicted that at sufficiently high energy densities, it would be possible to create a dense nuclear matter composed of asymptotically free quarks and gluons. Such a state is expected to exist in extreme environments, such as the cores of neutron stars, during black hole explosions, and under the conditions that existed shortly after the Big Bang in the early universe.

While quarks and gluons are the fundamental degrees of freedom in the quark-gluon plasma (QGP) phase, a deconfined state of quarks and gluons alone does not fully define QGP. A more accurate definition describes QGP as a (locally) thermally equilibrated state of matter in which quarks and gluons are deconfined from hadrons, allowing the manifestation of color degrees of freedom over volumes significantly larger than typical nucleonic scales [6].

Using perturbation theory, QCD can be treated in a manner similar to QED at sufficiently high energies, where the coupling constant is small. However, at lower energies, the perturbative approach breaks down, and the self-interaction of gluons further complicates calculations, making analytical solutions challenging. In such scenarios, a non-perturbative, first-principle numerical approach, known as lattice QCD, is employed [73–76]. In the LQCD framework, the QCD is solved on a discrete space-time grid.

For QCD with two flavors of quarks, LQCD predicts a transition from hadronic matter (quarks and gluons are confined within the hadrons) to deconfined state of quarks and

gluons at a energy density of $\approx 1 \text{ GeV}/fm^3$ and a transition temperature (T_c) of around 170 MeV [73, 77]. This energy density is significantly higher than that of normal cold nuclear matter, which is around $0.16 \text{ GeV}/fm^3$. However, more recent calculations considering three quark flavors estimate the transition temperature T_c to be $156.5 \pm 1.5 \text{ MeV}$ at zero baryon chemical potential [73, 77].

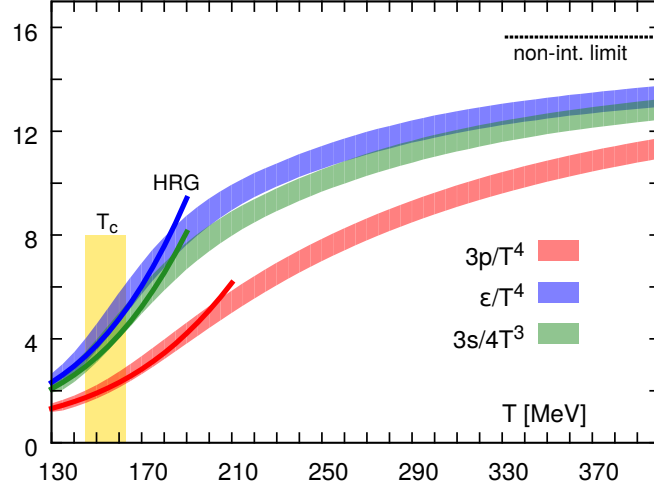


Figure 1.3: The variation of energy density, pressure density and entropy density as a function of temperature from (2+1) flavor lattice QCD calculations represented by coloured bands. The results from hadron resonance gas (HRG) model is presented by the solid lines at the lower temperature side. The dashed lines at the higher temperature side denotes, the non-interacting HRG or the Stefan-Boltzmann ideal gas limit. The figure has been sourced from [3].

Fig 1.3, shows the calculations of bulk thermodynamic variables from LQCD, considering (2+1) quark flavors (2 light quarks (u, d) which are assumed to have degenerate masses, $m_u = m_d$, and a heavier strange quark (s), with mass m_s) as a function of temperature. Each observable is normalised to certain powers of temperature in order to make it dimensionless.

Several experimental and theoretical studies have been conducted to determine the emergent properties of the Quark-Gluon Plasma (QGP). These studies suggest that the medium formed in typical central Au+Au collisions at $\sqrt{s_{NN}} = 200 \text{ GeV}$ reaches a temperature of approximately 10^{12} K . It exhibits a ratio of shear viscosity to entropy density (η/s) close to the theoretical lower bound of $1/4\pi$, and it has an estimated vorticity of about $10^{21} s^{-1}$. Consequently, the QGP is often regarded as the most "perfect" fluid [78–81] and the most vortical fluid [82, 83] in the universe.

1.2.1 QCD phase diagram

In 1975, Cabibbo and Parisi proposed the first version of a phase diagram illustrating a confined state of quarks and gluons in hadronic matter and a deconfined state in the vacuum [84]. While many aspects of QCD phase diagram remain conjectural, continuous advancements in experimental and theoretical studies have significantly enhanced the understanding of the QCD phase diagram as it is known in the present day.

Although various representations exist for phase diagrams, the QCD phase diagram is typically depicted in terms of temperature (T) and the chemical potential (μ) associated with conserved charges such as baryon number (B), electric charge (Q) and strangeness

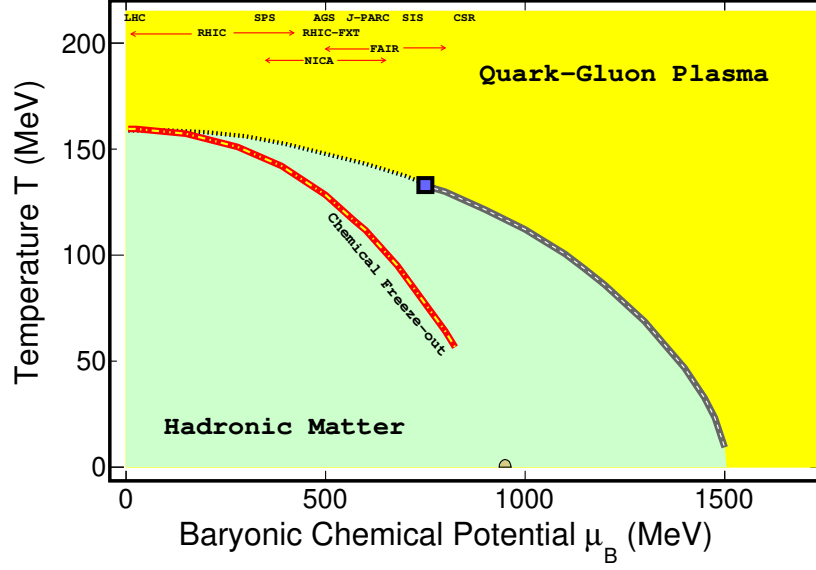


Figure 1.4: The conjectured QCD phase diagram depicts various phases of strongly interacting matter. It illustrates a transition from a hadron gas to a deconfined quark-gluon plasma (QGP) phase through smooth crossover transition (represented by the dashed line) at the transition temperature, and first-order phase transition (indicated by the solid black line), that is theorized to terminate at the possible QCD critical point (marked by a solid-square). The chemical freeze-out curve is indicated by the red-yellow dotted line, obtained through thermal model fits to particle yield data. The semi-circular marker at $T \approx 0$ and $\mu_B \approx 925$ MeV represents ground-state nuclear matter. Different regions of the phase diagram are accessible through various experimental facilities, as indicated in the upper section of the figure. The figure has been sourced from [4].

(S) in strong interactions, assuming thermal equilibrium. The chemical potential (μ) denotes the energy required to alter the conserved quantum numbers (B , Q , S) in a system. In relativistic heavy-ion collisions, the nuclei taking part in the collision possess fixed electric charge-to-baryon number ratio, and the net strangeness of the system is zero. Consequently, in experimental contexts, the QCD phase diagram is effectively reduced to a temperature (T) versus the baryon chemical potential (μ_B) plot, where each point, where the T or μ_B is non zero, presents a thermal equilibrium state.

Figure 1.4 shows the conjectured QCD phase diagram on the $T-\mu_B$ plane, presenting two separate phases of strongly interacting matter: the confined phase of quarks and gluons within the hadrons commonly known as hadronic phase and the deconfined state of quarks and gluons referred as quark-gluon plasma (QGP) phase. The region at $T = 0$ and $\mu_B = 0$ represents the QCD vacuum, while that for $T = 0$ and $\mu_B \approx 925$ MeV corresponds to normal cold nuclear matter at its ground state [85]. At small μ_B ($\mu_B \approx 0$) and high temperatures (T), presents conditions similar to those of the early universe. In this region, lattice QCD (LQCD) predicts a smooth crossover transition, where the order parameter (susceptibility) changes gradually [86, 87]. In contrast, at large μ_B , LQCD and other QCD-based theories predict a first-order phase transition [88–90]. The QCD critical point (CP) is expected to lie at the point where the first-order phase transition terminates and the crossover region begins [91]. For an in-depth discussion on the phases of QCD matter at even higher μ_B , the book chapter titled "The Condensed Matter Physics of QCD" by Krishna Rajagopal and Frank Wilczek provides valuable insights [92].

1.3 Relativistic Heavy-Ion collisions : The Experimental realisation

In the experimental context, heavy nuclei are accelerated nearly to the speed of light and then collided to deposit a large amount of energy within a very small spatial region of the order of nuclear volume. This energy density is expected to be sufficient to achieve the high temperatures required for a deconfined state of quarks and gluons. The first attempts at such experiments began in the 1970s with the Bevalac experiment at Lawrence Berkeley National Laboratory (LBNL), USA, where nuclear collisions at energies of 1-2 GeV per nucleon were realized [93]. Subsequent progress came from facilities like the Alternating Gradient Synchrotron (AGS) at Brookhaven National Laboratory (BNL) and the Super Proton Synchrotron (SPS) at the European Organization for Nuclear Research (CERN), which enabled nuclear collisions at intermediate energy scales. In the present day, advanced experimental facilities such as the Relativistic Heavy Ion Collider (RHIC) at BNL and the Large Hadron Collider (LHC) at CERN have extended achievable energy ranges up to 200 GeV per nucleon pair at RHIC and several TeV at the LHC.

1.3.1 Space-time evolution

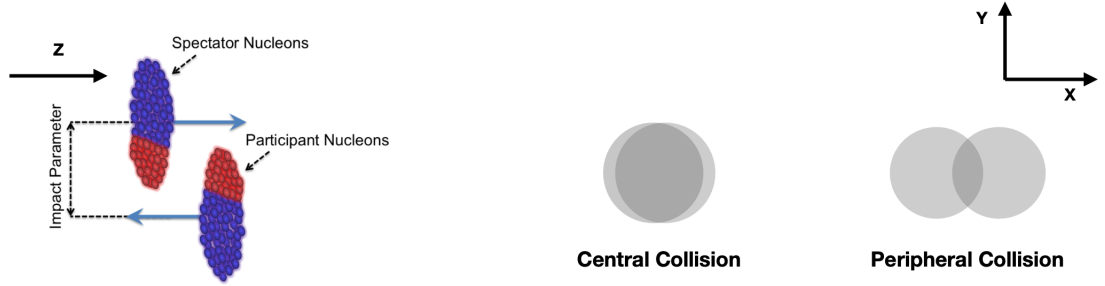


Figure 1.5: Left side: A schematic picture of a relativistic nuclear collision along z -direction, where the nucleons denoted by red colour are participant nucleons and those in blue colours are the spectator nucleons. Right side : The same collision picture in the transverse plane (xy -plane) for a central and peripheral collision.

Figure 1.5 illustrates a typical depiction of a heavy-ion collision. Two nuclei travel toward each other at nearly the speed of light along the z -axis in the laboratory frame. Due to relativistic effects, the spherical nuclei appear flattened like pancakes. During a collision event, the nucleons that participate in the interaction are referred to as participant nucleons, while those that do not interact are termed spectator nucleons. In a collision, the impact parameter describes the perpendicular distance between the centers of the two nuclei. On right side of Fig. 1.5, the collision is represented in the transverse plane (xy -plane), highlighting the overlap region between the two nuclei. A small impact parameter corresponds to a large overlap region, indicating a central collision, while a large impact parameter leads to a small overlap region, thus classifying the collision as peripheral.

Figure 1.6 shows the spacetime evolution of a relativistic heavy-ion collision, in a co-ordinate plane, where the vertical axis represents time (t) and the horizontal axis represents the spatial co-ordinate (z). Two nuclei approach each other at nearly the speed of light, colliding at $(0,0)$ coordinate in the $t - z$ plane. Here the upper half presents the

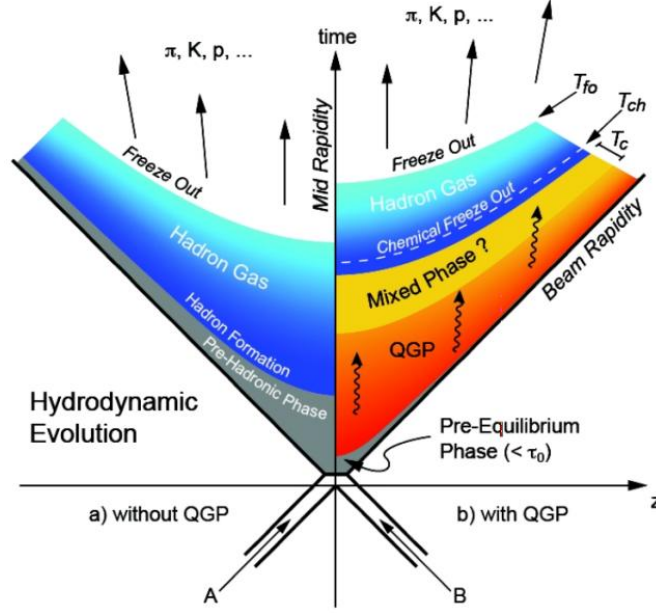


Figure 1.6: Schematic illustration of the space-time evolution of a relativistic heavy ion collision. The figure has been sourced from [5].

epoch after the collision while the lower half denotes the same before the collision. The lines $t^2 - z^2 = 0$ define the light cone, separating the time-like region ($t^2 - z^2 > 0$) within the cone, where particle production occurs after the collision, from the space-like region ($t^2 - z^2 < 0$) outside the cone, where particle production is absent. Proper time of the particles is given by $\tau = \sqrt{t^2 - z^2}$, is meaningful only within the time-like region, describing the system's evolution after the collision. Similarly, spacetime rapidity (η_s) is given by;

$$\eta_s = \frac{1}{2} \ln \left(\frac{t+z}{t-z} \right) \quad (1.3.1)$$

The variable can be defined only within the time-like region, further emphasizing that particle production occurs exclusively inside the light cone.

After the collision of two nuclei, energy is deposited in a very small volume, leading to two distinct possible scenarios depending on the energy density achieved. If the energy density is below the minimum threshold of approximately $1 \text{ GeV}/fm^3$ predicted by LQCD, the resulting system is a hadron gas phase, as depicted on the left side of Fig 1.6. Exceeding this threshold, a deconfined phase of quarks and gluons, known as the quark-gluon plasma (QGP), is expected to form. With further interactions among the particles, the medium reaches a local thermal equilibrium for a brief proper time, allowing the QGP to evolve. As the system evolves, it expands, and the temperature decreases. Relativistic hydrodynamics effectively describes this expansion. When the temperature falls below the critical or transition temperature (T_c), hadron formation begins. For a first-order phase transition, a mixed phase of partonic and hadronic matter may coexist at some point for a brief time. At the stage where inelastic collisions cease, fixing the relative particle abundances, the system undergoes "chemical freeze-out." Continued expansion increases the mean free path of particles, and when it becomes large enough to stop elastic collisions, "kinetic freeze-out" occurs. Beyond this point, particles freely

stream toward the detectors.

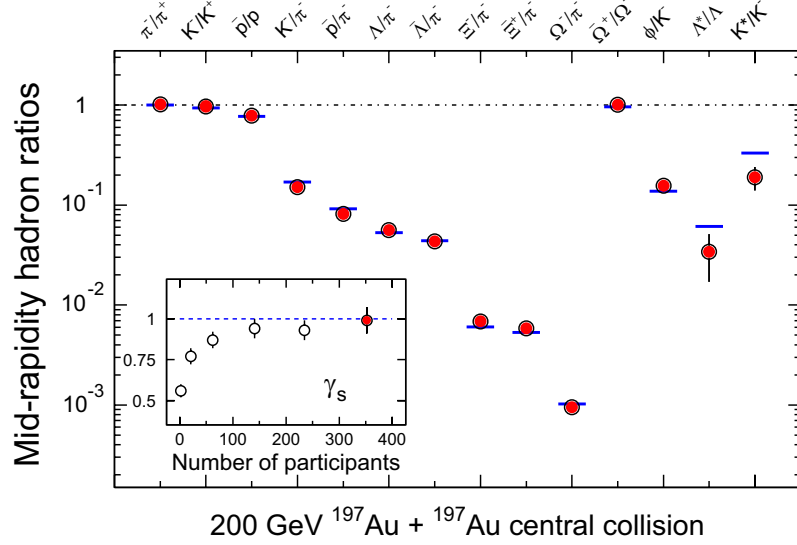


Figure 1.7: The mid-rapidity p_T -integrated particle yield ratios for central Au+Au collisions at $\sqrt{s_{NN}} = 200$ GeV. Fitting of experimental data to the statistical thermal model is shown by blue horizontal lines. The figure has been sourced from [6].

Figure 1.7 presents the comparison of the p_T -integrated particle ratios measured by the STAR experiment for central Au+Au collisions with predictions from statistical thermal model. The thermal model fits, represented by horizontal lines, assume thermal and chemical equilibrium at the freezeout surface. These measured particle ratios provide crucial constraints on the system's temperature and baryon chemical potential at chemical freezeout. The freezeout parameters obtained from the fits are: chemical freezeout temperature (T_{ch}) = 163 ± 5 MeV, baryon chemical potential (μ_B) = 24 ± 4 MeV, and strangeness saturation factor (γ_s) = 0.99 ± 0.07 [6, 94–96]. The estimated temperature is comparable with the lattice QCD (LQCD) predictions for the transition from a quark-gluon plasma phase to a hadron gas phase [97, 98]. The extracted T_{ch} is considered a lower limit for the thermalization temperature, assuming that thermalization occurs before chemical freezeout due to interactions among medium constituents. The strangeness saturation factor (γ_s), a non-equilibrium parameter in the thermal model fit [99], is kept as a free parameter. Its value ranges from ≈ 0.75 in peripheral collisions to unity in central collisions, indicating that the strange sector in the system produced during central Au+Au collisions at $\sqrt{s_{NN}} = 200$ GeV may also reach thermal equilibrium.

In the context of a hard-sphere uniform density particle source, the transverse momentum (p_T) spectral shape for particles at kinetic freeze-out is typically described by the Blast-Wave (combination of thermal source and radial flow) Model. The spectra distribution is given by as follows [100];

$$\frac{dN}{p_T dp_T} \propto \int_0^R r dr m_T I_0 \left(\frac{p_T \sinh \rho}{T_{kin}} \right) K_1 \left(\frac{m_T \cosh \rho}{T_{kin}} \right) \quad (1.3.2)$$

Where,

T_{kin} and β are the kinetic freeze-out temperature and transverse radial flow velocity respectively. I_0 and K_1 are the modified Bessel functions of the first and second kinds, respectively. $\rho = \tanh^{-1} \beta$. p_T and $m_T = \sqrt{p_T^2 + m^2}$ denotes the transverse momentum and transverse mass, respectively.

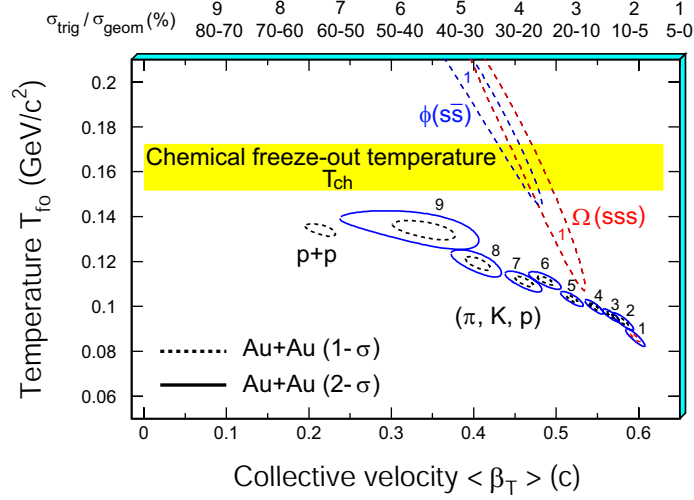


Figure 1.8: The χ^2 contours of kinetic freezeout temperature (T_{fo}) and mean radial velocity $\langle \beta \rangle$, extracted from thermal+radial flow fits (Blast-wave function fits) to the light (π , K , p) and multi-strange (ϕ , Ω) hadron p_T -spectra for Au+Au collisions at 200 GeV. The figure has been sourced from [6].

Hence the p_T spectra, along with the fitting using the Blast-Wave function for various hadron species, serves as an excellent tool to estimate the average radial flow velocity ($\langle \beta \rangle$) and the kinetic freeze-out temperature (T_{kin}). Figure 1.8 shows the χ^2 contours for the T_{kin} and $\langle \beta \rangle$ parameters obtained from fits to light hadrons (π , K , p) and multi-strange hadrons (ϕ , Ω) in Au+Au collisions at $\sqrt{s_{NN}} = 200$ GeV. The results for light hadrons are presented for nine centrality bins, whereas those for multi-strange hadrons are shown only for central collisions. From the figure, it is evident that the system exhibits enhanced collective flow from peripheral to central collisions. This suggests that the system produced in central Au+Au collisions expands more rapidly than in peripheral collisions. Additionally, multi-strange hadrons (ϕ , Ω) exhibit higher T_{kin} , indicating that these particles decouple from the system earlier [101]. Their smaller hadronic interaction cross-section [102] makes them an ideal probe for studying the collectivity in the initial partonic medium [6].

1.3.2 Glossary of kinematic variables

In this section, some of the fundamental kinematic variables [103] utilized in the data analysis for the studies presented in this thesis, are defined. In heavy-ion collision experiments, particles travel at relativistic speeds. To simplify the physics analysis, the kinematic variables used are chosen to be either invariant or additive under Lorentz transformations. It is important to note that, by convention, the detector coordinate system assumes the beam axis to be parallel to the laboratory frame's z -axis, while the impact parameter direction lies along the x -axis. The collision is expected to take place at the detector's geometric center, designated as the primary vertex of the event, at coordinates $(0, 0, 0)$. However, in real-world experiments, the primary vertex exhibits a spread along the z -axis.

In heavy-ion collisions, it is more convenient to describe the momenta of the produced particles using transverse momentum (p_T), azimuthal angle (ϕ), and rapidity (y) rather than the Cartesian coordinates (E, p_x, p_y, p_z) . Some of useful terminology have

been explained in the following discussions.

A. Center of mass energy

The center of mass energy is often expressed as \sqrt{s} , where, s is the Mandelstam's variable [104], which is the quadrature sum of four-momenta of the two colliding particles. If (E_A, \vec{p}_A) and (E_B, \vec{p}_B) , are the four momenta of two colliding particles A and B ,

$$s = (E_A + E_B)^2 - (\vec{p}_A + \vec{p}_B)^2 \quad (1.3.3)$$

In Center of mass frame $\vec{p}_A = -\vec{p}_B$, Hence equation 1.3.3 reduces to;

$$s = (E_A + E_B)^2 \quad (1.3.4)$$

Again, if the collision is happening between two particles of same species (having same mass), $E_A = E_B = E'$. Hence equation 1.3.4 reduces to;

$$\sqrt{s} = 2E \quad (1.3.5)$$

For a heavy-ion collision, all the nucleons in a nucleus are accelerated to the same center-of-mass energy. Therefore, the center-of-mass energy is often expressed per nucleon, denoted as \sqrt{s} . However, for proton-proton ($p+p$) collisions, the same quantity is simply referred to as \sqrt{s} . For instance, at the top RHIC energy for Au+Au collisions, the energy per nucleon in the center-of-mass system ($\sqrt{s_{NN}}$) is 200 GeV. This indicates that each of the 197 nucleons in the gold (Au) nucleus is accelerated in opposite directions to 100 GeV for the collision.

B. Transverse momentum (p_T)

Given that the beam axis (z axis) is perpendicular to the $x - y$ plane, a particle's momentum can be divided into two components: (i) Along the longitudinal direction (p_z) (ii) Along the transverse direction (p_T). Where

$$p_T = \sqrt{p_x^2 + p_y^2} \quad (1.3.6)$$

Here the p_x and p_y refers to the momentum of the particle in the x and y direction respectively. Since initially the beam was moving along the z -axis, finite p_T , is solely is a property of the particle produced after the collision, which is invariant under the Lorentz transformation.

C. Azimuthal angle (ϕ)

In the transverse plane ($x - y$ plane) the angle made by a particular track with the laboratory frame x -axis, is termed as the azimuthal angle. It is defined as follows;

$$\phi = \tan^{-1} \left(\frac{p_y}{p_x} \right) \quad (1.3.7)$$

D. Rapidity (y)

Rapidity is a dimensionless quantity, and defined as;

$$y = \frac{1}{2} \ln \left(\frac{E + p_z}{E - p_z} \right) \quad (1.3.8)$$

Equation 1.3.8, shows that if $p_z = 0$, $E = 0$, that denotes the region of mid rapidity. Further from equation 1.3.8,

$$y = \frac{1}{2} \ln \left(\frac{1 + p_z/E}{1 - p_z/E} \right) \quad (1.3.9)$$

$$y = \frac{1}{2} \ln \left(\frac{1 + \beta}{1 - \beta} \right) \quad (1.3.10)$$

Where, β is the velocity along z -direction. In non-relativistic limit where $p \ll m$, β becomes infinitesimally small that reduces the y to the velocity along z direction, as follows.

$$y = \frac{1}{2} [\ln(1 + \beta) - \ln(1 - \beta)] \quad (1.3.11)$$

$$y = \frac{1}{2} [1 + \beta - (-\beta)] \approx \beta \quad (1.3.12)$$

In the relativistic regime, the Lorentz transformation of particle velocity is not linear. However, rapidity offers a significant advantage in such cases, as it transforms linearly under a Lorentz boost ($y' = y + \Delta y$). Hence shape of the rapidity spectra remains invariant under Lorentz transformation. However, the calculation of y , requires the energy (E), information (ultimately the mass information), hence to calculate the rapidity, proper particle identification is needed in the experiments.

E. Pseudo-rapidity (η)

Firstly, the momentum of a charged particle track can be measured, through the tracking detectors in experiments. When the mass information of the particle is not relevant for a particular analysis, one can calculate pseudo-rapidity, which depends solely on the momentum information of the particle and is defined as:

$$\eta = \frac{1}{2} \ln \left(\frac{p + p_z}{p - p_z} \right) \quad (1.3.13)$$

$$\eta = \frac{1}{2} \ln \left(\frac{p + p \cos \theta}{p - p \cos \theta} \right) \quad (1.3.14)$$

$$\eta = - \ln \tan \left(\frac{\theta}{2} \right) \quad (1.3.15)$$

where the polar angle θ represents the angle formed by the charged particle track with the beam axis (z -axis). Pseudo rapidity (η), is invariant under Lorentz transformation.

F. Particle Multiplicity

Since the tracking and PID detectors can only track the charged particles, the number of charged particles produced in a particular event is referred as the multiplicity of that event. At mid-rapidity it is often measured as the charged particle multiplicity per unit rapidity.

From the rapidity expression in equation 1.3.8, we have:

$$e^y = \sqrt{\frac{E + p_z}{E - p_z}} \quad (1.3.16)$$

and

$$e^{-y} = \sqrt{\frac{E - p_z}{E + p_z}} \quad (1.3.17)$$

By adding and subtracting Eq. 1.3.16 and 1.3.17, we obtain:

$$E = m_T \cosh(y) \quad (1.3.18)$$

and

$$p_z = m_T \sinh(y) \quad (1.3.19)$$

where $m_T = \sqrt{p_T^2 + m^2}$ is the transverse mass, with m being the rest mass of the particle. As discussed earlier, the advantage of rapidity over longitudinal momentum (p_z) is that rapidity is additive under a longitudinal boost. If a particle has rapidity y in one inertial frame, it will have a rapidity of $y' = y + \Delta y$ in another inertial frame moving with rapidity Δy or with a longitudinal velocity $v_z = \tanh(\Delta y)$ relative to the first frame.

In addition to rapidity, pseudo-rapidity (η) is another important kinematic variable, defined as:

$$\eta = \frac{1}{2} \ln \left(\frac{|\vec{p}| + p_z}{|\vec{p}| - p_z} \right) = -\ln \left(\tan \frac{\theta}{2} \right) \quad (1.3.20)$$

where $|\vec{p}| = \sqrt{p_T^2 + p_z^2}$, and θ is the angle between \vec{p} and the z-axis, with $p_z = |\vec{p}| \cos(\theta)$. Using a similar method as for deriving Eq. 1.3.18 and 1.3.19, we can obtain:

$$|\vec{p}| = p_T \cosh \eta \quad (1.3.21)$$

and

$$p_z = p_T \sinh \eta \quad (1.3.22)$$

For high-momentum or low-mass particles, where $|\vec{p}| \gg m$, $E \approx |\vec{p}|$, and thus $y \approx \eta$. However, in general conditions, the relationship between y and η is more complex and can be expressed as [105]:

$$\begin{aligned} y &= \frac{1}{2} \ln \frac{E + p_z}{E - p_z} \\ &= \frac{1}{2} \ln \left(\frac{\sqrt{p_T^2 \cosh^2 \eta + m^2} + p_T \sinh \eta}{\sqrt{p_T^2 \cosh^2 \eta + m^2} - p_T \sinh \eta} \right) \end{aligned} \quad (1.3.23)$$

Taking the derivative of y with respect to η , we obtain:

$$\frac{dy}{d\eta} = \frac{|\vec{p}|}{E} \quad (1.3.24)$$

The region of phase space near $y = \eta = 0$ is known as the central rapidity or mid-rapidity region. In this region, the distribution of produced particles in y and η are related as follows:

$$\begin{aligned} \left(\frac{dN}{d\eta} \right)_{\eta=0} &= \left(\frac{dy}{d\eta} \frac{dN}{dy} \right)_{y=0} \\ &= \frac{p_T}{m_T} \left(\frac{dN}{dy} \right)_{y=0} \end{aligned} \quad (1.3.25)$$

Here, $\frac{p_T}{m_T} = v_T$ is the transverse velocity of the particles at mid-rapidity, which is always less than 1. Therefore, the η distribution of the produced hadrons is always lower than the corresponding y distribution at $y \approx 0$. If the rapidity(y) distribution is flat (as in the case of boost invariance), the Jacobian factor $\frac{dy}{d\eta}$ causes the η distribution to be non-flat, introducing a minimum at $\eta = 0$. This effect is demonstrated in Fig. 1.9, where a flat rapidity distribution of produced particles ($dN/dy = 1$) is assumed, and the corresponding η distribution is calculated using:

$$\frac{dN}{d\eta} = \frac{dN}{dy} \frac{p_T \cosh \eta}{m_T \cosh y} \quad (1.3.26)$$

Four different cases were considered: (1) $p_T = 1$ GeV/c and $m = 0.15$ GeV/c², (2) $p_T = 2$ GeV/c and $m = 0.15$ GeV/c², (3) $p_T = 1$ GeV/c and $m = 0.5$ GeV/c², and (4) $p_T = 2$ GeV/c and $m = 0.5$ GeV/c². In all cases, a dip in the η distribution is observed, with a minimum at $\eta = 0$. The dip is more pronounced for more massive particles at a given p_T . There is also a p_T dependency in the dip of η distribution, larger the p_T of the considered particles there is less dip.

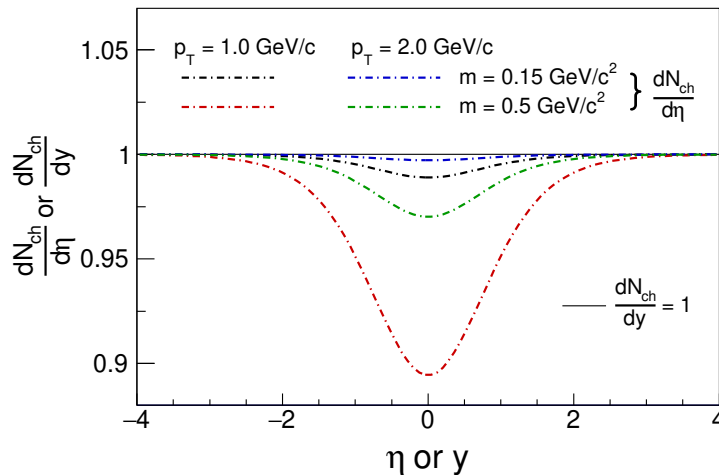


Figure 1.9: The pseudo-rapidity distribution of the produced particles ($\frac{dN_{ch}}{d\eta}$) of different p_T and mass, which is converted from a flat rapidity distribution ($\frac{dN_{ch}}{dy} = 1$), using equation 1.3.26.

At larger rapidity, the cosh values of y or η become large enough to dominate over p_T and m_T , making the value of $\frac{dy}{d\eta}$ approach unity. As a result, the η and y distributions

become similar at large rapidities. The mid-rapidity dip in the η distribution is a consequence of the Jacobian factor presented in Eq. 1.3.24. Therefore, there is a dip observed in the experimental measurement of η distribution of charged particles at mid-rapidity.

1.3.3 Natural units

In high energy physics to make calculations easier, we take the help of natural units, In this convention universal constants like planks constant (\hbar), speed of light in vacuum (c) and Boltzmann's constant (k_B) are considered to be unity. Using the natural units, every physical quantity can be expressed in the unit of energy (e.g GeV/MeV). According to this convention $\hbar c \approx 197.5$ MeV fm. Table 1.1 highlights the conversion of some of the basic physical quantities in natural units.

Table 1.1: Conversion of some basic physical quantities in terms of natural units.

Physical Quantities	Units	Conversion
Mass	GeV	1 kg = 5.61×10^{26} GeV
Length	GeV ⁻¹	1 m = 5.07×10^{15} GeV
Temperature	GeV	1 K = 8.62×10^{-14} GeV
Time	GeV ⁻¹	1 sec = 1.52×10^{24} GeV

1.4 Experimental signatures of Quark Gluon Plasma

In heavy-ion collision experiments we try to probe a system which is of the order of femto scale size. The system is extremely short-lived and undergoes rapid expansion. Confirming the existence of a deconfined and locally thermalised phase of quarks and gluons commonly referred to as the Quark-Gluon Plasma (QGP), remains a significant challenge. Over the years, robust experimental observables have been proposed and extensively studied to address this. A detailed summary of experimental measurements conducted at the STAR experiment, focusing on the search for QGP, is available in [6]. In the following discussion, several widely accepted experimental signatures of QGP formation are presented.

1.4.1 Strangeness enhancement

In both $p + p$ and Au+Au collisions, the net strangeness before and after the collision remains zero. In high-energy collisions, strange quarks are mainly produced through processes like flavor excitation ($gs \rightarrow gs$, $qs \rightarrow qs$) and flavor creation ($g\bar{q} \rightarrow s\bar{s}$, $q\bar{q} \rightarrow s\bar{s}$) during the early stages. Additionally, gluon splitting ($g \rightarrow s\bar{s}$) contributes to their formation in the later stages of partonic evolution. If a Quark-Gluon Plasma (QGP) is present, its gluon-rich environment favors the production of strange quarks through gluon-mediated processes, which become more dominant than $q\bar{q}$ annihilation [106–108]. In addition to that strange quark containing hadrons can also be formed along with production of a strange baryon through associated production [15, 26]. This makes enhanced production of strange particles in heavy-ion collisions, compared to an environment where QGP medium is not expected, as one of the primary experimental signatures of Quark-Gluon Plasma (QGP) formation.

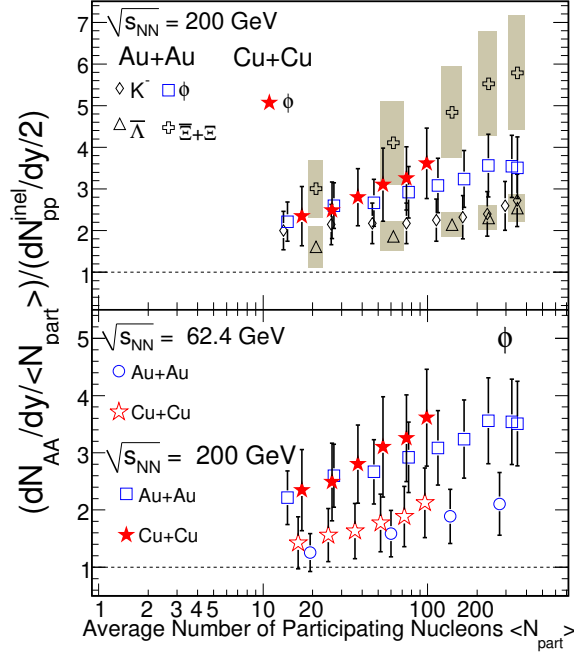


Figure 1.10: Strangeness enhancement factor (ϵ), for K ($s = 1$), ϕ ($s = 0$), Λ ($s = 1$) and Ξ ($s = 2$) as a function of $\langle N_{part} \rangle$ for Au+Au and Cu+Cu collisions at 200 and 62.4 GeV. The figure has been sourced from [7].

The enhancement is primarily quantified by the ratio of strange hadron yield per participant nucleon in A+A collisions to that of $p + p$ collision and defined as;

$$\epsilon = \frac{\left(\frac{dN^{AA}}{dy} \right) / N_{part}}{\left(\frac{dN^{pp}}{dy} \right) / 2} \quad (1.4.1)$$

An increase in the value of ϵ beyond unity indicates an enhancement in the strangeness production. However, in small systems such as $p + p$ collisions, strangeness production can be suppressed due to canonical suppression, potentially leading to an increase in ϵ . In this context, the ϕ meson ($s\bar{s}$) serves as an excellent probe because its net strangeness is zero, rendering it immune to canonical suppression effects. Figure 1.10 shows the strangeness enhancement factor (ϵ) as a function of $\langle N_{part} \rangle$ for Au+Au and Cu+Cu collisions at 200 and 62.4 GeV. The figure clearly demonstrates that strange particle production increases from peripheral to central collisions and further enhances with the valence strange quark content in the hadrons. A similar trend is observed for both open (K , Λ , Ξ) and hidden (ϕ) strangeness, indicating that the production of strange hadrons due to the hot, dense medium created in heavy-ion collisions is not limited by the canonical suppression observed in $p + p$ collisions.

Additionally, strangeness enhancement can be estimated as the ratio of kaon to pion yields. Earlier measurements at the SPS and STAR experiments observed enhanced production of kaons relative to pions in heavy-ion collisions compared to that in $p + p$ collisions at the same center-of-mass energy [109–111]. A similar enhancement has also been reported in high-multiplicity $p + p$ collisions by the ALICE experiment, inline with efforts to investigate the potential formation of QGP in small system collisions [108].

1.4.2 Suppression of high p_T particle yield

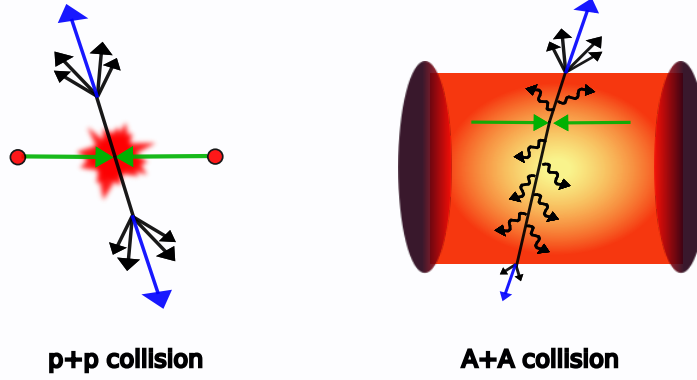


Figure 1.11: Schematic representation of jet formation in $p + p$ and A+A collisions.

Jets are clusters of highly energetic hadrons within a narrow cone, produced from the fragmentation of high- p_T partons in hard scatterings. Due to momentum conservation, jets are produced back-to-back, and commonly referred to as di-jets. The phenomenon of jet quenching is considered one of the key signatures of Quark-Gluon Plasma (QGP) formation [112]. In heavy-ion collisions, if a di-jet is formed close to the surface of the medium, one of the jet clusters may escape the medium without significant interaction. However, the opposing jet traverses the dense medium, losing a substantial amount of energy or potentially being completely absorbed before fragmenting into hadrons. This energy loss phenomenon is referred to as jet quenching. In contrast, in smaller systems such as $p + p$ collisions, where the formation of a dense medium is not expected, no jet quenching effect is observed. Figure 1.11 illustrates this phenomenon schematically. Experimentally, jet quenching effect is studied by measuring di-hadron azimuthal correlations for high- p_T particles (jets).

Figure 1.12 presents the measurements from STAR experiment for di-jet azimuthal correlations in $p + p$, d+Au, and Au+Au collisions at 200 GeV [6]. The observable is measured for hadrons with $p_T > 2$ GeV/c, reference to a trigger hadron with $p_T > 4$ GeV/c. For small-system collisions ($p + p$ and central d+Au), the distribution exhibits a double-peak structure with a near-side peak ($\Delta\phi = 0$) and an away-side peak ($\Delta\phi = \pi$). However, in Au+Au collisions, the suppression of the away-side peak is observed, providing clear evidence of jet quenching effects.

Another approach to study the suppression of high- p_T particle yields is through the measurement of the nuclear modification factor (R_{AA}). This is defined as the ratio of given hadron yield in heavy-ion collisions with its yield in $p + p$ collisions, scaled by the number of binary nucleon-nucleon collisions.

$$R_{AA} = \frac{1}{\langle T_{AA} \rangle} \frac{\left(\frac{d^2 N}{dp_T dy} \right)^{AA}}{\left(\frac{d^2 N}{dp_T dy} \right)^{pp}} \quad (1.4.2)$$

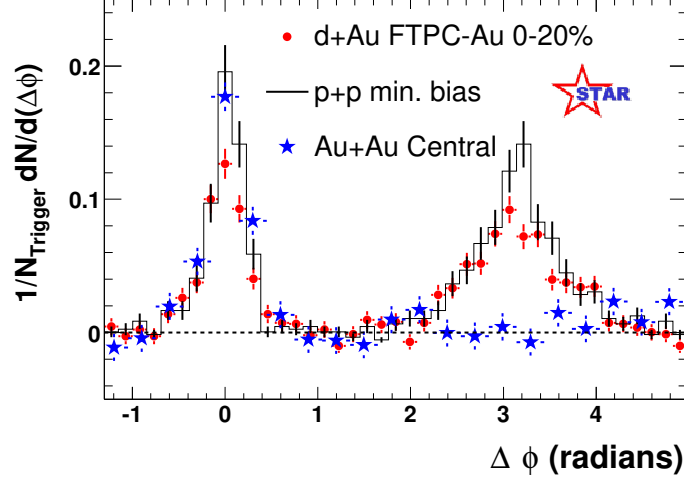


Figure 1.12: Systematic measurement of di-jet azimuthal correlation at $\sqrt{s_{NN}} = 200$ GeV by the STAR experiment. The figure has been sourced from [6].

Here, $\langle T_{AA} \rangle$ represents the average nuclear thickness, calculated as the ratio of the average number of binary collisions ($\langle N_{coll} \rangle$) to the inelastic $p + p$ interaction cross-section (σ_{NN}). In a heavy-ion collision, if the nucleus-nucleus interaction is essentially a superposition of multiple $p + p$ collisions, the value of R_{AA} is expected to approach unity at high transverse momentum (p_T), which is predominantly the region of hard-scattering. However, any deviation from unity indicates in-medium effects. Specifically, if R_{AA} is less than one at high p_T , it suggests the presence of a strongly interacting medium and the dominance of partonic energy loss.

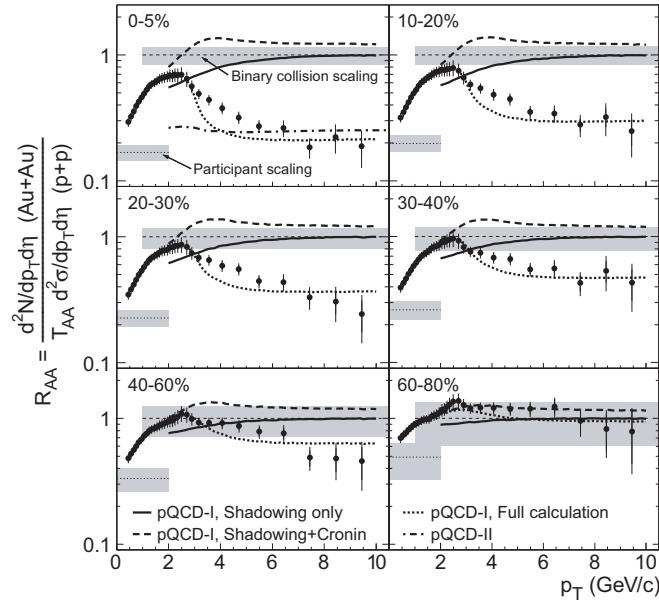


Figure 1.13: The measurement nuclear modification factor (R_{AA}) from STAR experiment for different centrality classes, for center of mass energy of 200 GeV. The figure has been sourced from [8].

Figure 1.13 presents the measurement of the nuclear modification factor (R_{AA}) for Au+Au collisions at $\sqrt{s_{NN}} = 200$ GeV across different centralities, as observed by the STAR experiment for the charged hadrons [8]. The value of R_{AA} is significantly lower

than unit for higher p_T with the suppression being more pronounced in central collisions compared to peripheral ones. This indicates the possible creation of a dense medium in central Au+Au collisions at 200 GeV. Furthermore, even stronger suppression of R_{AA} is observed at LHC energies [113].

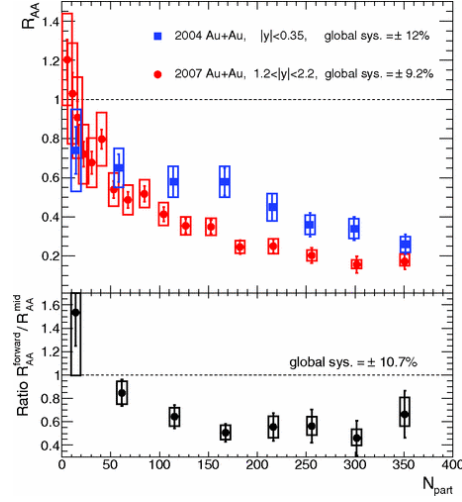


Figure 1.14: The measurement nuclear modification factor (R_{AA}) from STAR experiment for different centrality classes, for center of mass energy of 200 GeV. The figure has been sourced from [9].

1.4.3 Quarkonia suppression

In the context of the nuclear modification factor, R_{AA} , the suppression of heavy quark bound states, known as quarkonia suppression, also serves as a signature of QGP formation. This effect was first proposed by Matsui and Satz [114]. Heavy quarks, such as charm (c) and bottom (b), have masses approximately 10 and 40 times larger than that of strange (s) quarks, respectively. Due to their substantial mass, the minimum energy required to produce these quarks is available only during the initial stages of the collision. The bound states of these quarks, collectively known as quarkonia (e.g., $J/\Psi(c\bar{c})$ and $\Upsilon(b\bar{b})$). If the hot and dense QGP medium is produced then these heavy quark pairs ($c\bar{c}$ and $b\bar{b}$), experience the whole expansion of the medium. The presence of lighter quarks in the vicinity of these pairs, weakens the binding between the heavy quark pairs, leading to the dissociation of quarkonia into open charm or bottom quarks, this phenomena is often referred as Debye's color screening [115]. These quarks subsequently combine with lighter quarks to form hadrons such as D -mesons, resulting in a suppression of the quarkonia yield.

The suppression level depends on the binding energy between the quark-antiquark pairs within the bound state and the temperature of the medium. Quarkonia suppression has been extensively studied in various experiments [116–119]. Figure 1.14 presents the PHENIX collaboration's measurement of R_{AA} for J/Ψ as a function of $\langle N_{part} \rangle$ for Au+Au collisions at 200 GeV [9]. A strong J/Ψ yield suppression is observed in central heavy-ion collisions with respect to $p + p$ collisions, providing further evidence of expected QGP formation.

1.4.4 Collectivity in the medium

The expansion of the medium and its constituents in heavy-ion collisions is often characterized by their collective behavior. In non-central heavy-ion collisions, the colliding nuclei create an almond-shaped overlap region. This initial spatial anisotropy in the medium generates azimuthally varying pressure gradients, which are reflected as anisotropies in momentum space. In momentum space the azimuthal distribution of the produced particles can be described using a Fourier series expansion, expressed as follows [120, 121]:

$$E \frac{d^3N}{dp^3} = \frac{1}{2\pi} \frac{d^2N}{p_T dp_T dy} [1 + 2v_1 \cos(\phi - \psi_R) + 2v_2 \cos 2(\phi - \psi_R) + \dots] \quad (1.4.3)$$

Here, ϕ denotes the azimuthal angle of each particle track, while ψ_R represents the reaction plane angle, defined as the plane subtended by the impact parameter and the laboratory frame z -axis. The coefficients v_n correspond to the n^{th} order harmonic flow and are sensitive observables for studying the collective expansion of the medium. In the following discussion, particular focus will be given to the elliptic flow coefficient (v_2).

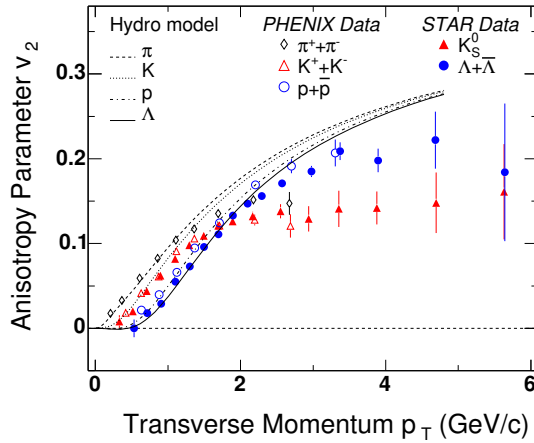


Figure 1.15: The measurement of elliptic flow coefficient (v_2) for identified hadrons in Au+Au collisions at $\sqrt{s_{NN}} = 200$ GeV by STAR and PHENIX experiment. The flow parameter for different particles predicted by hydrodynamic model has been shown by solid and dashed lines. The figure has been sourced from [10].

Figure 1.15 presents the experimental measurements of the elliptic flow coefficient (v_2) alongside hydrodynamic model calculations for identified hadrons (π , K , K_s^0 , p , Λ) in Au+Au collisions at $\sqrt{s_{NN}} = 200$ GeV [10]. For p_T up to 2 GeV/c, a distinct mass ordering is observed in the measured v_2 where lighter particles exhibit higher elliptic flow compared to heavier particles. This phenomenon arises from the interplay between radial flow and spatial anisotropy. At low p_T , radial flow dominates, pushing heavier particles to higher p_T , which flattens their p_T spectra and reduces their elliptic flow. However, at higher p_T , the elliptic flow coefficient exhibits a clear dependence on particle species, with baryons showing higher v_2 than mesons. Up to $p_T = 1$ GeV/c, hydrodynamic models qualitatively describe the experimental data.

As shown in Figure 1.16, when the experimental data is scaled by the number of constituent quarks (n_q), the v_2/n_q exhibits a universal scaling for different particles when

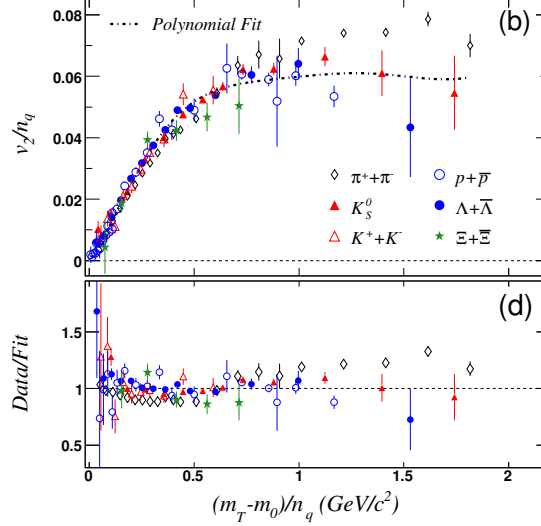


Figure 1.16: The elliptic flow coefficient (v_2) scaled by no. of constituent quarks (n_q) for identified hadrons in Au+Au collisions at $\sqrt{s_{NN}} = 200$ GeV with n_q scaled transverse kinetic energy $((m_T - m_0)/n_q)$. The figure has been sourced from [11].

plotted as a function of the n_q -scaled transverse kinetic energy, $((m_T - m_0)/n_q)$. Here, $m_T = \sqrt{p_T^2 + m^2}$ represents the transverse mass (m is the rest mass). This phenomenon is referred to as ncq -scaling [122, 123]. Any differences in the measured v_2 arising from the particle mass are effectively removed when v_2/n_q is plotted as a function of $(m_T - m_0)/n_q$. The observed universal ncq -scaling in Au+Au collisions at $\sqrt{s_{NN}} = 200$ GeV suggests that quark recombination or coalescence is the dominant mechanism for hadron production [122, 123]. The recombination model assumes that quarks retain their individual v_2 , which is subsequently carried over to the hadrons during hadronization. This observation indicates that collectivity is developed at the partonic level, providing evidence for the formation of a deconfined state of matter.

1.5 Investigating freeze-out dynamics through resonance production

As discussed in section 1.3.1, the evolution of the QGP phase is followed by chemical and kinetic freeze-out stages. These stages play a significant role in particle production mechanisms such as coalescence, decay, and annihilation etc. It should be noted that the freeze-out phase occurs regardless of whether a QGP is formed or not. While the primary objective of heavy-ion collisions is to investigate the QGP phase, studying the late-stage evolution, particularly the freeze-out phase, is equally crucial. Resonances serve as excellent probes for this purpose due to their short lifetimes, which cause them to decay within the medium. As a result, they are highly susceptible to in-medium effects during the freeze-out phase, which can alter the observables associated with their properties.

1.5.1 Resonances

Resonances are short-lived particles with lifetimes on the order of 10^{-23} seconds, decaying via strong interactions. The production probability of a resonance follows a Breit-Wigner distribution, characterized by its natural width (Γ). The resonance lifetime (τ) is inversely proportional to this width, following $\tau \propto \frac{1}{\Gamma}$.

This thesis focuses on the study of the K^{*0} meson, a vector meson ($J^P = 1^-$) resonance with a lifetime of 4.16 fm/c. The K^{*0} has a 100% probability of decaying into the $K - \pi$ channel. However, a proper calculation using Clebsch-Gordan coefficients for a isospin-1/2 particle decaying into daughters with isospins -1 and +1/2 reveals that the decay probability is split between the charged decay channel ($K^{*0} \rightarrow K^+\pi^-$) with 2/3 probability and the neutral decay channel ($K^{*0} \rightarrow K^0\pi^0$) with 1/3 probability (explanation is in Appendix). The probability for both charged and neutral decay channel is also same for the \bar{K}^{*0} . Since charged particles can be easily identified in experiments, the reconstruction of K^{*0} is typically performed using its charged decay channel.

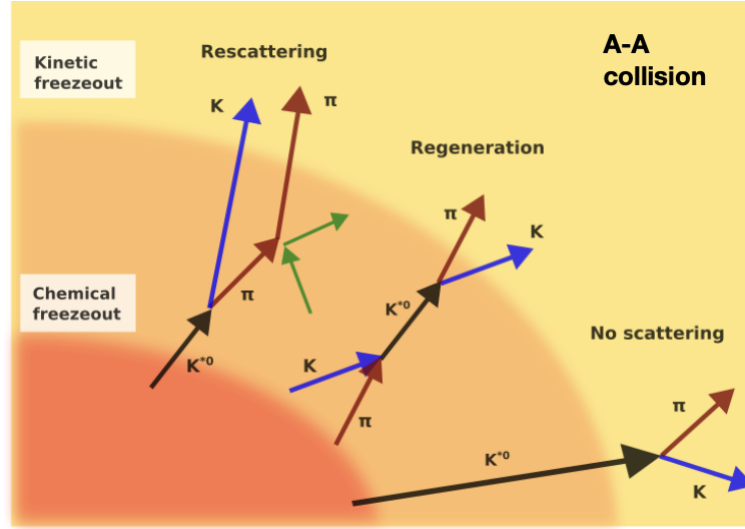


Figure 1.17: Pictorial representation of in-medium interactions for the K^{*0} decay daughters.

The lifetime of the K^{*0} meson is comparable to that of the fireball produced in heavy-ion collisions, meaning it often decays within the medium. Consequently, its decay daughters experience the dynamics of the medium and may interact with its constituents. If the decay daughters do not interact with the medium, they can faithfully carry information about the parent particle, facilitating its reconstruction. However, if even one of the decay daughters undergoes elastic interaction with the medium constituents, its momentum may be altered. This makes it impossible to reconstruct the parent resonance using the four-momentum information of the decay products. This process, which leads to a reduction in the K^{*0} yield in an event, is known as the rescattering process. On the other hand, random K and π particles in the medium can undergo pseudo-elastic scattering to form a K^{*0} resonance state, which subsequently decays back into $K\pi$. Reconstructing the K^{*0} meson from these decay products increases the K^{*0} yield, a process referred to as the regeneration process. In the context of pseudo-elastic scattering ($K\pi \rightarrow K^* \rightarrow K\pi$), it is worth noting that the initial and final states of the interaction remain the same ($K\pi$). This satisfies the criterion for elastic interaction. However, the interaction involves the formation of an intermediate K^{*0} state, making it inaccurate to classify this as purely elastic or inelastic. For this reason, the term pseudo-elastic is used.

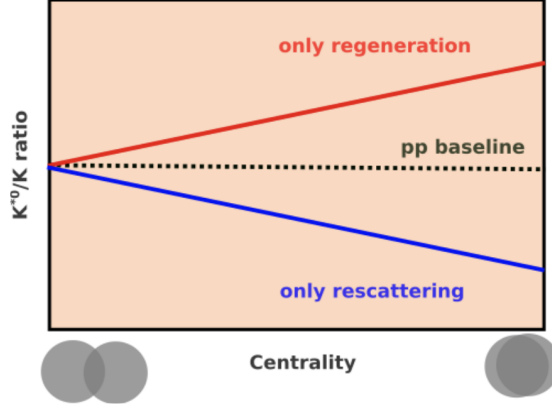


Figure 1.18: Naive expectation of the centrality dependence of the K^{*0}/K ratio in a context of re-scattering/regeneration dominant picture.

Phenomenological models indicate that rescattering and regeneration processes can influence the mass, width, yield, and flow observables of resonances. However, compared to measurement of flow coefficients, which require extensive statistics, yield measurements provide a more efficient approach to investigate these effects. Therefore, this thesis focuses on studying the spectra measurements of the K^{*0} meson at STAR energies.

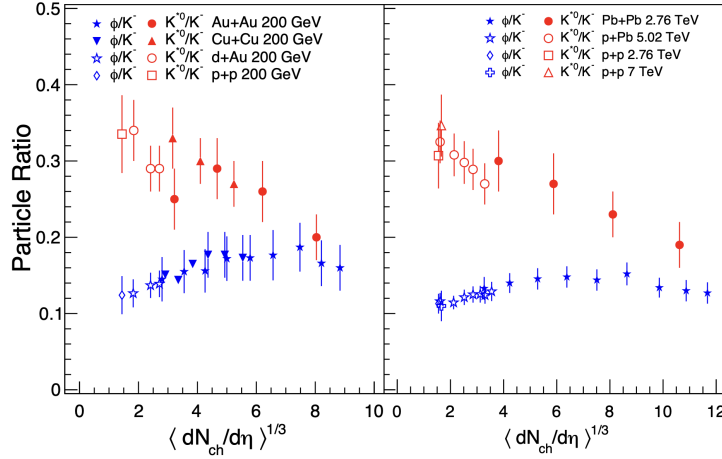


Figure 1.19: Previous experimental measurement of resonance to no-resonance ratio ($K^{*0}/K, \phi/K$) from STAR and ALICE. The figure has been sourced from [12–14].

It should be noted that these two in-medium interactions: rescattering and regeneration occur simultaneously. To determine which process dominates, the ratio of the resonance yield to a non-resonance particle yield is studied. The non-resonance particle chosen should have a quark content similar to that of the resonance, preferably one of its decay daughters. This choice minimizes the contribution of additional effects, such as strangeness enhancement, to the observable. For the K^{*0} resonance in heavy-ion collisions, the K^{*0}/K ratio is analyzed as a function of collision centrality. As a baseline, the same ratio is measured in $p + p$ or peripheral collisions, where the hadronic phase (the phase between chemical and kinetic freeze-out) is expected to be minimal. This reduces the likelihood of in-medium interactions, providing a reference point. The expected behavior of the K^{*0}/K ratio is illustrated in the cartoon plot in Fig. 1.18. In heavy-ion collisions, if the rescattering effect dominates over the regeneration effect, the ratio will decrease relative to the $p + p$ baseline. Conversely, if the regeneration effect dominates,

the ratio will increase compared to the baseline.

Figure 1.19 presents the ratios of ϕ/K and K^{*0}/K as functions of multiplicity for various collision systems at top RHIC and LHC energies. The K^{*0}/K ratio decreases from peripheral to central collisions, as well as in comparison to the ratio measured in $p+p$ collisions. In contrast, the ϕ/K ratio remains unaffected by collision centrality because the ϕ meson, with its significantly longer lifetime (about ten times that of the K^{*0}), primarily decays outside the medium. These findings suggest that hadronic rescattering plays a more dominant role than regeneration in central heavy-ion collisions.

1.6 Thesis motivation

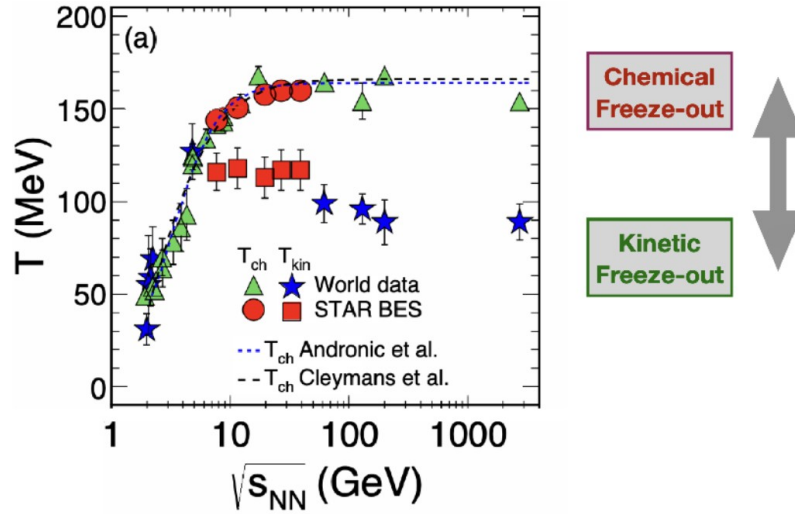


Figure 1.20: The collision energy dependence of kinetic and chemical freezeout temperature. The figure has been sourced from [15].

Fig 1.20, shows compilation of measurement of chemical and kinetic freeze-out temperatures measured by different experiments as a function of center of mass energy. It is evident that the difference between the chemical freeze-out temperature (T_{ch}) and kinetic freeze-out temperature (T_{kin}) decreases with decreasing collision energy. In addition to that the medium created in lower collision energy have lesser particle density as compared to that in higher collision energies. As the collision energy decreases, the baryon chemical potential increases, ranging from nearly zero at LHC energies to approximately 400 MeV at SPS energies, which are comparable to RHIC BES energies. This leads to a higher baryon-to-meson ratio at RHIC BES energies compared to top RHIC and LHC energies. Consequently, distinct rescattering effects can be expected in the medium formed at both high and low collision energies.

This thesis investigates the production of K^{*0} mesons using STAR BES-I and BES-II datasets in Au+Au collisions at $\sqrt{s_{NN}} = 7.7\text{--}39$ GeV from the STAR experiment, the results are compared with various phenomenological model studies to probe the hadronic rescattering at BES energies. Transport model studies has been employed to understand the observed experimental outcomes. Additionally, the UrQMD model is used to investigate the effects of hadronic interactions on flow observables, with a particular focus on examining their impact on the difference in directed flow between oppositely charged identified hadrons.

Chapter 2

The STAR Detector Setup at RHIC

This chapter provides a brief overview of the Solenoidal Tracker at RHIC (STAR) detector facility at the Relativistic Heavy-Ion Collider (RHIC). The emphasis will be on the sub-detector systems within the STAR detector that were used in the analysis for this thesis.

2.1 Introduction

To recreate the conditions of the early universe on a subatomic scale, heavy-ion collider experiments were conceptualized. The RHIC facility at BNL in New York, USA, was the first successful collider experiment of its kind. RHIC was designed for $p + p$ and Au+Au collisions at center-of-mass energies of $\sqrt{s_{NN}} = 500$ and 200 GeV, respectively—the highest at the time [124, 125]. It became operational in 2000 and, after nearly 24 years, continues to collect data, with multiple upgrades along the way. Currently, RHIC is the second highest-energy heavy-ion collider globally, surpassed only by the Large Hadron Collider (LHC). The RHIC facility is also capable of colliding polarized protons, that can be useful for proton spin related studies.

As a versatile collider, RHIC has successfully provided data from both symmetric and asymmetric collisions using a variety of collision systems, ranging from small systems ($p + p$, $p + \text{Al}$, $p + \text{Au}$, $d + \text{Au}$, $\text{He} + \text{Au}$) to heavy ions ($\text{Cu} + \text{Cu}$, $\text{Cu} + \text{Au}$, $\text{Ru} + \text{Ru}$, $\text{Zr} + \text{Zr}$, $\text{Au} + \text{Au}$, $\text{U} + \text{U}$) over a broad range of center-of-mass energies ($\sqrt{s_{NN}} = 7.7\text{--}200$ GeV) with collider mode. Additionally, fixed-target Au+Au collisions have been conducted at center-of-mass energies of $\sqrt{s_{NN}} = 3.0\text{--}13.7$ GeV.

A bird's-eye view of the RHIC collider site is shown in Fig.2.1. RHIC is an approx-

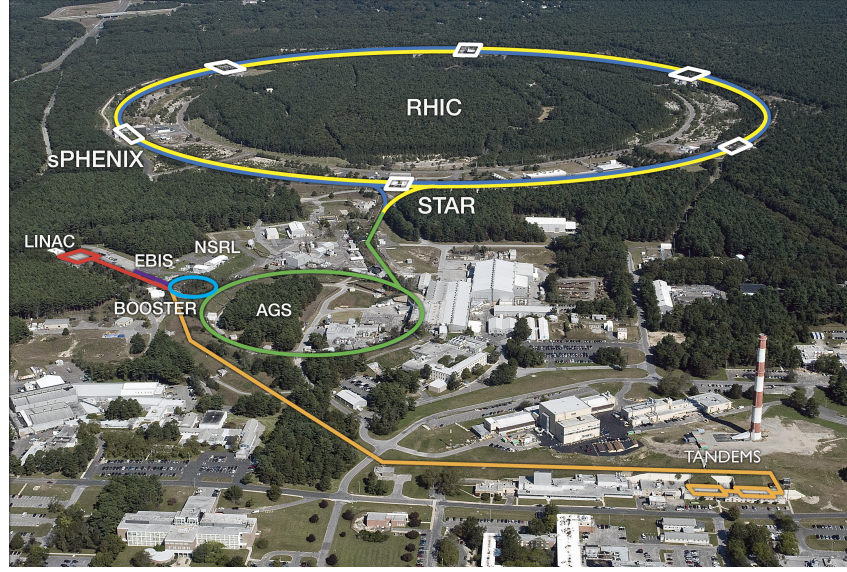


Figure 2.1: Overview of RHIC experimental facility at Brookhaven National Laboratory taken from the Ref [16].

imately circular, superconducting synchrotron-type particle accelerator that accelerates particles in a circular path by synchronously varying electric and magnetic fields. It has a circumference of 3.8 km and contains two concentric rings that accelerate heavy ions in opposite directions. The ions circulating clockwise are referred to as the "blue beam", while those circulating counterclockwise are known as the "yellow beam".

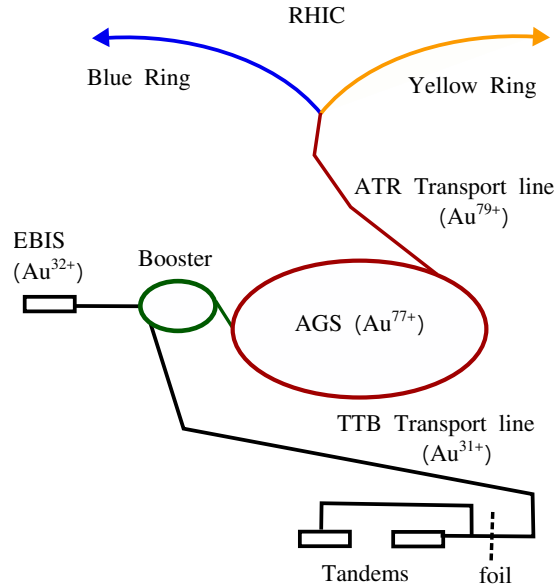


Figure 2.2: Schematic diagram of ion-beam injection into the RHIC ring.

The injection of heavy-ion beams into the rings involves multiple steps. An schematic illustration has been shown in fig.2.2. The process begins by obtaining the ion source. Earlier at RHIC, negatively charged gold ions are produced from a cesium pulsed sputter ion source. These ions were then fed into the Tandem Van de Graaff [126] and passed through a carbon stripping foil, which partially removed electrons from these ions via

a two-stage acceleration. This produces a Au^{31+} having kinetic energy of 1 MeV per nucleon. These ions travels along the 850 m long, Tandem-To-Booster (TTB) transport line, to a Booster synchrotron, reaching about 5% of the speed of light. Through this process, the Tandem could supply ions ranging from hydrogen to iron in atomic numbers.

Since 2012, the Electron-Beam Ion Source (EBIS) [127, 128] along with two linear accelerators has replaced the Tandem Van de Graaff. EBIS is more efficient, easier to operate and maintain, and capable of accelerating a broader range of ion species, including uranium. EBIS produces Au^{32+} ions by colliding electron beams with a gold gas and accelerates them to a kinetic energy of 2 MeV per nucleon. For $p + p$ collisions, the Linac provides protons with 200 MeV of energy, transferring them to the Booster.

The Booster synchrotron, with a circumference of 201.8 m, further accelerates ions to about 37% of the speed of light. After additional electron stripping, a state of Au^{77+} with a kinetic energy of 95 MeV per nucleon is achieved before the ions are transferred to the Alternating Gradient Synchrotron (AGS). In the AGS, ions are accelerated to 8.86 GeV per nucleon, reaching 99.7% of the speed of light. The ions are then passed through the AGS To RHIC (ATR) transfer line, where they encounter a stripping foil that removes the remaining electrons, resulting in Au^{79+} ions. At the end of the transfer line, a "Y"-shaped divergence point with a switching magnet diverts the ion bunches toward the clockwise or counterclockwise RHIC ring.

After entering the RHIC ring, the two independent beams circulate multiple times in opposite directions and are accelerated until they achieve the required center-of-mass energy. In the main collider ring the ions typically reach speeds approaching 99.995% of the speed of light and collisions are then permitted only at six designated interaction points. The interaction rate (R) is expressed as $R = \mathcal{L} \times \sigma$, where \mathcal{L} is the luminosity and σ is the collision cross-section, The term "luminosity" refers to the number of collisions occurring per unit area, per unit time. In experiments, it is only possible to control the luminosity, not the cross-section.

Table 2.1: Beam parameters achieved during the phase-I of RHIC Beam Energy Scan (RHIC-BES) program, for different center of mass energies in Au+Au collisions. The data is collected from [46].

Beam Energy Scan (BES) phase-I					
Au+Au $\sqrt{s_{NN}}$ (GeV)	Year	Ions/bunch ($\times 10^9$)	\mathcal{L}_{int} (μb^{-1})	\mathcal{L}_{peak} ($cm^{-2}s^{-1}$)	\mathcal{L}_{avg} ($cm^{-2}s^{-1}$)
7.7	2010	0.5	5.0	6.5×10^{24}	2.6×10^{24}
11.5	2010	1.1	7.82	3.3×10^{25}	1.5×10^{25}
14.5	2014	1.1	21.2	1.0×10^{26}	0.2×10^{26}
19.6	2011	0.9	17.5	8.0×10^{25}	4.0×10^{25}
27	2011	1.45	30.4	2.0×10^{26}	1.2×10^{26}
39	2010	1.3	99	2.2×10^{26}	1.3×10^{26}

If there are N_{Blue} particles per bunch in the blue beam, N_{Yellow} particles per bunch in the yellow beam, and n bunches per beam circulating in the RHIC ring with a revolution frequency f , The corresponding luminosity can be expressed as:

$$\mathcal{L} = f \frac{n N_{Blue} N_{yellow}}{A} \quad (2.1.1)$$

Where A denotes the overlapping cross-sectional area of two colliding beams.

The Blue and Yellow rings each have dedicated sets of superconducting magnets to bend and focus the ion beams [129]. Beam acceleration and storage within RHIC are facilitated by two Radio Frequency (RF) cavities, operating at frequencies of 28 MHz and 197 MHz, respectively. The accelerated ion beams are stored to enable collisions for data collection. Collisions occur at the interaction points (IP), and, once the luminosity falls below a reaches a certain low level, the beams are taken out (or dumped) from the rings.

From 2010 to 2014, Au+Au collisions were performed at RHIC as part of the Beam Energy Scan (BES) Phase-I program, covering a broad range of center-of-mass energies. Table 2.1 lists the beam parameters achieved during those RHIC physics runs. For precision measurement, the BES Phase-II program was conducted from 2019-2021, where high-statistics data were collected under improved detector conditions, with luminosity increased by 5 to 20 times. The corresponding beam parameters for the BES-II runs are listed in Table 2.2. A detailed information about of RHIC physics runs, collision systems, center of mass energy projected and achieved event statistics along with the luminosity values can be found in the ref [46].

Table 2.2: Beam parameters achieved during the phase-II of RHIC Beam Energy Scan (RHIC-BES) program for different center of mass energies in Au+Au collisions. The data is collected from [46].

Beam Energy Scan (BES) phase-II					
Au+Au $\sqrt{s_{NN}}$ (GeV)	Year	Ions/bunch ($\times 10^9$)	\mathcal{L}_{int} (μb^{-1})	\mathcal{L}_{peak} ($cm^{-2}s^{-1}$)	\mathcal{L}_{avg} ($cm^{-2}s^{-1}$)
7.7	2021	1.4	152	7.9×10^{25}	2.9×10^{25}
11.5	2020	1.7	143	1.37×10^{26}	7.0×10^{25}
14.6	2019	1.75	132	2.1×10^{26}	7.9×10^{25}
19.6	2019	1.85	151	5.0×10^{26}	1.5×10^{26}
27	2018	2.0	282	5.8×10^{26}	3.0×10^{26}

Four of the six interaction points at RHIC, is occupied by various experimental detector setups. The STAR experiment (positioned at 6 o' clock location) [6] is one of four experiments located at RHIC, alongside PHENIX (positioned at 8 o' clock location) [130], PHOBOS (positioned at 10 o' clock location) [131], and BRAHMS (positioned at 2 o' clock location) [132]. The PHOBOS experiment, primarily designed for bulk particle measurements with limited particle identification capabilities, had the largest pseudorapidity coverage at RHIC and concluded operations in 2005. The BRAHMS experiment, focused on momentum spectroscopy studies within a narrow solid angle, completed data collection in 2006. The PHENIX experiment, designed to measure rare hard probes such as electrons, muons, and photons to investigate the medium created in heavy-ion and proton-proton collisions, ceased data taking in 2016 and is currently undergoing a significant upgrade to become the new sPHENIX [133] experiment. Data used in this thesis were collected by the STAR experiment, which is detailed in the following section.

2.2 The STAR Experiment

Figures 2.3 and present the 3-dimensional and cross-sectional views of the major sub-detector systems within the STAR detector, respectively. The integrated arrangement and technology of these detectors enable full azimuthal coverage, precise particle identification, accurate tracking and detailed momentum analysis. In Figure 2.4, the first recorded Au+Au collision event in STAR is illustrated, showcasing an Au+Au collision at a center-of-mass energy of 200 GeV.

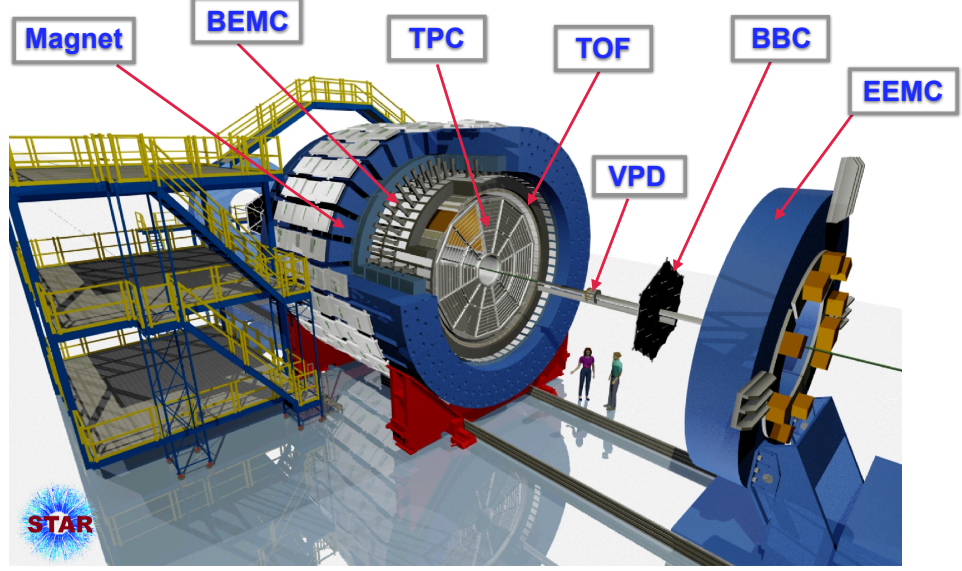


Figure 2.3: The schematic picture of the Solenoidal Tracker at RHIC (STAR) detector illustrating the layout and arrangement of its various sub-detector systems. The figure has been sourced from Chi Yang’s presentation in ICNFP-2017 (STAR Collaboration).

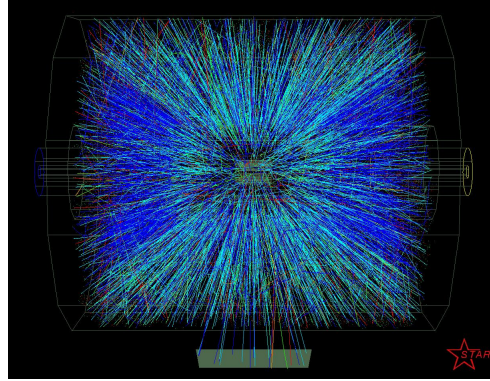


Figure 2.4: The first collision event recorded by the STAR TPC detector for Au+Au collisions at $\sqrt{s_{NN}} = 200$ GeV, in 2001. The colored lines show the tracks of different charged particles. The figure has been sourced from [17].

The extensive and complex sub-detector systems of the STAR experiment are enclosed within a solenoidal magnet that can operate at magnetic field strengths of 0.25 Tesla (half-field mode) and 0.5 Tesla (full-field mode) [134]. The STAR detector’s orientation is defined within a local right-handed Cartesian coordinate system. In this system, the x-axis runs parallel to the ground and points outward from the RHIC center, the

y-axis is perpendicular to the ground, and the z-axis points westward at STAR [135]. A schematic picture of the STAR coordinate system, showing the layout of different sub-detector positions, is presented in Fig. 2.5.

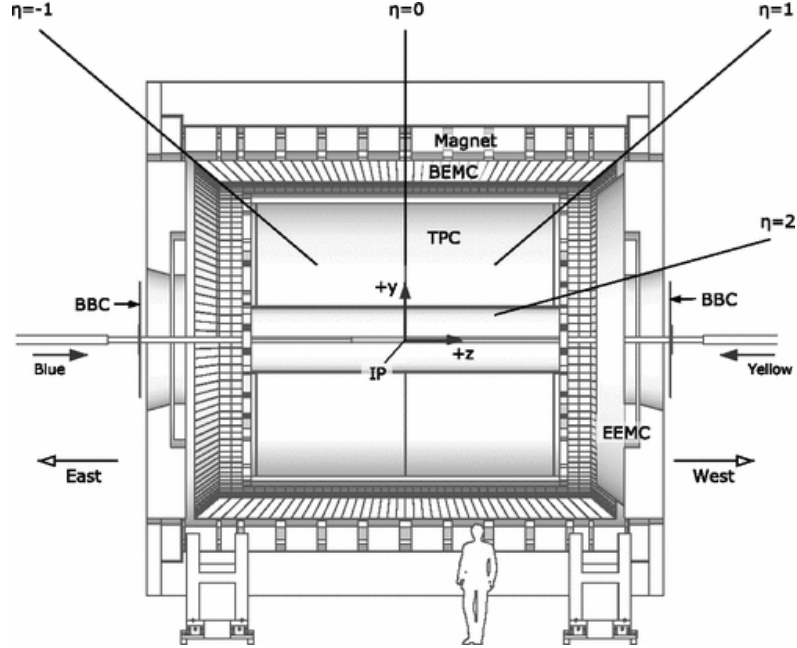


Figure 2.5: Arrangement of sub detector systems along with the co-ordinates in STAR. The figure has been sourced from [18].

The solenoidal magnet in the STAR experiment provides an uniform magnetic field along the z-axis, or beam direction, which bends the paths of charged particles to enable momentum measurement of the corresponding track. The beam pipe is constructed from Beryllium [136] due to its lightweight and low nuclear interaction probability. STAR's primary tracking detector, the Time Projection Chamber (TPC), spans approximately 4.2 meters in length and can track charged particles within $|\eta| < 1.8$, covering the full azimuthal angle in the plane perpendicular to the beam axis [20].

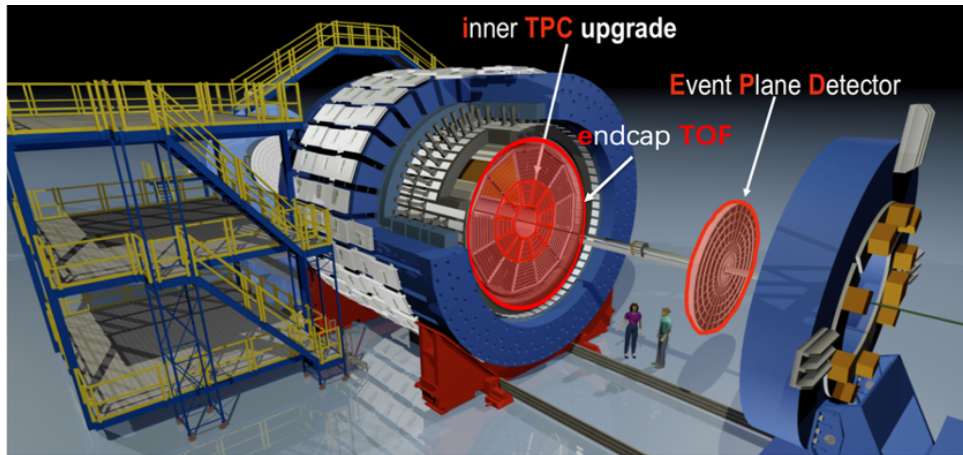


Figure 2.6: Upgraded sub detector in BES-II program. The figure has been sourced from [19].

Electrons, high- p_T photons, and electromagnetically decaying particles like π^0 and η mesons are detected using the Barrel Electromagnetic Calorimeter (BEMC) and the

Endcap Electromagnetic Calorimeter (EEMC). The BEMC covers $|\eta| < 1$, while the EEMC extends coverage to $1 < |\eta| < 2$. Both calorimeters are azimuthally symmetric and enhance STAR's ability to trigger on high- p_T particles and jets [137, 138].

In the subsequent sections we will discuss major sub detector systems of STAR, focusing on those, most relevant to the scope of this thesis.

2.2.1 The Time Projection Chamber: TPC

The Time Projection Chamber (TPC) is at the central sub-detector system in the suite of the STAR experiment, playing a vital role in tracking the hundreds of charged particles generated in an collision [20]. Its primary functions include tracking particles, measuring their momenta, and identifying them through their characteristic energy loss within the TPC gas volume. The TPC covers the entire azimuthal angle and spans 1.8 units in pseudorapidity. It can measure particle momenta up to 30 GeV/c and offers excellent particle identification up to 1 GeV/c. During the BES-II program, upgrades were made to the TPC, particularly to the inner sectors, enhancing momentum resolution. In the next discussion, the details of the TPC design and upgrades will be explained.

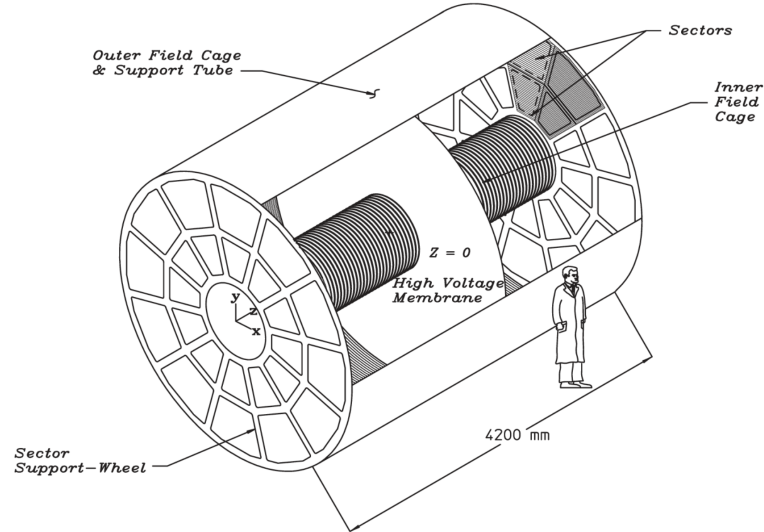


Figure 2.7: Three dimensional technical layout of the STAR-TPC, indicating major structural elements. The figure has been sourced from [20].

Figure 2.7 depicts the 3D schematic design of the TPC detector. Entire TPC system is located inside a solenoidal magnet that creates a 0.5 Tesla magnetic field along the z-axis. The TPC is a concentric cylindrical gas detector, 4.2 m in length and 4.0 m in diameter, surrounding the beam line. The active drift volume of the TPC has an inner diameter of 1.0 m and an outer diameter of 4.0 m. Its structure comprises a thin conductive Central Membrane (CM), an inner field cage, an outer field cage, and two end caps, which serve as readout plates. At the center of the TPC in the xy-plane lies the 70 μm thick central membrane (CM), made of carbon-coated Kapton, which divides the cylinder into two equal halves: the east and west ends, as shown in Figure 2.7. The CM is maintained at a potential of -28 kV, functioning as the cathode, while the end caps of the TPC, act as the anode, which is kept at ground potential. An electric field of approximately 135 V/cm is established between the CM, and the readout end caps, ensuring uniformity along the beam direction within the concentric field-cage cylinders.

The TPC volume is filled with P10 gas, a mixture of 90% argon (Ar) and 10% methane (CH₄). Argon, an inert gas, does not interact with other detector materials and serves as the primary source of ionization electrons. Methane, on the other hand, acts as a quenching gas, efficiently absorbing photons. The P10 gas is maintained at approximately 2 mbar above atmospheric pressure to prevent potential leaks. Its composition is optimized to achieve a fast electron drift velocity, reaching a maximum even at relatively low electric field strengths. At a uniform electric field of 130 V/cm, electrons within the P10 gas attain a drift velocity of approximately 5.5 cm/μs.

A uniform electric field between the CM and the endcap anode plates is essential for electron drift and is maintained by 183 equally spaced equipotential rings along the field cage cylinders. This setup ensures that recorded tracks remain undistorted by multiple Coulomb scattering. Additionally, the concentric field cage cylinders prevent contamination of the TPC gas from the external environment.

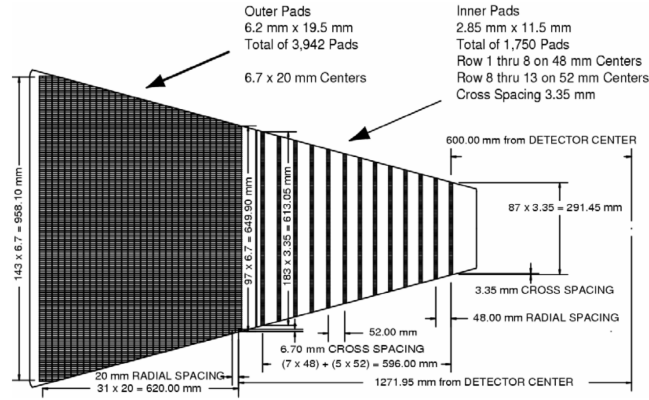


Figure 2.8: The layout of the TPC anode sector showing the outer and inner sub-sectors, located on the left and right, respectively. The figure has been sourced from [20]. This design corresponds to the BES-I data-taking period.

The TPC endcap readout planes are based on Multi-Wire Proportional Chambers (MWPC), which consist of four main components: three wire planes and one pad plane. Each endcap readout plane is divided into 12 trapezoidal readout sectors. These sectors are mounted inside the support wheel with a 3 mm gap between them, minimizing the dead area between chambers. Within each sector there are many smaller pads organized in different pad rows. Furthermore, each sector is divided into two parts: the inner and outer sectors, distinguished by the arrangement of pad rows along the radial direction from the beamline. An example of this TPC readout sector configuration is shown in Fig. 2.8.

The inner sector consists of 13 widely spaced pad rows. Being closer to the interaction region, where particle density is higher, this arrangement enhances position and track resolution in environments with high particle density. In contrast, the outer sector, located farther from the interaction region, contains 32 closely spaced pad rows. This design optimizes ionization energy loss measurements in low-particle-density regions. Therefore, if a particle traverses all the pad rows of the TPC, it would encounter a maximum of 45 hits (13 from the inner sector and 32 from the outer sector). These numbers are in accordance with the TPC design during the BES-I data-taking period.

In the Beam Energy Scan Phase-II program, STAR focuses on precision measure-

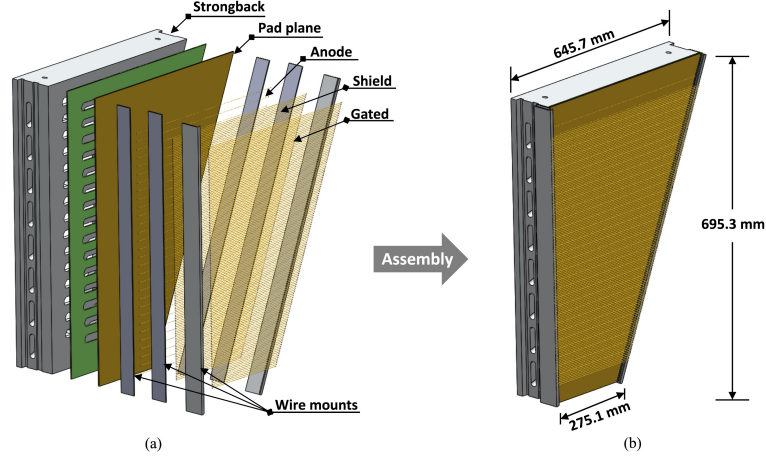


Figure 2.9: (a) A detailed view of the STAR iTPC sector with its components, that includes a supporting aluminum strongback, pad plane and three layers of wires supported on the corresponding wire mounts. (b) The final lay-out of the iTPC sector. The picture has been sourced from ref [21].

ments of key observables, which needs better momentum and dE/dx resolution. To achieve this, the inner sector of the TPC (iTPC) was upgraded in 2019. Figure 2.9 provides a detailed view of the upgraded STAR iTPC and its components [21]. The iTPC has been designed by the Shandong University (SDU).

As part of the upgrade, the number of pad rows in the inner TPC sector was increased from 13 to 40. This enhancement expanded the pseudorapidity coverage of the STAR TPC from $|\eta| < 1.0$ to $|\eta| < 1.5$. With the additional pad rows, a particle track can now achieve can attain maximum up to 72 hit points (40 from the inner sector and 32 from the outer sector) within the TPC. This upgrade has significantly improved the momentum resolution and lowered the minimum transverse momentum threshold for charged particle selection from $p_T = 150 \text{ MeV}/c$ to $60 \text{ MeV}/c$.

The TPC of the STAR detector has excellent track reconstruction ability. To reconstruct a particular track, the 3D space co-ordinates, needs to be identified properly. In the presence of a magnetic field, charged particle tracks bend into helices. As a charged particle moves trough the TPC, it ionizes the TPC gas atoms, creating electron clusters. These electrons drift towards the anodes under the influence of the electric field, creating avalanches through further ionization. This process generates signals on the TPC pad rows, which are then amplified and digitized by Analog-to-Digital Converters (ADCs) and sent to the Data Acquisition (DAQ) system [139] for event recording.

The x-y coordinates of the ionization cluster are determined by detecting signals across neighboring pads within a specific pad row. However, the drift time of the electron cluster, from its origin to the TPC endcaps, is utilized to calculate the z-coordinate. Dividing the drift time by the average electron drift velocity in the TPC gas ($\approx 5.5, \text{ cm}/\mu\text{s}$) provides the z-coordinate. Once the spatial coordinates of the electron array are established, the TPC track reconstruction algorithm, known as the Time Projection Chamber Tracker (TPT), that applies a helical fit to the TPC hit points to reconstruct the track.

If a track's distance of closest approach to the primary vertex is less than 3 cm, the primary vertex is included as one additional fit point and the track is fitted again, defining it as a primary track. Track reconstruction efficiency depends on the type of the particle, track selection criteria, acceptance range, and centrality. For instance, under BES-I detector conditions, the tracking efficiency for π^\pm , K^\pm , $p(\bar{p})$ in the intermediate

p_T region at mid-rapidity ($|y| < 0.1$) is approximately 70%, 60% and 70% respectively.

2.2.2 The Time Of Flight Detector set up

At higher p_T , the ionization energy loss (dE/dx) curves for different particles begin to overlap, reducing the reliability of particle identification (PID) using the TPC alone. The primary role of the TOF detector is to extend particle identification capabilities into this higher p_T range [140]. The Time of Flight system operates using combined information from the Pseudo Vertex Position Detector (pVPD) and the TOF detector, ultimately measuring the flight time of the charged particle tracks.

A. The Vertex Position Detector: VPD

There are two VPD detectors are positioned approximately 5.7 m away from the center of the TPC detector on opposite sides. It covers a rapidity range within $4.25 < |\eta| < 5.1$. Each detector consists of photomultiplier tubes and operates on the principle of plastic scintillator readout, designed to measure high-energy, fast-forward photons. By analyzing the arrival time of photon pulses on the equally spaced VPDs, the start time of an event is determined [141].

B. The Time Of Flight Detector: TOF

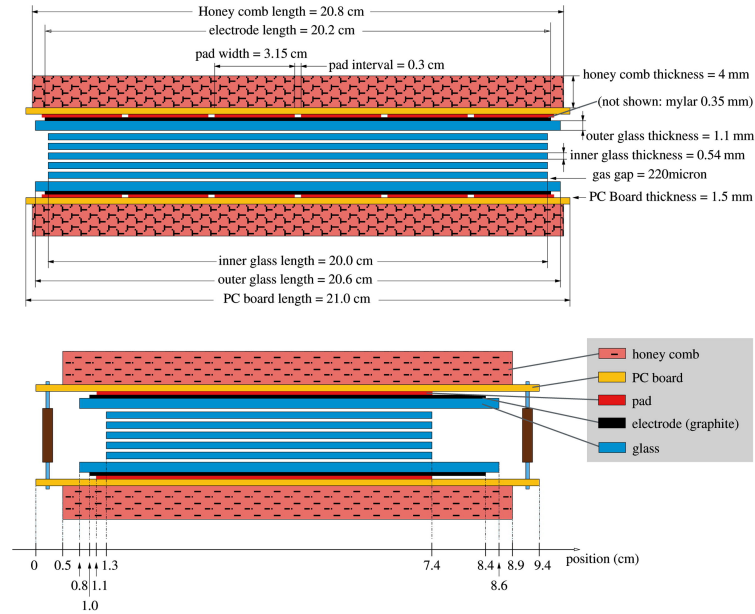


Figure 2.10: The top and bottom figure shows the longitudinal and side wise cut view of Multi Resistive Plate Chambers module of the STAR TOF. The plots have been scaled arbitrarily. The figure has been sourced from [22].

The TOF detector is a co-axially placed cylindrical detector situated right above the TPC detector, providing full azimuthal coverage and a pseudorapidity range of $|\eta| < 0.9$. It comprises 120 TOF trays (each measuring 2.4 m in length, 21.3 cm in width, and 8.5 cm in depth) distributed equally between the east and west sides, with 60 trays on each side. The trays are mounted at a 6-degree angle in the azimuthal plane surrounding the TPC. Each TOF tray contains 32 Multi-Gap Resistive Plate Chambers (MRPCs)

equipped with readout pads and aligned along the beam direction (z-direction). Figure 2.10 presents a cross-sectional view of an MRPC module in both longitudinal (top figure) and transverse (bottom figure) directions, along with the dimensions of its components. The MRPC modules measure $94 \text{ mm} \times 212 \text{ mm} \times 12 \text{ mm}$, in dimension, with an active area of $61 \text{ mm} \times 200 \text{ mm}$. The MRPCs consist of parallel resistive plates separated by gaps. These gaps contains a mixture of 5% isobutane and 95% R-134a (also known as freon gas). Graphite electrodes apply a high potential across the plates to generate a strong electric field.

When a charged particle passes through an MRPC, it ionizes the gas in the gaps, creating electron avalanches. These avalanches induce signals on the readout pads, which are arranged as a 1×6 array of copper pickup pads. The dimension of these pads measures approximately $3.1 \times 6.1 \text{ cm}^2$, with a gap of 0.3 cm between adjacent pads.

The complete TOF detector system operates using combined information from the VPD and TOF. The VPDs determine the start time of a track, while the TOF measures the end time. The difference between these times provides the total time of flight for a given track. With a time resolution of approximately 80–100 ps, the TOF detector is considered as a fast detector. A matching algorithm is used to match track hits recorded in the TOF with those in the TPC. If a track detected by the TPC has at least one corresponding hit in the TOF, it is termed as a "TOF-matched track." The TOF matching efficiency for π^\pm , K^\pm , $p(\bar{p})$ in the intermediate p_T region at mid-rapidity ($|y| < 0.1$) is around 60%.

Since the TPC detector has a relatively slower response, charged particle tracks from a prior event may occasionally be carried over and included in the multiplicity count of a subsequent event, creating pile-up events. These pile-up events can affect the analysis of sensitive observables. The fast response of the TOF detector is useful in identifying and removing these pile-up events. A condition is applied to ensure a proportional relationship between the number of charged particles observed in the TPC and TOF detectors, which helps removing pile-up events from the analysis.

2.2.3 Particle identification (PID): Using both TPC and TOF

As discussed in the previous section, the charge particle track loses energy while traversing through the TPC. This characteristic ionization energy loss (dE/dx) caused by a particular track, is utilized for particle identification (PID) within the TPC. As this energy loss is measured in a small scale distance and there is significant fluctuations in ionization, the accuracy in measuring the average dE/dx is limited. To address this, the most probable dE/dx is calculated. This involves discarding approximately 30% of the largest ionization clusters and using the truncated mean of the remaining 70% clusters for the calculation.

The mean value of the ionization energy loss for a charged particle track passing through the active detector medium is described by the Bichsel function [24], a modified version of the Bethe-Bloch formula [142]. The corresponding expression is given as:

$$\left\langle -\frac{dE}{dx} \right\rangle = Kz^2 \frac{Z}{A\beta^2} \left[\frac{1}{2} \ln \left(\frac{2m_e c^2 \beta^2 \gamma^2 T_{max}}{I^2} \right) - \beta^2 - \frac{\delta^2(\beta\gamma)}{2} \right] \quad (2.2.1)$$

Where,

K = Constant

z = Atomic number of the incident particle

Z = Atomic number of the absorbing material

A = Atomic mass of the absorbing material

m_e = Electron mass

T_{max} = maximum kinetic energy of an electron in an interaction

I = Mean ionisation energy of the material

δ = Correction related to energy density

$\beta\gamma = p/mc$, where m and p is the corresponding mass and momentum of the charged particle.

From equation 2.2.1, it can be observed that the mean ionisation energy loss of a particle within the TPC, depends on its mass, hence this can be used to identify the particle type.

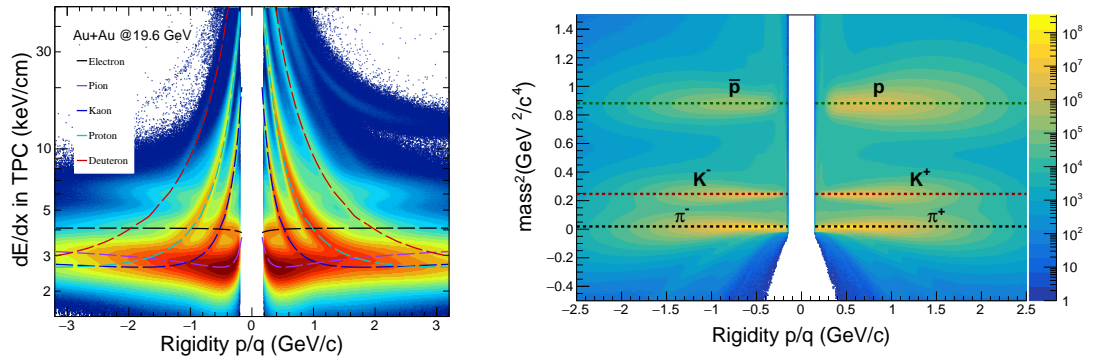


Figure 2.11: Left Panel: The ionisation energy loss (dE/dx) as a function of rigidity (p/q) for different charged particles for minimum bias Au+Au collisions at $\sqrt{s_{NN}} = 19.6$ GeV. Different colored lines represent the Bichsel function expectations for different particles **Right panel:** The $Mass^2$ as a function of rigidity (p/q) for different charged particles for minimum-bias Au+Au collisions at $\sqrt{s_{NN}} = 19.6$ GeV. The dashed line represents the PDG values for different particles.

The Left panel of fig 2.11 shows the variation of the ionisation energy loss as a function of rigidity (p/q) along with the theoretical values obtained from the bichsel function. Various bands smeared around the theoretical curves are that obtained from experiment.

to identify the particles from the dE/dx information, one observable called $n\sigma_y$ is constructed, that measures the standard deviation of the distribution from its expected theoretical value. The observable is expressed as:

$$n\sigma_y = \frac{1}{R_{TPC}} \frac{\langle dE/dx \rangle|_{y,measured}}{\langle dE/dx \rangle|_{y,theory}} \quad (2.2.2)$$

Here $\langle dE/dx \rangle|_{y,measured}$ and $\langle dE/dx \rangle|_{y,theory}$, are the ionisation energy loss measured from the experiment and that obtained from the bichsel expectation for a given particle type y respectively and R_{TPC} , is the dE/dx resolution of the TPC detector that comes around 7 – 8%. However after the iTPC upgrade, this number has been enhanced by around 25%, the TPC resolution for the BES-II datasets is around 6 – 7% [143].

From fig 2.11, it is evident that distinct difference in the dE/dx bands can be observed in low momentum, where pions and kaons can be distinguishable up-to $p \approx 0.6$ GeV/c and that of (anti)protons up-to $p \approx 1.1$ GeV/c in momenta. But beyond that the bands starts to merge. Hence to further identify the particle TOF is needed. As discussed

earlier, the TOF detector provides the flight time (t) of a given track. The path length (l) information of the corresponding track can be obtained from TPC, . Using this the velocity of the track $\beta = \frac{l}{ct}$ can be calculated. Since

$$\beta = \frac{p}{E} = \frac{p}{\sqrt{p^2 + m^2}} \quad (2.2.3)$$

$$m^2 = p^2 \left(\frac{1}{\beta^2} - 1 \right) = p^2 \left(\left(\frac{ct}{l} \right)^2 - 1 \right) \quad (2.2.4)$$

The right panel of the fig 2.11, shows the variation of $mass^2$ bands as a function of rigidity (p/q). It can be observed that the $mass^2$ bands obtained using TOF for different particles are well separated up-to relatively larger momentum region as compared to the dE/dx band in TPC. Using the TOF detector the pions and kaons can be separated up-to $p \approx 1.6$ GeV/c and that of (anti)protons up-to $p \approx 3.0$ GeV/c in momenta.

For the analysis presented in this thesis, a hybrid PID scheme has ben adopted, that uses the TOF PID, when the track is matched in the TOF detector, other wise the TPC PID is used. Suitable cuts on the $n\sigma$ and m^2 values has been put to select the particles. The detailed description will be provided in chapter 3.

2.2.4 Trigger detectors

The data acquisition (DAQ) system of STAR [139] is highly efficient, flexible, and capable of recording data simultaneously from multiple detectors with varying readout rates. The primary sub-detectors used for particle identification operate at relatively slow rates, typically around 100 Hz. In contrast, the interaction rate for the highest luminosity beams at RHIC reaches approximately 10 MHz. A fast detector sustem is essential to bridge this substansial gap, that ensure recording of every useful event.

This challenge is addressed in STAR by employing trigger detectors, which are exceptionally fast at selecting events of interest for physics analysis. The STAR trigger system [23] activates other sub-detectors to record useful data, enabling efficient event selection. Key components of the STAR trigger system include the ZDC, BBC, VPD, BEMC, and EEMC.

Table 2.3: The pseudo-rapidity coverage of various trigger detectors in STAR experiment. The data is collected from [47].

Mid-rapidity detectors	Forward rapidity detectors	Vertex detectors
MTD : $ \eta < 0.5$	FMS : $2.5 < \eta < 4.0$	BBC : $2.2 < \eta < 5.0$
TOF : $ \eta < 0.9$	RPD : $7.0 < \eta < 9.0$	VPD : $4.25 < \eta < 5.1$
BEMC : $ \eta < 1.0$		ZDC : $ \eta > 6.0$
EEMC : $1.07 < \eta < 2.0$		

A schematic diagram, with arrangement of different trigger systems [23] used in STAR is shown in Figure 2.12. The pseudo rapidity coverage of different trigger detectors used in STAR detector is listed in table 2.3. Some of the trigger detectors are disscussed below.

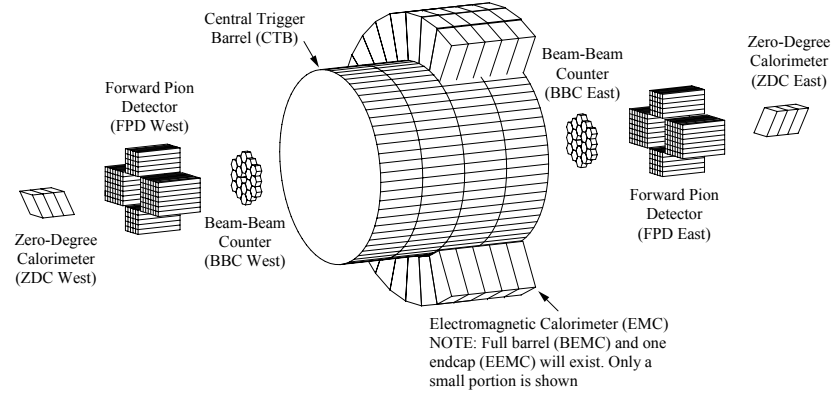


Figure 2.12: The diagram showing the arrangement of different trigger detectors in STAR experiment. The figure has been sourced from [23]. Currently, central trigger barrel (CTB) has been replaced by the TOF detector system and Forward Pion Detector (FPD) has been replaced by the Forward Meson Spectrometer (FMS).

A. Zero Degree Calorimeter: ZDC

The Zero Degree Calorimeters (ZDCs) [144] are part of all four experimental setups at RHIC. These small transverse-area calorimeters are located on either side (east and west) of the TPC center at a distance of 18 m, with a horizontal acceptance of ± 5 cm. As the name suggests, it is placed very close to the beam axis ($\theta < 2$ mrad). Each ZDC consists of three modules, with each module comprising alternating layers of tungsten plates and wavelength-shifting fibers, that are connected to a photomultiplier tube (PMT). The primary function of the ZDC is to measure the multiplicity and energy deposited by spectator neutrons following a collision event. Additionally, it detects coincident signals from both sides of the interaction region, which are used for luminosity monitoring [145]. A simultaneous signal from both ZDCs characterizes a minimum bias heavy-ion collision event. The ZDC has a time resolution of approximately 100 ps and can determine the collision vertex by measuring the time difference between coincident signals from either side. To enhance functionality, the Shower Maximum Detector (SMD) is installed between the first and second ZDC modules. The SMD captures the spatial distribution of spectator neutron hits in the transverse plane. This ZDC-SMD setup also supports other areas of research, including ultra-peripheral collisions, anisotropic flow, and spin physics [146].

B. Beam Beam Counters: BBC

The Beam Beam Counters (BBCs) are primarily designed to trigger minimum bias p+pp+p collisions [147]. These detectors have a hexagonal geometry with full azimuthal coverage and are located on each sides of the interaction region at a distance of 3.7 m from the $z = 0$ position. The BBCs provide a pseudorapidity coverage of $2.2 < |\eta| < 5.0$ [47]. To classify an event as minimum bias, a coincidence of signals from both BBCs is required. The time difference between these signals is used to determine the primary vertex of the collision event and to reject background events, such as beam-gas interactions. Additionally, the small tiles in the BBC detectors facilitate the reconstruction of the first-order event plane, which is useful for anisotropic flow analyses [148].

C. Vertex Position Detectors: VPD

The Vertex Position Detectors (VPDs) have been operational since 2009 for event triggering [141]. VPD consists of 19 lead converters and plastic scintillators coupled with photomultiplier tube (PMT) readouts. These detectors are installed on both sides of the interaction point, approximately 5.7 m away, and provide a pseudorapidity coverage of $4.25 < \eta < 5.14$. Similar to other trigger detectors, a minimum bias collision event requires simultaneous hits on both VPDs. The coincidence time between the detectors is used to determine the primary vertex position. Compared to the BBCs, the VPDs offer better time resolution.

D. Electro Magnetic Calorimeters: EMC

Electromagnetic calorimeters (EMCs) are designed to measure the energy of particles that interact through electromagnetic interactions. In STAR, electromagnetic calorimeters are used to trigger rare and high- p_T processes, such as jets, leading hadrons, direct photons, and heavy quarks. These processes involve significant energy deposition in the EMC towers or patches. They also provide broad acceptance for detecting photons, electrons (e.g., from J/Ψ and Υ decays), π^0 , and η mesons across polarized $p + p$ collisions and Au+Au collisions. These detectors are also useful to categorize ultra peripheral collisions. The STAR experiment employs two electromagnetic calorimeters: the Barrel Electromagnetic Calorimeter (BEMC) [137] and the Endcap Electromagnetic Calorimeter (EEMC) [138].

In addition to all these detectors several other sub detector systems are also present at the STAR experiment. These include the Muon Tracking Detector (MTD), which is mounted outside the STAR magnet and is used to detect muon tracks [149]. The Forward Pion Detector (FPD), installed in 2003, was upgraded to the Forward Meson Spectrometer (FMS) in 2008 [150]. The FMS is designed to measure photons and electrons produced at high rapidity, and serves as a fast detector for triggering purposes.

2.3 Summary

This chapter provides a brief overview of different sub-detector systems present in the STAR experiment at the Relativistic Heavy Ion Collider (RHIC) facility stationed at Brookhaven National Laboratory (BNL), USA.

Chapter 3

K^{*0} production in Au+Au collisions from RHIC beam energy scan phase-I

This chapter includes the results for K^{*0} -meson production measured at mid rapidity ($|y| < 1.0$) in Au+Au collisions at $\sqrt{s_{NN}} = 7.7, 11.5, 14.5, 19.6, 27$ and 39 GeV using BES-I data.

3.1 Introduction

Resonances have short lifetimes, comparable to the duration of the fireball produced in heavy-ion collisions. The production of short-lived resonances like K^{*0} offers a unique opportunity to probe the hadronic phase formed during these collisions. Due to its brief lifetime, the decay products of K^{*0} may interact with the surrounding medium, potentially altering the properties of the resonance. Within the medium, the decay particles can undergo rescattering or re-generation processes. Studying the centrality-dependent yield ratios of resonances to stable hadrons with similar quark content (e.g., K^{*0}/K and ϕ/K^{*0}) can provide insights into the in-medium effects and their interplay. Previous measurements at top RHIC and LHC energies have shown that hadronic rescattering dominates over regeneration in central heavy-ion collisions [12, 14, 28].

The Beam Energy Scan (BES) Program at the STAR experiment at RHIC, which spans a wide range of collision energies, provides a unique opportunity to explore QCD matter with varying net baryon content at mid-rapidity. Studying resonances at BES energies will help reveal the dynamics of the hadronic phase at lower collision energies. In this chapter, the production of the K^{*0} meson is analyzed in Au+Au collisions

at $\sqrt{s_{NN}}=7.7 - 39$ GeV. The multiplicity-dependent yield and $\langle p_T \rangle$ are measured. The $K^{*0}K$ ratio is examined as a function of multiplicity and compared with the ϕ/K ratio across different collision energies to investigate in-medium effects.

3.2 Data sets, events and track selection cuts

3.2.1 Data set

The results presented here are obtained from the data collected by the STAR experiment at RHIC for Au+Au collisions at $\sqrt{s_{NN}} = 7.7, 11.5, 14.5, 19.6, 27,$ and 39 GeV during the Beam Energy Scan (BES) phase-I program . The data set is taken with a minimum bias trigger. The Min-bias events are those which requires a coincidence of signals from the Zero Degree Calorimeters (ZDCs), Vertex Position Detectors (VPDs) and/or Beam-Beam Counters (BBCs) situated at the either side from the center of the STAR detector [141, 147, 151] . The events are also assigned production tags that are related to the software libraries used in the event reconstruction for different collision energies by STAR. All these details about the BES data sets are listed in table 3.1.

Table 3.1: Collision energy, production year, production tag, and triggers used.

Au+Au, $\sqrt{s_{NN}}$	Production Year	Production id	Trigger ids
7.7 GeV	2010	P10ih	290001, 290004
11.5 GeV	2010	P10ih	310004, 310014
14.5 GeV	2014	P10ih	440005, 440015
19.6 GeV	2011	P11id	340001, 340011, 340021, 430002, 340012, 340022
27 GeV	2011	P11id	360001, 360002
39 GeV	2010	P10ik	280001, 280002

3.2.2 Event cuts

The primary vertex of an event is determined using the TPC detector subsystem and represents the most common origin of tracks produced by the collision. Different cuts on the primary vertex position along the longitudinal beam direction (V_z) are applied for various collision energies. These vertex cuts are carefully studied and optimized to maximize event statistics while ensuring uniform efficiency and detector acceptance. At lower collision energies, the colliding beams are less collimated, which significantly affects event collection due to reduced beam luminosity. As a result, a relatively larger cut on the z -vertex was used for $\sqrt{s_{NN}} = 7.7$ GeV to improve statistical precision. To eliminate background events, such as those involving beam-pipe and beam-gas interactions, the transverse $x - y$ coordinates of the primary vertex (V_x, V_y) are constrained by the condition $V_r = \sqrt{V_x^2 + V_y^2} < 2$ cm. For $\sqrt{s_{NN}} = 14.5$ GeV, the vertex is slightly offset at (0.0, -0.89) in the $x - y$ plane instead of being centered at (0, 0). This offset is due to the installation of the Heavy-Flavor Tracker (HFT) during that year's data collection. Hence the V_r is selected to be $V_r = \sqrt{V_x^2 + V_y^2} < 1$ cm.

The vertex cuts applied for all collision energies, along with the number of minimum bias events remaining after these selection cuts, are summarized in the table 3.2.

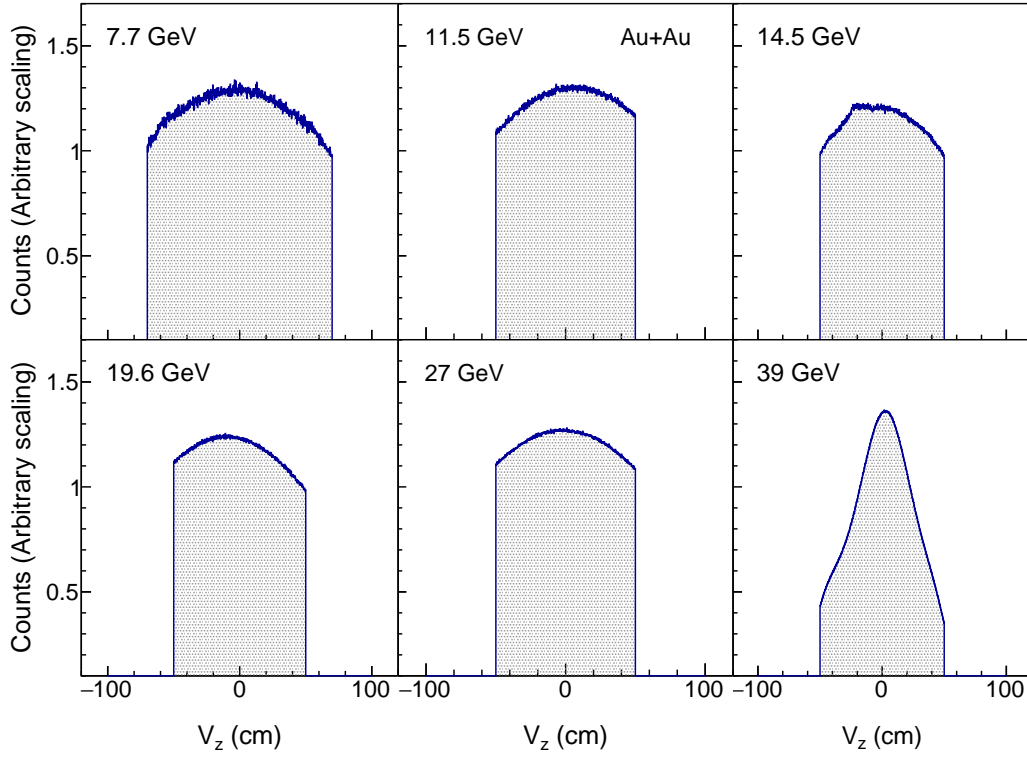


Figure 3.1: The distribution of the z-component of the primary vertex from Au+Au collisions after applying cuts at six different center-of-mass energies.

Additionally, several representative plots illustrating event selection using these cuts for various collision energies are shown in the Fig. 3.1, 3.2

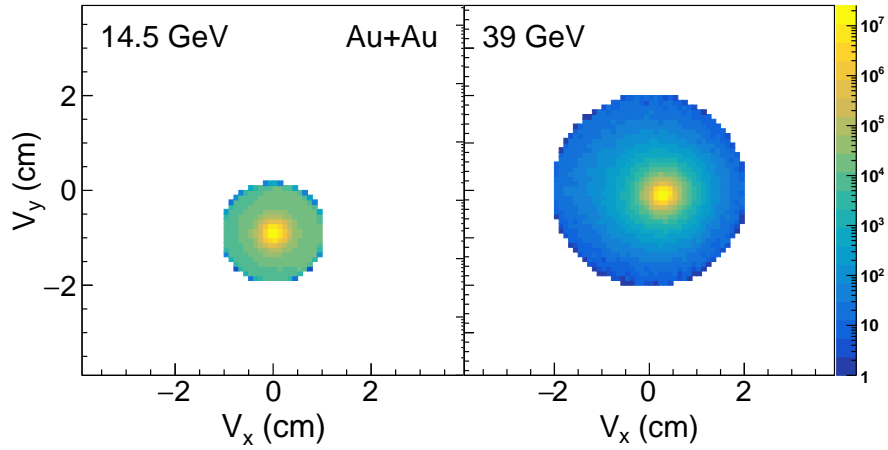


Figure 3.2: The distribution of V_x vs. V_y from Au+Au collisions after applying cuts at six different center-of-mass energies.

Table 3.2: List of event cuts applied on primary vertex selection for each collision energy and number of minimum bias good events.

Au+Au, $\sqrt{s_{NN}}$	V_z (cm)	V_r (cm)	Events (in millions)
7.7 GeV	< 70 cm	< 2 cm	4.7 M
11.5 GeV	< 50 cm	< 2 cm	12.1 M
14.5 GeV	< 50 cm	< 1 cm	15.3 M
19.6 GeV	< 50 cm	< 2 cm	27.7 M
27 GeV	< 50 cm	< 2 cm	53.7 M
39 GeV	< 50 cm	< 2 cm	128.5 M

3.2.3 Centrality determination

As the name suggests, centrality in heavy-ion collisions is associated with the impact parameter, which refers to the perpendicular distance between the centers of the two colliding nuclei in an event. A large overlap region during the collision indicates a small impact parameter, classifying the event as central. Conversely, a small overlap region corresponds to a larger impact parameter, categorizing the event as peripheral. In central events, a large number of particles are generated, resulting in high event multiplicity, whereas in peripheral events, the multiplicity is low. While the concept of collision centrality seems straightforward, determining the centrality in practice is quite complex. In real experiments, the impact parameter cannot be directly measured. Instead, an experimental observable, referred to as "reference multiplicity" or " N_{ch}^{raw} " is used to correlate with the impact parameter and determine centrality. This represents the raw charged hadron multiplicity measured by the TPC within the pseudo-rapidity range $|\eta| < 0.5$, without corrections for detector efficiency and acceptance effects. The measured reference multiplicity $dN_{ch}/d\eta$ distribution from real data is compared with that obtained from a two component model [152] as described ;

$$\frac{dN_{ch}}{d\eta} = n_{pp} \left[(1 - x) \frac{N_{part}}{2} + x N_{coll} \right] \quad (3.2.1)$$

Here, the fitting parameter n_{pp} represents the average charged particle multiplicity in minimum-bias $p + p$ collisions, while x denotes the fraction of charged particles produced from hard processes. N_{part} refers to the total number of nucleons that have participated in at least one collision, and N_{coll} corresponds to the number of nucleon-nucleon binary collisions determined from Glauber Monte-Carlo simulations [153]. The value of x is kept constant at 0.12 ± 0.02 , based on the linear interpolation of PHOBOS results at $\sqrt{s_{NN}} = 19.6$ and 200 GeV [154]. Systematic uncertainties on n_{pp} are assessed by varying both n_{pp} and x within the quoted uncertainty of x to achieve the minimum χ^2 value that best describes the measured multiplicity distribution from. The inelastic nucleon-nucleon cross-section, σ_{NN}^{inel} , is determined by fitting available NN data for total and elastic $p+p$ cross-sections from the Particle Data Group [155]. The experimental values of σ_{NN}^{inel} and n_{pp} that has been used in Monte-Carlo Glauber simulations for BES energies are summarized in Table 3.3

In MC Glauber simulations, the nucleus are independently generated with the density of the nucleons inside the nucleus are sampled by wood-saxon profile as,

$$\rho = \frac{\rho_0}{1 + e^{\frac{r-r_0}{a}}} \quad (3.2.2)$$

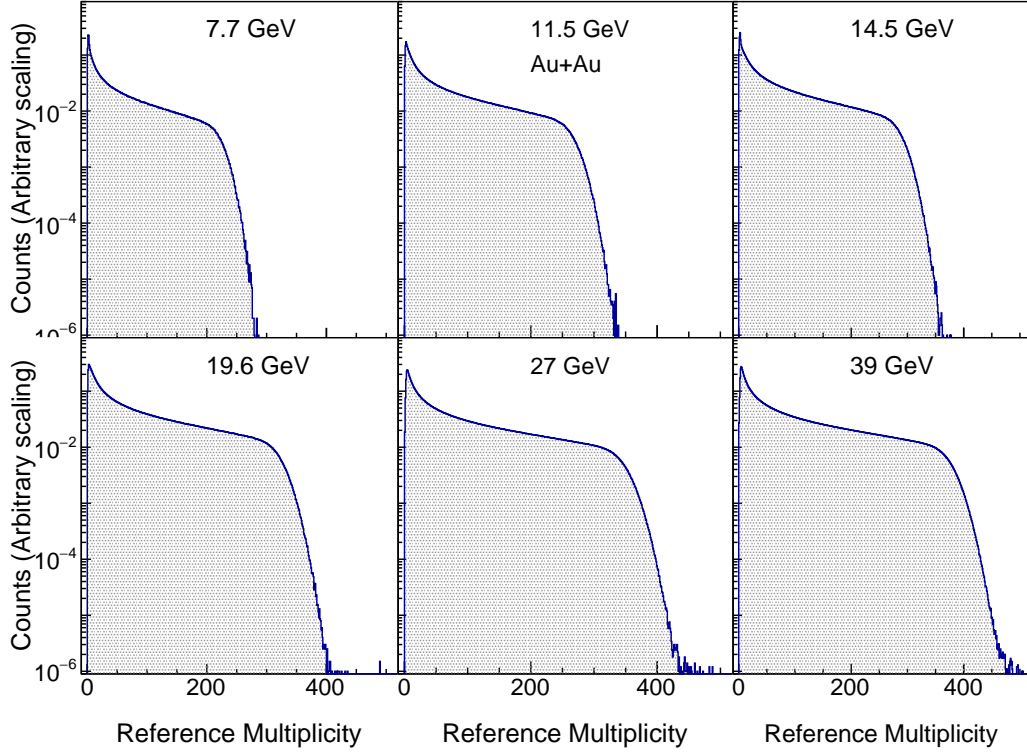


Figure 3.3: The uncorrected charged particle multiplicity (Refmult) distribution of reconstructed per unit pseudo-rapidity interval at mid-rapidity at six different centre-of-mass energies for minimum bias Au+Au collisions.

Table 3.3: experimental values of σ_{NN}^{inel} and n_{pp} .

$\sqrt{s_{NN}}$ (GeV)	n_{pp}	σ_{NN}^{inel} (mb)
7.7	0.89 ± 0.04	30.8 ± 1.20
11.5	1.07 ± 0.05	31.2 ± 1.13
14.5	1.15 ± 0.05	31.5 ± 1.10
19.6	1.29 ± 0.05	32.0 ± 1.11
27	1.39 ± 0.06	33.0 ± 1.10
39	1.52 ± 0.08	34.0 ± 1.10

where ρ_0 represents the nuclear density, r_0 denotes the nuclear radius, and a is the skin depth. If the distance between two nuclei is less than a certain threshold ($d \leq \sqrt{\frac{\sigma_{NN}^{inel}}{\pi}}$), they are considered as participants, otherwise spectators. The nuclei are repeatedly sampled and collided with random impact parameter b . Distributions such as $d\sigma/db$, $d\sigma/dN_{part}$, and $d\sigma/dN_{coll}$ are determined. These distributions are segmented as fractions of the total measured cross-section, and the average values of N_{part} and N_{coll} are calculated for each centrality bin.

Fig 3.3 shows the reference multiplicity distribution for minimum bias events at $\sqrt{s_{NN}} = 7.7-39$ GeV. The $\langle N_{part} \rangle$, $\langle N_{coll} \rangle$ and corresponding values of reference multiplicity for different collision centralities are provided in appendix 3.8.35.

The minimum-bias trigger events are categorized into nine centrality classes: 0-5%, 5-10%, 10-20%, 20-30%, 30-40%, 40-50%, 50-60%, 60-70%, and 70-80%. The last

centrality bin, corresponding to 80-100%, is excluded from calculations due to considerable trigger and vertex reconstruction inefficiencies at low multiplicity associated with this centrality range.

3.2.4 Track cuts

In the analysis presented in this chapter, only primary tracks are selected for all the data sets. The invariant mass reconstruction of K^{*0} signals is performed using charged K and π tracks originating from the primary vertex of the collision, hence referred to as primary tracks. Track selection criteria are applied to maximize tracking efficiency, ensuring good particle identification (PID) with enhanced dE/dx and momentum resolution for primary charged particles, and to reduce contamination from secondary particles. To guarantee good-quality tracks, several quality cuts are implemented, as detailed in Table 3.4.

Table 3.4: List of track selection cuts applied for the analysis presented in this chapter.

Track parameter	default value
Transverse Momentum (p_T)	$0.15 < p_T < 10.0$ (GeV/ c)
Pseudo-rapidity ($ \eta $)	< 1.0
Pair-rapidity ($ y_{K\pi pair} $)	< 1.0
Distance closest approach (DCA)	< 2 cm
No. of fit points (nHitsFit)	> 15
nHitsFit/nHitsPoss	≥ 0.55

i) Kinematic cuts

The solenoidal magnetic field in the detector causes charged particles to bend as they traverse the detector. This bending is more pronounced for particles with low p_T , which impacts their reconstruction. To mitigate this effect, a standard cut of $p_T > 0.15$ GeV/ c is applied. To take full advantage of the TPC's acceptance range, daughter particles are selected within $|\eta| < 1.0$.

ii) Distance closest approach (DCA)

The distance of closest approach (DCA) of a track refers to the shortest distance between the track and the primary vertex. The highly energetic particles produced in collisions (primarily pions) can interact with the detector apparatus, such as beam pipe, resulting in the creation of particles not originating from the intended heavy ion collision. These secondary particle tracks tend to have a large DCA relative to the primary vertex. To exclude such tracks from analysis, a DCA cut of less than 2 cm ($DCA < 2$ cm) is applied. This cut also helps in eliminating tracks from particles originating from weak decays.

iii) No. of fit points (nHitsFit)

During track reconstruction in the TPC, the hit points generated by a track as it passes through the TPC gas are mapped along the TPC pad rows. As the name suggests, These hit points are then fitted using a reconstruction algorithm, and extrapolated back to origin. Requiring a higher number of fit points, helps to avoid short tracks and enhances momentum resolution but also reduces the total number of tracks. Hence an optimised

selection cut of $n\text{HitsFit}/n\text{HitsPoss}$ greater than 15 is selected for this analysis.

iv) $n\text{HitsFit}/n\text{HitsPoss}$

During track reconstruction, improper association of TPC hit points in different regions of the detector can cause a single track to be reconstructed as two separate tracks, an effect known as track splitting. This effect can be minimized by requiring more than half the total possible hits for the given track geometry, with a maximum limit of 45 (the total number of pad rows available in the TPC for mapping hits). For this analysis, a selection criterion of $n\text{HitsFit}/n\text{HitsPoss} > 0.55$ is applied.

3.3 Particle Identification (PID)

In this analysis, K^{*0} mesons were reconstructed through their hadronic decay channel $K^{*0} \rightarrow K\pi$ [39, 155]. Hence the first step is to identify the daughter particles among all detected particles. A particle is primarily identifiable by its mass, which is unique for each particle type, and its charge, which distinguishes particles from their antiparticles. In a heavy-ion collision experiment, the charge of a track can only be determined from its curvature in a magnetic field, as there are no direct measurements of its mass. However, additional information recorded by the detector provides indirect way to obtain the particle's mass information. For particle identification, both Time Projection Chamber (TPC) [20] and Time of Flight (TOF) [140] detectors are used in this analysis.

3.3.1 Particle Identification from TPC

The Time Projection Chamber (TPC) is the primary tracking detector in the STAR experiment and has excellent particle tracking and identification capabilities, particularly at low momentum. The TPC is used to measure particle momentum, ionization energy loss per unit path length (dE/dx), and to reconstruct the trajectory of charged particles. By comparing the measured dE/dx as a function of momentum with the theoretical values derived from the Bichsel formula [24], the particle type can be identified. To facilitate particle identification in the STAR experiment, a specific variable is defined as follows [156]:

$$N\sigma(\pi, K) = \frac{1}{R_{TPC}} \log \frac{(dE/dx)_{\text{measured}}}{\langle dE/dx \rangle_{\text{theory}}}, \quad (3.3.1)$$

Here, R_{TPC} represents the dE/dx resolution of the TPC detector, which is approximately 8.1%. A characteristic plot from Au+Au collisions at $\sqrt{s_{NN}} = 19.6$ GeV, showing dE/dx as a function of track momentum rigidity (momentum/charge) (p/q), is shown in Fig. 3.4. From the figure one can observe that at higher momentum, the particle tracks start to merge. In the STAR TPC, pions and kaons can be distinguished up to about $p_T = 0.7$ GeV/c, while (anti-) protons can be distinguished up to about $p_T = 1.1$ GeV/c.

In this analysis, we primarily use the TPC with $|N\sigma| < 2.0$ to select pions and kaons.

3.3.2 Particle Identification from TOF

The TOF detector enhances particle identification capabilities at intermediate and high p_T . With the TOF data, pions and kaons can be separated up to $p \approx 1.6$ GeV/c, and

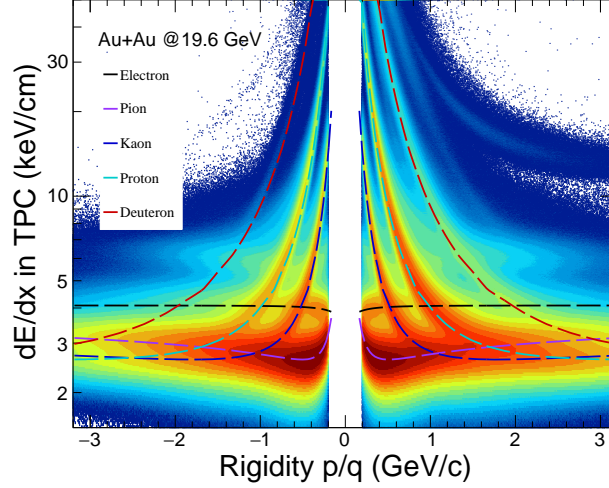


Figure 3.4: Ionization energy loss(dE/dx) deposited by various charged particles in TPC for Au+Au collisions at $\sqrt{s_{NN}} = 19.6$ GeV vs. Rigidity ($p \times q$). The dashed curves represent the theoretical expectation of mean ionisation energy loss (dE/dx) values for each corresponding particle, calculated using the Bichsel function [24].

protons and kaons up to $p \approx 3.0$ GeV. The TOF detector measures the time a track takes to travel from the collision's primary vertex to reach the TOF. Using this time of flight and the track length, the particle's mass can be calculated as follows :

$$m^2 = p^2((t_{\text{TOF}} \times c/l)^2 - 1), \quad (3.3.2)$$

In this equation, p represents the momentum, t_{TOF} is the time of flight, c is the speed of light in vacuum, and l is the particle's flight path length. The TOF detector has a time resolution of approximately 80 to 100 ps. For pion and kaon selection, the required m^2 ranges are $-0.2 < m^2 < 0.15$ (GeV/c²)² for pions and $0.16 < m^2 < 0.36$ (GeV/c²)² for kaons. Figure 3.5 shows the measured m^2 at $\sqrt{s_{NN}} = 19.6$ GeV for various charged particles, where different charged particles are distinctly separated into different bands of m^2 values.

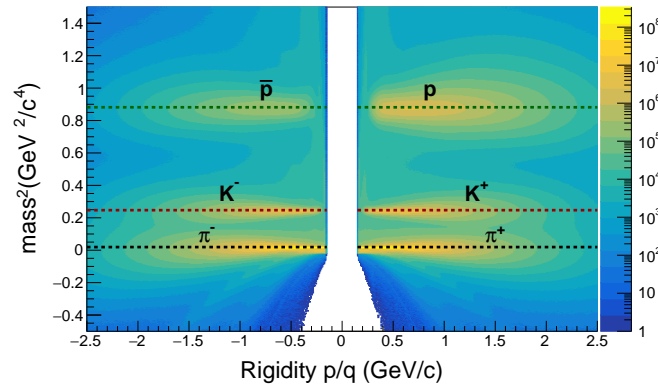


Figure 3.5: Mass-squared ($mass^2$) of various charged particles measured by TOF for Au+Au collisions at $\sqrt{s_{NN}} = 19.6$ GeV as a function of Rigidity (p/q). The dashed lines represent the PDG $mass^2$ values for each corresponding particle.

To enhance particle identification efficiency, this analysis utilizes a hybrid approach that combines information from both the TPC and TOF detectors. If TOF information is available, the TOF PID is used; otherwise, the TPC PID is applied.

3.4 Signal Extraction

The K^{*0} meson, being an unstable hadron, decays into its daughter particles according to specific branching ratios, and thus cannot be directly detected in the detectors. It must be reconstructed. In this analysis, the K^{*0} is reconstructed from its hadronic decay channel $K^{*0}(\bar{K}^{*0}) \rightarrow K^\pm \pi^\mp$ (branching ratio 2/3) [155]. Since the exact decay daughters of the K^{*0} mesons cannot be identified experimentally, the invariant mass of the K^{*0} meson is reconstructed by considering all possible combinations of oppositely charged pion and kaon pairs within the same event, as defined by the equation [12, 39]:

$$M_{\pi K} = \sqrt{(E_K + E_\pi)^2 - (\vec{p}_K + \vec{p}_\pi)^2} \quad (3.4.1)$$

Where, $E_K = \sqrt{p_K^2 + m_K^2}$ and $E_\pi = \sqrt{p_\pi^2 + m_\pi^2}$

However, this event-by-event reconstruction also includes background combinations of πK pairs that do not originate from K^{*0} . Due to the large uncorrelated background, a clear signal peak is not immediately visible. To observe the signal one need to get rid of the combinatorial background from the same event πK pair distribution. In this analysis, the combinatorial background is estimated using two methods: track rotation and event mixing, which are described in the following section.

3.4.1 Track rotation method

In this method, the momentum vector of one of the decay daughters is rotated by a random angle in the transverse plane (the plane perpendicular to the beam direction). In this analysis, a fixed rotation of 180 degrees is applied to the momentum vector of pion track. Rotating the track by 180 degrees in the transverse plane, flips its transverse momentum direction while keeping its magnitude unchanged. This operation destroys any real physical correlation between the two tracks that would have existed if they had originated from a common parent (like a K^{*0} decay). As a result, the new $K\pi$ pairs formed after rotation represent purely uncorrelated/combinatorial background [39].

3.4.2 Mixed event method

In this method, kaons from one event are artificially combined with pions from another event, ensuring no physical correlation between unlike-sign tracks that could produce a K^{*0} meson. For the reconstruction of event-mixing pairs, five events with similar multiplicity and z-vertex position are mixed [157]. After event mixing, the invariant mass distribution of the combinatorial background has statistics that are eight times higher than those of the invariant mass distribution obtained from the same-event pairs.

Once a suitable invariant mass distribution is obtained for the combinatorial background, it is normalized in the mass region of 1.05-1.10 GeV/ c^2 and subtracted from the same-event unlike-sign $K\pi$ pair invariant mass distribution to obtain the K^{*0} meson signal peak.

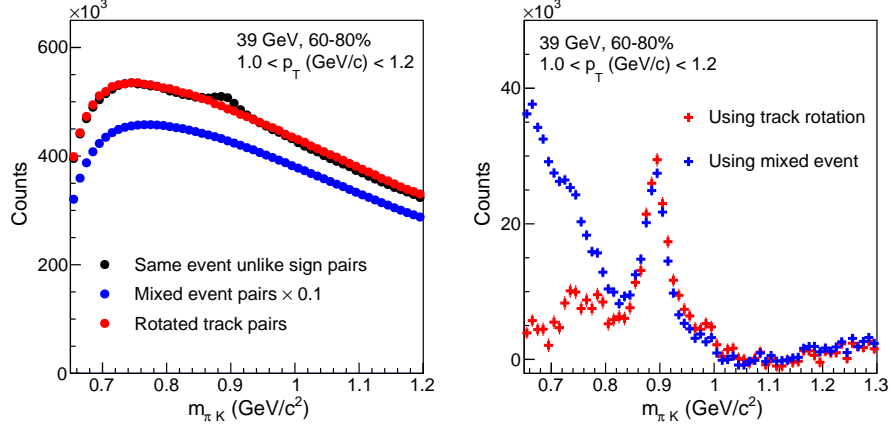


Figure 3.6: Left panel: The invariant mass distribution of πK pairs reconstructed using unlike-charge pairs from the same event, unlike-charge pairs from mixed events, and rotated track pairs from the same event in 60-80% Au+Au collisions at $\sqrt{s_{NN}} = 39$ GeV. Right panel: The πK pair invariant mass distribution after subtracting the normalized background pair distributions, measured using different methods, from the unlike-charge same event distribution.

From Fig. 3.6, we can observe that the combinatorial background is better described by the track rotation method than the mixed event method, mostly at low mass region. Additionally, the track rotation method is more time-efficient compared to the mixed event method. Hence in the present analysis the track-rotation method is used as the default method to estimate the combinatorial background where as mixed event method has been used for the consistency check.

After the subtraction of the combinatorial background, the background still associated with the K^{*0} invariant mass distribution, known as residual background. This can arise from various sources, such as correlated decay daughters from higher mass resonances (e.g., $K_1(1400)$, $K^*(1410)$, $K^*(1680)$, $K_2(1770)$ etc.) decaying into kaons and pions, or misidentified daughter tracks. To account for this, the signal peak is fitted using a Breit-Wigner function combined with a first-order polynomial, where the later one fits the residual background distribution. The fitting function used for the K^{*0} meson can be written as follows [25];

$$\frac{Y}{2\pi} \times \frac{\Gamma_0}{(m_{\pi K} - m_0)^2 + \frac{\Gamma_0^2}{4}} + \text{Res. Bkg} \quad (3.4.2)$$

Where, $\text{Res. Bkg} = Am_{\pi K} + B$, Γ and m_0 is the mass and width of K^{*0} meson in vacuum and Y is the area under the Breit-Wigner function.

Figure 3.7 shows the K^{*0} invariant mass signal in the $1.2 < p_T < 1.6$ GeV/c range for two beam energies, $\sqrt{s_{NN}} = 14.5$ and 39 GeV, and two centralities, 0-10% and 60-80%. The K^{*0} invariant mass distribution is obtained across different transverse momentum bins and collision centrality intervals for six different beam energies.

Equation 3.4.2 is commonly referred to as the non-relativistic Breit-Wigner function. For a comprehensive analysis, the results are also compared by fitting the signal peak using the relativistic Breit-Wigner function [25]. The comparison of p_T -spectra obtained from the yields extracted using both functions is presented in Appendix 3.63. It is observed that the yields obtained from both fitting approaches are consistent within the statistical uncertainties.

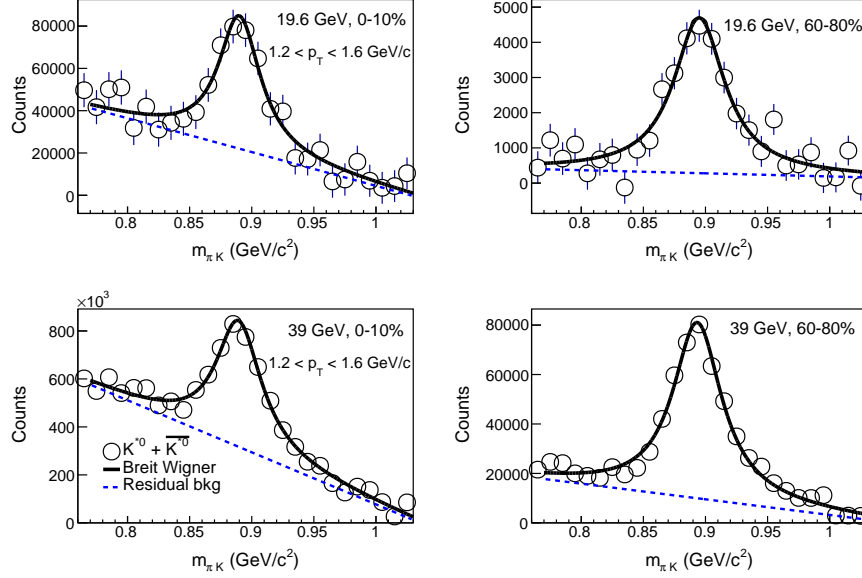


Figure 3.7: The track-rotation combinatorial background-subtracted $K\pi$ invariant mass distribution for $1.2 < p_T < 1.6$ GeV/c (at 14.5 and 39 GeV) is shown for central (0-10%) and peripheral (60-80%) centralities. The data are fitted with a Breit-Wigner function combined with a first-order polynomial (as described in equation 3.4.2), represented by the solid line and the dashed line represents the residual background. The uncertainties on the data points are statistical and are indicated by error bars.

3.4.3 Raw Yield extraction

The yield is estimated by integrating the signal histogram bins within the range of 0.77 to 1.04 GeV/c². Additionally, we account for the yields of K^{*0} outside this range, which correspond to the tails of the Breit-Wigner function. Yields are obtained from the left tail of the Breit-Wigner function (0.6 – 0.77 GeV/c²) and the right tail (0.77 – 1.5 GeV/c²). Hence to obtain the final particle yield We add yields from left and right part of BW to the yield from measured histogram integration.

3.5 Correction factors

3.5.1 Detector tracking efficiency and acceptance

Particle detectors have their own limitations while reconstructing the tracks, in the high multiplicity environment of heavy-ion collisions. Not all particles produced in a collision are detected, as some may hit the detector's dead regions, while others may have poorly reconstructed tracks due to missing hits or detector geometry. Therefore, the raw spectra obtained through the methods described in the previous section must be corrected for detector efficiency and acceptance.

The tracking and strange hadron reconstruction efficiency depends on the final state particle multiplicity in an event. This can be around thousands of tracks in a typical central collision to about a few tracks in a peripheral collision. As a result, the efficiency slightly increases in peripheral collisions compared to central collisions due to the lower track multiplicities.

In this analysis the detector acceptance and reconstruction efficiency is estimated by using STAR embedding method [15, 39, 40]. In this process, simulated Monte Carlo (MC) K^{*0} mesons, distributed uniformly in rapidity ($|y| < 1.0$), transverse momentum ($0 < p_T < 10$ GeV/c), and azimuthal angle ($0 < \phi < 2\pi$), were embedded into real events. The embedded K^{*0} mesons were about 5% of the measured charged particles in each event.

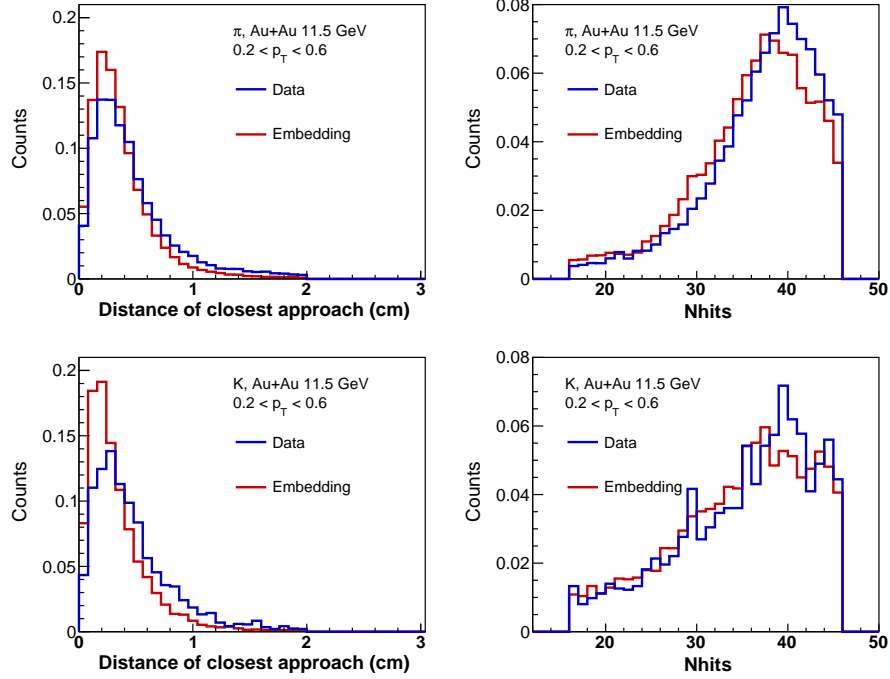


Figure 3.8: The Distribution of DCA and TPC hit points, of pions (top panel) and kaons (Bottom panel) from embedding (solid red line) and real data (solid blue line) for $0.2 < p_T < 0.6$ GeV/c in Au+Au collisions at $\sqrt{s_{NN}} = 11.5$ GeV. The distributions have been normalized to unit area.

These embedded particles were all assumed to originate from the true primary vertex in an event and successive propagation of strange hadrons through STAR, their decay, and the propagation of daughter particles were simulated using the GEANT3 package [158]. The TPC detector response was simulated with TPC response simulator (TpcRS). The STAR reconstruction algorithm processes data by combining simulated signals with those from real events. A quality assurance of the embedding sample is done to make sure that the MC simulation sample reproduces the characteristics of real data. For this, various track parameter distributions such as DCA, nFit points, nHits dEdx and ϕ are compared between real data and that obtained from embedding. Figure 3.8 shows the distribution of DCA and TPC hits of K^{*0} daughter tracks (π and K) from both real data and embedding simulations. The distributions are normalized to unit area to facilitate shape comparison. The shapes of the distributions in the embedding data are qualitatively consistent with those observed in the real data.

Finally the reconstruction efficiency \times acceptance is determined by dividing the number of reconstructed K^{*0} mesons after passing through the detector simulations with similar track/event selection criteria, used in real data analysis to that of simulated MC K^{*0} , within identical rapidity interval.

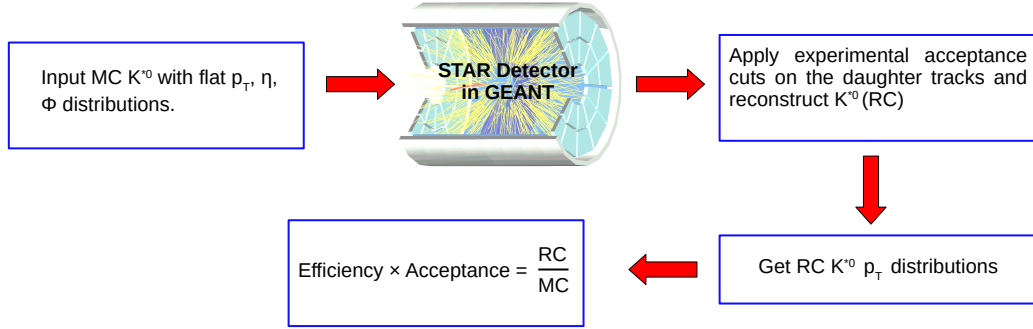


Figure 3.9: Flow chart of efficiency calculation for K^{*0} meson.

$$\epsilon_{acc \times reco} = \frac{N_{K^{*0}}^{RC}}{N_{K^{*0}}^{MC}} \quad (3.5.1)$$

The Fig. 3.9 presents the flow chart for the efficiency calculations. Figure 3.10 presents the detector acceptance and reconstruction efficiency as a function of p_T for different collision centrality intervals in $\sqrt{s_{NN}} = 7.7, 11.5, 14.5, 19.6, 27$ and 39 GeV collisions. The absence of clear centrality dependence in $\epsilon_{acc \times reco}$ could be due to the small variation in total multiplicity across the collision centrality and beam energy studied. Low momentum tracks, due to their high curvature under the influence of the solenoidal magnetic field, fail to traverse the entire TPC volume. In contrast, high momentum tracks, being more collimated, are less influenced by the external magnetic field. This results in a smooth increase in efficiency from low to intermediate p_T , which then saturates at higher p_T .

3.5.2 Efficiency re-weighting

The default analysis use efficiency from STAR embedding. Note that the input (generated) MC distribution in embedding is uniform in p_T . We have tested the impact if the input p_T spectra shape is taken from data. We call this efficiency re-weighting. So, We start with the corrected p_T spectra. Then we apply weight on both numerator and denominator of efficiency based on this spectra.

- We start with unweighted efficiency, which is used in the analysis for correcting the spectra.
- Fit the corrected spectra with Levy function and generate p_T dependent weight
- Apply p_T -dependent weight from the fit on generated and reconstructed K^{*0} p_T distribution from embedding
- Get efficiency from such p_T weighted generated and reconstructed distributions

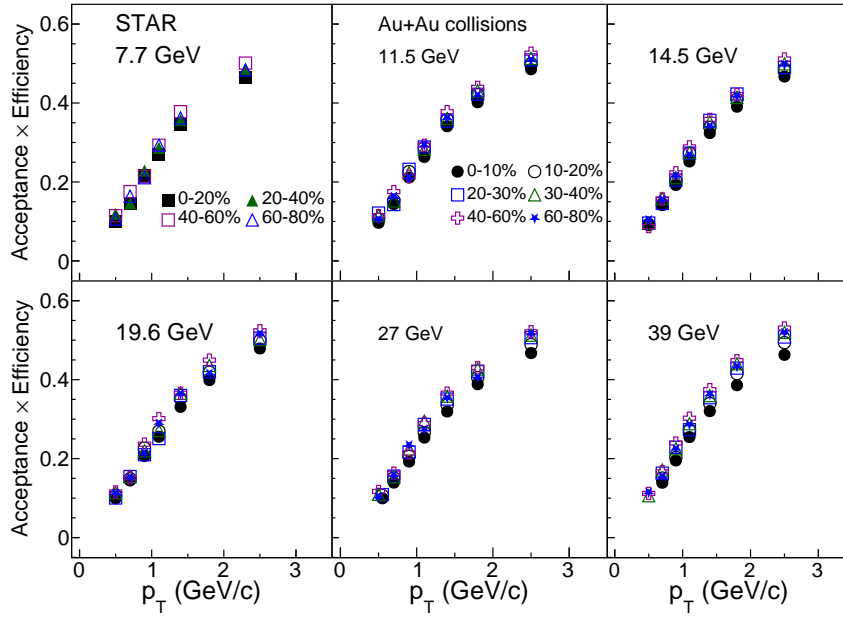


Figure 3.10: The detector tracking efficiency for K^{*0} meson as a function of p_T at various collision centralities in Au+Au collisions at $\sqrt{s_{NN}} = 7.7\text{--}39$ GeV. The statistical uncertainties are within the marker size.

- We repeat the p_T -weighting until the change in weighted efficiency is reached below a tolerance level (0.0001%)
- We observed 4-5 iterations are sufficient for convergence.

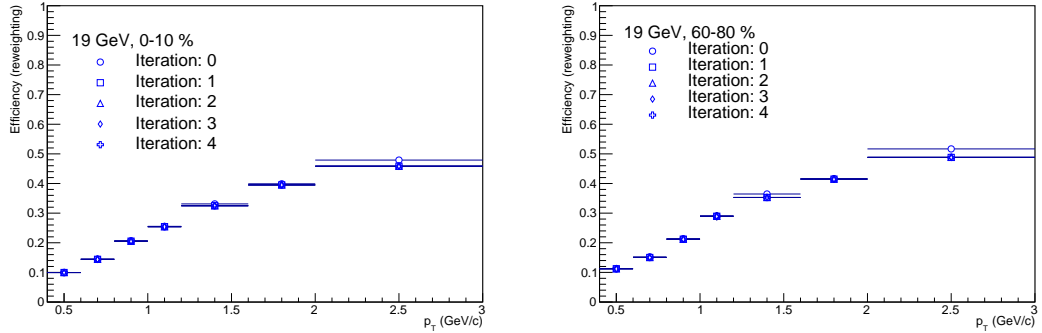


Figure 3.11: Test of re-weighting of efficiency using 19.6 GeV data and simulation.

The test of re-weighting is shown in Fig 3.11 using 19.6 GeV data and corresponding embedding. We found that the change in efficiency is about $\sim 1\%$.

3.5.3 PID efficiency calculation

Since both TPC and TOF detector has been used for daughter particle identification, the final PID efficiency is calculated using the following formula,

$$\text{Eff}_{\text{PID}} = \text{TOF match} \times \text{Eff}_{\text{TOF PID}} + (1 - \text{TOF match}) \times \text{Eff}_{\text{TPC PID}} \quad (3.5.2)$$

A. TPC PID efficiency

In order to calculate the TPC PID efficiency the TPC $N\sigma$ distributions are obtained in various p_T ranges and with stricter TOF cuts are applied on them.

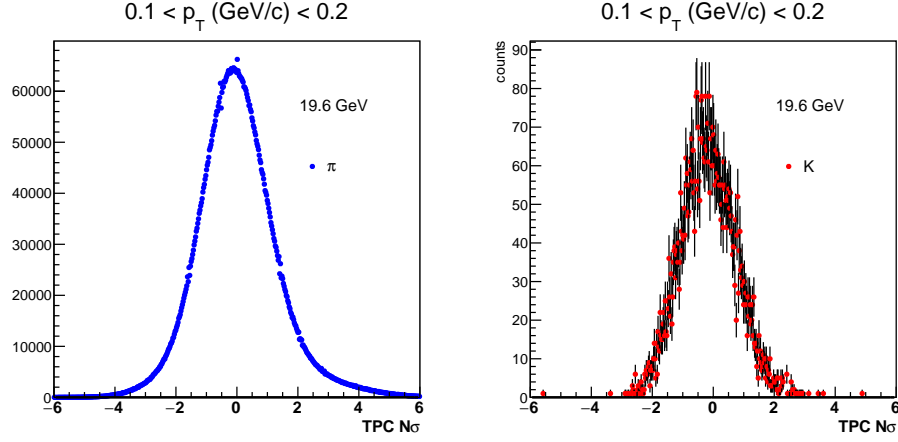


Figure 3.12: TPC $N\sigma$ distribution for pion and kaon in $0.1 < p_T(\text{GeV}/c) < 0.2$ for 19.6 GeV.

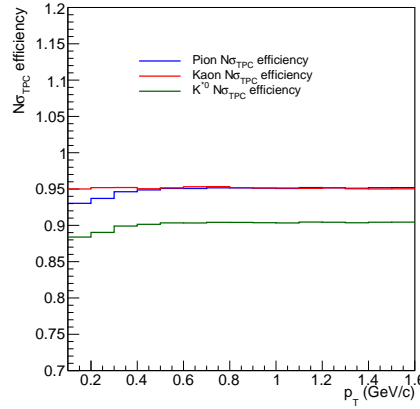


Figure 3.13: Variation of $N\sigma_{TPC}$ efficiency with p_T for 19.6 GeV.

Here ,

$$\text{TPC PID efficiency} = \frac{\text{No. of particles with TPC } |N\sigma| < 2}{\text{No. of particles with TPC } |N\sigma| < 5} \quad (3.5.3)$$

B. TOF PID efficiency

In order to calculate the TOF PID efficiency the $mass^2$ distributions are obtained in various p_T ranges and with stricter TPC cuts ($N\sigma < 0.1$) are applied on them. The student - t function is used to fit the pion and kaon $mass^2$ distribution.

Here ,

$$\text{TOF PID efficiency} = \frac{\text{Area under the fit function within default PID cuts}}{\text{Area under the fit function within } 5\sigma} \quad (3.5.4)$$

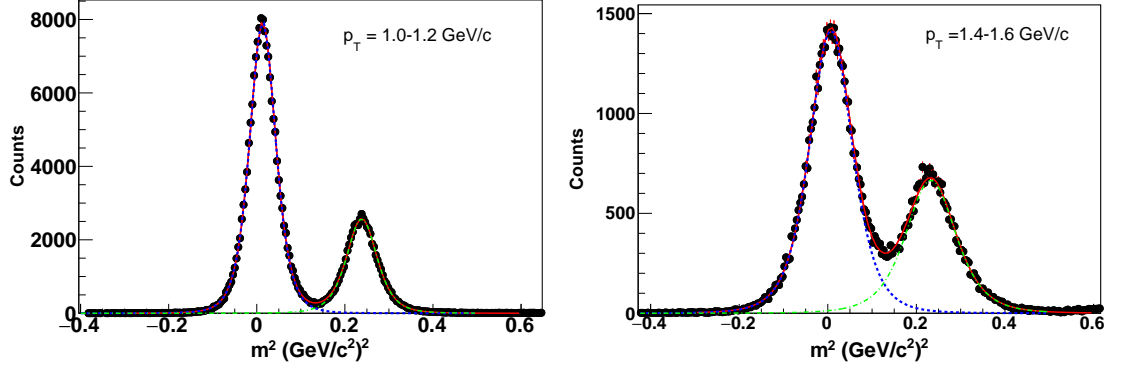


Figure 3.14: $mass^2$ distribution for pion and kaon in different p_T ranges for 19.6 GeV.

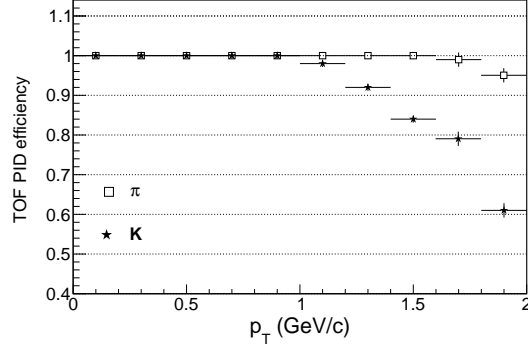


Figure 3.15: Variation of TOF PID efficiency with p_T for 19.6 GeV.

The ratio of the no. of particle reaching at the tof to the no. of particles reaching at TPC is called as the TOF matching efficiency.

So,

$$\text{TOF match efficiency} = \frac{\text{No. of particles with TPC}|N\sigma| < 2 \text{ with } \beta > 0}{\text{No. of particles with TPC}|N\sigma| < 2} \quad (3.5.5)$$

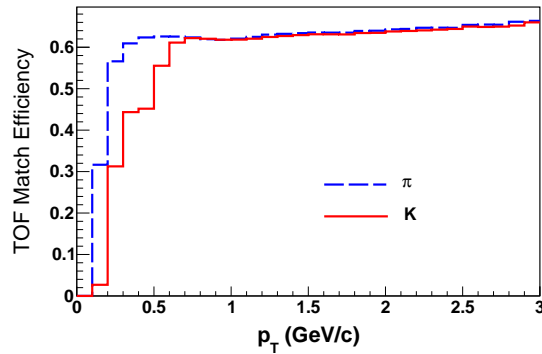


Figure 3.16: Variation of TOF match efficiency with p_T for 19.6 GeV.

C. PID efficiency for K^{*0}

After calculating all these we calculate the PID efficiency for K^{*0} in following steps:

- 1) Generate K^{*0} particle in a given p_T range (0.0 - 3.0 GeV/c).

- 2) Decay it into the daughter particles using **TGenPhaseSpace** decay function in ROOT.
- 3) Apply TPC and TOF PID efficiency on the daughter particles using equation 3.5.3.
- 4) Calculate PID efficiency for K^{*0} .

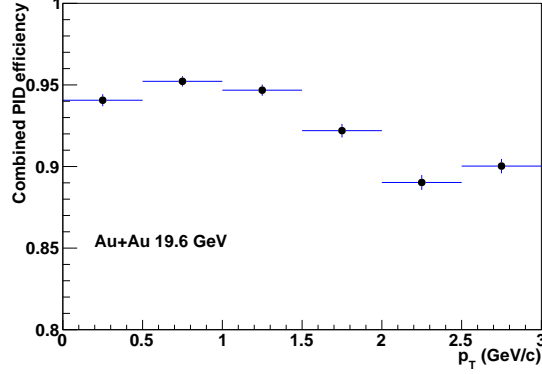


Figure 3.17: Variation of K^{*0} PID efficiency with p_T for 19.6 GeV.

Here we have used the same PID efficiency for the energy sets in which the data are taken in the same year due to similar detector conditions. The data for 7.7, 11.5, 14.6, 19.6, 27 and 39 GeV center of mass energy has been collected in the year 2010, 2010, 2014, 2011, 2011, 2010 respectively.

3.6 Systematic Uncertainties

Measured experimental results are always accompanied by uncertainties arising from various systematic sources. To assess these systematic effects, the measurements were repeated while varying different selection criteria, keeping all other conditions the same as the default criteria.

The sources of systematic uncertainties in the measurement are as follows:

3.6.1 Uncertainty from signal extraction method:

The shape of the residual background associated with the K^{*0} signal peak, after subtracting the combinatorial background, changes with varying p_T due to the misidentification of decay daughters. To account for the systematic uncertainty associated with the shape of the residual background, the following methods were applied in the analysis

1. variation in the fit-range (9 variations).
2. variation in residual background fitting function (first and second order polynomial)

3.6.2 Uncertainty from yield extraction method:

The following methods were employed to assess the systematic uncertainties associated with the K^{*0} meson yield extraction:

1. Yield calculated using the histogram bin counting method.

2. Yield obtained from the integration of the Breit-Wigner function.
3. Yield extracted by treating the width of the Breit-Wigner function as either a fixed or free parameter during fitting the signal peak.
4. Using different fitting functions, (relativistic and non-relativistic Breit Wigner function).

3.6.3 Uncertainty from PID, Event and Track selection cuts:

Kaons and pions were selected by applying a cut of less than 2 standard deviations (σ) from the expected energy loss in the TPC. Good events and quality tracks used in the analysis were chosen based on the criteria outlined in table 3.2 and table 3.4. To account for systematic uncertainties arising from PID selection cuts, the number of $|\sigma|$ was varied. Additionally, the z-vertex selection cut was varied to estimate systematic uncertainty due to event selection criteria. Similarly, the number of TPC hit points and DCA values associated with the tracks were varied to address the systematic uncertainty due to track selection cuts. The variations considered were:

1. TPC $|n\sigma| < 2.0$, $|n\sigma| < 1.8$, $|n\sigma| < 1.6$
2. $|V_z| < 40$ cm.
3. TPC Nhits > 15 , Nhits > 18 , Nhits > 20
4. $|dca| < 2.0$ cm, $|dca| < 1.8$ cm, $|dca| < 1.6$ cm

3.6.4 Uncertainty due to low p_T extrapolation:

The p_T -integrated particle yield (dN/dy) and the average transverse momentum ($\langle p_T \rangle$) are extracted from the p_T spectra using data within the measured p_T range, with extrapolation applied for the unmeasured regions based on certain functional forms. This extrapolation introduces an additional source of systematic uncertainty. To estimate this, different fit functions are compared to the p_T spectra. The variations considered are as follows:

1. Levy–Tsallis function
2. p_T –exponential function
3. m_T –exponential function
4. Maxwell–Boltzmann function

3.6.5 Uncertainty due to global tracking efficiency

A 5% uncertainty due to global tracking efficiency is considered for each charged particles, Since K^{*0} meson has two decay daughters, the combined uncertainty for a track pair results to be 7.1%.

3.6.6 Total systematic uncertainty:

The final systematic uncertainty is obtained using following steps:

1. First, values are obtained using the default analysis cuts outlined in Section 5.2, along with results from different systematic cut variations described in this section.
2. Then we obtain the minimum and maximum values, called minValue and max-Value, between the default and alternative cut variations.
3. Assuming a flat distribution of values derived from various cut parameters, for each systematic cut variation, the uncertainty due to that particular source is calculated as equation 3.

$$\sigma_{syst}^i = \frac{maxValue - minValue}{\sqrt{12}} \quad (3.6.1)$$

4. Finally, the systematic uncertainties from each variation source are combined in quadrature to obtain the total systematic uncertainty.

$$\sigma_{syst} = \sqrt{\sum_i (\sigma_{syst}^i)^2} \quad (3.6.2)$$

Table 3.5: Fractional systematic uncertainties (in %) for the p_T spectra, dN/dy and $\langle p_T \rangle$ of K^{*0} meson at $\sqrt{s_{NN}} = 7.7 - 39$ GeV.

Cut Variations	$d^2N/dydp_T$	dN/dy	$\langle p_T \rangle$
fitting region	1 – 3	1	1
residual background	2 – 4	1 – 2	1
fitting function	1	1	1
yield extraction	4	4	1
particle identification	2 – 5	1 – 2	1 – 2
track selection	1 – 3	1 – 2	1 – 2
tracking efficiency	7.1	7.1	7.1
low p_T extrapolation	—	5 – 6	3
width fix/free	2 – 3	2 – 3	1
Total	9 – 12	10 – 11	8 – 8.5

3.7 Results

3.7.1 Mass and Width of K^{*0} meson:

The mass and width of the K^{*0} meson are determined from a Breit-Wigner fit to the signal peak as a function of p_T . Panels (a) and (b) of Fig. 3.18 display the mass and width of the K^{*0} meson for 0-10% centrality in Au+Au collisions at 11.5 GeV. These results are compared with previous measurements from pp and Au+Au collisions at 200 GeV [25].

The width is consistent with the PDG value of $0.048 \text{ GeV}/c^2$ [155], while the measured mass is within 2σ of the PDG value of $0.896 \text{ GeV}/c^2$ [155]. In the higher p_T range (above $1 \text{ GeV}/c$), both the mass and width remain consistent with PDG values, similar to observations in pp and Au+Au collisions at 200 GeV . No significant dependence of the K^{*0} mass and width on beam energy is observed. Panels (c) and (d) show the K^{*0} mass and width for different centralities in Au+Au collisions at 11.5 GeV . The results are consistent across centrality classes within the uncertainties.

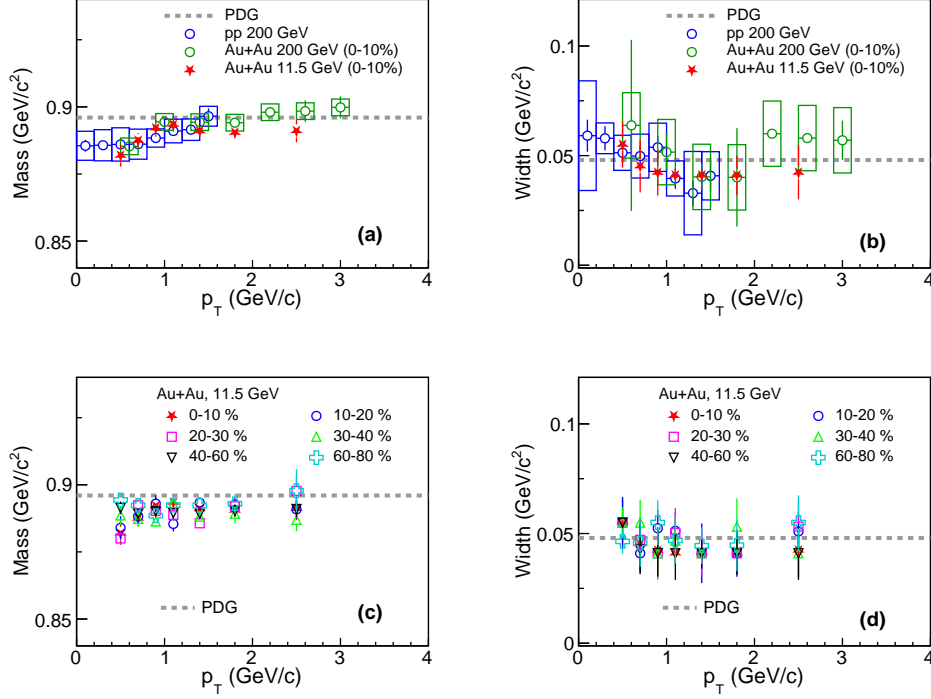


Figure 3.18: Upper Panel: K^{*0} mass and width as a function of p_T for Au+Au collisions at 11.5 GeV compared with the results for $p + p$ and Au+Au at 200 GeV [25]. Lower Panel: K^{*0} mass and width as a function of p_T for Au+Au collisions at 11.5 GeV for different centralities.

3.7.2 Transverse momentum (p_T) spectra:

The particle production mechanism and the system dynamics experienced by the particles can be inferred from their p_T distribution. Therefore, as an initial step, it is necessary to determine the particle yield as a function of transverse momentum.

Following the methods outlined in section 3.4, the raw yield is obtained in various p_T bins and centrality intervals for different collision energies to obtain the raw p_T spectra. These spectra are then corrected for the number of events (N_{events}), detector acceptance \times reconstruction efficiency ($\epsilon_{acc \times rec}$), particle identification efficiency (ϵ_{PID}), and branching ratio (BR), resulting in the final corrected p_T spectra. The Correction factors are already described in section 3.5. Hence the expression of the final corrected spectra is as follows.

$$\frac{d^2 N}{dp_T dy} = \frac{1}{N_{evt}} \times \frac{N^{raw}}{dy dp_T} \times \frac{1}{\epsilon_{acc \times rec} \times \epsilon_{PID} \times BR}, \quad (3.7.1)$$

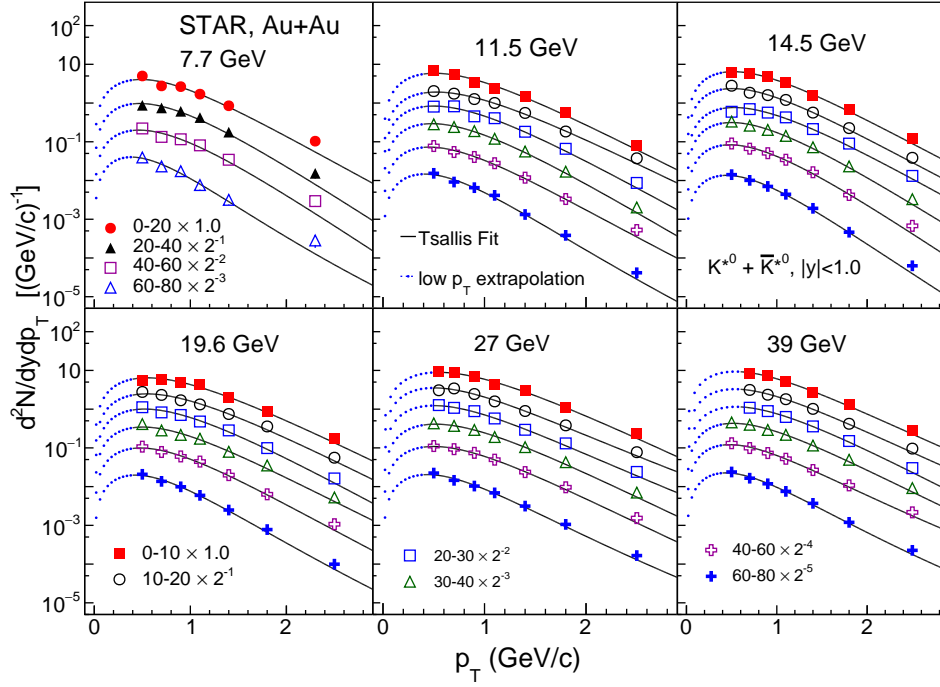


Figure 3.19: The K^{*0} meson transverse momentum (p_T) spectra at mid-rapidity ($|y| < 1$) are shown for various collision centrality intervals in Au+Au collisions at $\sqrt{s_{NN}} = 7.7, 11.5, 14.5, 19.6, 27$, and 39 GeV. The solid lines depict the Levy-Tsallis fit to the measured data, while the dashed lines represent the extrapolation to the unmeasured low p_T region. Both statistical and systematic uncertainties are smaller than the marker size.

The particle production at low p_T is largely driven by non-perturbative soft processes, leading to an expected exponential shape in the p_T distribution. In contrast, at higher p_T , particle production is dominated by hard processes described by perturbative QCD, which results in a power-law behavior. This dual nature makes the Levy-Tsallis function an ideal fit for the data, as it captures both the exponential trend at low p_T and the power-law behavior at higher p_T .

The data are fitted using the Levy-Tsallis function [159], which is defined as follows:

$$\frac{d^2N}{dp_T dy} = p_T \frac{(n-1)(n-2)}{nT + (nT + m(n-2))} \frac{dN}{dy} \left(1 + \frac{m_T - m}{nT}\right)^n, \quad (3.7.2)$$

where $m_T = \sqrt{m^2 + p_T^2}$ represents the transverse mass, T denotes the inverse slope parameter, and n is the exponent. The Levy-Tsallis function provides a reasonable fit to the spectra across all collision centrality intervals and beam energies, with $\chi^2/\text{NDF} < 2$. This fit is utilized to extrapolate the yield in the unmeasured p_T regions. The typical ranges of the fit parameters are n between 12–100, and T between 150–285 MeV.

Figure 3.19 displays the K^{*0} p_T spectra at mid-rapidity ($|y| < 1.0$) for various collision centrality intervals in Au+Au collisions at $\sqrt{s_{NN}} = 7.7\text{--}39$ GeV. Some of the p_T spectra have been scaled for clarity. The solid and dashed lines represent the fit to the data points, while the dotted lines indicate the low p_T extrapolation.

3.7.3 K^{*0} meson yield per unit rapidity:

Figure 3.20 illustrates the centrality dependence of the K^{*0} yield in Au+Au collisions at $\sqrt{s_{NN}} = 7.7, 11.5, 14.5, 19.6, 27$, and 39 GeV. The final yield per unit rapidity (dN/dy) of the K^{*0} meson is determined by integrating the spectra within the measured p_T range and extrapolating the fit function in the unmeasured regions of the p_T spectra. The low p_T extrapolation (0.0 – 0.4 GeV/ c) accounts for approximately 20–40% of the total particle yield, while the high p_T extrapolation (3.0 – 10.0 GeV/ c) contributes less than 1% to the yield.

$$(dN/dy)_{K^{*0}} = I_{low\ p_T} + I_{measured} + I_{high\ p_T} \quad (3.7.3)$$

where $I_{low\ p_T} = \int_{0.0}^{0.4} f(p_T) dp_T$, $I_{high\ p_T} = \int_{3.0}^{10.0} f(p_T) dp_T$ and $f(p_T) = \frac{d^2N}{dydp_T}$

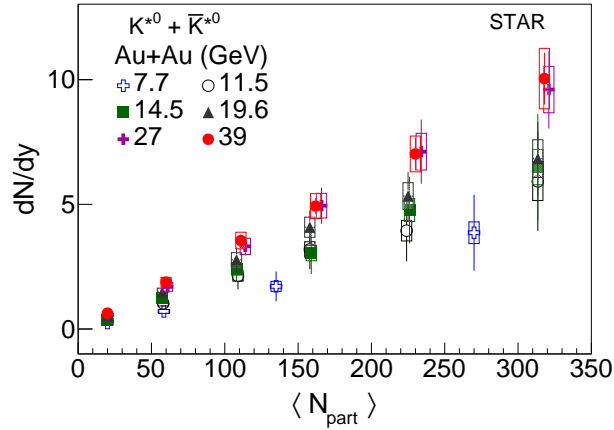


Figure 3.20: The mid-rapidity yield of K^{*0} meson as a function of the average number of participating nucleons ($\langle N_{part} \rangle$) in Au+Au collisions at $\sqrt{s_{NN}} = 7.7, 11.5, 14.5, 19.6, 27$, and 39 GeV is shown. The vertical bars represent the statistical uncertainties, while the open boxes indicate the systematic uncertainties.

The K^{*0} is observed to increase with both collision centrality and energy. shows the centrality dependence of dN/dy per average number of participant nucleons for K^{*0} , compared with BES-I measurements for K^\pm , p , and \bar{p} . Unlike K^\pm and p [15,26], where the yield exhibits a slight increase from peripheral to central collisions, the normalized K^{*0} yield demonstrates weak centrality dependence, similar to \bar{p} . For \bar{p} , this trend is often attributed to enhanced baryon-antibaryon annihilation with increasing centrality. Similarly, the centrality-dependent trend observed for K^{*0} may be attributed to increased signal loss due to hadronic rescattering as centrality increases. However, the large uncertainties prevent drawing any firm conclusion.

3.7.4 Mean transverse momentum ($\langle p_T \rangle$) of K^{*0} meson:

Figure 3.22 shows the centrality dependence of the K^{*0} yield in Au+Au collisions at $\sqrt{s_{NN}} = 7.7, 11.5, 14.5, 19.6, 27$, and 39 GeV. The $\langle p_T \rangle$ is measured by using the following expression 3.7.4.

$$\langle p_T \rangle = \frac{\int p_T f(p_T) dp_T}{\int f(p_T) dp_T} \quad (3.7.4)$$

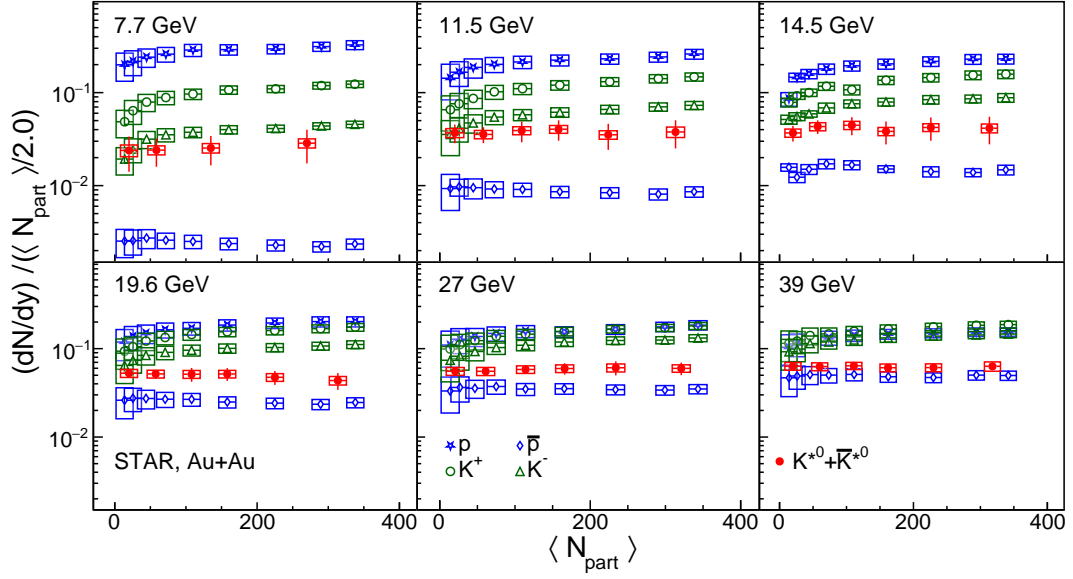


Figure 3.21: The mid-rapidity yield per average number of participating nucleons for K^{*0} , K^\pm , p , and \bar{p} as a function of $\langle N_{\text{part}} \rangle$ in Au+Au collisions at $\sqrt{s_{\text{NN}}} = 7.7, 11.5, 14.5, 19.6, 27$, and 39 GeV is presented. The K^\pm , p , and \bar{p} yield has been taken from ref [15, 26]. The vertical bars indicate statistical uncertainties, while the open boxes represent systematic uncertainties.

Similar to dN/dy , the $\langle p_T \rangle$ is calculated from both measured p_T spectra plus low and high p_T extrapolation and follows.

$$\langle p_T \rangle_{K^{*0}} = \frac{\langle p_T \rangle_{\text{low } p_T} I_{\text{low } p_T} + \sum_j p_T^j dp_T^j I^j + \langle p_T \rangle_{\text{high } p_T} I_{\text{high } p_T}}{I_{\text{low } p_T} + I_{\text{measured}} + I_{\text{high } p_T}} \quad (3.7.5)$$

where,

$p_T^j = j^{\text{th}}$ bin centre

$dp_T^j = j^{\text{th}}$ bin width

$I^j = \text{yield in the } j^{\text{th}} p_T \text{ bin.}$

From fig 3.22 one can see the results are mostly associated with the large systematic uncertainties. When taking into account the systematic uncertainty that is uncorrelated across centrality bins (excluding the tracking efficiency uncertainty of approximately 7.1%, which is consistent across all centrality bins), an increasing trend in $\langle p_T \rangle$ is observed from peripheral to central collisions, as well as with rising collision energy. This trend is consistent with the expectation of enhanced radial flow in more central collisions, which also becomes stronger with higher collision energies [12, 39].

In Fig. 3.23, the $\langle p_T \rangle$ of the K^{*0} meson is compared with that of stable hadrons such as π^\pm , K^\pm , and p (\bar{p}) [15, 26]. The $\langle N_{\text{part}} \rangle$ for K^{*0} is greater than that for pions and kaons, aligning closely with the value for protons. This observation suggests that $\langle N_{\text{part}} \rangle$ increases with the mass of the hadron, indicating hydrodynamic-like behavior within the system; in a scenario with constant radial flow velocity, lighter particles tend to move faster than their heavier counterparts.

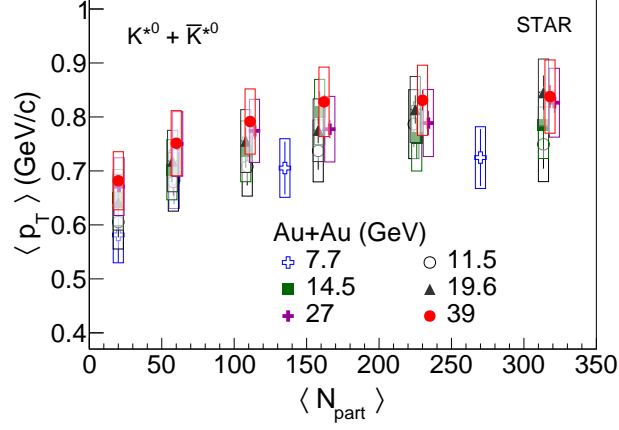


Figure 3.22: The mean transverse momentum of K^{*0} meson as a function of the average number of participating nucleons ($\langle N_{part} \rangle$) in Au+Au collisions at $\sqrt{s_{NN}} = 7.7, 11.5, 14.5, 19.6, 27$, and 39 GeV is shown. The vertical bars represent the statistical uncertainties, while the open boxes indicate the systematic uncertainties.

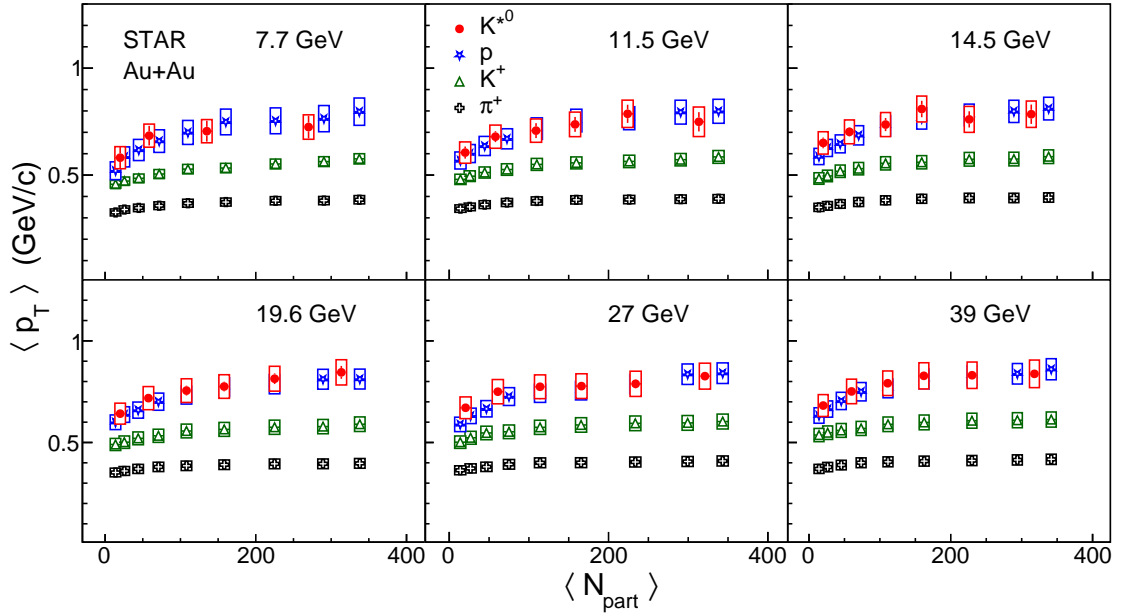


Figure 3.23: The mean transverse momentum for $K^{*0}, \pi^\pm, K^\pm, p(\bar{p})$ as a function of $\langle N_{part} \rangle$ in Au+Au collisions at $\sqrt{s_{NN}} = 7.7, 11.5, 14.5, 19.6, 27$, and 39 GeV is presented. The $\pi^\pm, K^\pm, p(\bar{p})$ results has been taken from ref. [15, 26] The vertical bars indicate statistical uncertainties, while the open boxes represent systematic uncertainties.

3.7.5 Particle ratios:

Due to their short lifetimes, the yield ratios of resonances to their corresponding stable hadrons, such as $\pi^\pm, K^\pm, p(\bar{p})$, can provide insights into the various in-medium dynamics occurring during the hadronic phase. A relevant example is the mesonic resonances like K^{*0} and ϕ , which have nearly the same mass and identical spin, but their lifetimes differ by an order of 10 in magnitude. Studying these particles offers a valuable opportunity to trace the temporal evolution of the hadron-resonance gas phase over a significant

timescale.

Figure 3.24 displays the p_T -integrated yield ratios, K^{*0}/K and ϕ/K , as a function of $\langle N_{part} \rangle$ in Au+Au collisions at $\sqrt{s_{NN}} = 7.7$ –39 GeV. In the current analysis at BES energies, K^{*0}/K corresponds to $(K^{*0} + \bar{K}^{*0})/(K^+ + K^-)$ and ϕ/K corresponds to $2\phi/(K^+ + K^-)$. A smooth evolution of these ratios is observed with increasing centrality, from peripheral to central collisions. The K^{*0}/K ratio decreases with increasing centrality, likely due to the rescattering of K^{*0} decay products in the hadronic phase, which becomes more prominent in central collisions and reduces the reconstruction of the K^{*0} signal. In contrast, the ϕ/K ratio remains independent of centrality, as the longer-lived ϕ meson's decay products are less affected by in-medium hadronic rescattering. The centrality dependence of the resonance-to-non-resonance ratios shows a similar trend across the BES energies.

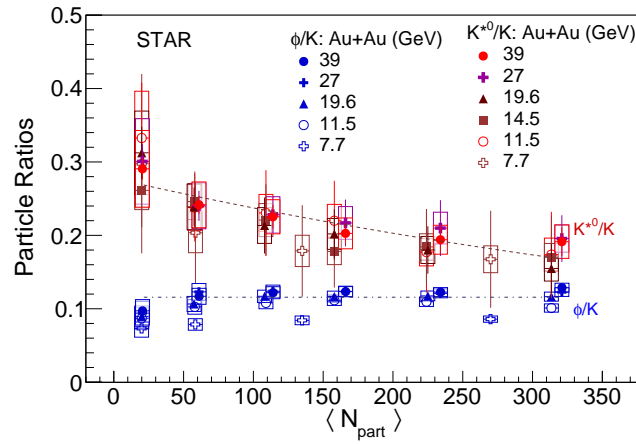


Figure 3.24: p_T -integrated yield ratios of resonances to their ground state particles (eg. K^{*0}/K and ϕ/K [27]) at midrapidity as a function of the average number of participating nucleons in Au+Au collisions at $\sqrt{s_{NN}} = 7.7, 11.5, 14.5, 19.6, 27$, and 39 GeV is shown. Vertical bars represent statistical uncertainties, while boxes indicate systematic uncertainties. Since error bars are large in the measurement, the dashed lines are included to guide the reader.

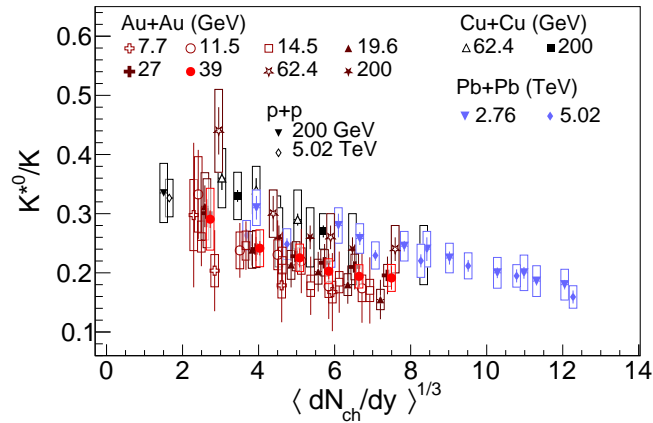


Figure 3.25: The K^{*0}/K ratio at mid-rapidity as a function of $(dN_{ch}/dy)^{1/3}$ in Au+Au collisions at $\sqrt{s_{NN}} = 7.7, 11.5, 14.5, 19.6, 27$, and 39 GeV is presented. Vertical bars denote statistical uncertainties, and boxes represent systematic uncertainties. The results are compared with previously published measurements from STAR [12, 25] and ALICE [14, 28].

In Hanbury Brown-Twiss (HBT) studies, the variable $(dN_{ch}/d\eta)^{1/3}$, measured at mid-rapidity, is used as a proxy for system size [160]. However, since published values of $(dN_{ch}/d\eta)^{1/3}$ for different centralities are not available at BES energies, $(dN_{ch}/dy)^{1/3}$ is used instead. This is calculated as the sum of the mid-rapidity yields of π^\pm , K^\pm , and $p(\bar{p})$ [15, 26].

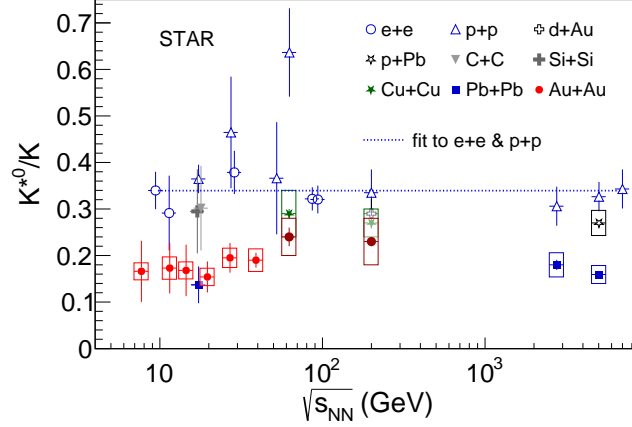


Figure 3.26: The beam energy dependence of K^{*0}/K ratio in e+e [29–32], p+p [25, 33–35], d+Au [13], p+Pb [36, 37] and most-central C+C [38], Si+Si [38], Au+Au [12], Cu+Cu [12] and Pb+Pb [14, 28] collisions. For e+e and p+p collisions, the bars denote the quadratic sum of statistical and systematic uncertainties. For p+A and A+A data, the bars denote the statistical uncertainties and the boxes denote the systematic uncertainties.

If it is assumed that the strength of rescattering is related to the distance traveled by the resonance decay products in the hadronic medium, the K^{*0}/K ratio would be expected to decrease exponentially with $(dN_{ch}/dy)^{1/3}$. Figure 3.25 shows the K^{*0}/K ratio as a function of $(dN_{ch}/dy)^{1/3}$ in Au+Au collisions at $\sqrt{s_{NN}} = 7.7\text{--}39$ GeV for BES energies. These results are compared with previous measurements from various collision systems and beam energies at RHIC [12, 25] and LHC [14, 28]. Although current data uncertainties limit strong conclusions, it is observed that the K^{*0}/K ratios across all BES energies exhibit a similar trend, while those from top RHIC and LHC energies appear slightly higher at comparable particle multiplicities.

The measurement of the K^{*0}/K ratio across a wide range of beam energies might offers valuable insights into the production mechanisms, particularly the energy dependence of the relative strength of rescattering and regeneration processes. Figure 3.26 shows the energy dependence of the K^{*0}/K ratio in small systems (e+e [29–32], p+p [25, 33–35], d+Au [13] and p+Pb [36, 37]) and central heavy-ion collisions (C+C [38], Si+Si [38], Au+Au [12], Cu+Cu [12] and Pb+Pb [14, 28]). In small systems, the ratio remains constant across all beam energies. A linear fit to the these data, including combined statistical and systematic uncertainties, gives a value of 0.34 ± 0.01 . The K^{*0}/K ratio from the STAR BES-I program is consistent with measurements from NA49 in Pb+Pb collisions at $\sqrt{s_{NN}} = 17.3$ GeV [38], though the latter was a 4π measurement. Overall, a significant suppression of the K^{*0}/K ratio is observed in central heavy-ion collisions compared to small systems, which supports the expectation that rescattering dominates over regeneration in the most central heavy-ion collisions.

As previously discussed in this section, both the K^{*0} and ϕ are vector mesons with nearly same masses, but the lifetime of the ϕ meson is approximately 46 fm/c, which

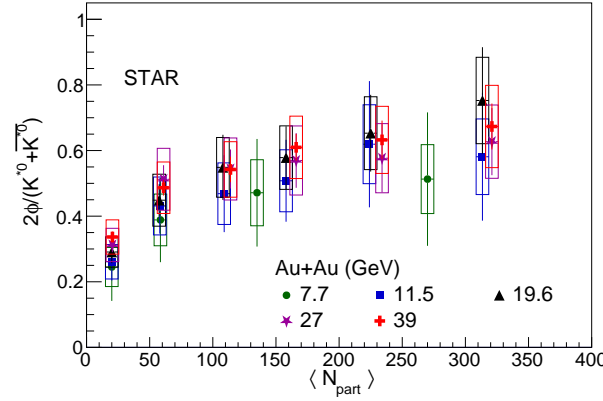


Figure 3.27: The ϕ/K^{*0} ratio at midrapidity as a function of the average number of participating nucleons in Au+Au collisions at $\sqrt{s_{NN}} = 7.7, 11.5, 14.5, 19.6, 27$, and 39 GeV is shown. Vertical bars represent statistical uncertainties, while boxes indicate systematic uncertainties.

is about ten times longer than that of the K^{*0} . This longer lifetime means that the decay products of the ϕ meson experience minimal re-scattering effects. Furthermore, the within a finite phase space, regeneration cross-section for the ϕ meson via pseudoelastic scattering of two kaons (σ_{KK}) is significantly smaller than that for $\sigma_{\pi K}$, which facilitates the regeneration of the K^{*0} . These factors render the ϕ meson negligibly affected by in-medium hadronic interactions within the hadronic phase, allowing the ϕ/K^{*0} ratio to serve as a useful probe for examining hadronic re-scattering effects. In addition, the ϕ meson, composed of $s\bar{s}$ quarks, contrasts with the K^{*0} meson, which consists of $d\bar{s}$. This distinction means that the ϕ/K^{*0} ratio may also provide insights into potential strangeness enhancement. Figure 3.27 presents the ϕ/K^{*0} ($2\phi/(K^{*0} + \bar{K}^{*0})$) ratio as a function of $\langle N_{part} \rangle$, in Au+Au collisions at $\sqrt{s_{NN}} = 7.7-39$ GeV. Although the uncertainties are substantial, preventing any definitive conclusions, the ratio appears to increase from peripheral to central collisions, supporting the scenario of re-scattering among the daughter particles of the K^{*0} . Additionally, this observed increase may also be influenced by strangeness enhancement in more central collisions [161].

3.7.6 Estimation of lower limit of hadronic phase lifetime:

Short-lived hadron resonances can also be helpful to investigate the duration of the hadronic phase. Although the precise definition may be open to interpretation, we are simplifying by considering the time difference between chemical and kinetic freeze-out as the hadronic phase. The discussion in the previous section indicates that the suppression of the K^{*0}/K ratio with increasing collision centrality reflects the predominance of hadronic rescattering of the decay daughters over the regeneration of the K^{*0} meson.

Therefore, the K^{*0}/K ratio can serve as a tool to estimate the lower bound of the hadronic phase using the following toy model, inspired by the nuclear decay law [28, 162].

$$\left(\frac{K^{*0}}{K} \right)_{\text{Kinetic}} = \left(\frac{K^{*0}}{K} \right)_{\text{Chemical}} \times e^{-\Delta t_{\text{hadronic}}/\tau_{K^{*0}}}, \quad (3.7.6)$$

where $\tau_{K^{*0}}$ is the lifetime of K^{*0} in vacuum (≈ 4.16 fm/c) and $\Delta t_{\text{hadronic}}$ is the lower

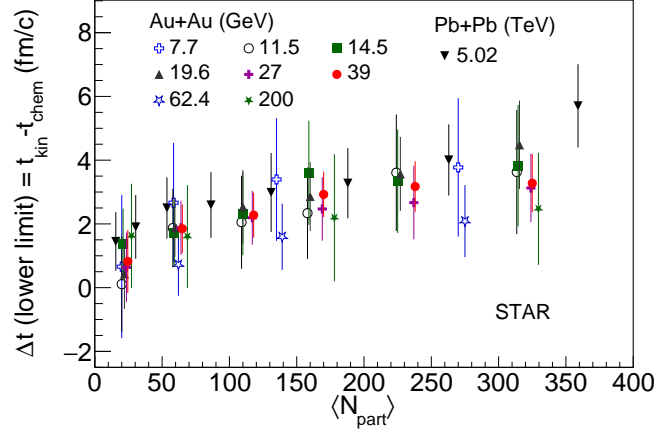


Figure 3.28: The lower bound on the time difference (Δt) between chemical and kinetic freeze-out is presented as a function of the average number of participating nucleons. These results are compared with prior measurements from STAR and ALICE. The error bars represent the combined statistical and systematic uncertainties, propagated from the uncertainties in the K^{*0}/K ratio.

bound of the time difference between Chemical and Kinetic freeze-out. The model, however, has certain caveats. Since only the final state particles can be measured experimentally, the yields of resonances at the chemical freeze-out surface cannot be directly observed. To address this, it is assumed that the resonance-to-stable particle ratio at chemical freeze-out in AA collisions is the same as the ratio measured in elementary (pp or e^+e^-) collisions. Due to unavailability small system collisions at BES-I energies, the K^{*0}/K ratio baseline at chemical freeze-out is taken from the energy-independent straight line fit (0.34 ± 0.01 , as shown in Fig. 3.26) based on global small system data, while the ratio at kinetic freeze-out is assumed to match that observed in heavy-ion collisions. The guiding assumptions are:

1. All K^{*0} mesons decayed before kinetic freeze-out are lost due to hadronic rescattering.
2. No regeneration of K^{*0} mesons occurs between chemical and kinetic freeze-out.

To account for the relative velocity of the K^{*0} meson with respect to the fireball center, which arises due to the fireball's expansion, the observed value of $\Delta t_{\text{hadronic}}$ is multiplied by a corresponding Lorentz factor, γ [28, 162]. Where, $\gamma = \sqrt{1 + (\langle p_T \rangle / mc)^2}$. The values of γ for different centrality in various collision energies are provided in appendix 3.9

Figure 3.28 shows the lower bound of the time difference between chemical and kinetic freeze-out as a function of $\langle N_{\text{part}} \rangle$. A smooth increase in the duration of the hadronic phase is observed in Au+Au collisions, which is consistent with the expectation of decrease in kinetic freeze-out temperature from peripheral to central collisions, provided a constant chemical freeze-out temperature is assumed. The $\Delta t_{\text{hadronic}}$ values from BES-I energies are compared with results from Au+Au collisions at 62.4 and 200 GeV [12, 25], as well as Pb+Pb collisions at 5.02 TeV [28]. The $\Delta t_{\text{hadronic}}$ from BES-I appears to follow the trend seen in previous RHIC and LHC data. However, the current uncertainties in BES-I data prevent a conclusive determination of the energy dependence of $\Delta t_{\text{hadronic}}$.

3.7.7 Summary:

In conclusion, the production of K^{*0} mesons at mid-rapidity ($|y| < 1.0$) in Au+Au collisions at $\sqrt{s_{NN}} = 7.7, 11.5, 19.6, 27,$ and 39 GeV is reported. In the higher p_T range (above 1 GeV/ c), both the mass and width remain consistent with the PDG values. The K^{*0} meson yield and $\langle p_T \rangle$ were measured across different centrality classes and collision energies. The $\langle p_T \rangle$ of K^{*0} was also compared with that of other identified hadrons measured by STAR. The observed increase in $\langle p_T \rangle$ of K^{*0} with increasing centrality in Au+Au collisions aligns with the expected increase in radial flow from peripheral to central collisions. The K^{*0}/K ratio in the most central Au+Au collisions is smaller than in small systems (such as e^+e^- or pp). Additionally, the K^{*0}/K ratio in central heavy-ion collisions appears lower than in peripheral collisions, while the ϕ/K ratio remains largely independent of centrality. These findings support a scenario where hadronic rescattering dominates over regeneration for K^{*0} at BES energies. Furthermore, the ϕ/K ratio seems to increase from peripheral to central collisions, possibly driven by both hadronic rescattering and strangeness enhancement in more central collisions. The observed increase in the lower limit of the time interval between chemical and kinetic freeze-out, estimated from the K^{*0}/K ratio, suggests a decrease in the kinetic freeze-out temperature from peripheral to central collisions. However, significant uncertainties in the measurements prevent drawing definitive conclusions.

3.8 Appendix

3.8.1 K^{*0} invariant mass distribution for 0-20% centrality in Au+Au collisions at $\sqrt{s_{NN}} = 7.7$ GeV

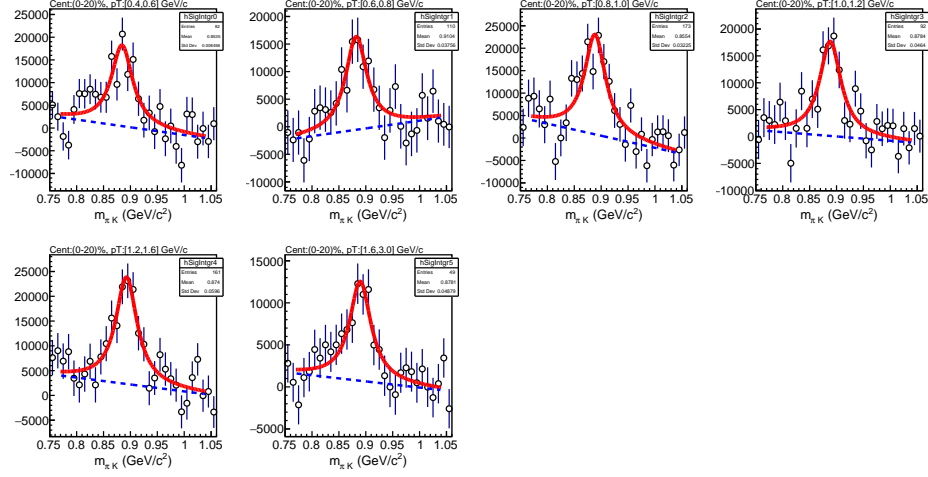


Figure 3.29: $K\pi$ invariant mass for 0-20 % centrality at $\sqrt{s_{NN}} = 7.7$ GeV.

3.8.2 K^{*0} invariant mass distribution for 20-40% centrality in Au+Au collisions at $\sqrt{s_{NN}} = 7.7$ GeV

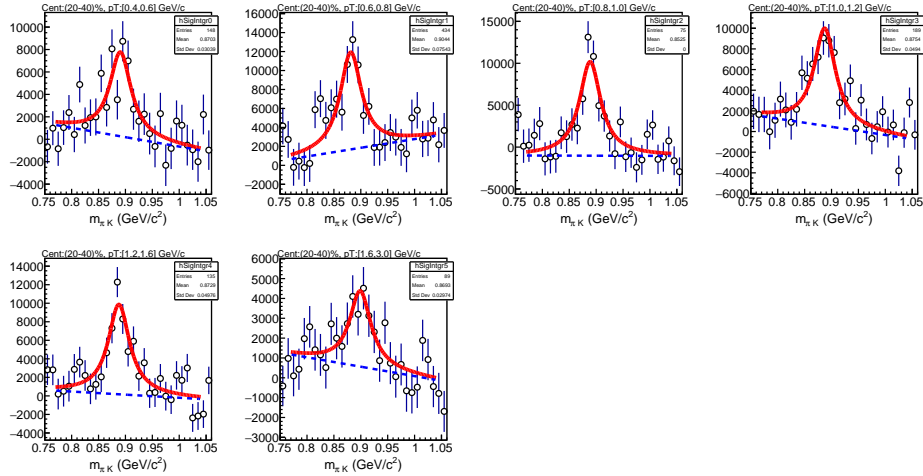


Figure 3.30: $K\pi$ invariant mass for 20-40 % centrality at $\sqrt{s_{NN}} = 7.7$ GeV.

3.8.3 K^{*0} invariant mass distribution for 40-60% centrality in Au+Au collisions at $\sqrt{s_{NN}} = 7.7$ GeV

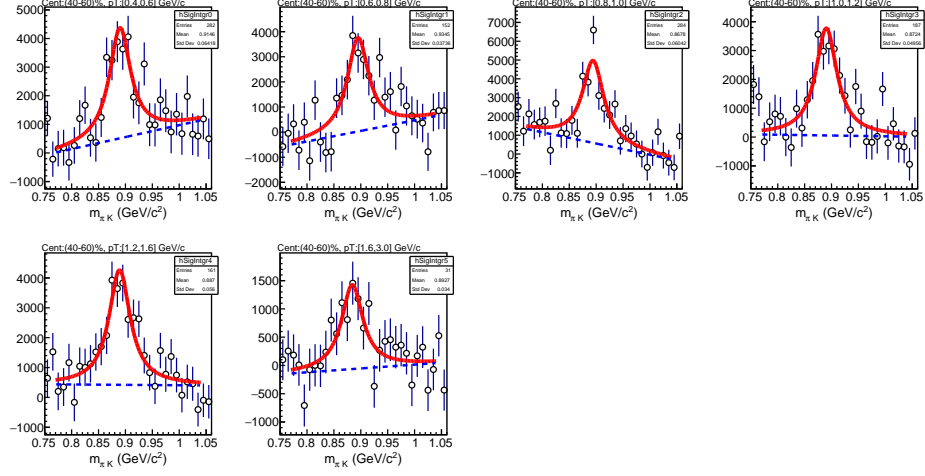


Figure 3.31: $K\pi$ invariant mass for 40-60 % centrality at $\sqrt{s_{NN}} = 7.7$ GeV.

3.8.4 K^{*0} invariant mass distribution for 60-80% centrality in Au+Au collisions at $\sqrt{s_{NN}} = 7.7$ GeV

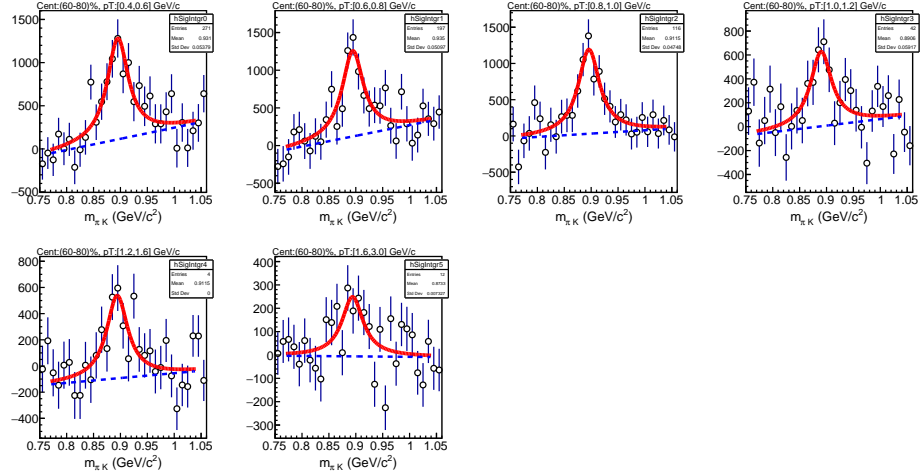


Figure 3.32: $K\pi$ invariant mass for 60-80 % centrality at $\sqrt{s_{NN}} = 7.7$ GeV.

3.8.5 K^{*0} invariant mass distribution for 0-10% centrality in Au+Au collisions at $\sqrt{s_{NN}} = 11.5$ GeV

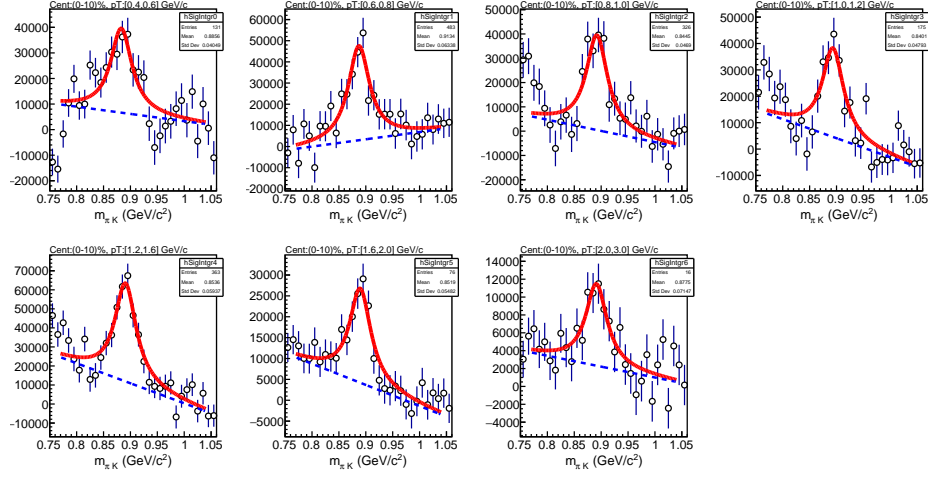


Figure 3.33: $K\pi$ invariant mass for 0-10 % centrality at $\sqrt{s_{NN}} = 11.5$ GeV.

3.8.6 K^{*0} invariant mass distribution for 10-20% centrality in Au+Au collisions at $\sqrt{s_{NN}} = 11.5$ GeV

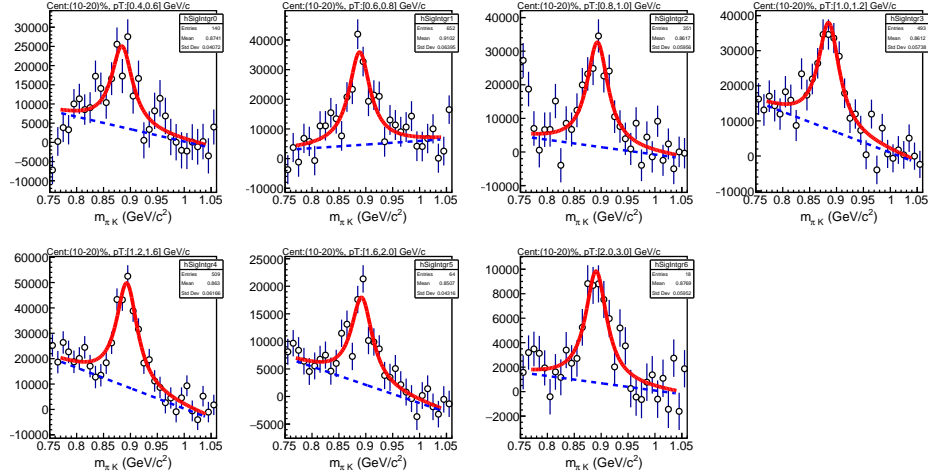


Figure 3.34: $K\pi$ invariant mass for 10-20 % centrality at $\sqrt{s_{NN}} = 11.5$ GeV.

3.8.7 K^{*0} invariant mass distribution for 20-30% centrality in Au+Au collisions at $\sqrt{s_{NN}} = 11.5$ GeV

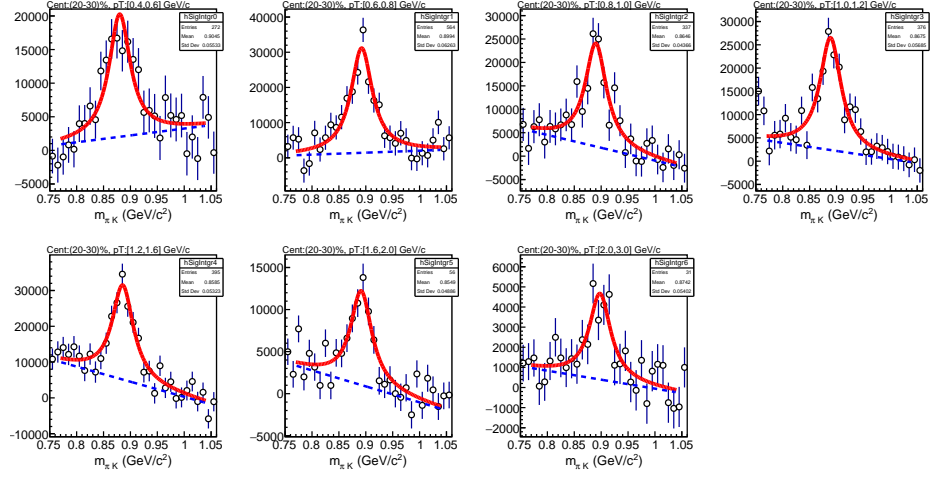


Figure 3.35: $K\pi$ invariant mass for 20-30 % centrality at $\sqrt{s_{NN}} = 11.5$ GeV.

3.8.8 K^{*0} invariant mass distribution for 30-40% centrality in Au+Au collisions at $\sqrt{s_{NN}} = 11.5$ GeV

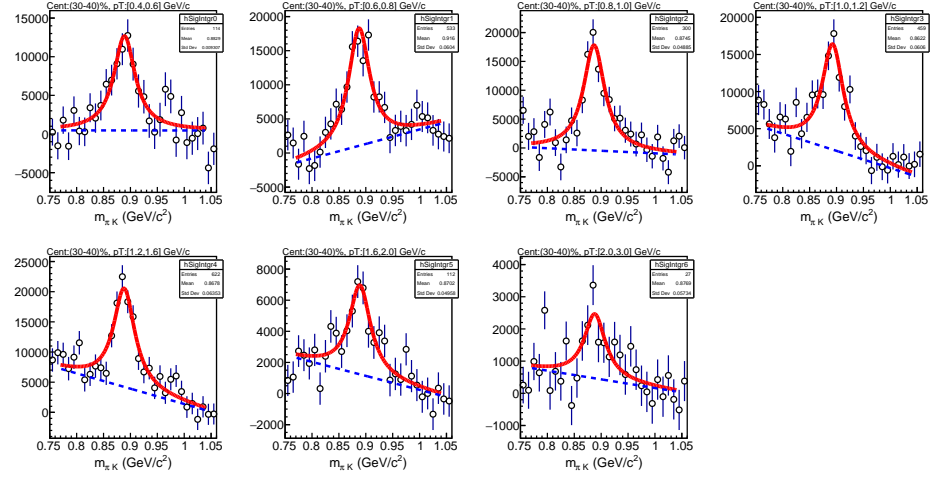


Figure 3.36: $K\pi$ invariant mass for 30-40 % centrality at $\sqrt{s_{NN}} = 11.5$ GeV.

3.8.9 K^{*0} invariant mass distribution for 40-60% centrality in Au+Au collisions at $\sqrt{s_{NN}} = 11.5$ GeV

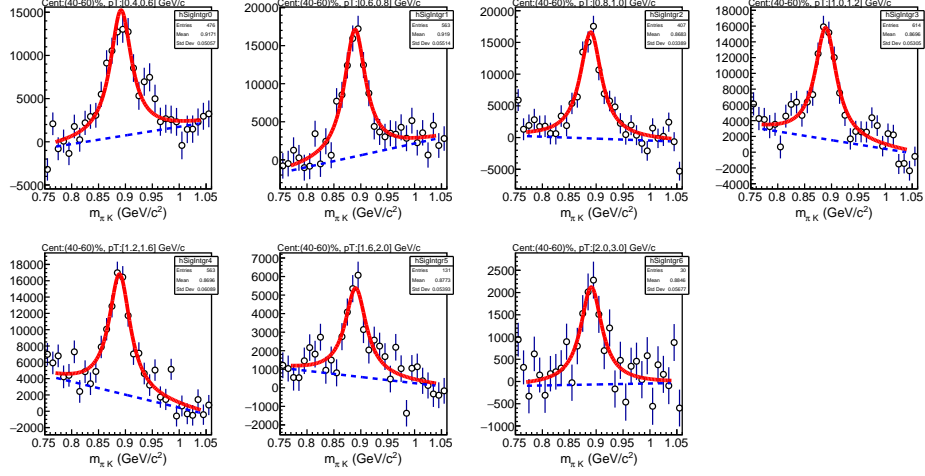


Figure 3.37: $K\pi$ invariant mass for 40-60 % centrality at $\sqrt{s_{NN}} = 11.5$ GeV.

3.8.10 K^{*0} invariant mass distribution for 60-80% centrality in Au+Au collisions at $\sqrt{s_{NN}} = 11.5$ GeV

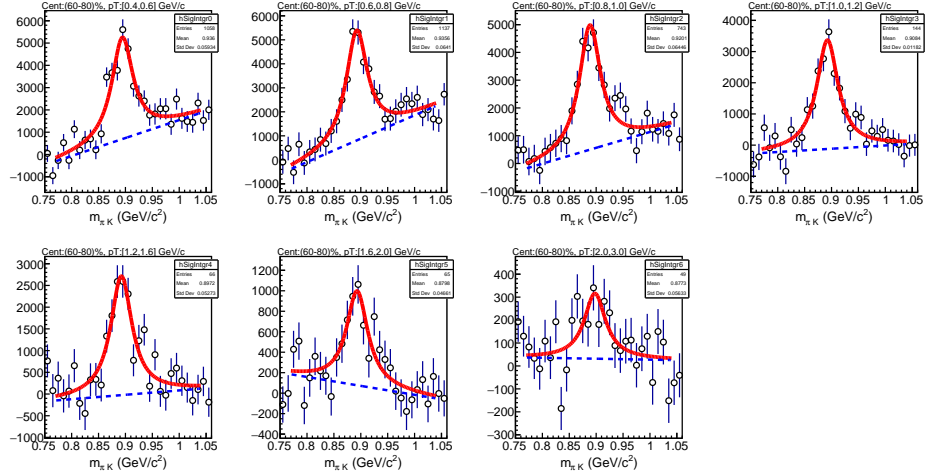


Figure 3.38: $K\pi$ invariant mass for 60-80 % centrality at $\sqrt{s_{NN}} = 11.5$ GeV.

3.8.11 K^{*0} invariant mass distribution for 0-10% centrality in Au+Au collisions at $\sqrt{s_{NN}} = 14.5$ GeV

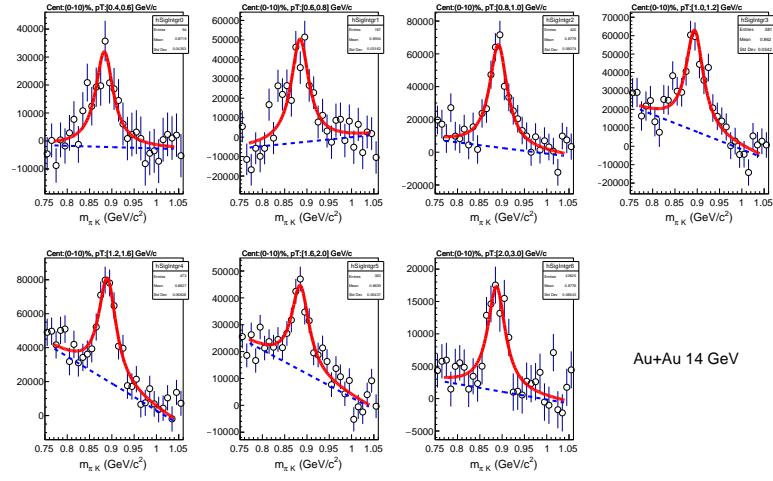


Figure 3.39: $K\pi$ invariant mass for 0-10 % centrality at $\sqrt{s_{NN}} = 14.5$ GeV.

3.8.12 K^{*0} invariant mass distribution for 10-20% centrality in Au+Au collisions at $\sqrt{s_{NN}} = 14.5$ GeV

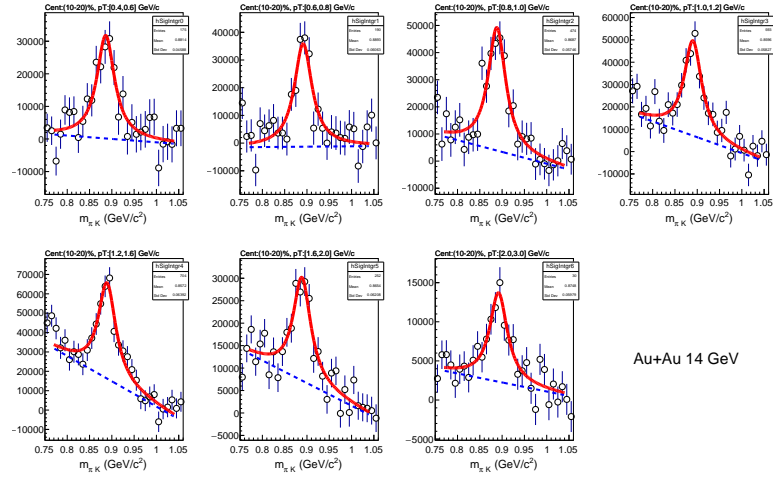


Figure 3.40: $K\pi$ invariant mass for 10-20 % centrality at $\sqrt{s_{NN}} = 14.5$ GeV.

3.8.13 K^{*0} invariant mass distribution for 20-30% centrality in Au+Au collisions at $\sqrt{s_{NN}} = 14.5$ GeV

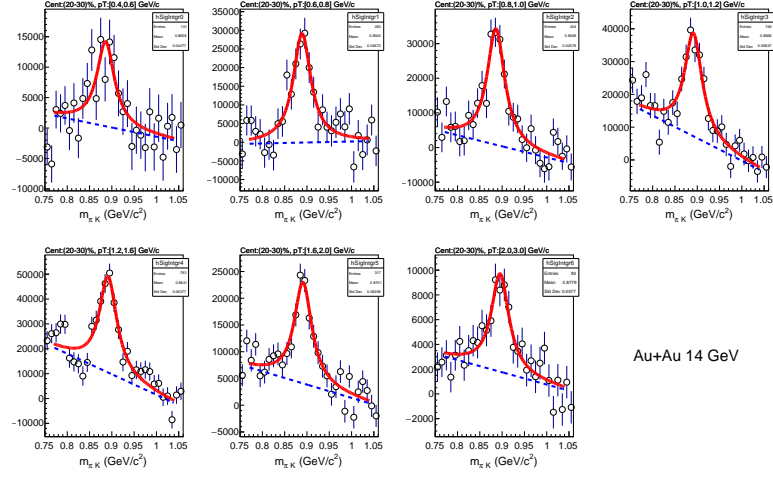


Figure 3.41: $K\pi$ invariant mass for 20-30 % centrality at $\sqrt{s_{NN}} = 14.5$ GeV.

3.8.14 K^{*0} invariant mass distribution for 30-40% centrality in Au+Au collisions at $\sqrt{s_{NN}} = 14.5$ GeV

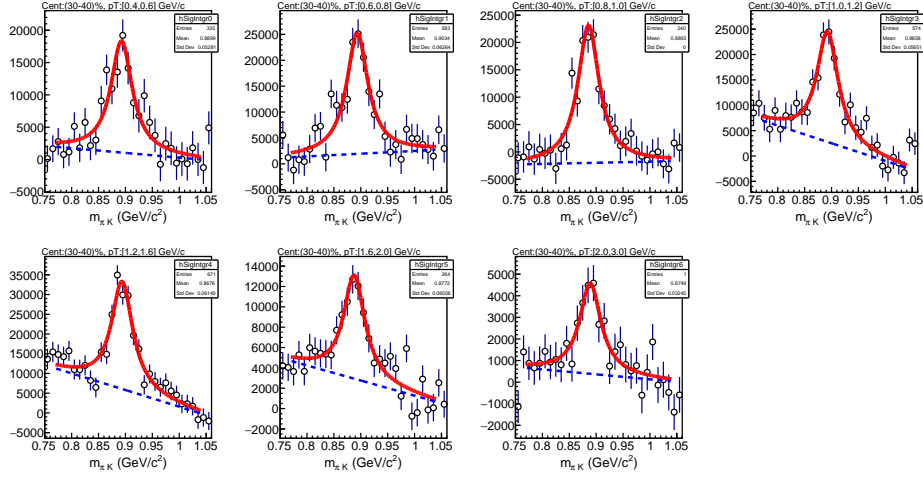


Figure 3.42: $K\pi$ invariant mass for 30-40 % centrality at $\sqrt{s_{NN}} = 14.5$ GeV.

3.8.15 K^{*0} invariant mass distribution for 40-60% centrality in Au+Au collisions at $\sqrt{s_{NN}} = 14.5$ GeV

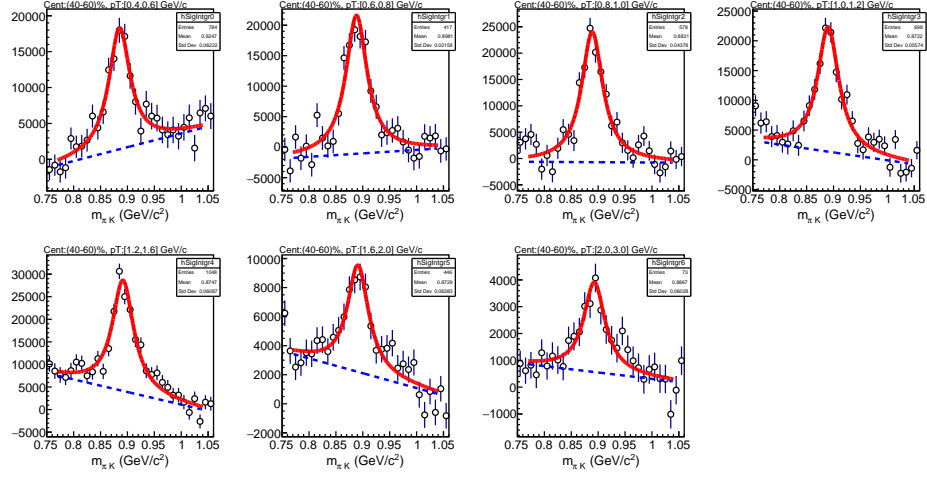


Figure 3.43: $K\pi$ invariant mass for 40-60 % centrality at $\sqrt{s_{NN}} = 14.5$ GeV.

3.8.16 K^{*0} invariant mass distribution for 60-80% centrality in Au+Au collisions at $\sqrt{s_{NN}} = 14.5$ GeV

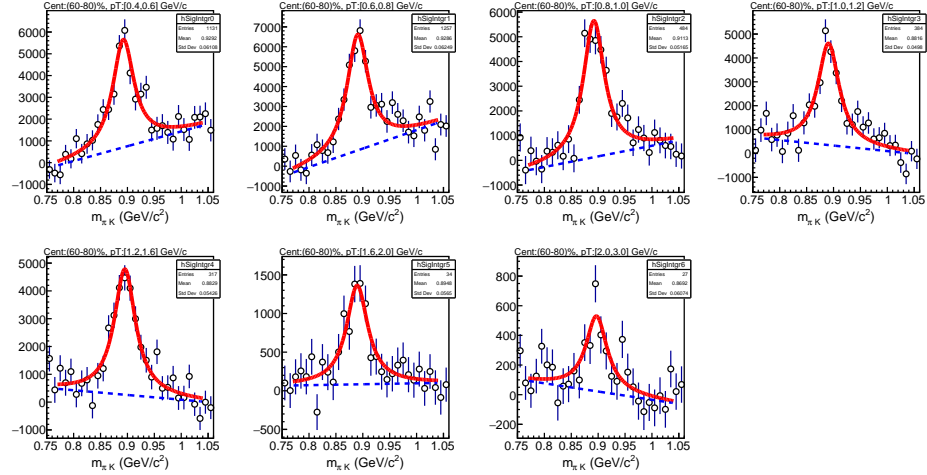


Figure 3.44: $K\pi$ invariant mass for 60-80 % centrality at $\sqrt{s_{NN}} = 14.5$ GeV.

3.8.17 K^{*0} invariant mass distribution for 0-10% centrality in Au+Au collisions at $\sqrt{s_{NN}} = 19.6$ GeV

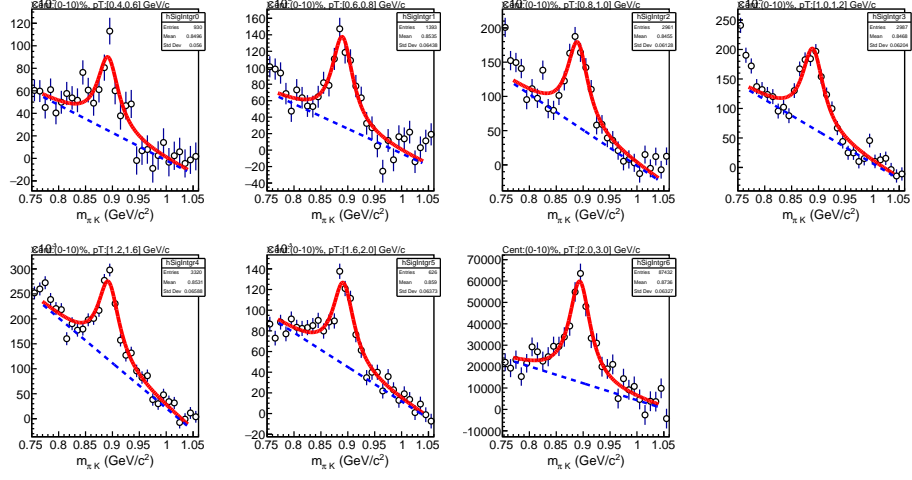


Figure 3.45: $K\pi$ invariant mass for 0-10 % centrality at $\sqrt{s_{NN}} = 19.6$ GeV.

3.8.18 K^{*0} invariant mass distribution for 10-20% centrality in Au+Au collisions at $\sqrt{s_{NN}} = 19.6$ GeV

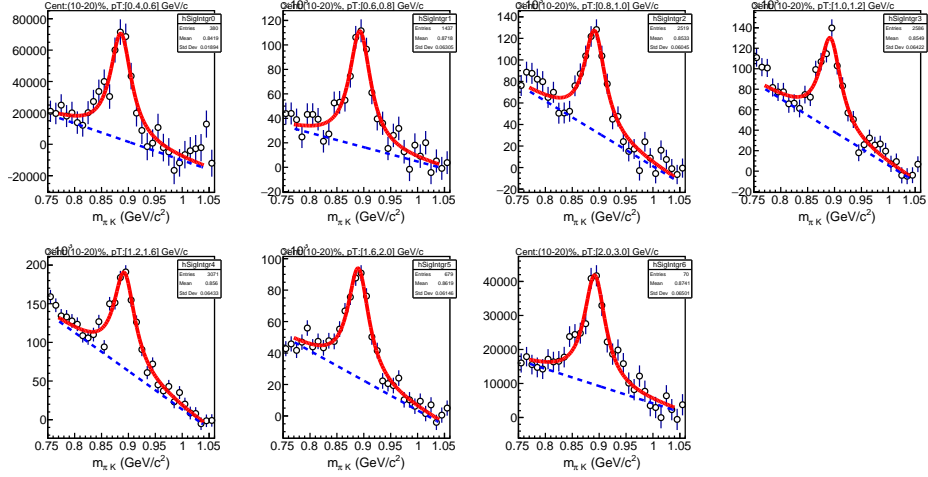


Figure 3.46: $K\pi$ invariant mass for 10-20 % centrality at $\sqrt{s_{NN}} = 19.6$ GeV.

3.8.19 K^{*0} invariant mass distribution for 20-30% centrality in Au+Au collisions at $\sqrt{s_{NN}} = 19.6$ GeV

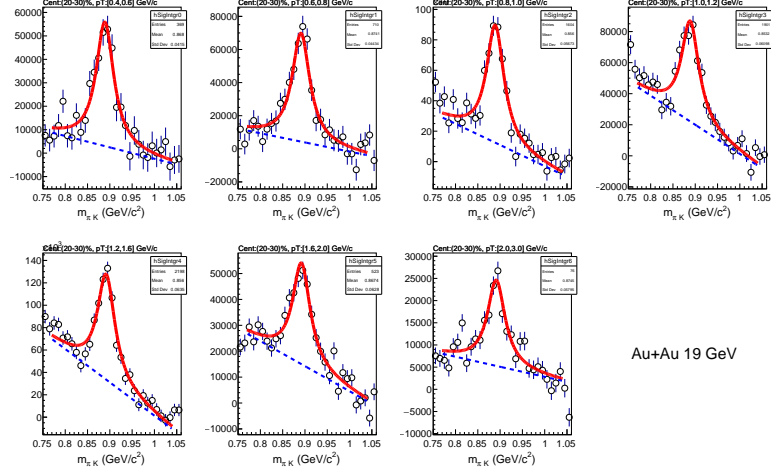


Figure 3.47: $K\pi$ invariant mass for 20-30 % centrality at $\sqrt{s_{NN}} = 19.6$ GeV.

3.8.20 K^{*0} invariant mass distribution for 30-40% centrality in Au+Au collisions at $\sqrt{s_{NN}} = 19.6$ GeV

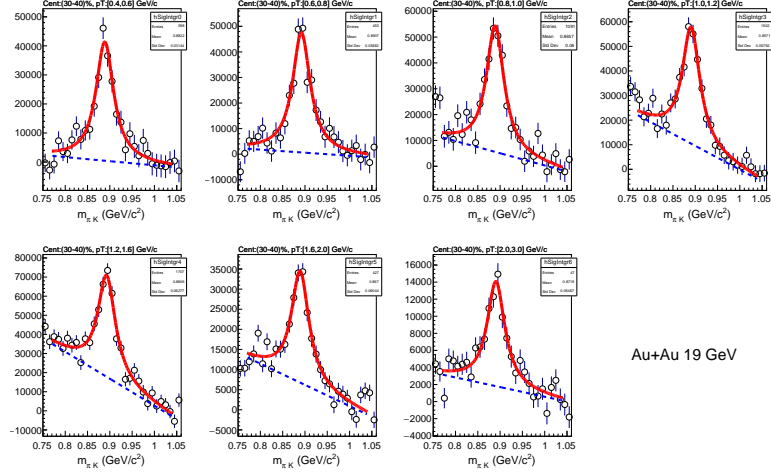
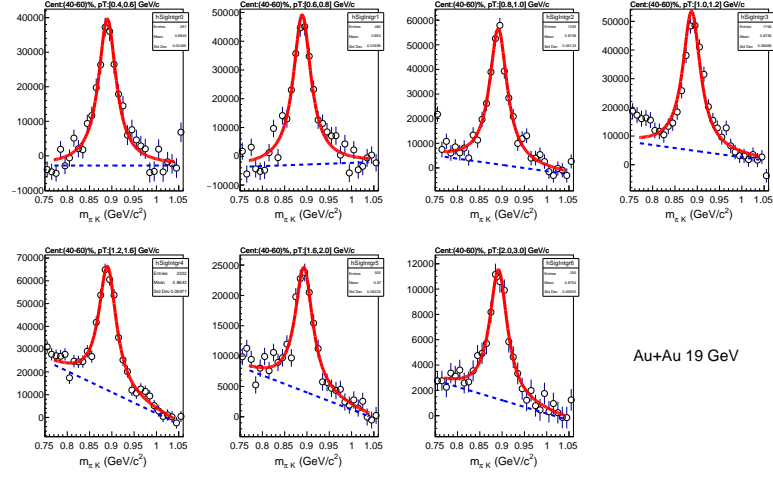


Figure 3.48: $K\pi$ invariant mass for 30-40 % centrality at $\sqrt{s_{NN}} = 19.6$ GeV.

3.8.21 K^{*0} invariant mass distribution for 40-60% centrality in Au+Au collisions at $\sqrt{s_{NN}} = 19.6$ GeV



Au+Au 19 GeV

Figure 3.49: $K\pi$ invariant mass for 40-60 % centrality at $\sqrt{s_{NN}} = 19.6$ GeV.

3.8.22 K^{*0} invariant mass distribution for 60-80% centrality in Au+Au collisions at $\sqrt{s_{NN}} = 19.6$ GeV

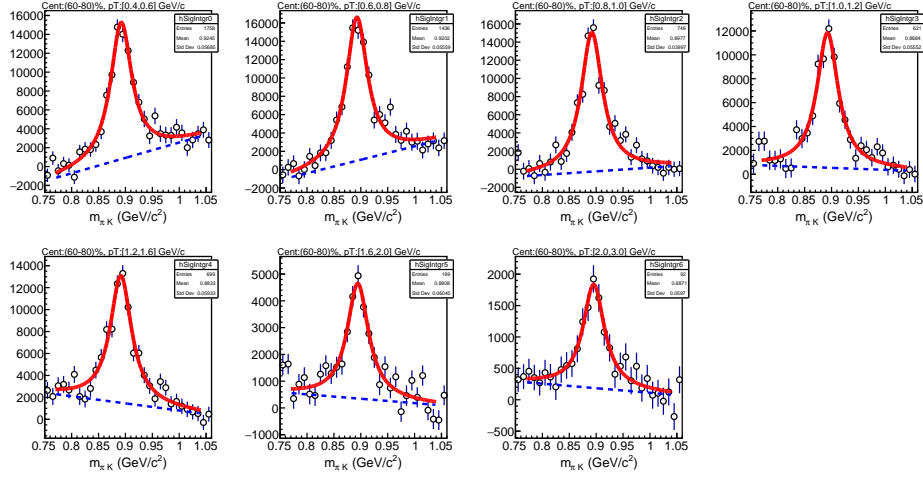


Figure 3.50: $K\pi$ invariant mass for 60-80 % centrality at $\sqrt{s_{NN}} = 19.6$ GeV.

3.8.23 K^{*0} invariant mass distribution for 0-10% centrality in Au+Au collisions at $\sqrt{s_{NN}} = 27$ GeV

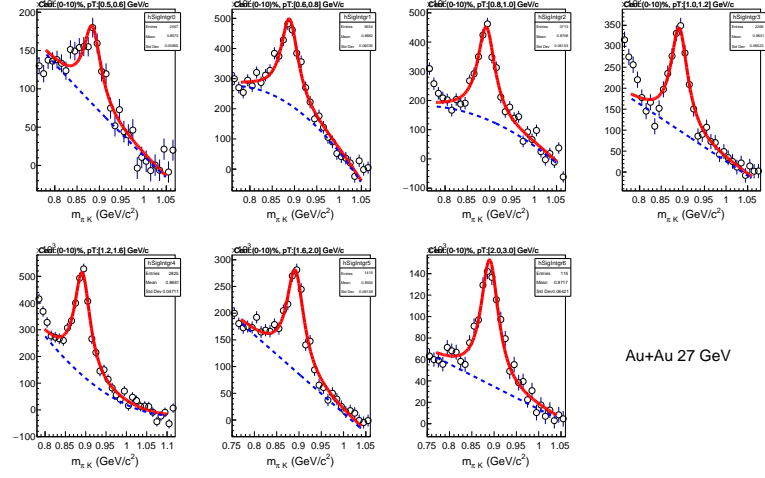


Figure 3.51: $K\pi$ invariant mass for 0-10 % centrality at $\sqrt{s_{NN}} = 27$ GeV.

3.8.24 K^{*0} invariant mass distribution for 10-20% centrality in Au+Au collisions at $\sqrt{s_{NN}} = 27$ GeV

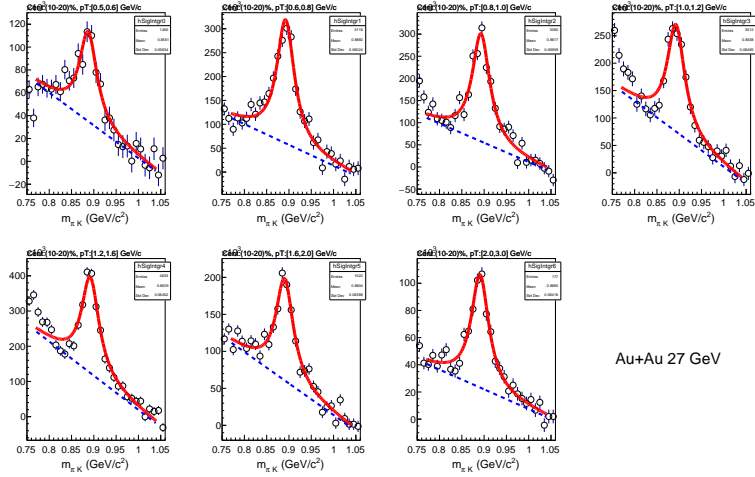


Figure 3.52: $K\pi$ invariant mass for 10-20 % centrality at $\sqrt{s_{NN}} = 27$ GeV.

3.8.25 K^{*0} invariant mass distribution for 20-30% centrality in Au+Au collisions at $\sqrt{s_{NN}} = 27$ GeV

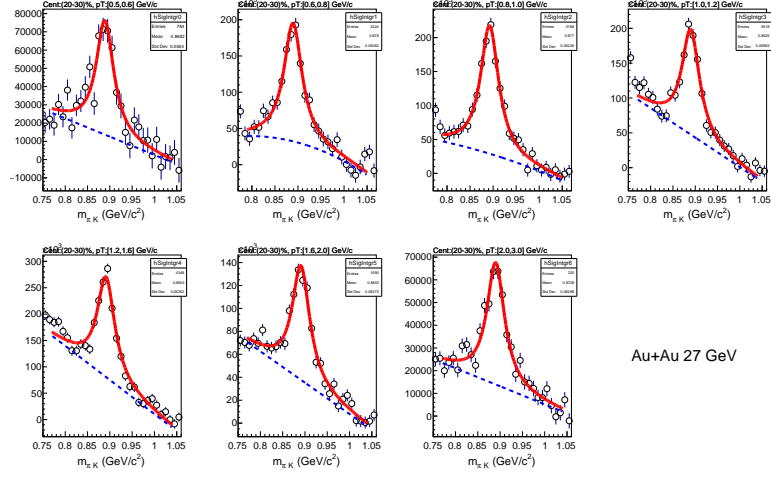


Figure 3.53: $K\pi$ invariant mass for 20-30 % centrality at $\sqrt{s_{NN}} = 27$ GeV.

3.8.26 K^{*0} invariant mass distribution for 30-40% centrality in Au+Au collisions at $\sqrt{s_{NN}} = 27$ GeV

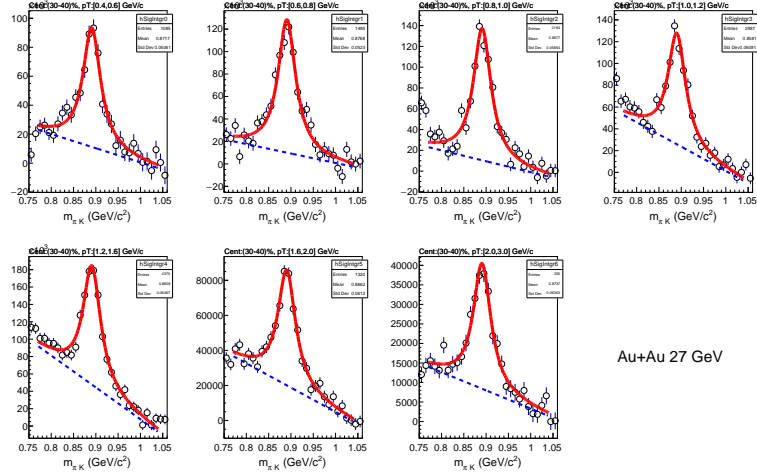


Figure 3.54: $K\pi$ invariant mass for 30-40 % centrality at $\sqrt{s_{NN}} = 27$ GeV.

3.8.27 K^{*0} invariant mass distribution for 40-60% centrality in Au+Au collisions at $\sqrt{s_{NN}} = 27$ GeV

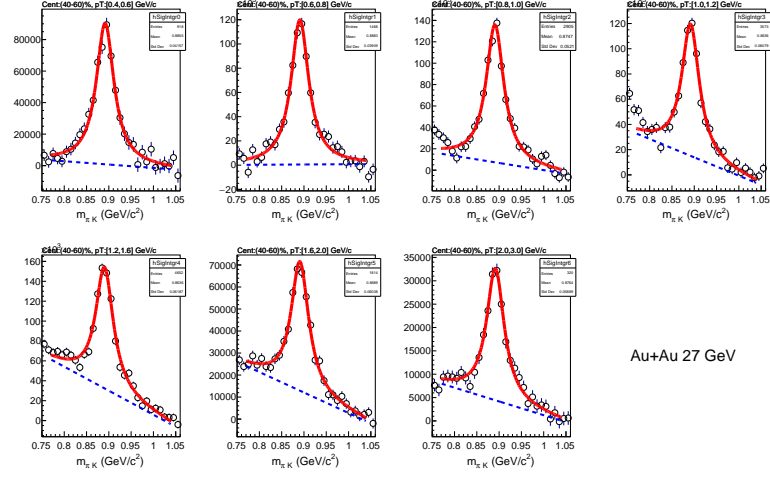


Figure 3.55: $K\pi$ invariant mass for 40-60 % centrality at $\sqrt{s_{NN}} = 27$ GeV.

3.8.28 K^{*0} invariant mass distribution for 60-80% centrality in Au+Au collisions at $\sqrt{s_{NN}} = 27$ GeV

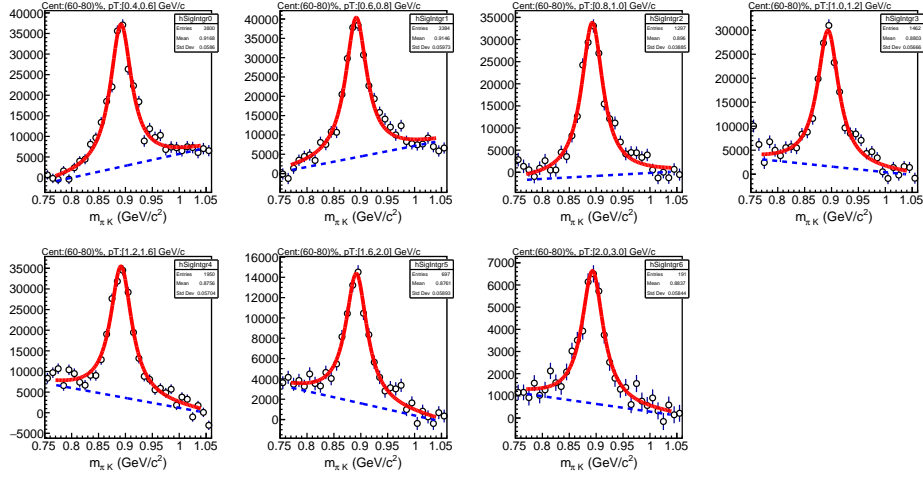
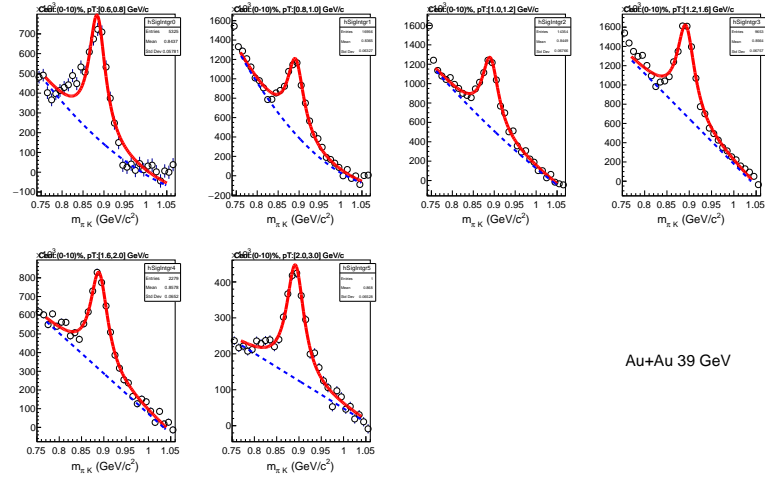


Figure 3.56: $K\pi$ invariant mass for 60-80 % centrality at $\sqrt{s_{NN}} = 27$ GeV.

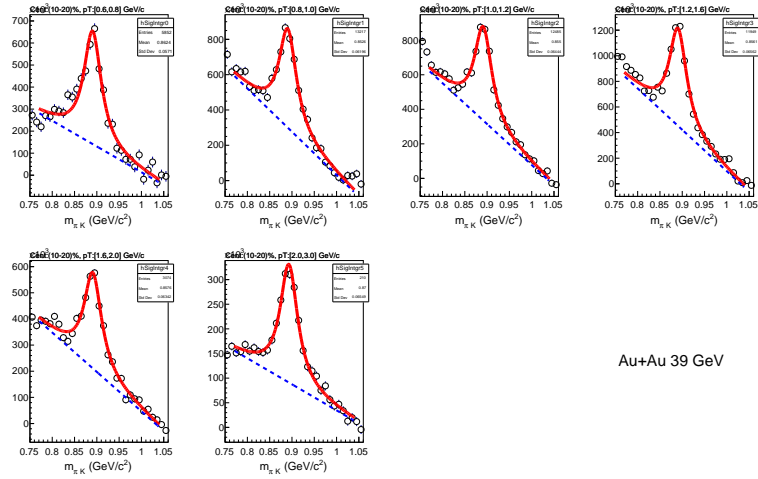
3.8.29 K^{*0} invariant mass distribution for 0-10% centrality in Au+Au collisions at $\sqrt{s_{NN}} = 39$ GeV



Au+Au 39 GeV

Figure 3.57: $K\pi$ invariant mass for 0-10 % centrality at $\sqrt{s_{NN}} = 39$ GeV.

3.8.30 K^{*0} invariant mass distribution for 10-20% centrality in Au+Au collisions at $\sqrt{s_{NN}} = 39$ GeV



Au+Au 39 GeV

Figure 3.58: $K\pi$ invariant mass for 10-20 % centrality at $\sqrt{s_{NN}} = 39$ GeV.

3.8.31 K^{*0} invariant mass distribution for 20-30% centrality in Au+Au collisions at $\sqrt{s_{NN}} = 39$ GeV

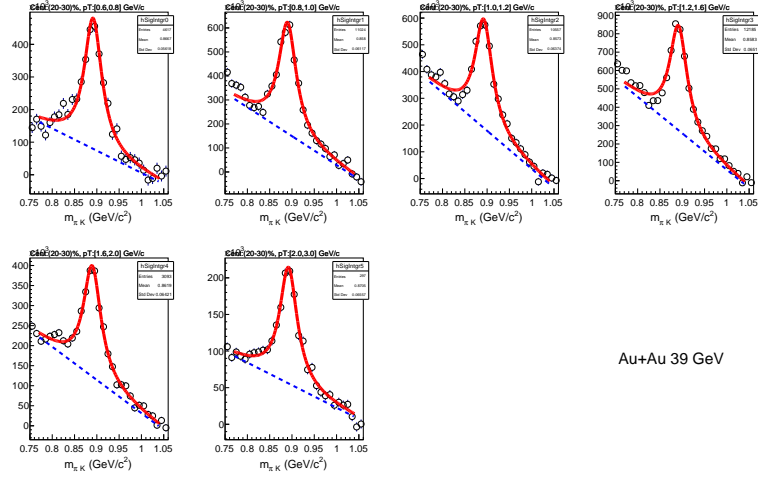


Figure 3.59: $K\pi$ invariant mass for 20-30 % centrality at $\sqrt{s_{NN}} = 39$ GeV.

3.8.32 K^{*0} invariant mass distribution for 30-40% centrality in Au+Au collisions at $\sqrt{s_{NN}} = 39$ GeV

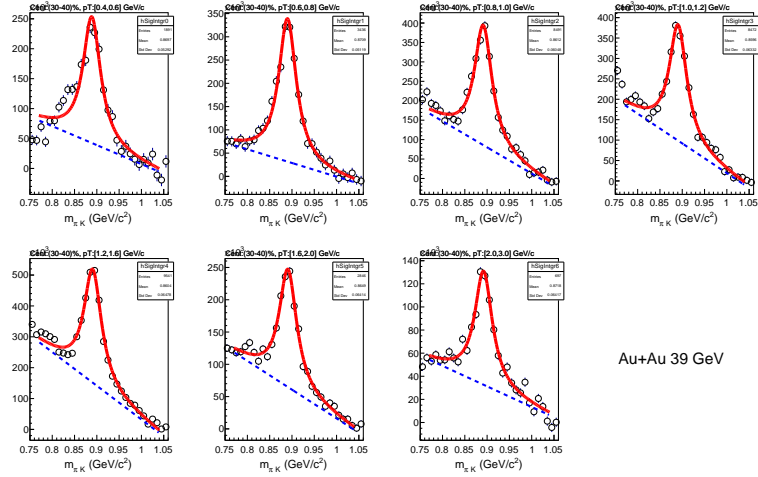


Figure 3.60: $K\pi$ invariant mass for 30-40 % centrality at $\sqrt{s_{NN}} = 39$ GeV.

3.8.33 K^{*0} invariant mass distribution for 40-60% centrality in Au+Au collisions at $\sqrt{s_{NN}} = 39$ GeV

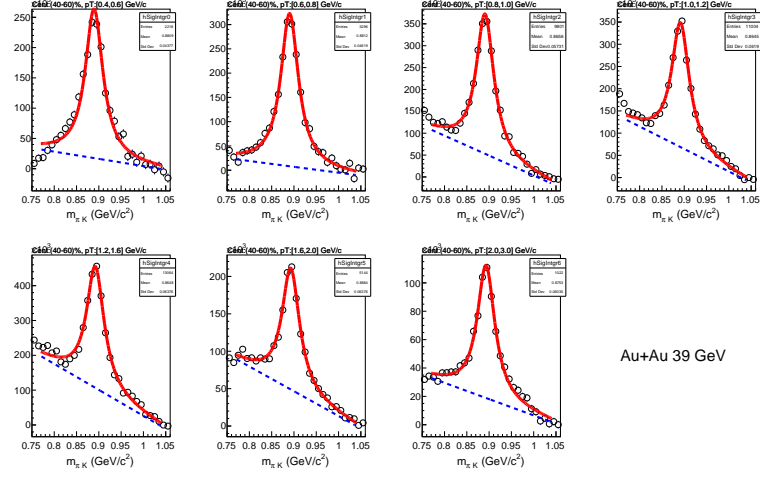


Figure 3.61: $K\pi$ invariant mass for 40-60 % centrality at $\sqrt{s_{NN}} = 39$ GeV.

3.8.34 K^{*0} invariant mass distribution for 60-80% centrality in Au+Au collisions at $\sqrt{s_{NN}} = 39$ GeV

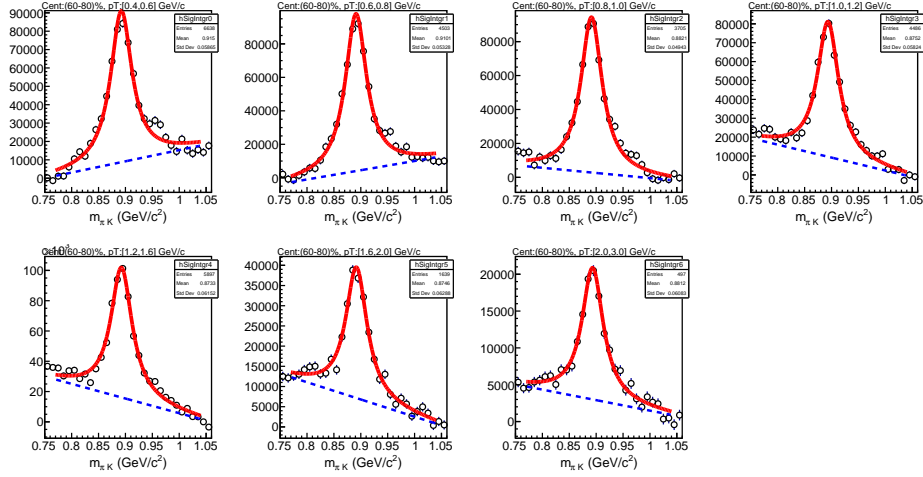


Figure 3.62: $K\pi$ invariant mass for 60-80 % centrality at $\sqrt{s_{NN}} = 39$ GeV.

3.8.35 Reference multiplicity, $\langle N_{part} \rangle$ and $\langle N_{coll} \rangle$

Table 3.6: Reference multiplicity or N_{ch}^{raw} values for different collision energies.

N_{ch}^{raw} values for different collision energies						
Centrality	7.7 GeV	11.5 GeV	14.5 GeV	19.6 GeV	27 GeV	39 GeV
0-5%	185	221	239	263	288	316
5-10%	154	184	200	220	241	265
10-20%	106	127	138	152	168	185
20-30%	72	86	93	102	114	125
30-40%	46	56	59	66	74	81
40-50%	28	34	36	40	45	50
50-60%	16	19	20	23	26	28
60-70%	8	10	11	12	13	15
70-80%	4	5	5	6	6	7

Table 3.7: $\langle N_{part} \rangle$ values for different collision energies.

$\langle N_{part} \rangle$ values for different collision energies						
Centrality	7.7 GeV	11.5 GeV	14.5 GeV	19.6 GeV	27 GeV	39 GeV
0-5%	337 ± 2	338 ± 2	338 ± 2	338 ± 2	343 ± 2	342 ± 2
5-10%	290 ± 6	291 ± 6	289 ± 6	290 ± 6	299 ± 6	294 ± 6
10-20%	226 ± 8	226 ± 8	226 ± 9	225 ± 9	234 ± 9	230 ± 8
20-30%	160 ± 10	160 ± 9	159 ± 10	158 ± 10	166 ± 11	162 ± 10
30-40%	110 ± 11	110 ± 10	108 ± 10	108 ± 11	114 ± 11	111 ± 11
40-50%	72 ± 10	72 ± 10	70 ± 10	71 ± 10	75 ± 10	74 ± 10
50-60%	45 ± 9	44 ± 9	44 ± 8	44 ± 9	47 ± 9	46 ± 9
60-70%	26 ± 7	26 ± 7	26 ± 7	25 ± 7	27 ± 8	26 ± 7
70-80%	14 ± 4	14 ± 6	14 ± 5	14 ± 5	14 ± 6	14 ± 5

Table 3.8: $\langle N_{coll} \rangle$ values for different collision energies.

$\langle N_{coll} \rangle$ values for different collision energies						
Centrality	7.7 GeV	11.5 GeV	14.5 GeV	19.6 GeV	27 GeV	39 GeV
0-5%	774 ± 28	784 ± 25	788 ± 30	800 ± 27	841 ± 28	853 ± 27
5-10%	629 ± 20	635 ± 20	634 ± 20	643 ± 20	694 ± 22	687 ± 21
10-20%	450 ± 22	453 ± 23	454 ± 24	458 ± 24	497 ± 26	491 ± 26
20-30%	283 ± 24	284 ± 23	283 ± 24	285 ± 26	312 ± 28	306 ± 27
30-40%	171 ± 23	172 ± 22	168 ± 22	170 ± 23	188 ± 25	183 ± 24
40-50%	96 ± 19	98 ± 18	94 ± 18	96 ± 18	106 ± 20	104 ± 20
50-60%	52 ± 13	52 ± 14	50 ± 12	51 ± 13	56 ± 15	55 ± 14
60-70%	25 ± 9	25 ± 9	25 ± 9	25 ± 8	27 ± 10	27 ± 9
70-80%	12 ± 5	12 ± 6	12 ± 5	12 ± 5	12 ± 6	12 ± 6

3.8.36 Comparision between yield extracted from simple and relativistic breit-wigner function:

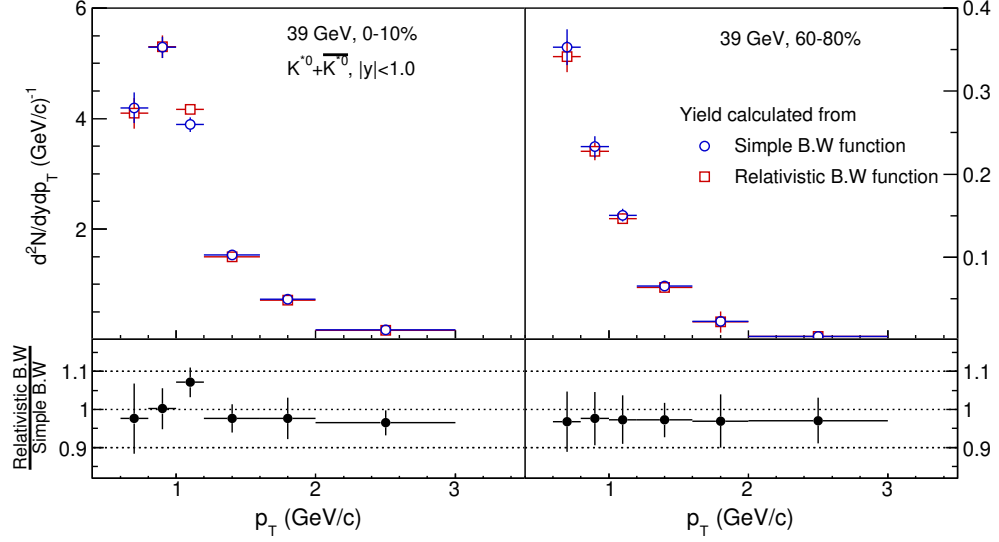


Figure 3.63: p_T -spectra comparison for yield extraction using simple and relativistic breit-wigner function.

3.8.37 Lorentz factor (γ):

We Know, from relativistic energy momentum relation

$$\begin{aligned}
 E^2 &= p^2 c^2 + m_0^2 c^4 \\
 \gamma^2 m_0^2 c^4 &= p^2 c^2 + m_0^2 c^4 \\
 (\gamma^2 - 1) m_0^2 c^4 &= p^2 c^2 \\
 \gamma &= \sqrt{1 + \left(\frac{p}{mc}\right)^2}
 \end{aligned} \tag{3.8.1}$$

Table 3.9: Lorentz factor (γ) for Au+Au collisions at $\sqrt{s_{NN}} = 7.7$ -39 GeV.

Centrality	7.7 GeV	11.5 GeV	14.5 GeV	19.6 GeV	27 GeV	39 GeV
0-10%	1.28 (0-20%)	1.30	1.33	1.37	1.36	1.37
10-20%		1.33	1.31	1.35	1.33	1.36
20-30%	1.27 (20-40%)	1.29	1.34	1.32	1.32	1.36
30-40%		1.27	1.29	1.31	1.32	1.33
40-60%	1.25	1.26	1.27	1.28	1.30	1.30
60-80%	1.19	1.21	1.24	1.23	1.25	1.26

3.8.38 Particle yield and mean transverse momentum:

Table 3.10: Mid rapidity dN/dy and $\langle p_T \rangle$ of K^{*0} meson in Au+Au collisions at $\sqrt{s_{NN}} = 7.7$ GeV.

Au+Au collisions, $\sqrt{s_{NN}} = 7.7$ GeV		
Centrality	dN/dy	$\langle p_T \rangle$ (GeV/c)
0-20%	$3.86 \pm 1.52 \pm 0.43$	$0.725 \pm 0.052 \pm 0.057$
20-40%	$1.71 \pm 0.59 \pm 0.20$	$0.705 \pm 0.048 \pm 0.054$
40-60%	$0.70 \pm 0.23 \pm 0.07$	$0.684 \pm 0.045 \pm 0.054$
60-80%	$0.24 \pm 0.10 \pm 0.04$	$0.581 \pm 0.051 \pm 0.051$

Table 3.11: Mid rapidity dN/dy and $\langle p_T \rangle$ of K^{*0} meson in Au+Au collisions at $\sqrt{s_{NN}} = 11.5$ GeV.

Au+Au collisions, $\sqrt{s_{NN}} = 11.5$ GeV		
Centrality	dN/dy	$\langle p_T \rangle$ (GeV/c)
0-10%	$5.92 \pm 1.98 \pm 0.76$	$0.750 \pm 0.045 \pm 0.069$
10-20%	$3.94 \pm 1.22 \pm 0.41$	$0.786 \pm 0.042 \pm 0.063$
20-30%	$3.19 \pm 0.78 \pm 0.30$	$0.737 \pm 0.035 \pm 0.057$
30-40%	$2.13 \pm 0.53 \pm 0.21$	$0.707 \pm 0.034 \pm 0.054$
40-60%	$1.03 \pm 0.20 \pm 0.10$	$0.679 \pm 0.025 \pm 0.054$
60-80%	$0.37 \pm 0.08 \pm 0.04$	$0.605 \pm 0.028 \pm 0.049$

Table 3.12: Mid rapidity dN/dy and $\langle p_T \rangle$ of K^{*0} meson in Au+Au collisions at $\sqrt{s_{NN}} = 14.5$ GeV.

Au+Au collisions, $\sqrt{s_{NN}} = 14.5$ GeV		
Centrality	dN/dy	$\langle p_T \rangle$ (GeV/c)
0-10%	$6.49 \pm 2.13 \pm 0.70$	$0.784 \pm 0.045 \pm 0.061$
10-20%	$4.77 \pm 1.34 \pm 0.46$	$0.760 \pm 0.038 \pm 0.060$
20-30%	$3.04 \pm 0.84 \pm 0.30$	$0.809 \pm 0.038 \pm 0.060$
30-40%	$2.40 \pm 0.53 \pm 0.24$	$0.736 \pm 0.030 \pm 0.056$
40-60%	$1.23 \pm 0.20 \pm 0.12$	$0.702 \pm 0.022 \pm 0.055$
60-80%	$0.36 \pm 0.07 \pm 0.03$	$0.650 \pm 0.025 \pm 0.052$

Table 3.13: Mid rapidity dN/dy and $\langle p_T \rangle$ of K^{*0} meson in Au+Au collisions at $\sqrt{s_{NN}} = 19.6$ GeV.

Au+Au collisions, $\sqrt{s_{NN}} = 19.6$ GeV		
Centrality	dN/dy	$\langle p_T \rangle$ (GeV/c)
0-10%	$6.83 \pm 1.47 \pm 0.75$	$0.845 \pm 0.031 \pm 0.062$
10-20%	$5.33 \pm 0.95 \pm 0.53$	$0.813 \pm 0.026 \pm 0.061$
20-30%	$4.08 \pm 0.67 \pm 0.40$	$0.775 \pm 0.023 \pm 0.058$
30-40%	$2.77 \pm 0.50 \pm 0.28$	$0.755 \pm 0.024 \pm 0.058$
40-60%	$1.48 \pm 0.16 \pm 0.15$	$0.718 \pm 0.015 \pm 0.057$
60-80%	$0.52 \pm 0.06 \pm 0.05$	$0.641 \pm 0.014 \pm 0.051$

Table 3.14: Mid rapidity dN/dy and $\langle p_T \rangle$ of K^{*0} meson in Au+Au collisions at $\sqrt{s_{NN}} = 27$ GeV.

Au+Au collisions, $\sqrt{s_{NN}} = 27$ GeV		
Centrality	dN/dy	$\langle p_T \rangle$ (GeV/c)
0-10%	$9.60 \pm 1.56 \pm 0.93$	$0.826 \pm 0.018 \pm 0.063$
10-20%	$7.11 \pm 1.28 \pm 0.73$	$0.788 \pm 0.022 \pm 0.062$
20-30%	$4.95 \pm 0.72 \pm 0.49$	$0.777 \pm 0.016 \pm 0.060$
30-40%	$3.31 \pm 0.36 \pm 0.32$	$0.774 \pm 0.015 \pm 0.058$
40-60%	$1.69 \pm 0.14 \pm 0.18$	$0.750 \pm 0.011 \pm 0.060$
60-80%	$0.57 \pm 0.04 \pm 0.06$	$0.670 \pm 0.010 \pm 0.053$

Table 3.15: Mid rapidity dN/dy and $\langle p_T \rangle$ of K^{*0} meson in Au+Au collisions at $\sqrt{s_{NN}} = 39$ GeV.

Au+Au collisions, $\sqrt{s_{NN}} = 39$ GeV		
Centrality	dN/dy	$\langle p_T \rangle$ (GeV/c)
0-10%	$10.04 \pm 1.04 \pm 1.21$	$0.837 \pm 0.021 \pm 0.067$
10-20%	$7.02 \pm 0.65 \pm 0.71$	$0.830 \pm 0.019 \pm 0.065$
20-30%	$4.92 \pm 0.33 \pm 0.49$	$0.828 \pm 0.012 \pm 0.064$
30-40%	$3.54 \pm 0.25 \pm 0.33$	$0.791 \pm 0.010 \pm 0.060$
40-60%	$1.87 \pm 0.09 \pm 0.19$	$0.751 \pm 0.006 \pm 0.060$
60-80%	$0.63 \pm 0.03 \pm 0.06$	$0.681 \pm 0.006 \pm 0.053$

3.8.39 Particle ratios:

Table 3.16: Mid rapidity particle ratios in Au+Au collisions at $\sqrt{s_{NN}} = 7.7$ GeV.

Au+Au collisions, $\sqrt{s_{NN}} = 7.7$ GeV			
Centrality	K^{*0}/K	ϕ/K	ϕ/K^{*0}
0-20%	$0.167 \pm 0.066 \pm 0.018$	$0.085 \pm 0.002 \pm 0.004$	$0.512 \pm 0.203 \pm 0.104$
20-40%	$0.178 \pm 0.062 \pm 0.021$	$0.084 \pm 0.003 \pm 0.005$	$0.471 \pm 0.163 \pm 0.100$
40-60%	$0.203 \pm 0.068 \pm 0.027$	$0.078 \pm 0.003 \pm 0.007$	$0.388 \pm 0.128 \pm 0.078$
60-80%	$0.297 \pm 0.122 \pm 0.060$	$0.073 \pm 0.004 \pm 0.011$	$0.245 \pm 0.103 \pm 0.059$

Table 3.17: Mid rapidity particle ratios in Au+Au collisions at $\sqrt{s_{NN}} = 11.5$ GeV.

Au+Au collisions, $\sqrt{s_{NN}} = 11.5$ GeV			
Centrality	K^{*0}/K	ϕ/K	ϕ/K^{*0}
0-10%	$0.173 \pm 0.058 \pm 0.022$	$0.101 \pm 0.002 \pm 0.005$	$0.581 \pm 0.194 \pm 0.115$
10-20%	$0.177 \pm 0.055 \pm 0.018$	$0.109 \pm 0.002 \pm 0.006$	$0.619 \pm 0.192 \pm 0.120$
20-30%	$0.220 \pm 0.054 \pm 0.022$	$0.111 \pm 0.003 \pm 0.007$	$0.507 \pm 0.124 \pm 0.094$
30-40%	$0.230 \pm 0.058 \pm 0.025$	$0.107 \pm 0.003 \pm 0.007$	$0.468 \pm 0.117 \pm 0.093$
40-60%	$0.238 \pm 0.046 \pm 0.031$	$0.102 \pm 0.002 \pm 0.009$	$0.431 \pm 0.084 \pm 0.088$
60-80%	$0.332 \pm 0.075 \pm 0.063$	$0.087 \pm 0.003 \pm 0.014$	$0.261 \pm 0.057 \pm 0.052$

Table 3.18: Mid rapidity particle ratios in Au+Au collisions at $\sqrt{s_{NN}} = 14.5$ GeV.

Au+Au collisions, $\sqrt{s_{NN}} = 14.5$ GeV			
Centrality	K^{*0}/K	ϕ/K	ϕ/K^{*0}
0-10%	$0.170 \pm 0.056 \pm 0.018$	— — —	— — —
10-20%	$0.184 \pm 0.051 \pm 0.018$	— — —	— — —
20-30%	$0.178 \pm 0.049 \pm 0.018$	— — —	— — —
30-40%	$0.220 \pm 0.048 \pm 0.022$	— — —	— — —
40-60%	$0.246 \pm 0.040 \pm 0.024$	— — —	— — —
60-80%	$0.261 \pm 0.050 \pm 0.026$	— — —	— — —

Table 3.19: Mid rapidity particle ratios in Au+Au collisions at $\sqrt{s_{NN}} = 19.6$ GeV.

Au+Au collisions, $\sqrt{s_{NN}} = 19.6$ GeV			
Centrality	K^{*0}/K	ϕ/K	ϕ/K^{*0}
0-10%	$0.154 \pm 0.033 \pm 0.017$	$0.116 \pm 0.002 \pm 0.006$	$0.752 \pm 0.162 \pm 0.131$
10-20%	$0.180 \pm 0.032 \pm 0.018$	$0.117 \pm 0.002 \pm 0.006$	$0.652 \pm 0.116 \pm 0.111$
20-30%	$0.201 \pm 0.033 \pm 0.021$	$0.116 \pm 0.002 \pm 0.007$	$0.578 \pm 0.095 \pm 0.096$
30-40%	$0.213 \pm 0.038 \pm 0.024$	$0.116 \pm 0.001 \pm 0.008$	$0.548 \pm 0.099 \pm 0.091$
40-60%	$0.238 \pm 0.026 \pm 0.031$	$0.106 \pm 0.001 \pm 0.010$	$0.448 \pm 0.048 \pm 0.079$
60-80%	$0.312 \pm 0.035 \pm 0.056$	$0.089 \pm 0.001 \pm 0.014$	$0.290 \pm 0.033 \pm 0.046$

Table 3.20: Mid rapidity particle ratios in Au+Au collisions at $\sqrt{s_{NN}} = 27$ GeV.

Au+Au collisions, $\sqrt{s_{NN}} = 27$ GeV			
Centrality	K^{*0}/K	ϕ/K	ϕ/K^{*0}
0-10%	$0.195 \pm 0.032 \pm 0.018$	$0.122 \pm 0.001 \pm 0.005$	$0.627 \pm 0.102 \pm 0.111$
10-20%	$0.209 \pm 0.038 \pm 0.021$	$0.121 \pm 0.001 \pm 0.006$	$0.576 \pm 0.103 \pm 0.105$
20-30%	$0.216 \pm 0.031 \pm 0.022$	$0.123 \pm 0.001 \pm 0.007$	$0.569 \pm 0.083 \pm 0.105$
30-40%	$0.228 \pm 0.025 \pm 0.024$	$0.123 \pm 0.001 \pm 0.008$	$0.543 \pm 0.059 \pm 0.094$
40-60%	$0.240 \pm 0.020 \pm 0.031$	$0.123 \pm 0.001 \pm 0.011$	$0.512 \pm 0.042 \pm 0.094$
60-80%	$0.300 \pm 0.023 \pm 0.058$	$0.094 \pm 0.001 \pm 0.016$	$0.312 \pm 0.022 \pm 0.050$

Table 3.21: Mid rapidity particle ratios in Au+Au collisions at $\sqrt{s_{NN}} = 39$ GeV.

Au+Au collisions, $\sqrt{s_{NN}} = 39$ GeV			
Centrality	K^{*0}/K	ϕ/K	ϕ/K^{*0}
0-10%	$0.191 \pm 0.021 \pm 0.022$	$0.128 \pm 0.001 \pm 0.006$	$0.673 \pm 0.070 \pm 0.125$
10-20%	$0.194 \pm 0.019 \pm 0.020$	$0.122 \pm 0.001 \pm 0.006$	$0.632 \pm 0.058 \pm 0.102$
20-30%	$0.202 \pm 0.012 \pm 0.021$	$0.123 \pm 0.001 \pm 0.006$	$0.609 \pm 0.041 \pm 0.095$
30-40%	$0.225 \pm 0.010 \pm 0.023$	$0.121 \pm 0.001 \pm 0.008$	$0.542 \pm 0.038 \pm 0.084$
40-60%	$0.241 \pm 0.006 \pm 0.031$	$0.116 \pm 0.001 \pm 0.010$	$0.486 \pm 0.023 \pm 0.078$
60-80%	$0.290 \pm 0.006 \pm 0.052$	$0.097 \pm 0.001 \pm 0.015$	$0.336 \pm 0.016 \pm 0.052$

Chapter 4

Understanding K^{*0} production using hadronic transport and statistical thermal model

Continuing the discussion from Chapter 1, this chapter presents the experimental results of K^{*0} measurements at STAR Beam Energy Scan (BES) energies and compares them with various phenomenological models to gain a better understanding of the dynamics within the hadronic phase formed in heavy-ion collisions. The results are compared with the Ultra Relativistic Quantum Molecular Dynamics (UrQMD) transport model as well as a basic thermal model. Additionally, predictions for measurements using the upcoming BES-II data set are also provided. [43, 44]

4.1 Model description:

4.1.1 The thermal model

The statistical thermal model, or the Hadron Resonance Gas (HRG) model [163], provides a good description of the thermal parameters at the freezeout hypersurface and the thermodynamics of the system following chemical freezeout. In the framework of the grand-canonical ensemble (GCE), the logarithm of the total partition function for a multi-component hadron gas at temperature T and volume V is given by:

$$\ln Z^{GC}(\mu_i, T, V) = \sum_i \frac{g_i V}{(2\pi)^3} \int d^3p \ln(1 \pm e^{-\beta(E_i - \mu_i)})^{\pm 1} \quad (4.1.1)$$

Where, g_i represents the degeneracy, and $\mu_i = \mu_S S_i + \mu_Q Q_i + \mu_B B_i$ is the chemical potential of i^{th} type of hadron species. S_i , Q_i and B_i correspond to the strangeness, charge, and baryon quantum numbers of the i^{th} species, respectively, with μ_S , μ_Q and μ_B being their associated chemical potentials. In the partition function equation, the plus sign is used for fermions, and the minus sign is used for bosons. $\beta = \frac{1}{T}$, where T is the temperature and $E_i = \sqrt{p^2 + m_i^2}$ represents the energy of the i^{th} hadron species, with m_i being the mass of that species.

We know the no. of the total particle of i^{th} species (N_i^{GC})

$$N_i^{GC} = T \frac{\partial \ln Z^{GC}}{\partial \mu_i} \quad (4.1.2)$$

So, using equation 4.1.1 and 4.1.2,

$$N_i^{GC} = \frac{g_i V}{2\pi^2} \sum_{k=1}^{\infty} (\mp 1)^{k+1} \frac{m_i^2 T}{k} K_2 \left(\frac{k m_i}{T} \right) e^{\beta \mu_j k} \quad (4.1.3)$$

Here K_2 is the Bessel function of second order. This is the expression for primary yield of i^{th} type of hadron.

To calculate the primary yield of a specific type of hadron at a given temperature (T), volume (V), and chemical potential (μ), one requires information such as the mass, spin, strangeness quantum number, baryon number, charge, and isospin of that particular particle. This data is obtained from the Particle Data Group (PDG) [155], an international collaboration of particle physicists that compiles and reanalyzes published results on particle properties, decay channels, decay probabilities, and fundamental interactions. In this model, PDG-2016 data is used to determine the primary yield and the total yield of hadrons after their eventual decay.

For the results presented in this chapter, the freeze-out parameters (T , μ_S , μ_Q , and μ_B) at STAR BES energies are taken from the ref [15]. These parameters are obtained by fitting the yields ratios of π^\pm , K^\pm , $p(\bar{p})$, $\Lambda(\bar{\Lambda})$ and $\Xi^-(\bar{\Xi}^-)$, under the assumption of the grand-canonical ensemble (GCE).

4.1.2 The UrQMD Model

The UrQMD (Ultra relativistic Quantum Molecular Dynamics) model [164, 165] is based on a microscopic transport theory. In this model the particle production mechanism includes resonance decays, string excitation and fragmentation. where the phase space description of the reactions considering the stochastic collisions of hadrons important. The projectile and target nuclei are initialised according to a Woods-Saxon profile in coordinate space and the stochastic hadron-hadron collisions are performed in a similar way as in the original cascade models, until the collision criteria is fulfilled. When the relative distance d_{trans} between two particles, in three dimensional configuration space gets smaller than a critical distance d_0 that is given by the corresponding total cross section σ_{tot} a collision takes place.

$$d_{trans} \leq d_0 = \sqrt{\frac{\sigma_{tot}}{\pi}}, \quad \sigma_{tot} = \sigma(\sqrt{s}, \text{type}) \quad (4.1.4)$$

The total cross section σ_{tot} again depends on the centre of mass energy \sqrt{s} and on the species and quantum numbers of the incoming particles. The UrQMD model includes more than 50 baryon species, that includes nucleon, delta and hyperon resonances with masses upto $2.25 \text{ GeV}/c^2$ and 45 meson species with masses upto $2 \text{ GeV}/c^2$, including strange meson resonances, they are supplemented by their corresponding anti particles and all isospin projected states [164]. It also incorporates baryon-baryon, meson-baryon and meson-meson interactions, providing a thorough understanding of the dynamics and interactions within the hadronic system.

In the current work the publicly available UrQMD model (version 2.3) has been used, selecting the default Equation of State (EoS) known as CASCADE mode, which operates without any potentials (EoS=0). In this model, resonance masses are distributed based on the Breit-Wigner function, allowing for the simulation of their decay processes. In the simulation, the natural decay processes of unstable particles were accounted by enabling their decay.

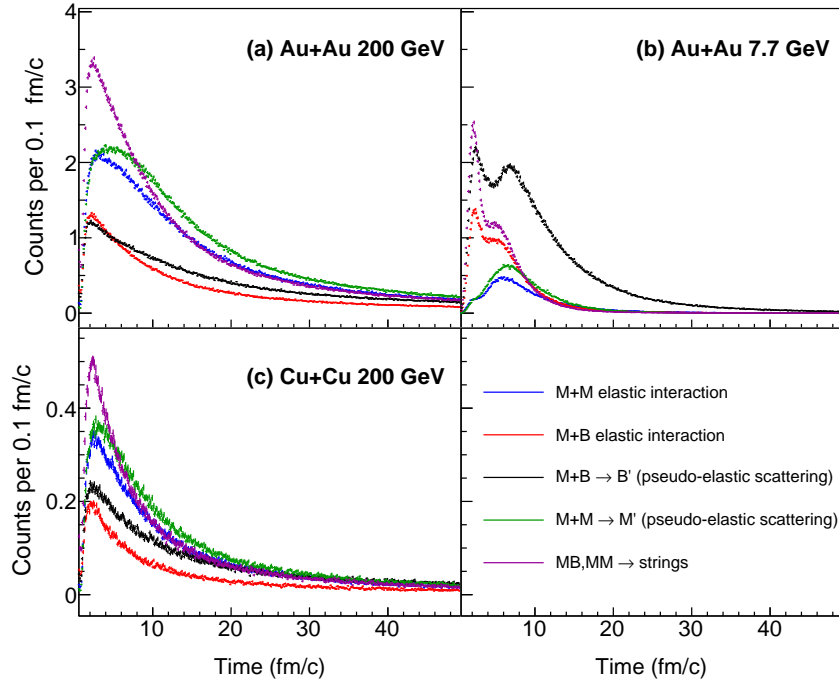


Figure 4.1: The evolution of hadronic interactions for meson-meson (M+M) and meson-baryon (M+B) pairs at $\sqrt{s_{NN}} = 7.7$ and 200 GeV (for Au+Au and Cu+Cu collisions) with hadronic cascade time based on the UrQMD model.

Figure 4.1 displays the meson-meson (M+M) and meson-baryon (M+B) pair interaction probabilities as a function of medium evolution time. The distributions correspond to two collision energies: $\sqrt{s_{NN}} = 7.7$ GeV (Au+Au) and 200 GeV (Au+Au and Cu+Cu). Only the interactions of meson-meson and meson-baryon pairs are shown, as the K^{*0} resonance decays into π and K particles. Inelastic interactions between meson-meson or meson-baryon pairs (MM, MB \rightarrow strings) are depicted in magenta. In the UrQMD output, it is not possible to separately distinguish inelastic scatterings between these pairs. Elastic scatterings of meson-meson and meson-baryon pairs are represented by blue and red lines, respectively. Green and black lines indicate pseudo-elastic scatterings for MM

and MB pairs, respectively, which involve the formation of an intermediate resonance state.

Figure 4.1 illustrates that, at $\sqrt{s_{NN}} = 200$ GeV, meson-meson interactions dominate over meson-baryon interactions, specifically for elastic and pseudo-elastic scatterings. This effect is independent of the collision system considered. At lower center-of-mass energies, where the pion-nucleon cross-section is notably large, meson-baryon interactions become particularly important. These interactions are largely driven by pseudo-elastic scatterings that lead to the formation of intermediate resonances. As noted in Ref [155] and implemented in UrQMD, the pseudo-elastic cross-section for forming the Δ^{++} resonance in the $\pi^+ + p$ system is approximately 200 mb—considerably higher than the 120 mb pseudo-elastic cross-section for ρ meson formation in the $\pi + \pi$ system. Similarly, the total cross-section for $K^- + p$ interactions can reach 120 mb at low kaon beam momenta, compared to only 20 mb at higher momenta [164–166].

4.2 Signal Reconstruction

Since the decay of unstable hadrons was enabled during the simulation, short-lived resonances need to be reconstructed. In this case, the K^{*0} resonance is reconstructed from its hadronic decay channel, $K^{*0}(\bar{K}^{*0}) \rightarrow K^\pm \pi^\mp$ (B.R. 66%) [155]. For the reconstruction, method similar to that used in experimental data analysis was applied [12, 39]. This involved accumulating invariant mass distributions from various combinations of daughter particles in each event and using track rotation method, to properly eliminate combinatorial background contributions. This method has already been well discussed in the previous chapter.

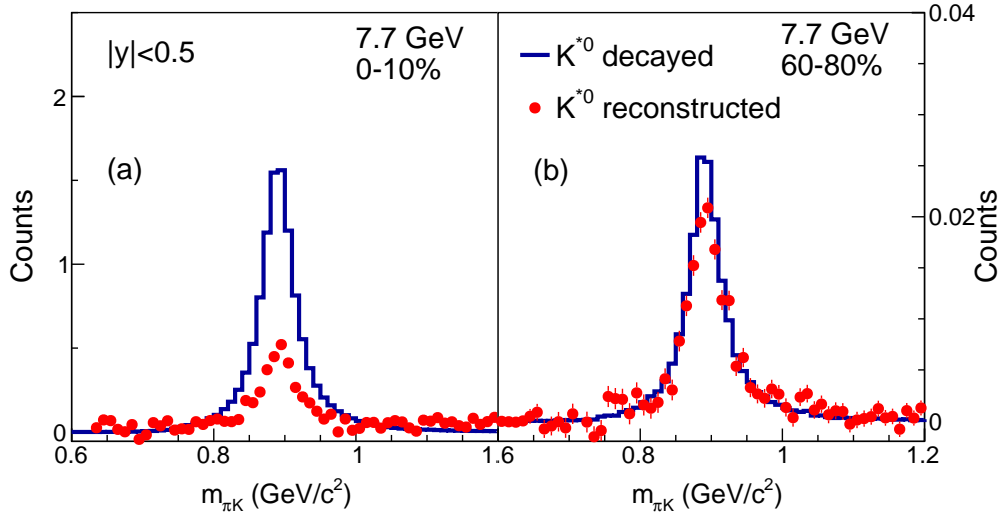


Figure 4.2: Invariant mass distribution of K^{*0} meson (blue line) and reconstructed $K\pi$ pairs (red dots) for (a) 0-10% and (b) 60-80% Au+Au collisions at 7.7 GeV from UrQMD model.

In UrQMD, it is possible to track the number of decayed K^{*0} mesons. Figure 4.3 illustrates the invariant mass distribution of K^{*0} mesons that decayed during the simulation, represented by the blue solid lines, which follows a Breit-Wigner distribution. The red dots show the invariant mass distributions of the reconstructed $K\pi$ pairs. The figure

indicates that the number of reconstructed particles is lower than those that actually decayed, suggesting a loss of the K^{*0} signal due to in-medium hadronic rescattering with other particles. This loss is more pronounced in 0-10% central collisions compared to 60-80% peripheral collisions. Finally the yield of K^{*0} meson is estimated by integrating the resonance mass peak and corrections are applied for the relevant branching ratio. In this chapter, both K^{*0} and \bar{K}^{*0} are combined and referred to as K^{*0} unless stated otherwise. Likewise, charged kaons are combined together and denoted as K .

4.3 Results and Discussions:

4.3.1 Effect of hadronic cascade time on K^{*0} meson

In the UrQMD model, the duration of hadronic simulation (τ) can be adjusted by modifying the input parameters [164]. In this approach, setting τ to a specific value effectively results in an immediate freeze-out. By increasing τ , the produced particles are allowed to interact with one another for a longer time. This enables to investigate the impact of hadronic rescattering and regeneration on the yield of resonance particles.

A. Yield of K^{*0} and charged kaons (K^\pm)

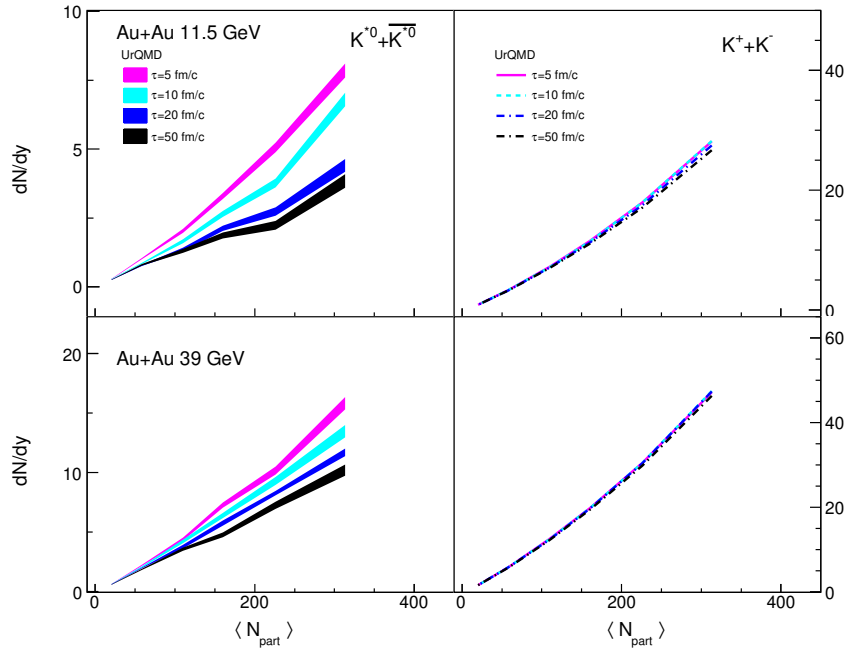


Figure 4.3: The p_T integrated yield of K^{*0} and charged kaons vs $\langle N_{part} \rangle$ in Au+Au collisions at 11.5 GeV (upper panel) and 39 GeV (lower panel), measured using the UrQMD model.

Figure 4.3 displays the yields (dN/dy) of K^{*0} and charged kaons (K^\pm) as a function of the number of participating nucleons ($\langle N_{part} \rangle$). Measurements were taken at midrapidity ($|y| < 1.0$ for K^{*0} and $|y| < 0.1$ for K^\pm) in Au+Au collisions at $\sqrt{s_{NN}} = 11.5$ and 39 GeV, aligning with previously published STAR results [15, 39]. The results are obtained by varying τ from 5 to 50 fm/c across all STAR BES energies from 7.7 to 39 GeV. Figure 4.3 reveals that while the yield of charged kaons shows no dependence on

τ , the K^{*0} yield decreases as τ increases. This reduction in K^{*0} yield is attributed to the rescattering of daughter particles in the hadronic phase, a process included in the UrQMD model.

B. Resonance to non-resonance ratio

The study of resonance to non-resonance particle as a function of multiplicity or centrality serves as a tool to probe the hadronic phase created in heavy-ion collisions. Figure 4.4 presents such particle ratios (K^{*0}/K and ϕ/K) as a function of N_{part} from the UrQMD model, alongside STAR data measured in Au+Au collisions at $\sqrt{s_{NN}} = 11.5$ and 39 GeV.

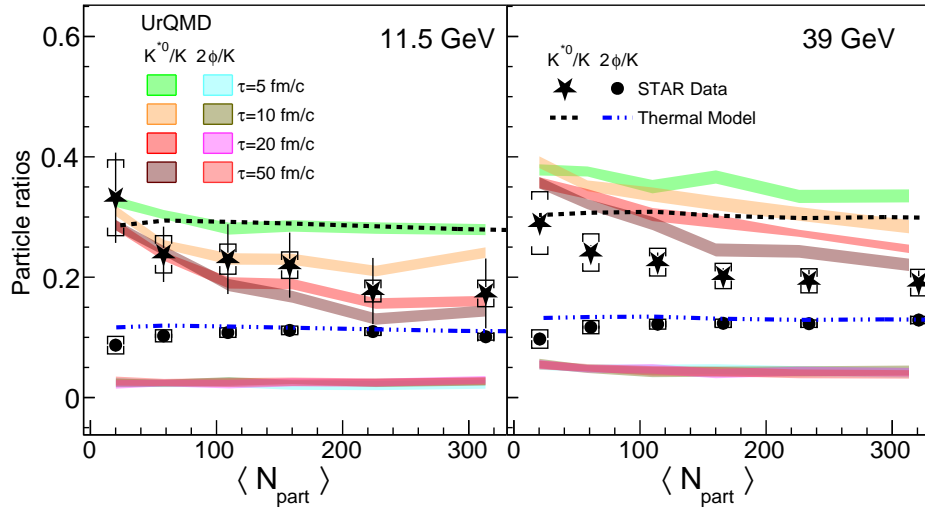


Figure 4.4: The resonance to non-resonance ratios (K^{*0}/K and ϕ/K) vs $\langle N_{part} \rangle$ measured at mid-rapidity from the STAR experiment [39] compared with corresponding thermal model and UrQMD model results at $\sqrt{s_{NN}} = 11.5$ and 39 GeV. The systematic and statistical uncertainties on the experimental data are shown by the caps and boxes respectively.

Figure 4.4 also displays particle ratios calculated using the thermal model described in Section 4.1.1. For these calculations, the freeze-out parameters for various centralities and collision energies are taken from Ref. [15]. As a straightforward statistical model, this thermal model does not account for any hadronic interactions. From Figure 4.4, it is evident that the K^{*0}/K ratio calculated by the thermal model is consistent with experimental data in peripheral collisions but overestimates it in central collisions. However, the centrality-dependent trend of the ϕ/K ratio is well captured by the thermal model.

The UrQMD measurements are done by varying the hadronic cascade time τ from 5 to 50 fm/c. The K^{*0}/K ratio at $\tau = 5$ fm/c remains almost independent of centrality, while a suppression can be observed for $\tau = 10$ fm/c or higher. N_{part} dependence of K^{*0}/K ratios is found to be similar to that measured by the STAR experiment for all STAR BES energies. For $\sqrt{s_{NN}} = 39$ GeV, UrQMD results with $\tau = 50$ fm/c appear to show better consistency with the data than those with $\tau = 20$ fm/c. At $\sqrt{s_{NN}} = 11.5$ GeV, the UrQMD calculations with $\tau = 20$ fm/c provide a good match to the data. Figure 4.1 shows that elastic interactions among hadrons nearly saturate beyond $\tau = 20$ fm/c for lower collision energies, resulting in similar K^{*0}/K ratios at 11.5 GeV for $\tau = 20$ and $\tau = 50$ fm/c, though a slight difference is seen in central collisions at 39 GeV.

Considering the large statistical uncertainties, the 11.5 GeV data are also consistent with UrQMD results at $\tau = 10$ fm/c. The high-statistics data from the STAR Beam Energy Scan Phase-II program will reduce experimental uncertainty. Since ϕ mesons have nearly ten times the lifetime of K^{*0} , they are expected to decay outside the medium, remaining largely unaffected by the hadronic medium created in heavy-ion collisions. Thus, the ϕ/K ratio shows no obvious dependence on centrality or τ . However, the UrQMD model quantitatively underpredicts the ϕ/K ratio [167].

The simultaneous comparison of the experimentally measured resonance-to-non-resonance ratios with UrQMD and the thermal model suggests that the decay products of K^{*0} undergo late-stage hadronic interactions, where hadronic rescattering has a more significant impact than regeneration.

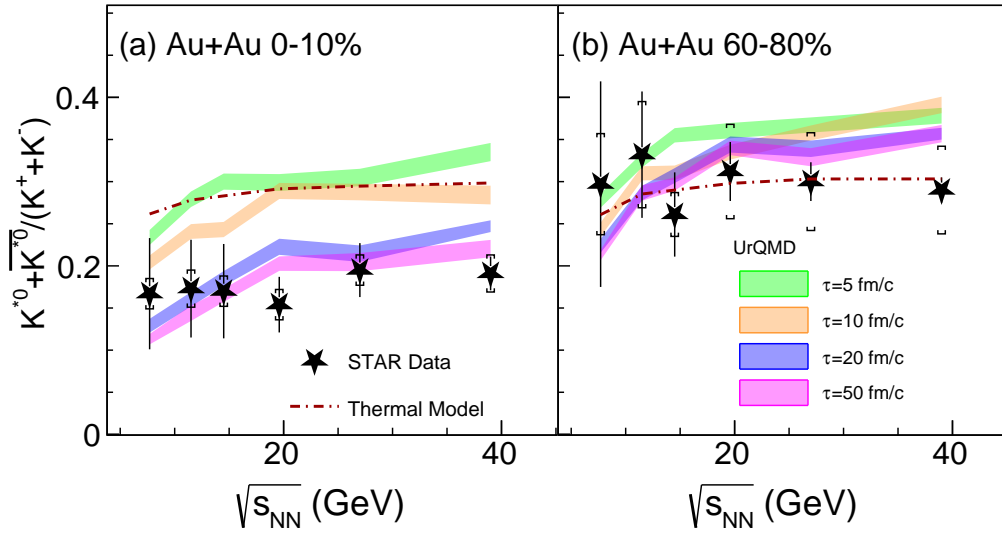


Figure 4.5: The K^{*0}/K ratio as a function of $\sqrt{s_{NN}}$ for central (0-10%) and peripheral (60-80%) Au+Au collisions at midrapidity [39] is shown alongside corresponding measurements from thermal and UrQMD models.

Figure 4.5 displays the center-of-mass energy dependence of the K^{*0}/K ratio for 0-10% central and 60-80% peripheral Au+Au collisions. Within current uncertainties, STAR data show no significant energy dependence for the K^{*0}/K ratio in either central or peripheral collisions. UrQMD model calculations are shown for different τ values, ranging from 5 to 50 fm/c, along with predictions from the thermal model.

The thermal model does not exhibit clear centrality or energy dependence. Its over-prediction of the K^{*0}/K ratio in central collisions aligns with expectations, where hadronic rescattering is likely dominant. The UrQMD model suggests an increase in the K^{*0}/K ratio with rising collision energy. Notably, a strong dependence on hadronic cascade lifetime (τ) is seen in central collisions, while peripheral results appear less sensitive. UrQMD results with τ values of 20 and 50 fm/c are consistent with the observed energy dependence of the K^{*0}/K ratio in central collisions, and results below $\sqrt{s_{NN}} = 14.5$ GeV align with model predictions at $\tau = 10$ fm/c within uncertainties. However, the model results in peripheral collisions appear τ -independent, indicating a negligible role for hadronic rescattering at peripheral collisions compared to central collisions.

C. Rapidity dependent K^{*0} production from UrQMD model

In Fig 4.7, the Rapidity dependent yield of K^{*0} meson is plotted for both central and peripheral collisions at $\sqrt{s_{NN}} = 11.5$ and 19.6 GeV respectively. A clear rapidity dependence is observed for the K^{*0} yield for all BES energies. A strong dependence of K^{*0} yield is observed in central collisions. However, the dependence is a weaker in case of peripheral collisions.

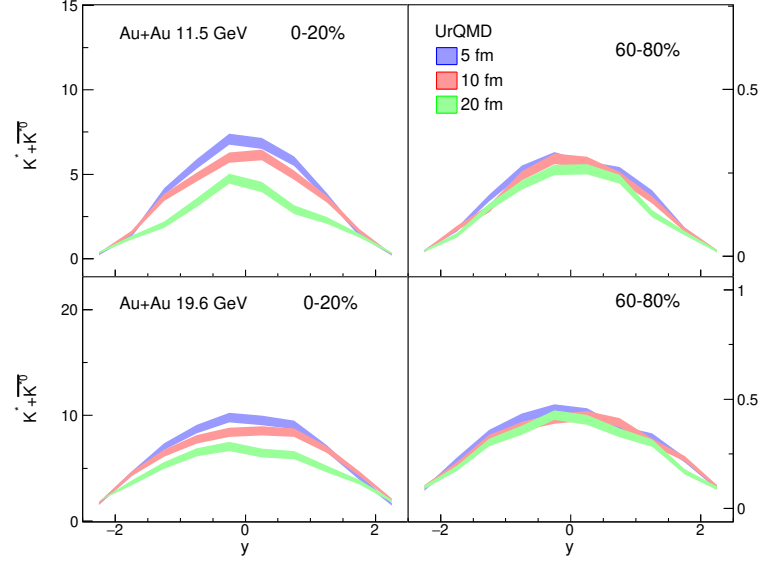


Figure 4.6: The p_T -integrated yield (dN/dy) for K^{*0} mesons as a function of rapidity is shown for 0-10% and 60-80% centralities at $\sqrt{s_{NN}} = 11.5$ GeV (upper panel) and 19.6 GeV (lower panel), respectively.

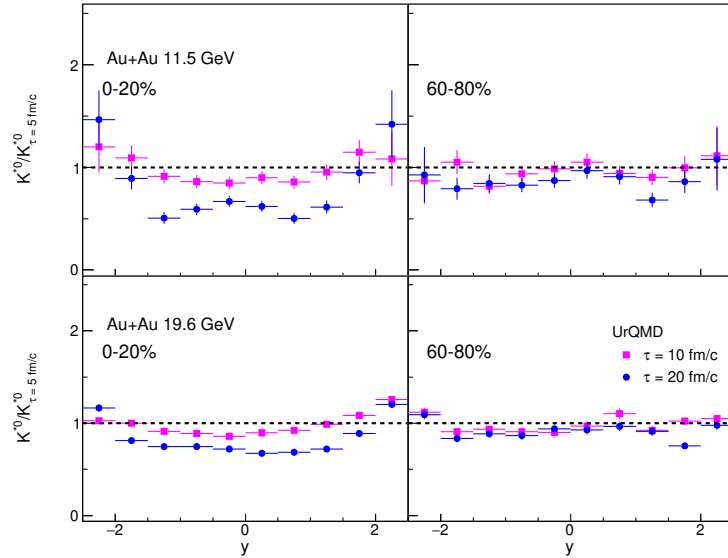


Figure 4.7: The p_T -integrated yield (dN/dy) for K^{*0} mesons with $\tau = 10$ and 20 fm/c, normalized by the dN/dy value at $\tau = 5$ fm/c, is plotted as a function of rapidity for both 0-10% and 60-80% centralities.

To explore the impact of rescattering as a function of rapidity (y), Figure 4.7 shows the ratio of K^{*0} yield (dN/dy) for $\tau = 10$ and 20 fm/c, normalized to the yield at $\tau = 5$ fm/c, plotted against rapidity. In central collisions, this ratio appears to increase at larger rapidities, suggesting that rescattering may have a stronger influence at mid-rapidity, where particle density is higher. This effect can also broaden the rapidity distribution shape, meaning that variations in the ratio with rapidity arise from these rescattering effects. In contrast, for peripheral collisions, the ratio remains nearly constant across rapidity, indicating that no significant rapidity-dependent rescattering is observed in these cases.

4.3.2 Hadronic rescattering in high baryon density region.

Figure 4.8 presents the multiplicity-dependent baryon-to-meson ratios, with p/π shown in the left panel and Λ/π in the right panel, for $\sqrt{s_{NN}} = 7.7$ and 200 GeV at mid-rapidity ($|y| < 0.5$) based on UrQMD model calculations. At 7.7 GeV, the baryon-to-meson ratio is considerably higher than at 200 GeV, indicating that the mid-rapidity region is predominantly baryon-dominated at lower collision energies, while it becomes primarily mesonic at higher energies.

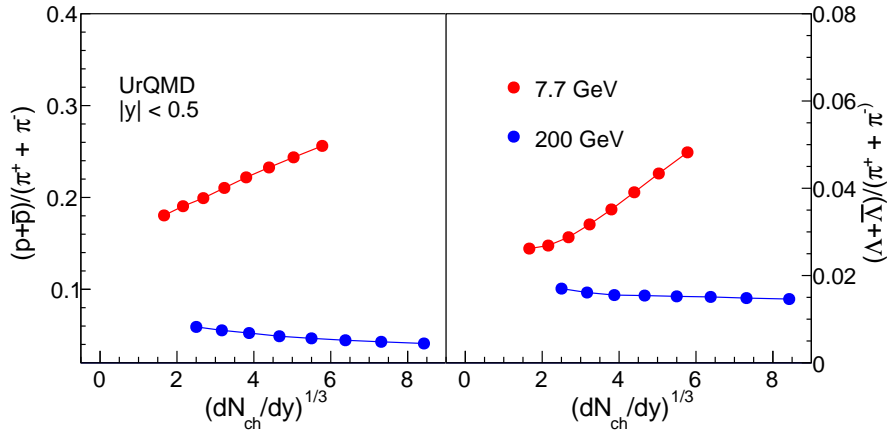


Figure 4.8: Left Panel: Multiplicity dependent p/π ratio (left panel) , Λ/π (right panel) ratio for $\sqrt{s_{NN}} = 7.7$ and 200 GeV at mid rapidity ($|y| < 0.5$) from UrQMD model.

Additionally, Figure 4.1 reveals that meson-meson (MM) elastic interactions prevail over meson-baryon (MB) elastic interactions at higher collision energies, whereas the opposite trend occurs at lower energies. Since resonance yields are sensitive to these interaction types, their production can be significantly impacted by these effects.

A. Multiplicity dependent particle yields

Figure 4.9 displays the mid-rapidity ($|y| < 0.5$) p_T -integrated yield (dN/dy) of K^{*0} mesons and charged kaons as a function of $(dN_{ch}/d\eta)^{1/3}$. The model calculations cover Au+Au and Cu+Cu collisions at $\sqrt{s_{NN}} = 200$ GeV, along with Au+Au collisions at $\sqrt{s_{NN}} = 7.7, 11.5$, and 19.6 GeV. These results show that both K^{*0} and charged kaon (K^\pm) yields increase steadily with rising multiplicity across all collision systems and beam energies. The K^\pm yields remain almost unaffected by changes in system type and

energy within a specific multiplicity range. In contrast, K^{*0} mesons exhibit a different trend, particularly at lower collision energies, where for a given multiplicity range, the K^{*0} yield is reduced compared to that at higher energies. This behavior at lower energies may reflect additional influences, such as yield loss from re-scattering effects, impacting the observed K^{*0} yields.

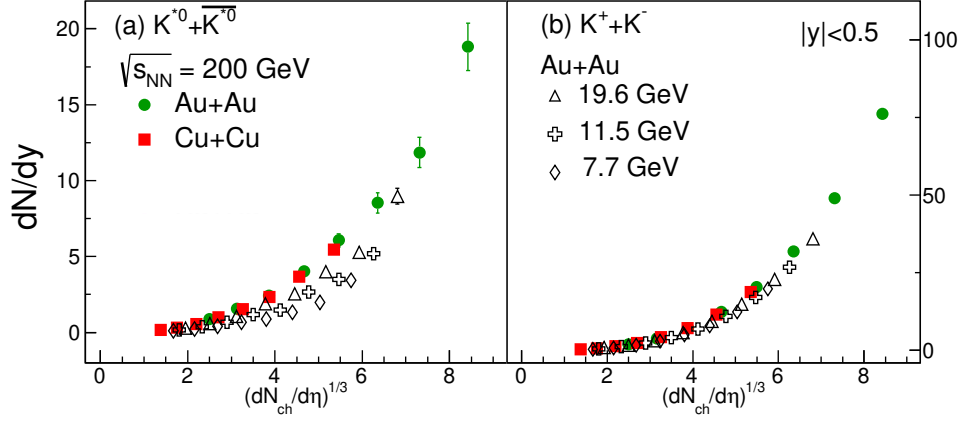


Figure 4.9: p_T -integrated K^{*0} and charged K yield in different collision systems and beam energies from UrQMD model.

As outlined in Section 4.2, within the UrQMD model it is possible to calculate the actual number of resonances that decay within the evolving hadronic medium. This allows the study of the effects of hadronic rescattering on the production of short-lived resonance particles. To explore the nature of rescattering at $\sqrt{s_{NN}} = 7.7$ and 200 GeV, the ratio of reconstructed to true resonances as a function of $(dN_{ch}/d\eta)^{1/3}$ is calculated.

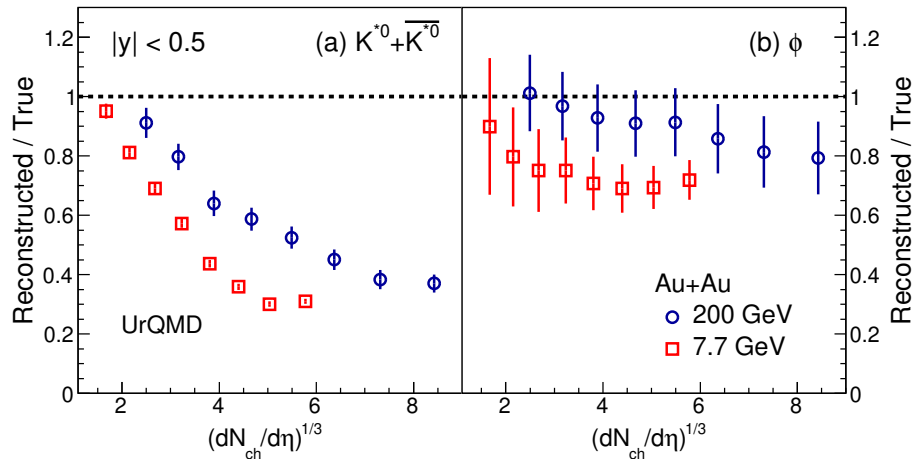


Figure 4.10: The ratio of reconstructed to true resonance counts for K^{*0} (left panel) and ϕ (right panel) resonances, respectively, as a function of $(dN_{ch}/d\eta)^{1/3}$ from the UrQMD model in Au+Au collisions at $\sqrt{s_{NN}} = 7.7$ and 200 GeV.

In Figure 4.10 (left panel), the ratio of reconstructed to true K^{*0} resonances is shown as a function of $(dN_{ch}/d\eta)^{1/3}$ for Au+Au collisions at 7.7 and 200 GeV. The results suggest a greater suppression in K^{*0} yield at 7.7 GeV than at 200 GeV during hadronic evolution, highlighting that rescattering effects are more pronounced at 7.7 GeV for a given

multiplicity. Additionally, Figure 4.10 (right panel) shows the ratio $\phi(\text{reconstructed})/\phi(\text{true})$ as a function of $(dN_{ch}/d\eta)^{1/3}$ for the same collision energies. The ϕ ratio exhibits weaker suppression than K^{*0} , likely due to the longer lifetime of the ϕ meson, which makes it less affected by hadronic rescattering. Moreover, the suppression in the $\phi(\text{reconstructed})/\phi(\text{true})$ ratio is more evident at 7.7 GeV compared to 200 GeV.

B. K^{*0}/K ratio

In Figure 4.11, the system size dependence of the K^{*0}/K ratio is shown as a function of $(dN_{ch}/d\eta)^{1/3}$ using the UrQMD model. At center-of-mass energies of $\sqrt{s_{NN}} = 200$ GeV and 62.4 GeV, the ratios demonstrate an approximate multiplicity scaling, largely independent of the collision species. However, as the energy decreases, the K^{*0}/K ratio shows a noticeable reduction compared to those values at 200 and 62.4 GeV. A similar trend has also been observed in experimental data Figure 3.25, discussed in the previous chapter. This difference implies that, even for the same multiplicity or system size, rescattering effects are more pronounced at lower energies, such as 7.7 GeV, compared to 200 GeV. Alternatively, the observed difference may reflect variations in the chemical composition of the hadronic medium at mid-rapidity, with RHIC BES conditions being baryon-rich compared to the meson-dominated environment at the top RHIC energy.

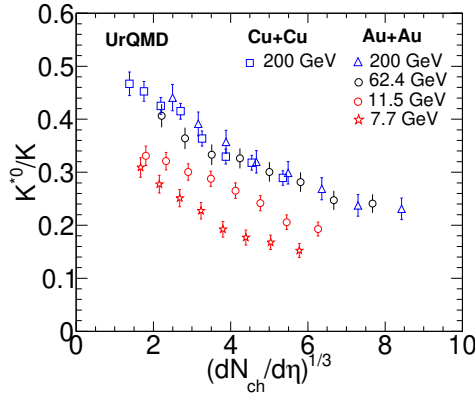


Figure 4.11: The K^{*0}/K ratio calculated at mid-rapidity as a function of $(dN_{ch}/d\eta)^{1/3}$ for various collision systems and beam energies from the UrQMD calculation.

4.4 Summary

In summary, this study provides a detailed comparison of mid-rapidity K^{*0} measurements at RHIC BES energies with predictions from both the thermal model and the UrQMD transport model. The thermal model, which excludes hadronic rescattering, is consistent with data for more peripheral collisions but overestimates the K^{*0}/K ratio in central Au+Au collisions. Meanwhile, the UrQMD model captures the observed centrality dependence of the K^{*0}/K ratio in the experimental data, revealing that the ratio decreases with longer hadronic interaction times. This suggests that the observed suppression of the K^{*0}/K ratio in central versus peripheral Au+Au collisions results from hadronic rescattering experienced by the K^{*0} decay products. Lastly, predictions of K^{*0} rapidity distributions from UrQMD indicate that rescattering effects are most pronounced at midrapidity.

In addition to that, the system size dependence of K^{*0} production across various collision systems and beam energies available at RHIC is studied, using the UrQMD model. At the highest RHIC energy, the K^{*0}/K ratio showed approximate scaling with collision multiplicity. However, at lower collision energies, the K^{*0}/K ratio was notably lower than at the top RHIC energy. The UrQMD model suggests that this deviation from multiplicity scaling in the K^{*0}/K ratio may arise from the dominance of baryon-meson interactions within the baryon-rich matter produced at lower center-of-mass energies.

Chapter 5

K^{*0} production in Au+Au collisions from RHIC beam energy scan phase-II

This chapter includes the precision measurement of K^{*0} -meson spectrum in Au+Au collisions at $\sqrt{s_{NN}} = 7.7, 11.5, 14.6, 19.6, 27$ GeV using high statistics BES-II data collected by the STAR experiment with upgraded TPC detector. Both mid rapidity ($|y| < 1.0$) and rapidity differential results has been included.

5.1 Introduction

In contrast to heavy-ion collisions at top RHIC or LHC energies, collisions at RHIC BES energies offer a unique and intriguing opportunity to probe various phenomena. High baryon stopping, low particle multiplicity, and a comparatively short-lived fireball motivate a deeper investigation into the dynamics of the hadronic phase at these lower energies. Earlier studies on the bulk properties of the medium created at BES energies show that, with decreasing collision energy, the difference between chemical and kinetic freeze-out temperatures gradually shortens [15]. The K^{*0} measurements at BES energies, presented in Chapter 3, indicate a decrease in the K^{*0}/K ratio with increasing collision centrality, suggesting the dominance of hadronic rescattering in the late stages of the hadronic phase. However, high experimental uncertainties prevent firm conclusions, particularly at the lowest energies.

Alongside experimental data, transport model studies presented in Chapter 4 suggest a possible breakdown in the approximate scaling of the resonance-to-non-resonance ratio at BES energies compared to top RHIC energies. This could be attributed to an increase

in meson-baryon elastic interactions relative to meson-meson elastic interactions in the baryon-rich, lower-energy regime. To confirm these findings, precise measurements with higher statistics are required.

At lower collision energies, the particle density significantly drops at higher rapidities due to smaller beam rapidity. Although rapidity-differential studies of the hadronic phase are interesting, they remain relatively unexplored. With high statistics and improved detector conditions at STAR, measurements can now extend to higher rapidities, as high as $|y| < 1.5$.

In this chapter, the measurement of the K^{*0} meson in Au+Au collisions at $\sqrt{s_{NN}} = 7.7 - 27$ GeV is presented. Multiplicity and rapidity-differential studies are carried out with better precision compared to those in BES-I.

5.2 Data sets, events and track selection

5.2.1 Data set

The results presented here are based on data collected by the STAR experiment at RHIC for Au+Au collisions at $\sqrt{s_{NN}} = 7.7, 11.5, 14.5, 19.6$, and 27 GeV during the second phase of the Beam Energy Scan (BES) program. The data set was obtained using a minimum bias trigger. Due to improved detector conditions in BES-II, the cuts on the vertex position along the longitudinal (z) direction were widened for data collected after 2019, which contributed to increased event statistics. However, the cut on the vertex position along the radial direction in the transverse plane remained unchanged. One can observe an increase in 10-15 time more event statistics in BES-II as compared to that in BES-I. Table 5.1 provides details on the minimum bias event selection cuts used for the BES-II data sets.

Table 5.1: Event selection cuts for min-bias events.

Au+Au, $\sqrt{s_{NN}}$	Year	Production id	Trigger ids	V_z (cm)	V_r (cm)	Events (Millions)
7.7 GeV	2021	P22ib	810010, 810020, 810030, 810040	145	2	90
11.5 GeV	2020	P23ia	710000, 710010, 710020	145	2	330
14.6 GeV	2019	P21ic	650000	145	2	394
19.6 GeV	2019	P23id	640001, 640011, 640021, 640031, 640041, 640051	145	2	775
27 GeV	2018	P19ib	610001, 610011, 610021, 610031, 610041, 610051	50	2	423

5.3 Track cuts and Particle identification

In BES-II, upgrades to the inner sector of the Time Projection Chamber (TPC) have improved both the dE/dx and momentum resolution [168]. This allows for a lower

selection cut on the transverse momentum of charged particle tracks, requiring each track to have $p_T > 0.06$ GeV/c. Additionally, charged particles are now selected from a wider rapidity window ($|y| < 1.5$). Other track selection parameters remain the same as in the BES-I analysis [39]: $DCA < 2$ cm, number of TPC hit points > 15 , and $N_{hits}/N_{hits}_{possible} > 0.55$ for charged particle track selection.

For particle identification, both TPC and TOF detectors are used. If a track has TOF information, TOF m^2 -selection cuts are applied; otherwise, particles are identified using the TPC $N\sigma$ cuts. The required m^2 ranges are $-0.2 < m^2 < 0.15$ GeV/c² for pions and $0.15 < m^2 < 0.36$ GeV/c² for kaons. For both pion and kaon selection in the TPC, a $|N\sigma| < 2$ cut is applied.

5.4 Signal extraction

The invariant mass distribution of $K^{*0}(\overline{K}^{*0})$ meson was reconstructed using the invariant mass technique [12, 39] from its hadronic decay channel $K^{*0}(\overline{K}^{*0}) \rightarrow K^\pm \pi^\mp$ (Branching ratio 66.6%) [155] using all combination of charged kaons and charged pions from same event. In this analysis the K^{*0} and \overline{K}^{*0} mesons are combined and collectively denoted as K^{*0} . Since all kaons and pions in a event are not daughters of K^{*0} mesons, the K^{*0} mesons signal sits on the top of combinatorial background of uncorrelated pairs, hence not visible. This has been shown by the red open markers in the left panel of Fig 5.1.

5.4.1 Combinatorial background estimation

The combinatorial background is estimated from "Track Rotation" technique [39]. In this method, the momentum of one of the decay daughter is rotated by 180 degree, in transverse plane, in order to break the correlation between the pairs. This has been shown by the black closed markers in the left panel of Fig 5.1. This method is the default way of the combinatorial background estimation in this analysis.

For cross check, we have also used the "Like-Sign" method to estimate the combinatorial background. In this technique, the combinatorial background is constructed through the invariant mass of pions and kaons of same charge ($++$, $--$) from same event. Since the number of positive and negative particles produced in relativistic heavy ion collisions are not same, the combinatorial background is constructed by taking the geometric mean of number of like sign pairs as shown in equation below.

$$N_{K^{*0}} = N_{K^+\pi^-} + N_{K^-\pi^+} - 2 \times \sqrt{N_{K^+\pi^+} \times N_{K^-\pi^-}} \quad (5.4.1)$$

5.4.2 Raw yield extraction

The raw K^{*0} yields are extracted by subtracting the scaled track-rotated background invariant mass distributions from the same-event invariant mass distributions, for each centrality and p_T window. The right panel of Fig. 5.1 illustrates example of the K^{*0} meson signal after combinatorial background subtraction in Au+Au collisions at $\sqrt{s_{NN}} = 7.7$ and 19.6 GeV for 0-10% centrality in a specific p_T bin. The K^{*0} signal is fitted using a Breit-Wigner function, while a second-order polynomial function is applied to fit the residual background. For systematic checks, a first-order polynomial was also tested.

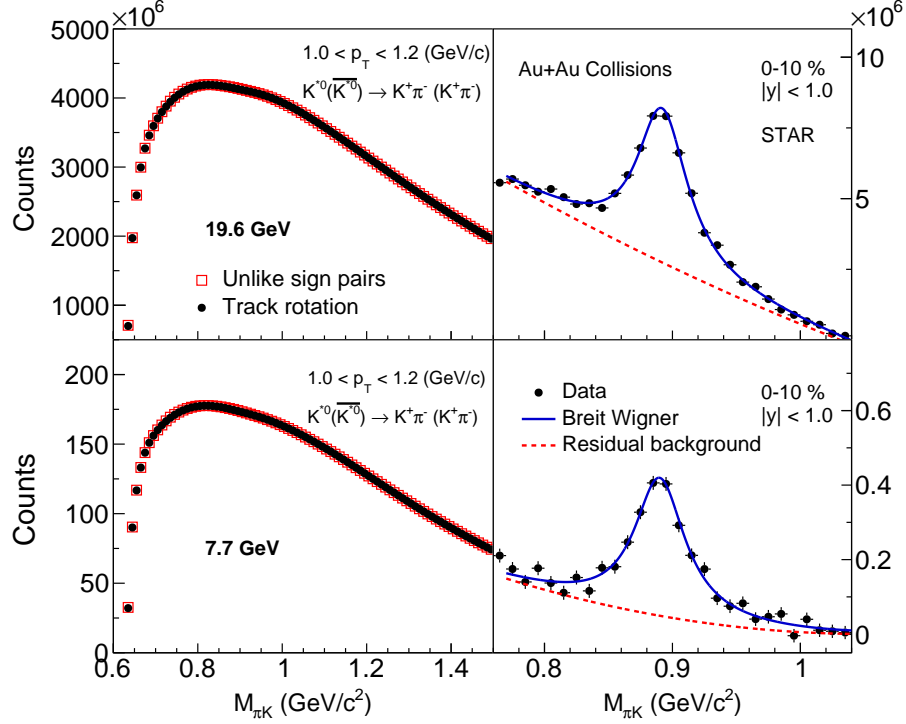


Figure 5.1: (Left panel) K^{*0} signal from unlike sign pair (red marker) and background estimated from track rotation method (black marker). (Right panel) Invariant mass distribution of $K\pi$ pairs after subtraction of background estimated from track rotation method. The blue line denotes the Breit Wigner fit and red line represents the fit for the residual background. The results are shown for $1.0 < p_T < 1.2$ GeV/c and 0 – 10% centrality at $\sqrt{s_{NN}} = 19.6$ (top panels) and 7.7 (bottom panels) GeV respectively. The error bars shown are statistical only.

The final raw yield of K^{*0} is then estimated using a histogram bin-counting method. The detailed explanation has already been presented in section 3.4 of chapter 3

Fig. 5.2 presents the significance of the K^{*0} signal over the background as a function of p_T for various centralities at $\sqrt{s_{NN}} = 19.6$ GeV, showing results from both BES-I and BES-II. It can be observed that the higher statistics in BES-II have led to a 4-15 times improvement in signal significance, effectively reducing the statistical uncertainty in the yield measurements.

5.5 Efficiency correction

Since detectors cannot achieve 100% efficiency in detecting particles of interest, the results need to be corrected for detector efficiency. The detector acceptance and reconstruction efficiency are determined using the STAR embedding method, which is detailed in Section 3.5 of Chapter 3. In this method, K^{*0} particles (5% of the total multiplicity) are embedded in each event, generated with uniform distributions in rapidity ($|y| < 1.5$), p_T ($0 < p_T < 5$ GeV/c), and ϕ ($0 < \phi < 2\pi$), and then processed through the STAR GEANT3 detector simulation package.

Prior to calculating the efficiency, various quality assurance (QA) checks are performed by comparing track parameters from both real data and embedding. The embedding QA plots are available here: <https://drupal.star.bnl.gov/STAR/blog/>

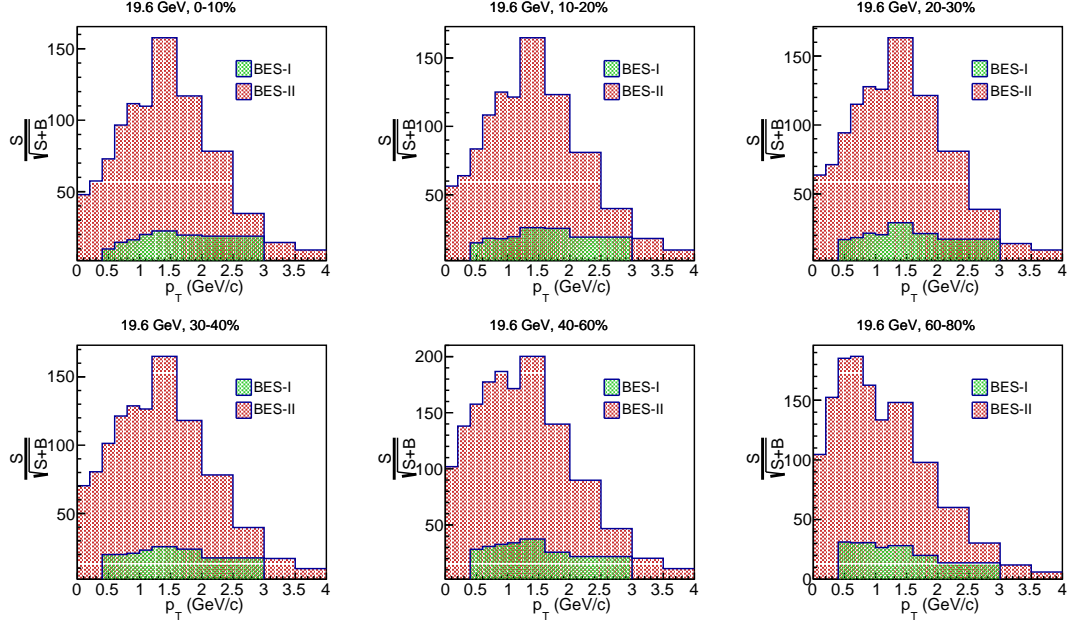


Figure 5.2: The Significance of the K^{*0} signal as a function of p_T for different centralities at $\sqrt{s_{NN}} = 19.6$ GeV. The green and red shaded areas denote the same for BES-I and BES-II respectively.

[aswini96/KstarmesonBES2embeddingQA](#)

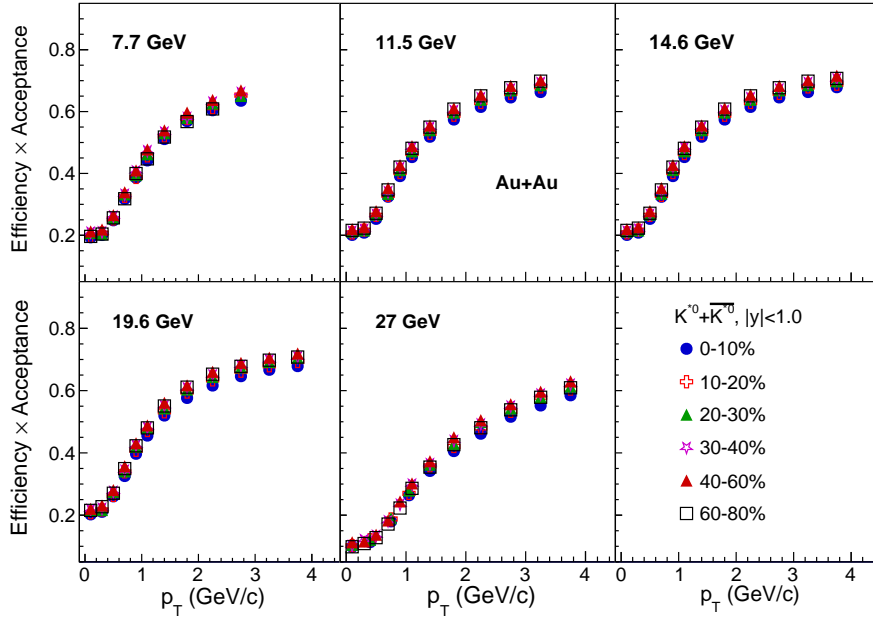


Figure 5.3: The p_T dependent detector efficiency \times Acceptance for K^{*0} meson in Au+Au collisions at $\sqrt{s_{NN}} = 7.7-27$ GeV. The statistical error bar shown here are within the marker size.

While reconstructing the tracks similar kinematic acceptance is used as that of real data. Finally, the ratio of number of reconstructed K^{*0} to the input number of MC K^{*0} tracks gives the reconstruction efficiency \times acceptance.

$$\epsilon_{reco \times acc} = \frac{N_{K^{*0}}^{RC}}{N_{K^{*0}}^{MC}} \quad (5.5.1)$$

Figure 5.3 presents the detector acceptance and reconstruction efficiency as a function of p_T for different collision centrality intervals in Au+Au collisions at $\sqrt{s_{NN}} = 7.7, 11.5, 14.5, 19.6, 27$ GeV for BES-II setup. No significant centrality dependence is observed in the tracking efficiency.

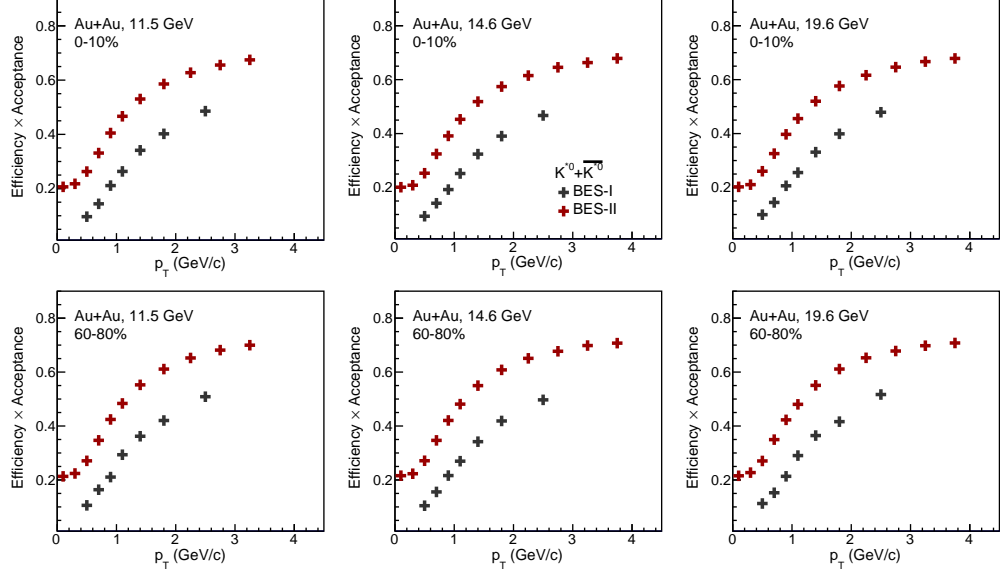


Figure 5.4: The tracking efficiency comparison for the K^{*0} meson in 0-10% (top panel) and 60-80% (bottom panel) centrality ranges is presented for both BES-I and BES-II. The statistical error bar shown here are within the marker size.

The iTPC upgrade in the BES-II program has significantly enhanced particle identification, especially in the low p_T region. Figure 5.4 compares the tracking efficiency of the K^{*0} meson in both central and peripheral collisions across the BES-I and BES-II data sets. While an overall improvement in efficiency is observed in BES-II, the enhancement is most significant at low p_T , where efficiency nearly doubles compared to BES-I. Other corrections like PID efficiency corrections has also been performed and the value of p_T dependent PID efficiency comes ≈ 90 -95%.

5.6 Systematic uncertainties

Systematic uncertainties on the measurements are estimated by varying potential sources like event/track selection cuts, PID selection cuts, Yield extraction methods, signal fitting region, spectra fit functions etc. Table 5.2 lists all the parameters that were varied for the systematic uncertainties together with the default value. However the variations considered for the systematic uncertainty estimation is similar to that of BES-I analysis.

Systematic uncertainties are calculated following the method proposed in Ref [169], which accounts for the statistical effects on these uncertainties. The calculation proceeds as follows:

1. The difference between the y values obtained from the default selection cut (as listed in Table 5.2) and that obtained from different variations are calculated, which

Table 5.2: Variation in selection criteria for systematic uncertainty estimation.

Sources	Default	Variations
Fit Range	0.77-1.04 GeV/ c^2	9 variations (within 2.5-3.5 σ)
Residual background	2 nd order polynomial	2 nd and 1 st order polynomial
Width of BW function	Fixed	Fixed, Free
Yield extraction	Histogram bin counting	Bin counting, Function integral, Fit func. Parameter
NHitsFit	NHits > 15	NHits > 13, NHits > 15, NHits > 18
DCA	DCA < 2 cm	DCA < 1.8 cm, DCA < 2 cm, DCA < 2.2 cm
TPC $N\sigma$	$ N\sigma < 2$	$ N\sigma < 2$, $ N\sigma < 1.8$, $ N\sigma < 1.6$
z-Vertex position	$ v_z < 145$ cm (50 cm for 27 GeV)	$ v_z < 145$ cm (50) cm, $ v_z < 130$ cm (40) cm, $ v_z < 100$ cm (30) cm
Low p_T extrapolation	Levy-Tsallis function (if needed)	Levy-Tsallis, Exp. p_T , Maxwell-Boltzmann
Tracking efficiency	4% due to uncertainty in tracking efficiency	

is denoted as:

$$\text{Systematic difference: } \Delta y = |y_{def} - y_{var}|$$

2. The quadratic difference between the statistical error on the values in default case and that in systematic variation is calculated as:

$$\text{Statistical Uncertainty: } \delta y = \sqrt{|stat_{def}^2 - stat_{var}^2|}$$

3. if $\delta y > \Delta y$, we take systematic error = 0
4. Otherwise, systematic error = $\sqrt{(\Delta y)^2 - (\delta y)^2}$
5. if we have n different variation cuts for one systematic source, then the systematic uncertainty for that particular source will be;

$$\text{systematic error } (sys_{source}) = \sqrt{\frac{sys_{var1}^2 + sys_{var2}^2 + sys_{var3}^2 + \dots + sys_{varn}^2}{n}}$$

6. Final systematic uncertainty: $\sqrt{sys_{source1}^2 + sys_{source2}^2 + \dots + sys_{source n}^2}$

In addition to the systematic uncertainties calculated from yield variations, a constant 4% uncertainty has been included to account for tracking efficiency. This value is based on the fact that the K^{*0} meson has two decay daughters, with a 2% uncertainty attributed to each daughter track.

Table 5.3 lists fractional contribution of different systematic sources towards final K^{*0} yield. how ever the systematic uncertainty on p_T spectra is also in the similar order that comes $\approx 10\%$.

It should be noted that during the estimation of the particle ratios (K^{*0}/K) we have excluded this 4% tracking efficiency from the K^{*0} yield, which is assumed to be correlated error that cancels out while measuring the ratio.

Table 5.3: The contribution of various sources to the systematic uncertainties for K^{*0} yield at $|y| < 1.0$ in Au+Au collisions at $\sqrt{s_{NN}} = 7.7$ -27 GeV.

Systematic sources	K^{*0} dN/dy
Fitting region (%)	1%
Residual background (%)	1-4%
Yield extraction (%)	5%
Track selection (%)	1%
Width fix/free (%)	5%
Particle identification (%)	3-5%
Global tracking efficiency (%)	4%
Total (%)	8.8-10.4%

5.7 Results

5.7.1 Transverse momentum spectra

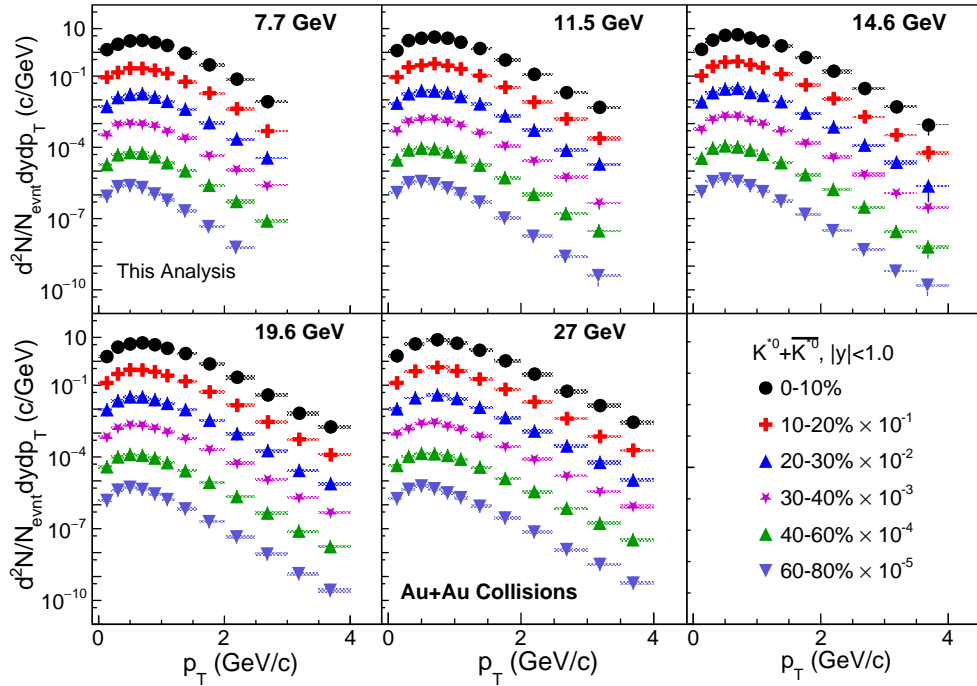


Figure 5.5: The K^{*0} meson transverse momentum (p_T) spectra at mid-rapidity ($|y| < 1$) are shown for various collision centrality intervals in Au+Au collisions at $\sqrt{s_{NN}} = 7.7, 11.5, 14.5, 19.6, 27$, and 39 GeV. Both statistical and systematic uncertainties are smaller than the marker size. These results are not published or approved as STAR preliminary and are currently under review within the collaboration.

Following the methods outlined in section 3.4, the raw yield is obtained in various p_T bins and centrality intervals for different collision energies to obtain the raw p_T spectra. These spectra are then corrected for the number of events (N_{events}), detector acceptance \times reconstruction efficiency ($\epsilon_{acc \times rec}$), particle identification efficiency (ϵ_{PID}),

and branching ratio (BR), resulting in the final corrected p_T spectra. The Correction factors are already described in section 3.5 and 5.6. Hence the expression of the final corrected spectra is as follows.

$$\frac{d^2N}{dp_T dy} = \frac{1}{N_{\text{evt}}} \times \frac{N^{\text{raw}}}{dy dp_T} \times \frac{1}{\epsilon_{\text{acc} \times \text{rec}} \times \epsilon_{\text{PID}} \times \text{BR}}, \quad (5.7.1)$$

Figure 3.19 displays the K^{*0} p_T spectra at mid rapidity ($|y| < 1.0$) for various collision centrality intervals in Au+Au collisions at $\sqrt{s_{\text{NN}}} = 7.7\text{--}39$ GeV. Some of the p_T spectra have been scaled for clarity. The solid and dashed lines represent the fit to the data points, while the dotted lines indicate the low p_T extrapolation.

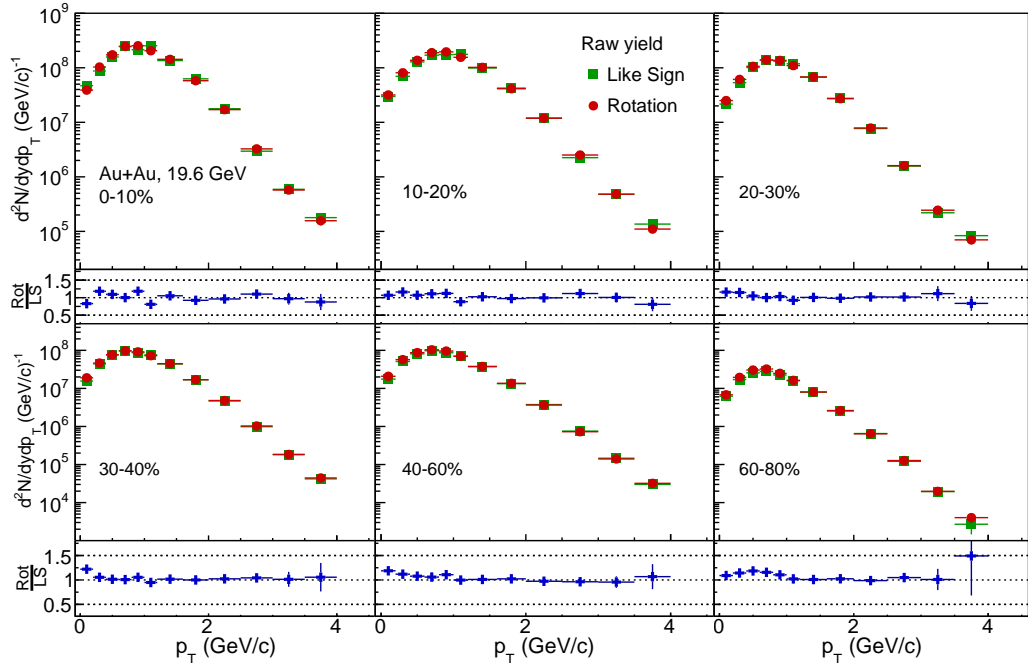


Figure 5.6: Comparison between like sign and track rotation method of background estimation for K^{*0} meson at Au+Au 19.6 GeV. Error bars shown are statistical only and within marker size.

After obtaining the corrected p_T spectra it is compared with that of BES-I. The results are consistent within uncertainties. The comparison plot has been kept in Appendix 5.13

Fig 5.13 shows the comparison between the corrected spectra obtained by considering both "Like-sign" and "Track-rotation" method. The results are consistent within 10-15%, that is comparable with the systematic uncertainty on the p_T spectra.

5.7.2 Mid-rapidity particle yield

The final yield per unit rapidity, dN/dy , for the K^{*0} meson is obtained by integrating the measured p_T spectra for different collision energies and centrality classes. The increased statistics and enhanced particle identification (PID) in BES-II have improved signal extraction, especially in the lower p_T region. Consequently, the lowest p_T range in BES-II spectra is now 0.0–0.2 GeV/c (compared to 0.4–0.6 GeV/c in BES-I measurements). This eliminates the need for low- p_T extrapolation in dN/dy calculations and reduces systematic uncertainties by avoiding contributions from extrapolated data.

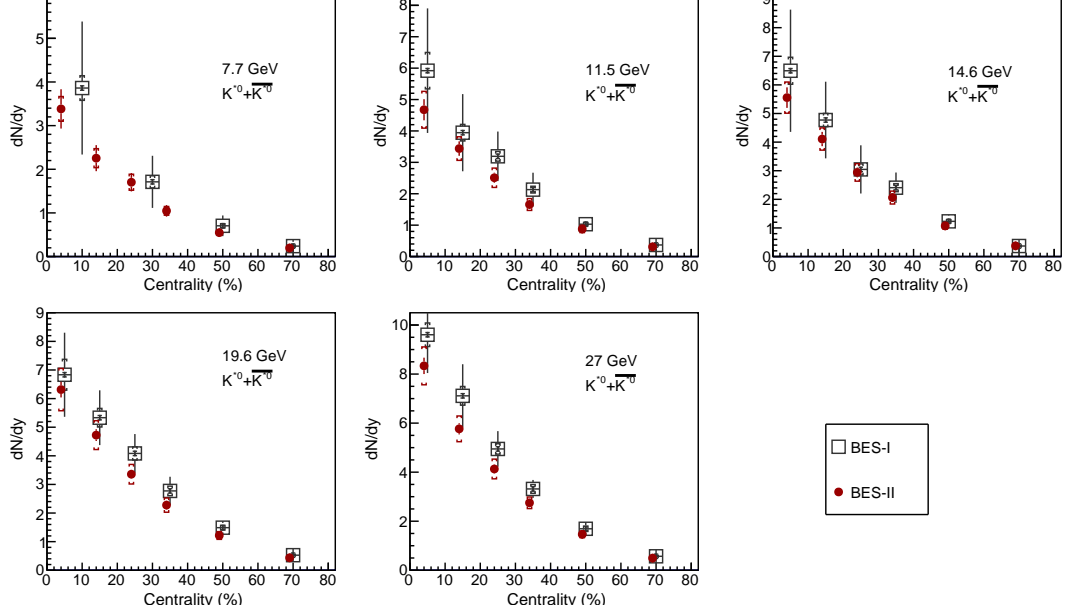


Figure 5.7: The mid-rapidity p_T -integrated yield of K^{*0} meson as a function of centrality for Au+Au collisions at $\sqrt{s_{NN}} = 7.7$ -27 GeV. The BES-II results are shown with red markers and compared with that of BES-I presented by gray markers. The statistical and systematic uncertainties are denoted by vertical bars and caps respectively.

Figure 5.7 presents a comparison of the mid-rapidity K^{*0} meson yield between the BES-I and BES-II data sets. With the enhanced statistics in BES-II, the statistical uncertainties in the yield measurements have been significantly reduced by a factor of 3-5, offering more precise measurements.

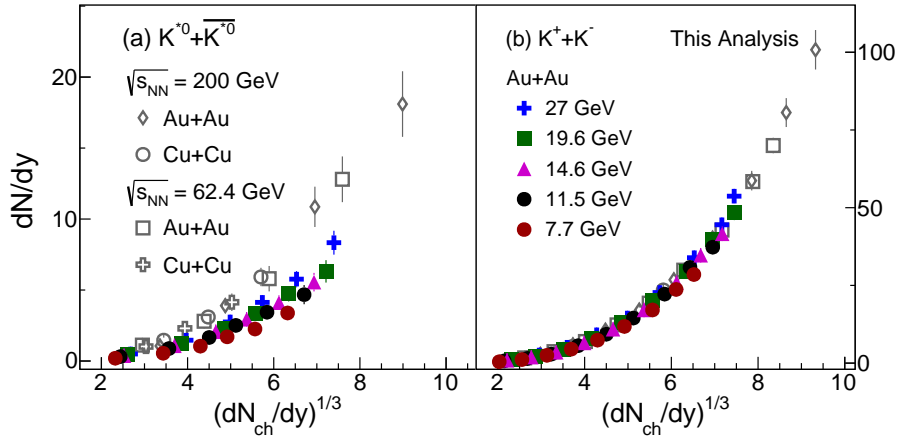


Figure 5.8: The mid-rapidity p_T -integrated yield of K^{*0} (left panel) and charged kaons (right panel) is shown as a function of multiplicity or $(dN_{ch}/dy)^{1/3}$ for different collision systems and center of mass energies [15,26,40,41]. The error bars displayed represent the quadrature sum of statistical and systematic uncertainties. The BES-II K^{*0} results are not published or approved as STAR preliminary and are currently under review within the collaboration.

Figure 5.8 presents the yields of K^{*0} mesons ($K^{*0} + \overline{K^{*0}}$) and charged kaons ($K^+ + K^-$) as a function of multiplicity for various collision systems and center-of-mass energies available at RHIC [12, 15, 26, 39–41]. Here, the multiplicity, or $(dN_{ch}/dy)^{1/3}$,

serves as an proxy of system size [160]. As detailed earlier in Chapter 3, the multiplicity is calculated as the sum of mid-rapidity yields of π^\pm , K^\pm and $p(\bar{p})$. The kaon yield shown in the left panel of 5.8 taken from previously published results [15, 26, 40, 41].

Here the particle of interest, K^{*0} and K , both are mesons with nearly similar quark content (assuming similar masses for up and down quarks), one would expect similar production mechanisms for both particles. Across all collision systems and beam energies, both K^{*0} and K meson yields increase with $(dN_{ch}/dy)^{1/3}$. While the charged kaon dN/dy displays a continuous dependence on $(dN_{ch}/dy)^{1/3}$ across different collision systems and energies attains an approximate multiplicity scaling, the K^{*0} yield shows a different behavior. For energies above 62.4 GeV, the K^{*0} yield trends smoothly with $(dN_{ch}/dy)^{1/3}$, much like the charged kaon. However, at energies below 62.4 GeV, the approximate multiplicity scaling breaks and the K^{*0} yield decreases with decreasing energy for a given system size or $(dN_{ch}/dy)^{1/3}$. Similar effects has already been observed in transport model studies [43, 44] and well discussed in the previous chapter 2, where the decrease in K^{*0} yield at lower energies as compared to higher energies, at similar multiplicity bin is attributed to enhanced loss in the K^{*0} due to increased rescattering effects at lower collision energies.

5.7.3 K^{*0}/K ratio

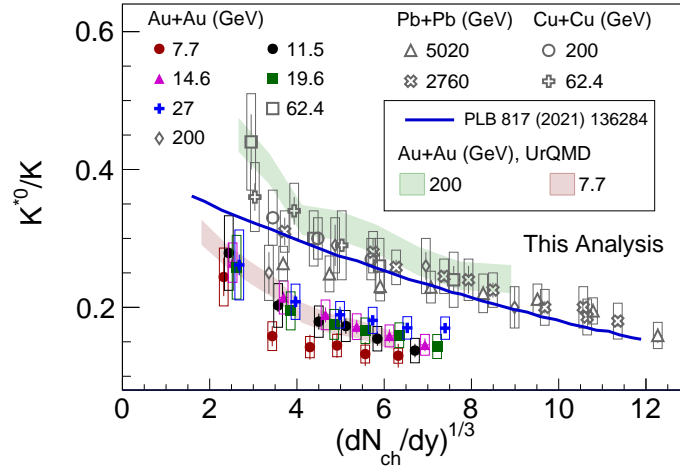


Figure 5.9: K^{*0}/K ratio as a function of multiplicity or $(dN_{ch}/dy)^{1/3}$ in Au+Au collisions at $\sqrt{s_{NN}} = 7.7\text{-}27$ GeV. The measurements are compared with previous experimental results [12, 14, 28]. The statistical and systematic uncertainties are shown by error bars and boxes respectively. The model calculation (blue solid line) has been taken from [42]. UrQMD results for $\sqrt{s_{NN}} = 7.7$ and 200 GeV Au+Au collisions are shown in colored bands and taken from [43]. The BES-II K^{*0} results are not published or approved as STAR preliminary and are currently under review within the collaboration.

As discussed in previous chapters, it is evident that short-lived resonances, such as the K^{*0} meson, are good probes for examining in-medium dynamics, such as processes like rescattering and regeneration. The BES-I measurements, described in section 3.7.5 of chapter 3, hinted at a decrease in the resonance-to-non-resonance ratio (K^{*0}/K) with increasing particle multiplicity. However, those measurements lacked statistical significance.

Figure 5.9 presents the K^{*0}/K ratio as a function of multiplicity across different collision energies at BES energies. With improved statistical precision in the BES-II dataset, it is now observable that the K^{*0}/K ratio in central collisions is significantly lower than in peripheral collisions, with a significance level ranging from 1.64 to 3.34σ . This suppression of the K^{*0}/K ratio in central heavy-ion collisions suggests that hadronic rescattering dominates over regeneration processes in central heavy-ion collisions. Additionally, for the first time at STAR, a suppression of the resonance-to-non-resonance ratio in central collisions compared to peripheral collisions has been observed at a significance level exceeding 3σ .

From Fig. 5.9, an approximate scaling of the K^{*0}/K ratio at the top RHIC and LHC energies is observed, showing little dependence on the collision system or center-of-mass energy. However, as collision energy decreases into the BES regime, the K^{*0}/K ratio drops significantly relative to higher energies. The BES-I measurements [39] reported in chapter 3 shows a similar trend, but the experimental uncertainties were too large to draw firm conclusions. With the precise BES-II measurement, the deviation of the K^{*0}/K ratio from approximate multiplicity scaling is more evident. This reduction in K^{*0}/K at lower energies suggests that even for comparable multiplicity or system size, the impact of rescattering processes varies with collision energy.

Earlier phenomenological models, which primarily consider interactions of K^{*0} and K mesons with light mesons in the hadronic medium, describes the multiplicity dependence of the K^{*0}/K ratio at 200 GeV and above [42]. This implies that, at high energies, rescattering is predominantly driven by meson-meson interactions. Transport model study, using the UrQMD model, that has been described in detail in the previous chapter has qualitatively reproduced the decreasing trend of the K^{*0}/K ratio observed both at BES as well as top-RHIC energies. The comparison between the model and data suggests that at lower collision energies, where the baryon-to-meson ratio is higher compared to higher energies, meson-baryon interactions dominate over meson-meson interactions. This dominance leads to an increased rescattering effect, reducing the measured K^{*0} yield.

These findings indicate that within baryon-rich environments at lower energies, the K^{*0} resonance undergoes significant hadronic rescattering compared to meson-rich environments at higher energies. However, further theoretical studies are needed to fully understand these results and explore other potential factors contributing to the observed trends in the K^{*0}/K ratio.

In Fig 5.10, the K^{*0}/K ratio is presented as a function of collision energy, alongside comparisons to predictions from both thermal and UrQMD models, as detailed in ref [43, 44]. In ref [44], it has been shown that, the thermal model, that does not incorporate final-state rescattering effects, provides a reasonable description of the ϕ/K ratio. However, it significantly overestimates the K^{*0}/K ratio in central collisions by $6.2\text{--}7.8\sigma$, while remaining consistent with data from peripheral collisions.

Conversely, the transport model, such as UrQMD, which includes in-medium interactions between particles, shows a closer match to the central collision data, successfully reflecting the influence of strong rescattering effects on the K^{*0}/K ratio. Such model to data comparison also supports the picture of stronger hadronic rescattering in central as compared to that in peripheral collisions.

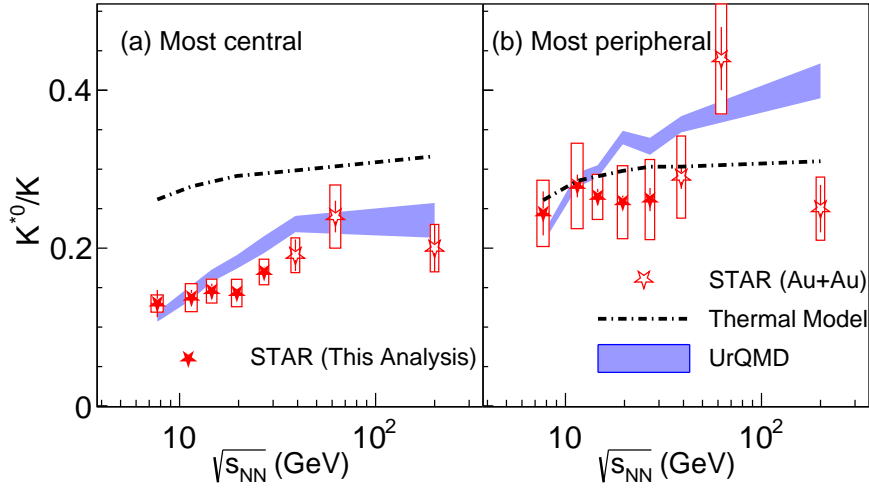


Figure 5.10: Collision energy dependence of K^{*0}/K ratio in Au+Au collisions in most central (left panel) and most peripheral (right panel) collisions. The results are compared with thermal model (dashed line) and transport model (blue band), taken from ref [43, 44]. The BES-II K^{*0} results are not published or approved as STAR preliminary and are currently under review within the collaboration.

5.7.4 Nuclear modification factor (R_{CP})

The nuclear modification factor, R_{CP} (ratio of central-to-peripheral), is one of the important observable in studying the medium effects in heavy-ion collisions [170]. It is sensitive to both the size and density of the medium created in these collisions, serving as an useful tool for probing the partonic energy loss within this medium. It is defined as the p_T differential ratio of the particle yield in central to that of peripheral collisions, scaled with the average in-elastic binary collisions, which is expressed as follows:

$$R_{cp} = \frac{(d^2N/dydp_T)/\langle N_{coll} \rangle_{0-10\%}}{(d^2N/dydp_T)/\langle N_{coll} \rangle_{60-80\%}} \quad (5.7.2)$$

Here, $\langle N_{coll} \rangle$ represents the average number of inelastic binary collisions for a given centrality class, obtained from Monte Carlo Glauber simulations [40] and serves as a normalization factor, allowing a meaningful comparison between central and peripheral collisions by accounting for the difference in collision frequency. Values of $\langle N_{coll} \rangle$ for various centralities and center-of-mass energies can be found in the Appendix section.

If nucleus-nucleus collisions were simply a sum of independent nucleon-nucleon collisions, then R_{CP} would equal one. Any deviation of R_{CP} from unity, however, signals contributions from nuclear or in-medium effects. Values significantly above or below one can indicate the presence of phenomena such as partonic energy loss, shadowing, or enhancement effects [27, 170].

Fig 5.11 shows the R_{CP} values of the K^{*0} meson in comparison with Λ baryons, K_s^0 , and ϕ mesons. It can be seen that for all particle types shown, the R_{CP} values exceed 1 as collision energy decreases, suggesting that partonic energy loss becomes less influential, while cold nuclear effects (such as enhancement at intermediate p_T or the Cronin effect) become more prominent. Similar behavior is observed in other identified hadrons like π^\pm , K^\pm , and $p(\bar{p})$. Additionally, at low p_T , the R_{CP} of the K^{*0} meson is smaller than

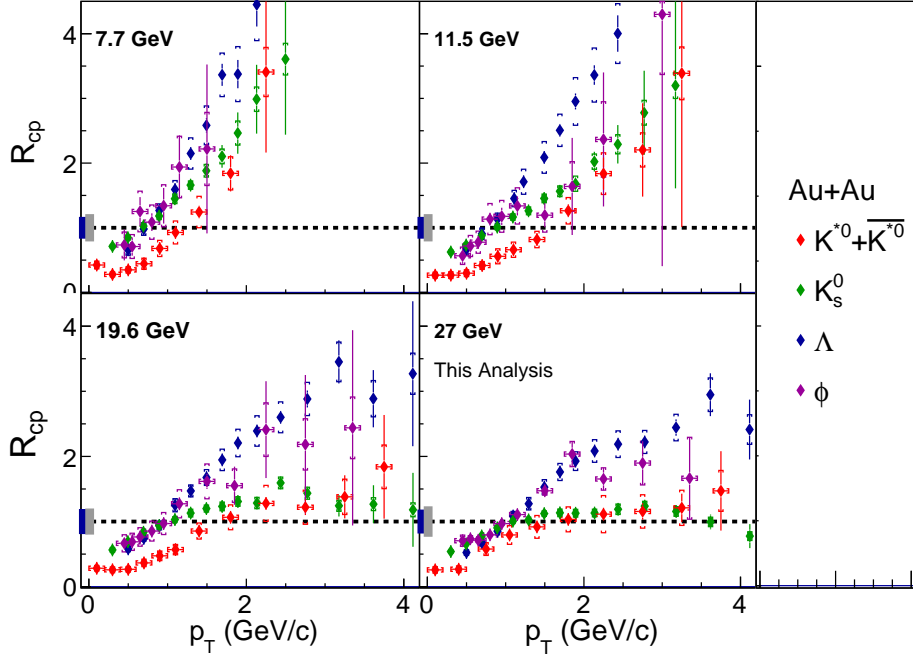


Figure 5.11: Nuclear modification factor (R_{cp}) of K^{*0} , K_s^0 , Λ and ϕ for Au+Au collisions at $\sqrt{s_{NN}} = 7.7, 11.5, 19.6$ and 27 GeV. The R_{cp} values for K_s^0 , Λ and ϕ are from BES-I measurements, taken from ref [27]. The results for K^{*0} meson is obtained within $|y| < 1.0$ with for other particles the calculation is done within $|y| < 0.5$. The vertical error bars represent statistical uncertainties, while caps indicate systematic uncertainties. On the left of each panel, the uncertainty in N_{coll} scaling for R_{cp} measurement in BES-I and BES-II is shown by gray and blue bands at unity. The BES-II K^{*0} results are not published or approved as STAR preliminary and are currently under review within the collaboration.

that of longer-lived hadrons like Λ , K_s^0 , and ϕ . This is consistent with the picture of dominant hadronic rescattering particularly at low p_T region.

5.7.5 Rapidity dependent K^{*0} yield

With the iTPC upgrade for the BES-II data sets, the pseudorapidity range for charged particle selection has expanded to $|\eta| < 1.5$. This, coupled with the higher statistics, has enabled rapidity-differential measurements. Figure 5.12 presents the rapidity spectra of the K^{*0} meson in Au+Au collisions at $\sqrt{s_{NN}} = 7.7$ – 27 GeV. Tracking efficiency and p_T spectra related to these measurements are provided in the appendix 5.9.3 and 5.9.4. Due to limited statistics at 7.7 and 11.5 GeV and the absence of the iTPC upgrade in the 27 GeV data set, the distribution is shown only up to $|y| < 1.0$. However, a clear dependence on rapidity and centrality is observed across BES energies. Future detailed studies will help to further explore rapidity-dependent in-medium dynamics.

5.8 Summary

To conclude, the analysis of K^{*0} meson production in Au+Au collisions at $\sqrt{s_{NN}} = 7.7, 11.5, 14.6, 19.6$, and 27 GeV is presented using high-statistics BES-II data sets. The

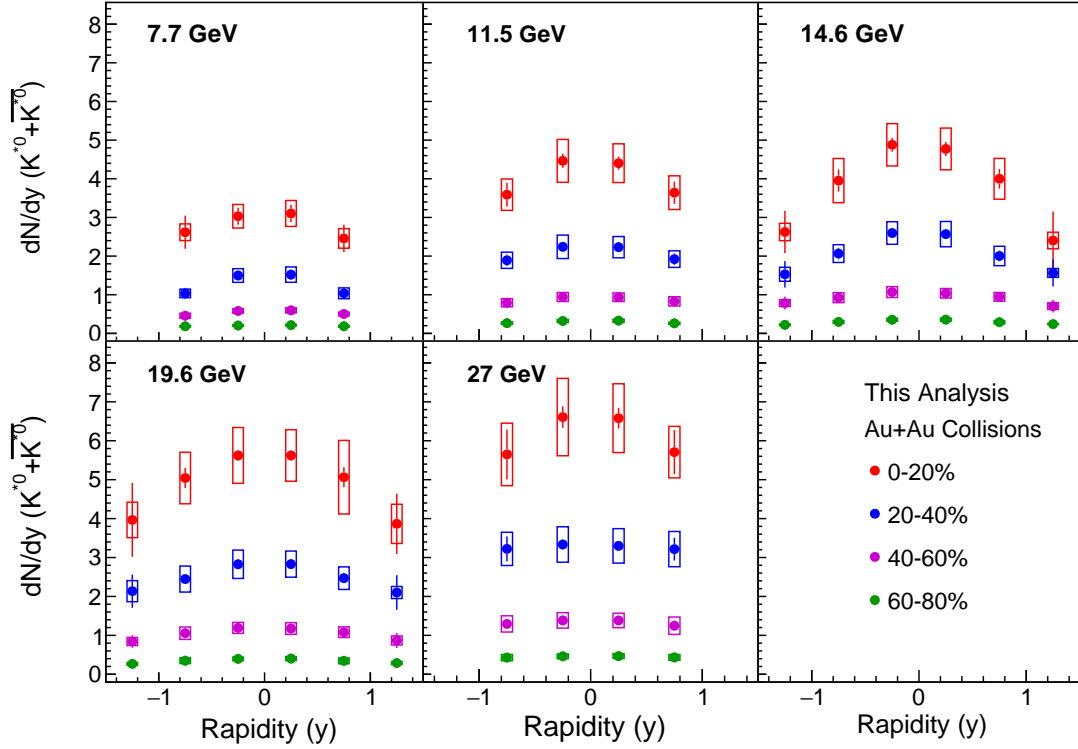


Figure 5.12: K^{*0} yield as a function of rapidity for different centralities and center of mass energies. The vertical error bars represent statistical uncertainties, while caps indicate systematic uncertainties. These results are not published or approved as STAR preliminary and are currently under review within the collaboration.

results include p_T spectra, dN/dy , particle ratios, nuclear modification factors, and rapidity spectra. The suppression of the K^{*0}/K ratio in central collisions, compared to peripheral collisions, indicates the dominance of hadronic rescattering experienced by the decay daughters of the K^{*0} meson within the hadronic phase created in heavy-ion collisions. This suppression is found to be greater than 3σ . The suppression of the K^{*0}/K ratio is more pronounced at BES energies compared to top RHIC or LHC energies, even with similar system multiplicities. Further comparison with transport model studies reveals differences in the hadronic interactions within the medium created in low- and high-energy collisions. Additionally, the R_{cp} values for the K^{*0} meson are found to be lower compared to Λ baryon, K_s^0 , and ϕ mesons, indicating dominant hadronic rescattering at the low p_T region. Finally, the rapidity spectra of the K^{*0} meson are presented for different centralities at BES energies.

5.9 Appendix

5.9.1 K^{*0} p_T spectra comparison between BES-I and BES-II

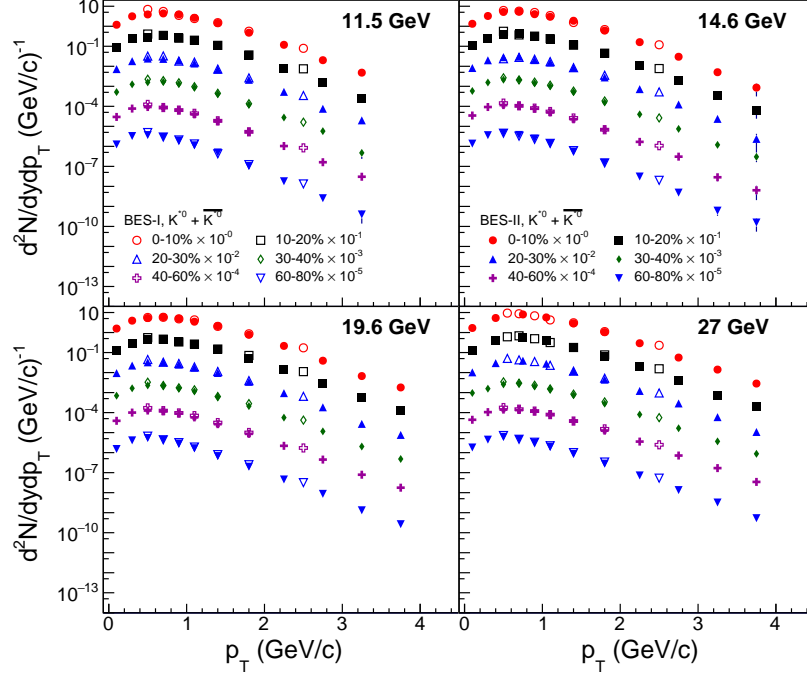


Figure 5.13: Comparison of The K^{*0} meson transverse momentum (p_T) spectra at mid-rapidity ($|y| < 1.0$) for BES-I and BES-II data sets. The error bars shown here are statistical only and are within the marker size.

5.9.2 Significance of K^{*0}/K suppression

Table 5.4: Level of suppression of K^{*0}/K ratio in central collisions w.r.t peripheral collisions or thermal model predictions.

Suppression of K^{*0}/K ratio in central collisions		
Au+Au, $\sqrt{s_{NN}}$	w.r.t peripheral colisions	w.r.t thermal model
7.7 GeV	2.10σ	6.44σ
11.5 GeV	2.37σ	6.94σ
14.6 GeV	3.39σ	7.81σ
19.6 GeV	2.27σ	8.03σ
27 GeV	1.64σ	7.10σ

5.9.3 Efficiency \times Acceptance

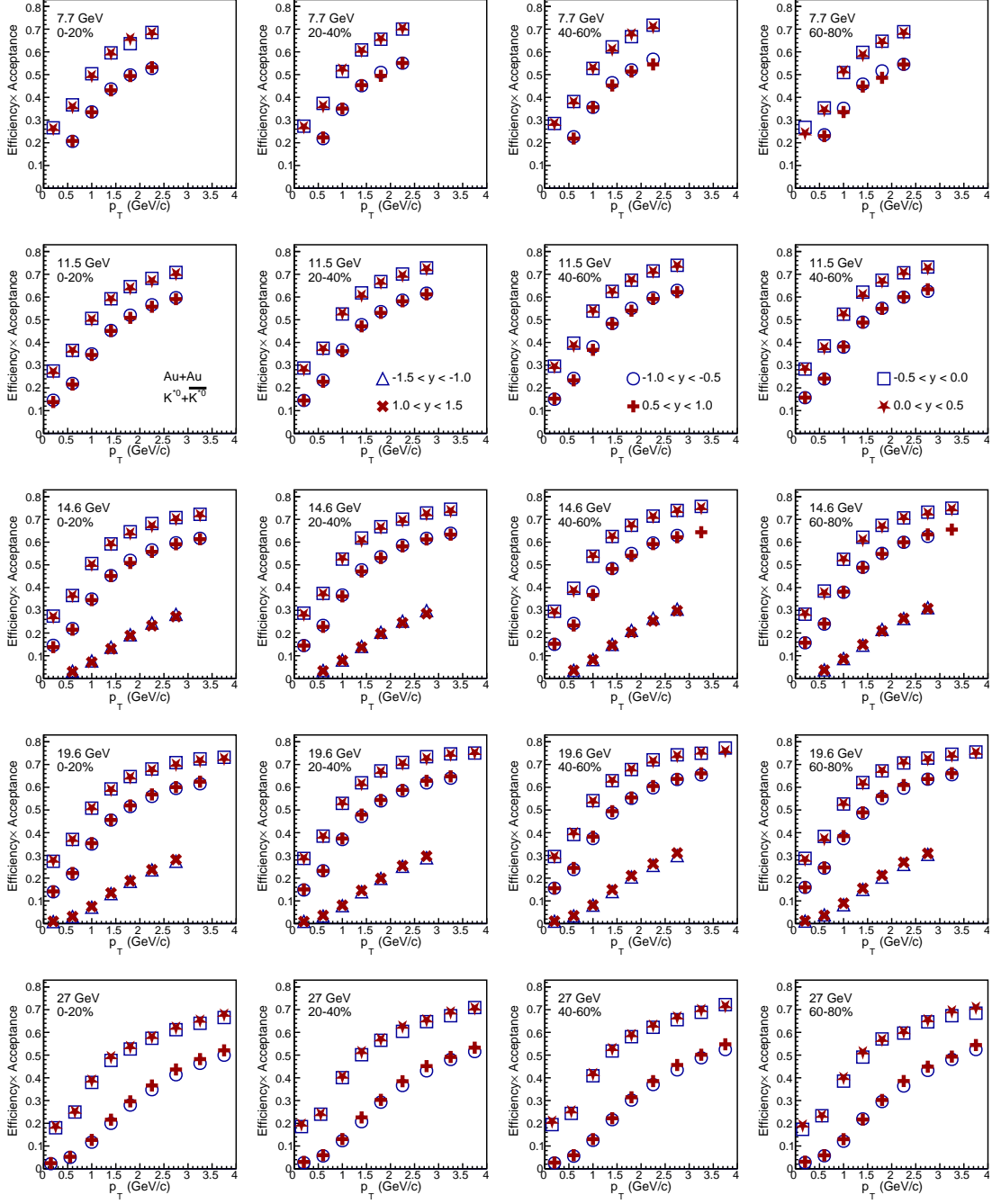


Figure 5.14: The tracking efficiency \times acceptance for the K^{*0} meson is presented across different centralities, rapidities, and collision energies, ranging from $\sqrt{s_{NN}} = 7.7$ -27 GeV for Au+Au collisions. The statistical errors are within the marker size.

5.9.4 Corrected p_T spectra for different rapidity bins

A. Au+Au, $\sqrt{s_{NN}} = 7.7$ GeV

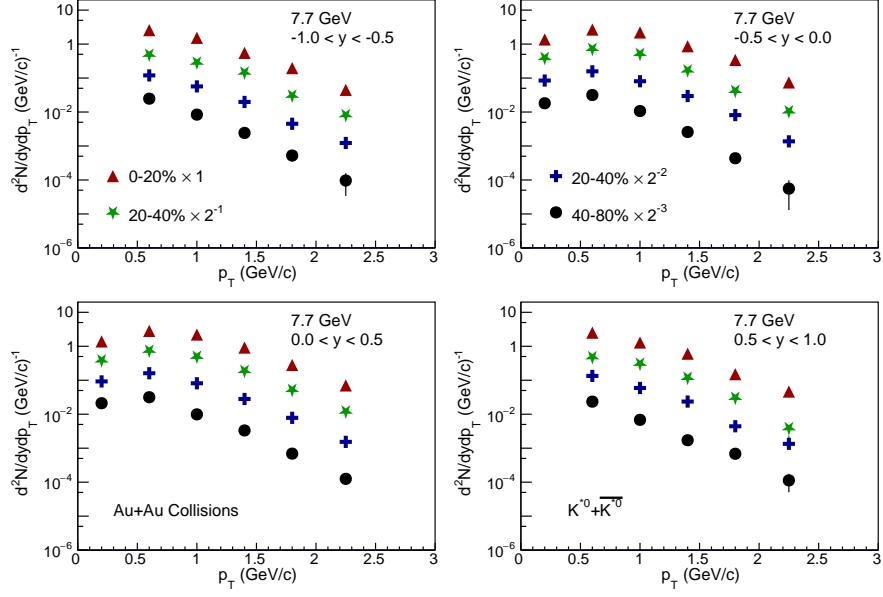


Figure 5.15: The corrected p_T spectra for K^{*0} meson in different rapidity bins for Au+Au collisions, $\sqrt{s_{NN}} = 7.7$ GeV. The error bars shown here are statistical only.

B. Au+Au, $\sqrt{s_{NN}} = 11.5$ GeV

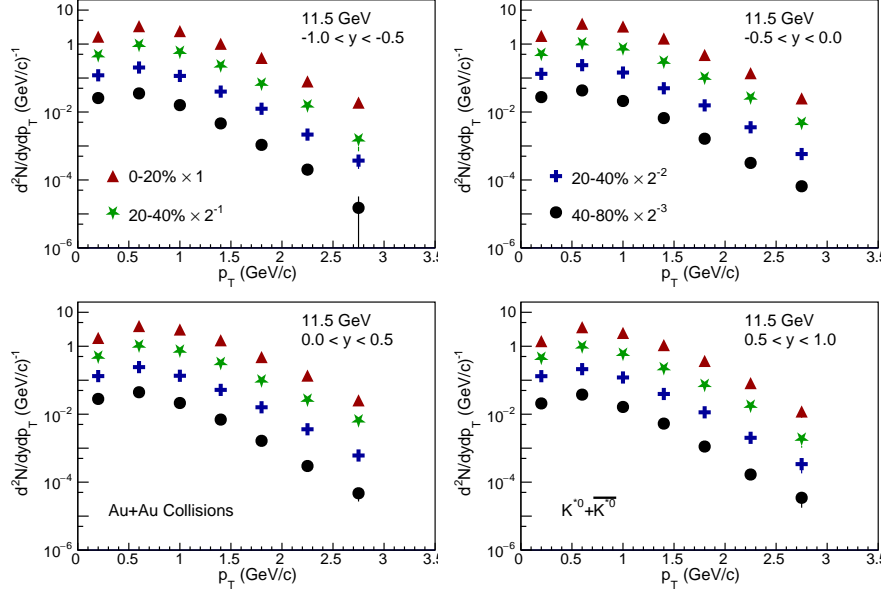


Figure 5.16: The corrected p_T spectra for K^{*0} meson in different rapidity bins for Au+Au collisions, $\sqrt{s_{NN}} = 11.5$ GeV. The error bars shown here are statistical only.

C. Au+Au, $\sqrt{s_{NN}} = 14.6$ GeV

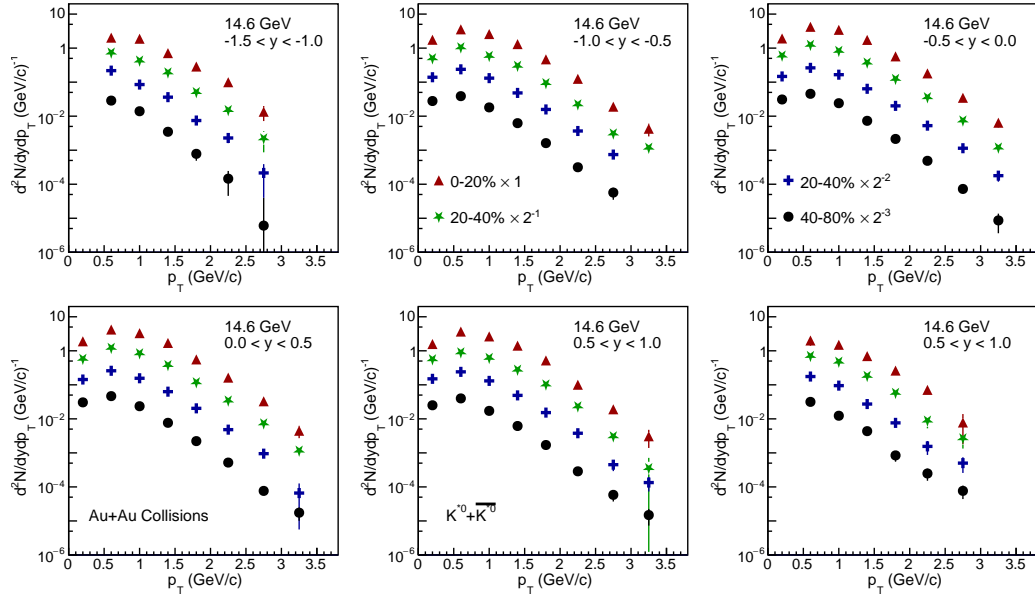


Figure 5.17: The corrected p_T spectra for K^{*0} meson in diferent rapidity bins for Au+Au collisions, $\sqrt{s_{NN}} = 14.6$ GeV. The error bars shown here are statistical only.

D. Au+Au, $\sqrt{s_{NN}} = 19.6$ GeV

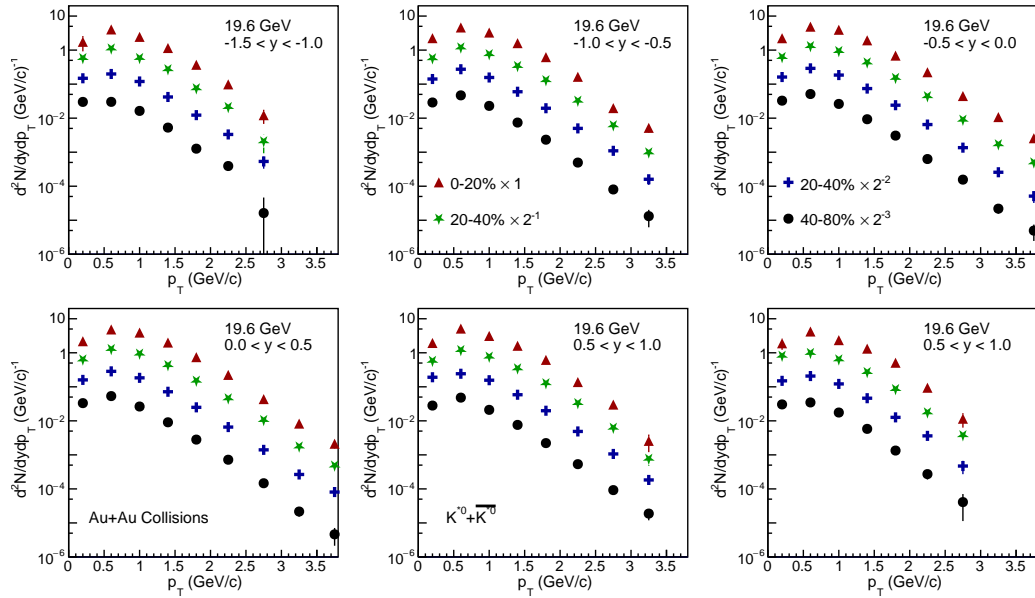


Figure 5.18: The corrected p_T spectra for K^{*0} meson in diferent rapidity bins for Au+Au collisions, $\sqrt{s_{NN}} = 19.6$ GeV. The error bars shown here are statistical only.

E. Au+Au, $\sqrt{s_{NN}} = 27$ GeV

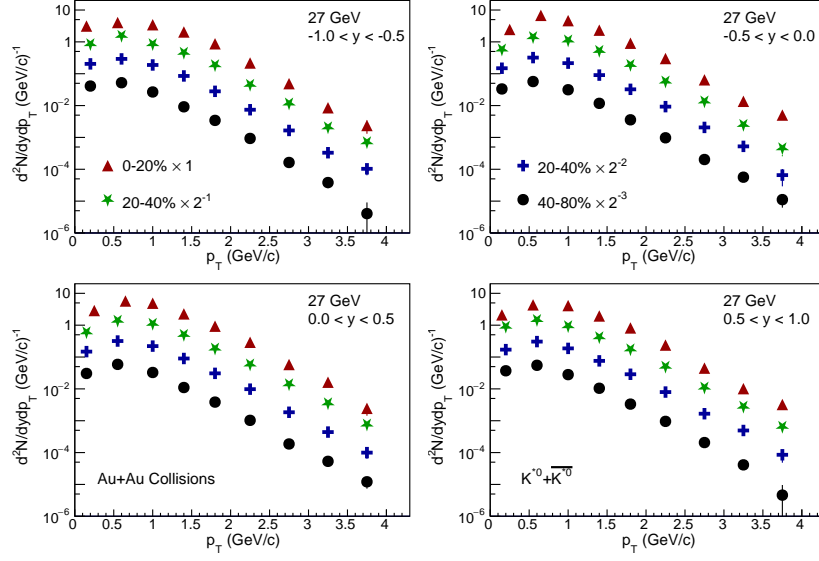


Figure 5.19: The corrected p_T spectra for K^{*0} meson in different rapidity bins for Au+Au collisions, $\sqrt{s_{NN}} = 27$ GeV. The error bars shown here are statistical only.

5.9.5 Reference multiplicity, Average multiplicity $((dN_{ch}/dy)^{1/3})$, $\langle N_{part} \rangle$ and $\langle N_{coll} \rangle$ for BES-II data sets

Table 5.5: Average multiplicity $(dN_{ch}/dy)^{1/3}$ values for different collision energies.

$(dN_{ch}/dy)^{1/3}$ values for different collision energies (BES-II data sets)					
Centrality	7.7 GeV	11.5 GeV	14.6 GeV	19.6 GeV	27 GeV
0-10%	6.321	6.705	6.934	7.212	7.396
10-20%	5.565	5.844	6.120	6.346	6.528
20-30%	4.918	5.120	5.370	5.567	5.735
30-40%	4.296	4.501	4.655	4.854	4.987
40-60%	3.433	3.567	3.695	3.856	3.967
60-80%	2.322	2.438	2.525	2.616	2.677

The Reference multiplicity, $\langle N_{part} \rangle$ and $\langle N_{coll} \rangle$ information for BES-II collider mode data sets has been collected from following links

Au+Au 7.7 GeV : https://drupal.star.bnl.gov/STAR/system/files/Centrality_7p7GeV_ver2.pdf

Au+Au 11.5 GeV : https://drupal.star.bnl.gov/STAR/system/files/11.5_GeV_centrality_Zhiwan_upd_v7.pdf

Au+Au 14.6 GeV : https://drupal.star.bnl.gov/STAR/system/files/ShuaiZhou_CentralityStudy_20220809.pdf

Au+Au 19.6 GeV : https://drupal.star.bnl.gov/STAR/system/files/19p6GeVCentrality_v1.pdf

Au+Au 27 GeV : https://drupal.star.bnl.gov/STAR/system/files/CentralityDefinition_Run18_27GeV_ZaochenYe_20190930.pdf

Table 5.6: Reference multiplicity or N_{ch}^{raw} values for different collision energies for BES-II data sets.

N_{ch}^{raw} values for different collision energies (BES-II data sets)					
Centrality	7.7 GeV	11.5 GeV	14.6 GeV	19.6 GeV	27 GeV
0-5%	201	247	270	296	295
5-10%	164	204	223	243	241
10-20%	112	140	154	165	168
20-30%	74	94	103	110	113
30-40%	47	61	67	70	72
40-50%	28	37	41	43	44
50-60%	16	21	24	24	25
60-70%	8	11	13	13	13
70-80%	4	6	6	6	6

Table 5.7: $\langle N_{part} \rangle$ values for different collision energies for BES-II data sets.

$\langle N_{part} \rangle$ values for different collision energies (BES-II data sets)					
Centrality	7.7 GeV	11.5 GeV	14.5 GeV	19.6 GeV	27 GeV
0-5%	336 ± 2	338 ± 2	339 ± 2	340 ± 3	340 ± 2
5-10%	288 ± 7	288 ± 6	289 ± 6	289 ± 7	291 ± 6
10-20%	224 ± 9	224 ± 8	226 ± 8	225 ± 9	227 ± 9
20-30%	158 ± 10	158 ± 9	160 ± 10	160 ± 11	160 ± 10
30-40%	109 ± 10	109 ± 10	110 ± 11	110 ± 11	111 ± 11
40-50%	72 ± 10	72 ± 10	72 ± 11	73 ± 10	73 ± 10
50-60%	45 ± 8	45 ± 9	45 ± 9	46 ± 8	45 ± 10
60-70%	26 ± 7	26 ± 7	26 ± 7	27 ± 7	27 ± 8
70-80%	14 ± 4	14 ± 6	14 ± 5	15 ± 5	15 ± 5

Table 5.8: $\langle N_{coll} \rangle$ values for different collision energies for BES-II data sets.

$\langle N_{coll} \rangle$ values for different collision energies (BES-II data sets)					
Centrality	7.7 GeV	11.5 GeV	14.5 GeV	19.6 GeV	27 GeV
0-5%	781 ± 28	792 ± 25	805 ± 29	820 ± 27	840 ± 27
5-10%	632 ± 20	637 ± 20	658 ± 20	656 ± 19	677 ± 19
10-20%	454 ± 23	457 ± 23	466 ± 24	470 ± 24	486 ± 25
20-30%	285 ± 24	287 ± 23	294 ± 25	296 ± 26	304 ± 26
30-40%	173 ± 22	175 ± 22	177 ± 23	180 ± 25	184 ± 24
40-50%	99 ± 18	100 ± 18	101 ± 20	103 ± 19	105 ± 19
50-60%	53 ± 13	53 ± 14	54 ± 14	55 ± 13	55 ± 15
60-70%	27 ± 9	27 ± 9	27 ± 9	28 ± 9	30 ± 10
70-80%	13 ± 5	12 ± 6	12 ± 6	13 ± 6	13 ± 5

Chapter 6

Studying effect of hadronic rescattering on flow observables using a transport based model

The discussions in chapters 3,4 and 5 explored the impact of hadronic interactions on the yield of resonance particles. Recent model calculations also indicate that the flow of K^{*0} mesons can be influenced by hadronic re-scattering [171]. This chapter, extends this analysis to examine the effect of hadronic re-scattering on the directed flow (v_1) of identified hadrons across RHIC Beam Energy Scan energies ($\sqrt{s_{NN}} = 7.7-39$ GeV) using the UrQMD model. Additionally, we investigate the differences in directed flow between particles and their corresponding anti-particles in the context of hadronic re-scattering.

6.1 Introduction

Relativistic heavy-ion collisions offer insights into nuclear matter under extreme conditions [6, 130–132]. The collective motion of particles emitted from these collisions is of particular interest as it reflects the equation of state in the early reaction stages [172–174]. In such events, the initial geometric anisotropies are transformed into momentum-space anisotropies due to medium expansion. Directed flow (v_1) represents the first-order harmonic in the Fourier expansion of the particle distribution relative to the reaction plane ψ_{RP} in momentum space. The Fourier expansion is given by:

$$\frac{d^2 N}{dy d\phi} = \frac{dN}{dy} \left(1 + \sum_{n=1}^{\infty} (2v_n \cos(\phi - \psi_{RP})) \right) \quad (6.1.1)$$

Here, y denotes the longitudinal rapidity, and ϕ is the azimuthal angle of an emitted particle.

The parameter v_n represents the magnitude of the n^{th} order flow coefficient, which quantifies the anisotropy in particle distribution, and ψ_{RP} refers to the corresponding reaction plane.

Typically, v_1 is presented as a function of rapidity (y) or pseudorapidity (η), though its dependence on transverse momentum (p_T) and collision centrality also provides additional physical insights.

Directed flow consists of two main components: an odd function of rapidity and an even function of rapidity. Fluctuations in the initial energy density can generate a rapidity-even directed flow component, v_1^{even} , which is uncorrelated with the reaction plane angle. In contrast, in non-central collisions, the initial state is expected to tilt, disrupting forward-backward symmetry and producing a rapidity-antisymmetric directed flow component, commonly referred to as v_1^{odd} . This v_1^{odd} component reflects the system's longitudinal evolution by capturing its tilt relative to the collision axis. To describe rapidity dependence, dv_1/dy near mid-rapidity is often reported. This chapter will focus primarily on the odd component of directed flow, henceforth denoted as v_1 .

Directed flow (v_1) has long been measured at various heavy-ion collider facilities over a broad range of collision energies, from lower energies at AGS [175, 176] and intermediate energies at RHIC [177, 178], to higher energies at LHC [179]. Hydrodynamic models propose that the negative slope of charged particle v_1 can provide insights into the initial condition of the tilted source [180]. However, it is also essential to investigate v_1 for identified hadrons. Notably, the observed change in sign of net proton v_1 slope from negative to positive as one goes down from higher to lower collision energies has been suggested as a signal of sensitivity to changes in the QCD equation of state near the phase transition [181–183]. Additional hydrodynamic studies indicate that, at lower collision energies in a baryon-rich environment, analyzing the p_T -differential v_1 split between p and \bar{p} may help constrain the baryon diffusion coefficient in the strongly interacting medium [184].

In non-central heavy-ion collisions, a strong magnetic field is anticipated to arise due to the approaching spectators. This magnetic field is estimated to reach magnitudes $\approx 10^{18}$ Gauss and exists for only a brief period [185, 186]. Phenomenological studies suggest that such a magnetic field can induce notable differences in the directed flow of particles with opposite charges [187, 188]. Charm hadrons, such as D^0 and \bar{D}^0 , which are generated early in the collision process, are particularly well-suited to retain signatures of this electromagnetic field [187]. However, significant uncertainties in experimental data currently prevent firm conclusions [189, 190].

Recent findings from the STAR Collaboration show a noticeable difference in the v_1 slope between particles with opposite charges, depending on collision centrality and considering light hadrons (π^\pm , K^\pm , $p(\bar{p})$) [45]. The slope difference, $\Delta v_1/dy$, shifts from positive in central collisions to a marked negative in peripheral collisions, an effect more pronounced for protons than for kaons and pions. The positive slope could arise from transported quarks [191], while the negative slope is thought to reflect the initial electromagnetic field, where Faraday induction outweighs the Coulomb effect. Another STAR publication reports that $\Delta v_1/dy$ increases with differences in electric charge and strangeness between the particle types [192]. Together, these findings suggest that the v_1 splittings arise from a balance between the Hall effect and the combined Faraday induction and Coulomb effects. Recent hydrodynamic simulations, which incorporate baryon diffusion and realistic baryon stopping but exclude electromagnetic effects, reproduce the observed proton splits [193]. However, the models fall short in capturing the trends seen in kaons and pions, likely due to incomplete treatment of strangeness and charge conservation.

The later stages of heavy-ion collisions involve a significant hadronic phase. Experimental observations at RHIC-BES energies, such as the centrality-dependent ratios of resonant to non-resonant particles and deviations from constituent quark scaling in v_n coefficients, offer strong evidence for this hadronic phase. Recent hydrodynamic model calculations suggest that hadronic rescattering could result in a sign change in the v_1 slope for short-lived resonances, such as the

K^{*0} meson [171]. Thus, it is essential to examine the influence of this late-stage hadronic phase on experimental observables, like directed flow (v_1).

6.2 Analysis details

In this chapter, the effect of late-stage hadronic interactions on the rapidity-odd directed flow (v_1^{odd}) has been investigated using UrQMD transport model. The details about the model has been discussed in chapter 4. Further details on the model can be found in ref [164, 165]. In the current approach, the duration of the hadronic cascade time (τ) is controlled by adjusting model parameters, where a fixed τ represents an instantaneous freeze-out, and increasing τ allows for prolonged interactions within the system. The similar approach has been implemented to study the impact of hadronic interactions on the production of resonances at RHIC-BES energies [43, 44].

6.3 Results and Discussion

6.3.1 Directed flow (v_1) vs rapidity from UrQMD model

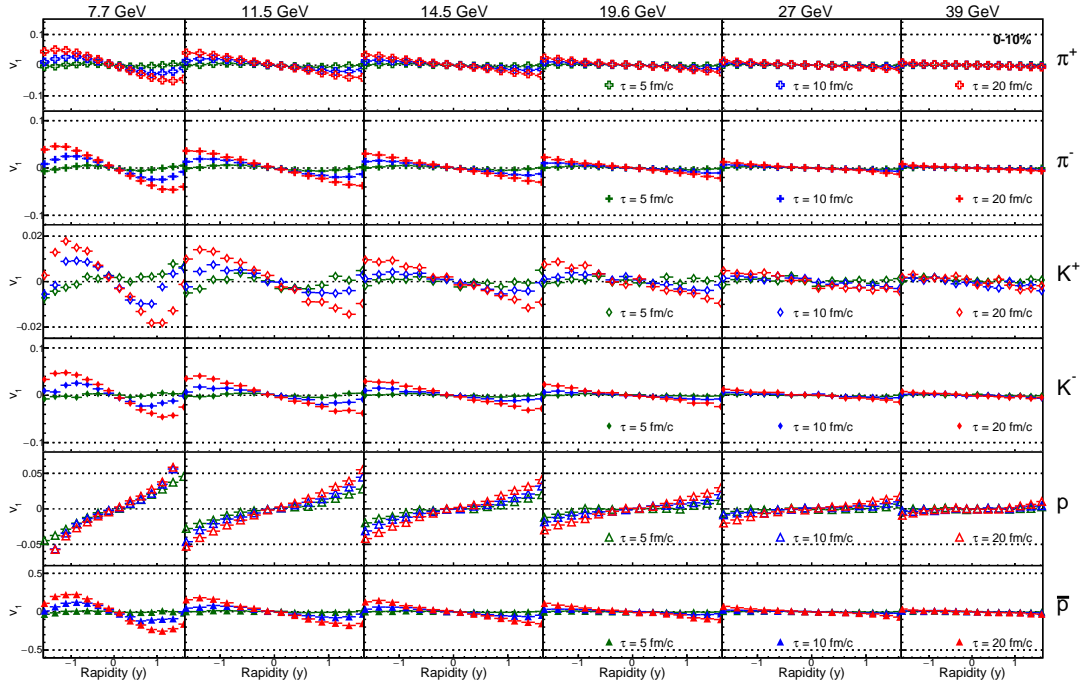


Figure 6.1: Directed flow (v_1) as a function rapidity (y) for identified hadrons (π^\pm , K^\pm , $p(\bar{p})$) in central (0-10%) Au+Au collisions at $\sqrt{s_{NN}} = 7.7, 11.5, 14.5, 19.6, 27$ and 39 GeV from UrQMD model. The results with different marker colors correspond to different hadronic cascade lifetime (τ) = 5, 10 and 20 fm/c.

Figures 6.1, 6.2, and 6.3 show the rapidity-dependent directed flow coefficient v_1 for various identified light-flavor hadrons, including π^\pm , K^\pm , $p(\bar{p})$, in Au+Au collisions at RHIC-BES energies ($\sqrt{s_{NN}} = 7.7-39$ GeV). The results are presented for different centrality ranges: 0-10%, 10-40%, and 40-80%. Each subplot uses distinct colors and markers to indicate results corresponding to various durations of hadronic cascade lifetimes (τ), ranging from 5 to 20 fm/c.

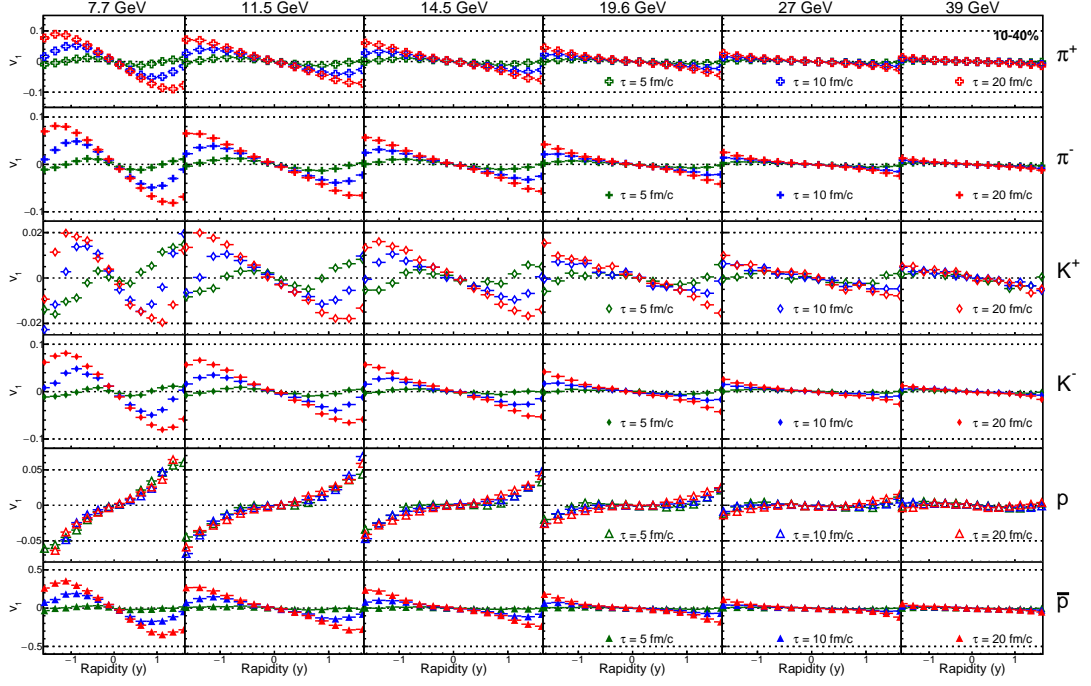


Figure 6.2: Directed flow (v_1) as a function rapidity (y) for identified hadrons (π^\pm , K^\pm , $p(\bar{p})$) in mid-central (10-40%) Au+Au collisions at $\sqrt{s_{NN}} = 7.7, 11.5, 14.5, 19.6, 27$ and 39 GeV from UrQMD model. The results with different marker colors correspond to different hadronic cascade lifetime (τ) = 5, 10 and 20 fm/c.

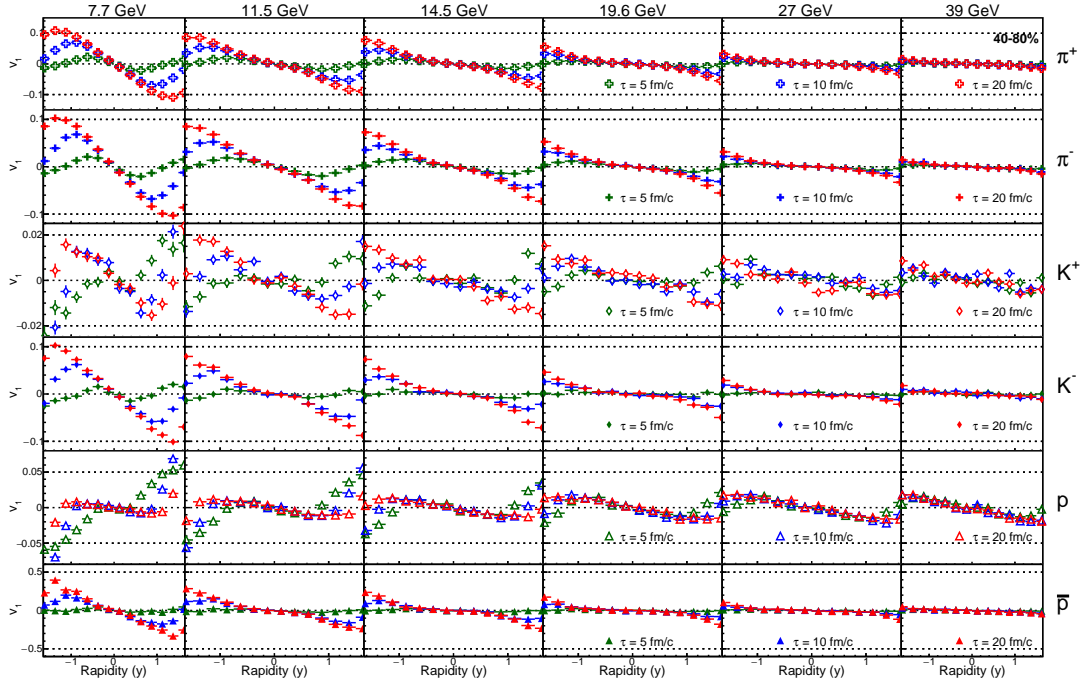


Figure 6.3: Directed flow (v_1) as a function rapidity (y) for identified hadrons (π^\pm , K^\pm , $p(\bar{p})$) in peripheral (40-80%) Au+Au collisions at $\sqrt{s_{NN}} = 7.7, 11.5, 14.5, 19.6, 27$ and 39 GeV from UrQMD model. The results with different marker colors correspond to different hadronic cascade lifetime (τ) = 5, 10 and 20 fm/c.

These results reveal that the magnitude of v_1 increases as the beam energy decreases, which aligns with expectations of more stopping near mid-rapidity at lower energies. With a longer hadronic cascade lifetime (τ), the produced particles have more opportunity for interactions among themselves, which enhances the development of directed flow. Consequently, a larger v_1 is observed with increasing τ values.

6.3.2 Collision energy and centrality dependence of dv_1/dy

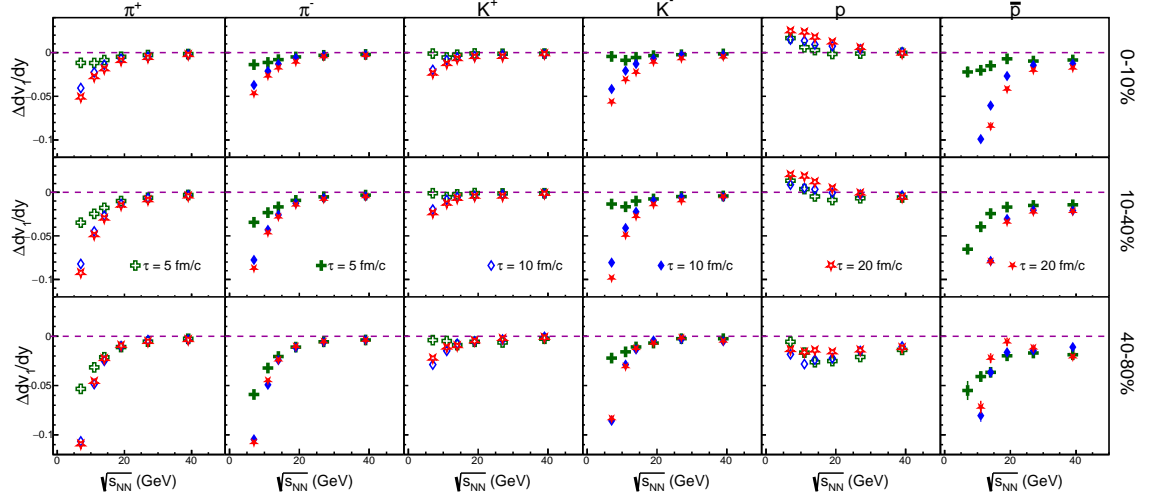


Figure 6.4: Slope of rapidity dependent v_1 (dv_1/y) as a function of collision energy ($\sqrt{s_{NN}}$) for identified hadrons (π^\pm , K^\pm , $p(\bar{p})$) with different hadronic cascade lifetime (τ) = 5, 10 and 20 fm/c.

To quantify the rapidity-dependent v_1 , the distribution is fitted with the function $p_0 y + p_1 y^3$ within $|y| < 1.5$, where p_0 represents dv_1/dy [183]. Figure 6.4 illustrates the dependence of dv_1/dy on collision energy for light-flavor hadrons. The figure shows that both π^+ and π^- have consistently negative dv_1/dy across $\sqrt{s_{NN}} = 7.7$ –39 GeV, with a more pronounced slope at higher hadronic phase times (τ). A similar trend is seen for K^+ and K^- , although the v_1 slope of charged kaons tends to become positive as τ increases, which could have contribution from associated production ($pp \rightarrow p\Lambda(\bar{\Lambda})K^+(K^-)$), which is prevalent at lower collision energies where kaon and proton production are strongly correlated [15, 26, 194, 195].

A distinct difference appears between the dv_1/dy of protons and anti-protons; while anti-protons consistently show negative dv_1/y across various τ values, proton dv_1/dy shifts from positive in central collisions to negative in peripheral collisions. This could arise from difference in v_1 between produced and transported quarks [183]. The fact that the sign change of proton dv_1/y varies with hadronic cascade duration suggests the importance of consideration of hadronic evolution and its duration during the interpretation of the proton v_1 sign reversal.

Theoretical calculations suggest that quarks originating from the initial participant nuclei (often called transported quarks) acquire a distinct v_1 compared to quarks produced through pair production (referred to as produced quarks) [196, 197]. These different sources of constituent quarks can lead to variations in v_1 for positively and negatively charged hadrons, reflected in the difference in the v_1 slope (characterized by $\Delta dv_1/dy$) between them [198]. Figure 6.5 presents the centrality dependence of $\Delta dv_1/dy$ for beam energies ranging from $\sqrt{s_{NN}} = 7.7$ to 39 GeV.

For all particle types analyzed, the magnitude of $\Delta dv_1/dy$ increases as beam energy decreases. At 7.7 GeV, $\Delta dv_1/dy$ shows a pronounced centrality dependence across particle species, particularly in central and mid-central collisions, where the magnitude of $\Delta dv_1/dy$ escalates

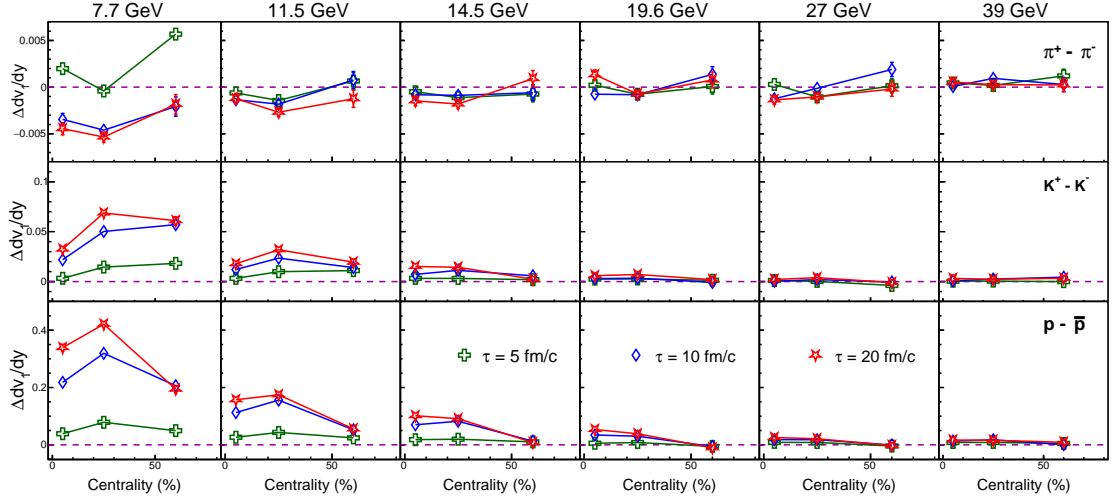


Figure 6.5: Difference in rapidity differential directed flow slope ($\Delta dv_1/y$) of positively and negatively charged light flavored hadrons (π , K and p) as a function of collision centrality for Au+Au collisions at $\sqrt{s_{NN}} = 7.7, 11.5, 14.5, 19.6, 27$ and 39 GeV with different hadronic cascade lifetime (τ) = 5, 10 and 20 fm/c.

with an increase in hadronic cascade duration (τ) from 5 to 20 fm/c. In contrast, peripheral collisions exhibit only a modest change in $\Delta dv_1/dy$ across different τ values. These observations suggest that a longer hadronic phase, characteristic of central collisions, enhances $\Delta dv_1/dy$ significantly, while hadronic interactions in peripheral collisions have a comparatively lesser effect on $\Delta dv_1/dy$.

6.3.3 Model to experimental data comparison

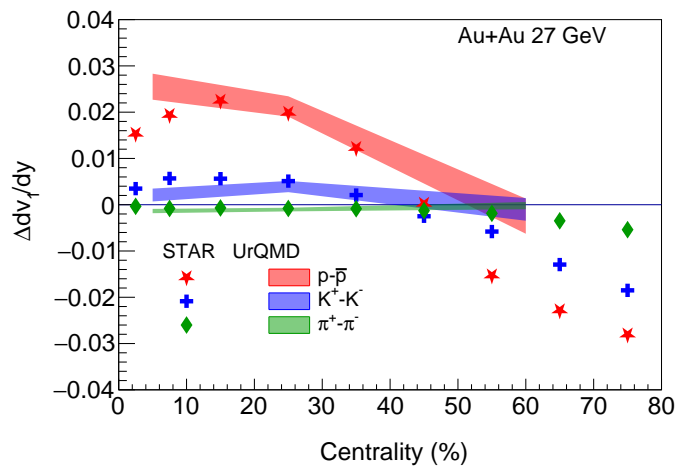


Figure 6.6: Comparison of difference in rapidity differential directed flow slope ($\Delta dv_1/y$) of positively and negatively charged light flavored hadrons (π , K and p) at 27 GeV Au+Au collisions by STAR [45] with UrQMD calculations with $\tau = 20$ fm/c.

Figure 6.6 presents a comparison of UrQMD calculations (with $\tau = 20$ fm/c) and experimental data for the charge splitting in $\Delta dv_1/dy$ for π^\pm , K^\pm , $p(\bar{p})$ in Au+Au collisions at $\sqrt{s_{NN}} =$

27 GeV, as observed by the STAR collaboration [45]. While the model calculations qualitatively reproduce the trend observed in experimental data for central and mid-central collisions, they fall short quantitatively. Additionally, the model does not capture the behavior of $\Delta dv_1/dy$ in peripheral collisions for any particle species considered, which has been depicted as a signature of electromagnetic field [45]. However, the positive $\Delta dv_1/dy$ observed for protons in UrQMD may be attributed to baryon stopping, along with contributions from interactions in the late hadronic phase.

6.4 Summary

The rapidity-dependent odd component of directed flow (v_1) and its slope near mid-rapidity (dv_1/dy) in Au+Au collisions at STAR-BES energies, analyzed using the UrQMD transport model. Notably, a significant difference is observed in dv_1/dy between protons and anti-protons. The difference in v_1 slope increases with increasing the hadronic cascade time. Additionally, the centrality-dependent difference in dv_1/dy between positively and negatively charged hadrons ($\Delta dv_1/dy$) varies significantly with particle type and hadronic phase duration. Results from UrQMD are compared to recent STAR collaboration measurements of $\Delta dv_1/dy$ for identified particles. While UrQMD reproduces certain qualitative trends in the data, it does not fully capture the quantitative details, suggesting a need for further study into the effects of the electromagnetic fields, baryon stopping, mean field and equation of state on directed flow.

Chapter 7

Thesis Summary

This thesis is dedicated to probe the hadronic medium produced in relativistic heavy-ion collisions. In the experimental data analysis section, light-flavor resonance K^{*0} meson production is studied in Au+Au collisions at STAR BES energies. The analysis presented in this thesis is carried out using the data from the STAR detector at RHIC, BNL.

The STAR BES program provides an unique opportunity to study the system created at lower collision energy (that have a baryon rich environment), which has different chemical composition compared to the same at top RHIC energies (that have a meson rich environment). Along with that the particle multiplicity decreases at lower energies, hence the measurement of resonances can offer valuable insights on the hadronic interactions and dynamics of the hadronic phase in such conditions.

The thesis begins with Chapter 1, which presents a brief overview of particle physics, focusing on concepts related to the quark-gluon plasma, and importance of studying resonances created in heavy-ion collisions. Chapter 2 provides a concise description of the STAR detector and its various sub-detector systems that are relevant to this analysis.

The Chapter 3, 4, 5 are dedicated to experimental and phenomenological study on the production of the K^{*0} meson in Au+Au collisions at BES energies. The analysis includes the measurement of mass, width, transverse momentum (p_T) spectra, p_T -integrated yield (dN/dy) and mean transverse momentum ($\langle p_T \rangle$) of the K^{*0} meson. To study the interplay of competing in medium processes the resonance to non-resonance particle yields (K^{*0}/K) with similar quark content is measured. The K^{*0}/K ratio decreases from peripheral to central collisions, indicating significant hadronic rescattering in central heavy-ion collisions. In contrast, the ϕ meson, with a lifetime approximately ten times longer than that of the K^{*0} , decays primarily outside the medium and remains unaffected by in-medium interactions. Consequently, the ϕ/K ratio remains nearly constant across different centralities. A comparison of the K^{*0}/K ratio at BES energies with global data shows suppression in central heavy-ion collisions relative to small sys-

tems like $e - e$ or $p - p$. This suppression supports the loss of resonance yield due to rescattering in central heavy ion collisions. The measurement of nuclear modification factor (R_{cp}) indicate that rescattering is more dominant for low- p_T particles.

The experimental results are compared with various phenomenological models. The statistical thermal model, which does not account for particle interactions, is consistent with the K^{*0}/K ratio in peripheral collisions but overestimates it in central collisions. However, the model's predictions for the ϕ/K ratio match the experimental data. Meanwhile, the UrQMD transport model, which incorporates hadronic rescattering, qualitatively captures the decreasing trend of the K^{*0}/K ratio with increasing centrality. These comparisons reinforce the evidence for hadronic rescattering effects in central heavy-ion collisions. At top RHIC or LHC energies, the K^{*0}/K ratio attains an approximate multiplicity scaling but the scaling observed to break at STAR BES energies. Comparison with transport model studies supports that, at low energies, enhanced meson-baryon elastic interactions over meson-meson elastic interactions, leads to significant resonance yield loss which could potentially contribute to the observed multiplicity scale breaking.

The lower limit of time difference between chemical and kinetic freezeout (Δt) is estimated using a simple toy-model. Under specific assumptions, Δt is found to increase smoothly from peripheral to central collisions, consistent with the expectation of a longer-lived fireball in central heavy-ion collisions. At BES energies in Au+Au collisions, the estimated lower limit of the hadronic phase lifetime is approximately 4 fm/c. Despite large uncertainties, this value appears shorter than the corresponding lifetime in central Pb+Pb collisions at LHC energies.

Given the significant impact of hadronic interactions on resonance yields, this study has been extended to investigate their effects on other experimental observables. Chapter 6 contains the transport model study on the effect of hadronic cascade lifetime on the flow co-efficients. The UrQMD model has been employed to study the effect on the directed flow (v_1) of identified hadrons in Au+Au collisions at $\sqrt{s_{NN}} = 7.7\text{--}39$ GeV. The charge-dependent splitting in v_1 slope ($\Delta dv_1/dy$) is calculated as the difference in v_1 slopes between positively and negatively charged particles. The $\Delta dv_1/dy$ found to increase with increasing hadronic cascade duration and the effect is pronounced in case of central and mid-central collisions, especially for protons, likely due to enhanced baryon stopping at mid-rapidity at lower collision energies. The UrQMD calculations for hadronic cascade time $\tau = 20$ fm is compared with the STAR data, the model qualitatively explains the results for central and mid-central collisions. This agreement suggests that hadronic interactions can also contribute to the charge-dependent splitting in directed flow.

7.1 Future Prospectives

In the BES-II program, STAR has accumulated a substantial amount of data for Au+Au collisions over a collision energy range of $\sqrt{s_{NN}} = 3.0\text{--}27$ GeV. These data sets include events recorded in both collider mode and fixed-target setups. Measuring resonances across this entire energy range and comparing the results with other published data from RHIC and LHC will provide valuable insights into the dynamics of the hadronic phase, spanning energies as low as $\sqrt{s_{NN}} = 3.0$ GeV to as high as 13 TeV. Recent work on baryonic resonances using the high-statistics isobar data sets is ongoing in STAR. With the improved statistics, studies of heavy baryonic resonances (such as Λ^* , Σ^* , and Ξ^*) can also be pursued at STAR BES-II.

This thesis presents the rapidity spectra of the K^{*0} meson at BES energies. With the availability of kaon rapidity spectra, future studies can further investigate hadronic rescattering effects as a function of rapidity.

Appendix

8.1 Branching ratios

if I and I_z are the isospin and z -component of isospin quantum numbers respectively, then the isospin eigen ket for any particle can be written as $|I, I_z\rangle$

Being doublets ($I = \frac{1}{2}$) in K -meson family, the corresponding eigen kets for different particles (pseudo-scalar mesons) can be written as;

$$K^+ = |\frac{1}{2}, \frac{1}{2}\rangle, \quad K^- = |\frac{1}{2}, -\frac{1}{2}\rangle, \quad K^0 = |\frac{1}{2}, \frac{1}{2}\rangle, \quad \overline{K}^0 = |\frac{1}{2}, \frac{1}{2}\rangle \quad (8.1.1)$$

Simillary the resonances states (vector mesons) in the K -meson family can be written as;

$$K^{*+} = |\frac{1}{2}, \frac{1}{2}\rangle, \quad K^{*-} = |\frac{1}{2}, -\frac{1}{2}\rangle, \quad K^{*0} = |\frac{1}{2}, \frac{1}{2}\rangle, \quad \overline{K}^{*0} = |\frac{1}{2}, \frac{1}{2}\rangle \quad (8.1.2)$$

For pions being isospin triplets ($I = 1$), the eigen kets can be written as;

$$\pi^+ = |1, 1\rangle, \quad \pi^0 = |1, 0\rangle, \quad \pi^- = |1, -1\rangle \quad (8.1.3)$$

From PDG it is known that K^{*-} meson has a 100% hadronic decay channel into $K\pi$ pairs. Hence the final K^{*0} state can be reduced in terms of combination of $K\pi$ pairs. The can be performed by calculating addition of angular momentum of two particle states with $I_1 = \frac{1}{2}$ (kaons) and $I_2 = 1$ (pions). With further calculation of Clebsh-Gorden coefficients, it can be found that;

$$|\frac{1}{2}, 1; \frac{1}{2}, -\frac{1}{2}\rangle = \sqrt{\frac{1}{3}}|\frac{1}{2}, 1; \frac{1}{2}, 0\rangle - \sqrt{\frac{2}{3}}|\frac{1}{2}, 1; \frac{1}{2}, -1\rangle \quad (8.1.4)$$

and

$$|\frac{1}{2}, 1; \frac{1}{2}, \frac{1}{2}\rangle = -\sqrt{\frac{1}{3}}|\frac{1}{2}, 1; \frac{1}{2}, 0\rangle + \sqrt{\frac{2}{3}}|\frac{1}{2}, 1; \frac{1}{2}, 1\rangle \quad (8.1.5)$$

From equation above equations, it can be loosely concluded that,

$$|K^{*0}\rangle = \sqrt{\frac{1}{3}}|K^0, \pi^0\rangle - \sqrt{\frac{2}{3}}|K^+, \pi^-\rangle \quad (8.1.6)$$

and

$$|K^{*+}\rangle = \sqrt{\frac{1}{3}}|K^+, \pi^0\rangle - \sqrt{\frac{2}{3}}|K^0, \pi^+\rangle \quad (8.1.7)$$

This indicates the decay channel $K^{*0} \rightarrow K^0\pi^0$ and $K^{*0} \rightarrow K^+\pi^-$ has a probability of 33% and 66% respectively. The same probability also holds for the decay of \bar{K}^{*0} for the neutral and charged decay channel.

Similarly the decay channel $K^{*\pm} \rightarrow K^\pm\pi^0$ and $K^{*\pm} \rightarrow K^0\pi^\pm$ has a probability of 33% and 66% respectively. However the discussion for the $K^{*\pm}$ production is out of the scope of this thesis.

References

- [1] A. Tarek Abouelfadl Mohamed, *The Standard Model of Particle Physics*. Cham: Springer International Publishing, 2020, pp. 3–35. [Online]. Available: https://doi.org/10.1007/978-3-030-59516-6_1
- [2] M. Niiyama, “Recent Results of Few Body System in the Hadron Physics with Photon Beam,” *Few Body Syst.*, vol. 62, no. 4, p. 99, 2021.
- [3] H.-T. Ding, F. Karsch, and S. Mukherjee, “Thermodynamics of strong-interaction matter from Lattice QCD,” *Int. J. Mod. Phys. E*, vol. 24, no. 10, p. 1530007, 2015.
- [4] A. Pandav, D. Mallick, and B. Mohanty, “Search for the QCD critical point in high energy nuclear collisions,” *Prog. Part. Nucl. Phys.*, vol. 125, p. 103960, 2022.
- [5] “Space-time evolution of relativistic heavy ion collisions.” [Online]. Available: <https://particlesandfriends.wordpress.com/2016/10/14/evolution-of-collisions-and-qgp/>
- [6] J. Adams *et al.*, “Experimental and theoretical challenges in the search for the quark gluon plasma: The STAR Collaboration’s critical assessment of the evidence from RHIC collisions,” *Nucl. Phys. A*, vol. 757, pp. 102–183, 2005.
- [7] B. I. Abelev *et al.*, “Energy and system size dependence of phi meson production in Cu+Cu and Au+Au collisions,” *Phys. Lett. B*, vol. 673, pp. 183–191, 2009.
- [8] J. Adams *et al.*, “Transverse momentum and collision energy dependence of high p(T) hadron suppression in Au+Au collisions at ultrarelativistic energies,” *Phys. Rev. Lett.*, vol. 91, p. 172302, 2003.
- [9] A. Adare *et al.*, “ J/ψ suppression at forward rapidity in Au+Au collisions at $\sqrt{s_{NN}} = 200$ GeV,” *Phys. Rev. C*, vol. 84, p. 054912, 2011.
- [10] M. Gyulassy and L. McLerran, “New forms of QCD matter discovered at RHIC,” *Nucl. Phys. A*, vol. 750, pp. 30–63, 2005.
- [11] B. I. Abelev *et al.*, “Mass, quark-number, and $\sqrt{s_{NN}}$ dependence of the second and fourth flow harmonics in ultra-relativistic nucleus-nucleus collisions,” *Phys. Rev. C*, vol. 75, p. 054906, 2007.
- [12] M. M. Aggarwal *et al.*, “ K^{*0} production in Cu+Cu and Au+Au collisions at $\sqrt{s_{NN}} = 62.4$ GeV and 200 GeV,” *Phys. Rev. C*, vol. 84, p. 034909, 2011.
- [13] B. I. Abelev *et al.*, “Hadronic resonance production in d+Au collisions at $\sqrt{s_{NN}} = 200$ -GeV at RHIC,” *Phys. Rev. C*, vol. 78, p. 044906, 2008.
- [14] J. Adam *et al.*, “ $K^{*}(892)^0$ and $\phi(1020)$ meson production at high transverse momentum in pp and Pb-Pb collisions at $\sqrt{s_{NN}} = 2.76$ TeV,” *Phys. Rev. C*, vol. 95, no. 6, p. 064606, 2017.
- [15] L. Adamczyk *et al.*, “Bulk Properties of the Medium Produced in Relativistic Heavy-Ion Collisions from the Beam Energy Scan Program,” *Phys. Rev. C*, vol. 96, no. 4, p. 044904, 2017.
- [16] “The RHIC collider complex.” [Online]. Available: <https://www.bnl.gov/rhic/complex.php>

- [17] “First event display at STAR.” [Online]. Available: <https://www.star.bnl.gov/public/imagelib/collisions2001/>
- [18] L. Adamczyk *et al.*, “Longitudinal and transverse spin asymmetries for inclusive jet production at mid-rapidity in polarized $p + p$ collisions at $\sqrt{s} = 200$ GeV,” *Phys. Rev. D*, vol. 86, p. 032006, 2012.
- [19] K. C. Meehan, “The fixed-target experiment at star,” *Journal of Physics: Conference Series*, vol. 742, no. 1, p. 012022, aug 2016. [Online]. Available: <https://dx.doi.org/10.1088/1742-6596/742/1/012022>
- [20] M. Anderson *et al.*, “The Star time projection chamber: A Unique tool for studying high multiplicity events at RHIC,” *Nucl. Instrum. Meth. A*, vol. 499, pp. 659–678, 2003.
- [21] F. Shen, S. Wang, F. Kong, S. Bai, C. Li, F. Videbæk, Z. Xu, C. Zhu, Q. Xu, and C. Yang, “MWPC prototyping and performance test for the STAR inner TPC upgrade,” *Nucl. Instrum. Meth. A*, vol. 896, pp. 90–95, 2018.
- [22] W. J. Llope, “The large-area time-of-flight upgrade for STAR,” *Nucl. Instrum. Meth. B*, vol. 241, pp. 306–310, 2005.
- [23] [Online]. Available: <https://www.star.bnl.gov/public/trg/trouble/operating-trigger/introduction/>
- [24] H. Bichsel, “A method to improve tracking and particle identification in TPCs and silicon detectors,” *Nucl. Instrum. Meth. A*, vol. 562, pp. 154–197, 2006.
- [25] J. Adams *et al.*, “K(892)* resonance production in Au+Au and p+p collisions at $s(\text{NN})^{1/2} = 200$ -GeV at STAR,” *Phys. Rev. C*, vol. 71, p. 064902, 2005.
- [26] J. Adam *et al.*, “Bulk properties of the system formed in $Au + Au$ collisions at $\sqrt{s_{\text{NN}}} = 14.5$ GeV at the BNL STAR detector,” *Phys. Rev. C*, vol. 101, no. 2, p. 024905, 2020.
- [27] —, “Strange hadron production in Au+Au collisions at $\sqrt{s_{\text{NN}}} = 7.7, 11.5, 19.6, 27$, and 39 GeV,” *Phys. Rev. C*, vol. 102, no. 3, p. 034909, 2020.
- [28] S. Acharya *et al.*, “Evidence of rescattering effect in Pb-Pb collisions at the LHC through production of $K^*(892)^0$ and $\phi(1020)$ mesons,” *Phys. Lett. B*, vol. 802, p. 135225, 2020.
- [29] H. Albrecht *et al.*, “Inclusive production of $K^*(892)$, $\rho^0(770)$, and $\omega(783)$ mesons in the Υ energy region,” *Z. Phys. C*, vol. 61, pp. 1–18, 1994.
- [30] Y.-J. Pei, “A Simple approach to describe hadron production rates in e^+e^- annihilation,” *Z. Phys. C*, vol. 72, pp. 39–46, 1996.
- [31] W. Hofmann, “Particle Composition in Hadronic Jets in e^+e^- Annihilation,” *Ann. Rev. Nucl. Part. Sci.*, vol. 38, pp. 279–322, 1988.
- [32] K. Abe *et al.*, “Production of π^+ , K^+ , K^0 , K^{*0} , ϕ , p and Λ^0 in hadronic Z^0 decays,” *Phys. Rev. D*, vol. 59, p. 052001, 1999.
- [33] M. Aguilar-Benitez *et al.*, “Inclusive particle production in 400-GeV/c $p p$ interactions,” *Z. Phys. C*, vol. 50, pp. 405–426, 1991.
- [34] D. Drijard *et al.*, “Production of Vector and Tensor Mesons in Proton Proton Collisions at $\sqrt{s} = 52.5$ -GeV,” *Z. Phys. C*, vol. 9, p. 293, 1981.

- [35] T. Akesson *et al.*, “Inclusive Vector - Meson Production in the Central Region of pp Collisions at $\sqrt{s} = 63\text{-GeV}$,” *Nucl. Phys. B*, vol. 203, p. 27, 1982, [Erratum: Nucl.Phys.B 229, 541 (1983)].
- [36] S. Acharya *et al.*, “ $K^*(892)^0$ and $\phi(1020)$ production in p-Pb collisions at $\sqrt{s_{NN}} = 8.16$ TeV,” 10 2021.
- [37] J. Adam *et al.*, “Production of $K^*(892)^0$ and $\phi(1020)$ in p-Pb collisions at $\sqrt{s_{NN}} = 5.02$ TeV,” *Eur. Phys. J. C*, vol. 76, no. 5, p. 245, 2016.
- [38] T. Anticic *et al.*, “ $K^*(892)^0$ and $\bar{K}^*(892)^0$ production in central Pb+Pb, Si+Si, C+C and inelastic p+p collisions at $158A\text{-GeV}$,” *Phys. Rev. C*, vol. 84, p. 064909, 2011.
- [39] M. Abdallah *et al.*, “ K^*0 production in Au+Au collisions at $\sqrt{s_{NN}} = 7.7, 11.5, 14.5, 19.6, 27,$ and 39 GeV from the RHIC beam energy scan,” *Phys. Rev. C*, vol. 107, no. 3, p. 034907, 2023.
- [40] B. I. Abelev *et al.*, “Systematic Measurements of Identified Particle Spectra in pp, d^+ Au and Au+Au Collisions from STAR,” *Phys. Rev. C*, vol. 79, p. 034909, 2009.
- [41] I. C. Arsene *et al.*, “Rapidity and centrality dependence of particle production for identified hadrons in Cu+Cu collisions at $\sqrt{s_{NN}} = 200$ GeV,” *Phys. Rev. C*, vol. 94, no. 1, p. 014907, 2016.
- [42] C. Le Roux, F. S. Navarra, and L. M. Abreu, “Understanding the K^*/K ratio in heavy ion collisions,” *Phys. Lett. B*, vol. 817, p. 136284, 2021.
- [43] A. K. Sahoo, S. Singha, and M. Nasim, “The study of hadronic rescattering on K^*0 resonance yield in baryon-rich QCD matter,” *J. Phys. G*, vol. 52, no. 1, p. 015101, 2025.
- [44] A. K. Sahoo, M. Nasim, and S. Singha, “ K^*0 meson production using a transport and a statistical hadronization model at energies covered by the RHIC beam energy scan,” *Phys. Rev. C*, vol. 108, no. 4, p. 044904, 2023.
- [45] M. I. Abdulhamid *et al.*, “Observation of the electromagnetic field effect via charge-dependent directed flow in heavy-ion collisions at the Relativistic Heavy Ion Collider,” *Phys. Rev. X*, vol. 14, no. 1, p. 011028, 2024.
- [46] “The RHIC performance parameters.” [Online]. Available: <https://www.agsrhichome.bnl.gov/RHIC/Runs/>
- [47] E. Judd, L. Bland, H. Crawford, J. Engelage, J. Landgraf, W. Llope, J. Nelson, M. Ng, A. Ogawa, C. Perkins, G. Visser, and Z. Xu, “The evolution of the star trigger system,” *Nuclear Instruments and Methods in Physics Research Section A: Accelerators, Spectrometers, Detectors and Associated Equipment*, vol. 902, pp. 228–237, 2018. [Online]. Available: <https://www.sciencedirect.com/science/article/pii/S0168900218304224>
- [48] J. J. Thomson, “Cathode Rays,” *The London, Edinburgh, and Dublin Philosophical Magazine and Journal of Science*, vol. 44, pp. 293–316, 1897.
- [49] E. Rutherford, “The scattering of alpha and beta particles by matter and the structure of the atom,” *Phil. Mag. Ser. 6*, vol. 21, pp. 669–688, 1911.
- [50] P. S. E. R. F. R. S., “LIV. Collision of α particles with light atoms. IV. An anomalous effect in nitrogen,” *Phil. Mag. Ser. 6*, vol. 37, no. 222, pp. 581–587, 1919.

- [51] J. Chadwick, “Possible Existence of a Neutron,” *Nature*, vol. 129, p. 312, 1932.
- [52] R. Brandelik *et al.*, “Evidence for Planar Events in e^+e^- Annihilation at High-Energies,” *Phys. Lett. B*, vol. 86, pp. 243–249, 1979.
- [53] S. L. Glashow, “Partial Symmetries of Weak Interactions,” *Nucl. Phys.*, vol. 22, pp. 579–588, 1961.
- [54] A. Salam and J. C. Ward, “Electromagnetic and weak interactions,” *Phys. Lett.*, vol. 13, pp. 168–171, 1964.
- [55] S. Weinberg, “A Model of Leptons,” *Phys. Rev. Lett.*, vol. 19, pp. 1264–1266, 1967.
- [56] C.-N. Yang and R. L. Mills, “Conservation of Isotopic Spin and Isotopic Gauge Invariance,” *Phys. Rev.*, vol. 96, pp. 191–195, 1954.
- [57] C. S. Wu, E. Ambler, R. W. Hayward, D. D. Hoppes, and R. P. Hudson, “Experimental Test of Parity Conservation in β Decay,” *Phys. Rev.*, vol. 105, pp. 1413–1414, 1957.
- [58] F. Abe *et al.*, “Observation of top quark production in $\bar{p}p$ collisions,” *Phys. Rev. Lett.*, vol. 74, pp. 2626–2631, 1995.
- [59] K. Kodama *et al.*, “Observation of tau neutrino interactions,” *Phys. Lett. B*, vol. 504, pp. 218–224, 2001.
- [60] S. Van Der Meer, “Stochastic Cooling and the Accumulation of Anti-Protons,” *Rev. Mod. Phys.*, vol. 57, pp. 689–697, 1985.
- [61] S. Chatrchyan *et al.*, “Observation of a New Boson at a Mass of 125 GeV with the CMS Experiment at the LHC,” *Phys. Lett. B*, vol. 716, pp. 30–61, 2012.
- [62] G. Aad *et al.*, “Observation of a new particle in the search for the Standard Model Higgs boson with the ATLAS detector at the LHC,” *Phys. Lett. B*, vol. 716, pp. 1–29, 2012.
- [63] P. W. Higgs, “Broken Symmetries and the Masses of Gauge Bosons,” *Phys. Rev. Lett.*, vol. 13, pp. 508–509, 1964.
- [64] ———, “Broken symmetries, massless particles and gauge fields,” *Phys. Lett.*, vol. 12, pp. 132–133, 1964.
- [65] D. J. Gross and F. Wilczek, “Ultraviolet Behavior of Nonabelian Gauge Theories,” *Phys. Rev. Lett.*, vol. 30, pp. 1343–1346, 1973.
- [66] J. S. Schwinger, “On Quantum electrodynamics and the magnetic moment of the electron,” *Phys. Rev.*, vol. 73, pp. 416–417, 1948.
- [67] D. J. Gross and F. Wilczek, “Asymptotically Free Gauge Theories - I,” *Phys. Rev. D*, vol. 8, pp. 3633–3652, 1973.
- [68] H. D. Politzer, “Reliable Perturbative Results for Strong Interactions?” *Phys. Rev. Lett.*, vol. 30, pp. 1346–1349, 1973.
- [69] K. Huang, *Statistical Mechanics, 2nd Edition*, 1987.
- [70] “Oxford University, Lecture 10 — Phase transitions.” [Online]. Available: https://www2.physics.ox.ac.uk/sites/default/files/2011-10-04/crystalstructure_handout10_pdf_19544.pdf

- [71] T. D. Lee and G. C. Wick, “Vacuum Stability and Vacuum Excitation in a Spin 0 Field Theory,” *Phys. Rev. D*, vol. 9, pp. 2291–2316, 1974.
- [72] J. C. Collins and M. J. Perry, “Superdense Matter: Neutrons Or Asymptotically Free Quarks?” *Phys. Rev. Lett.*, vol. 34, p. 1353, 1975.
- [73] F. Karsch, “Lattice results on QCD thermodynamics,” *Nucl. Phys. A*, vol. 698, pp. 199–208, 2002.
- [74] R. C. Hwa and X. N. Wang, Eds., *Quark-gluon plasma 3*. Singapore: World Scientific, 2004.
- [75] F. Karsch, “Lattice QCD at nonzero chemical potential and the resonance gas model,” *Prog. Theor. Phys. Suppl.*, vol. 153, pp. 106–117, 2004.
- [76] R. V. Gavai and S. Gupta, “The Critical end point of QCD,” *Phys. Rev. D*, vol. 71, p. 114014, 2005.
- [77] S. Gupta, X. Luo, B. Mohanty, H. G. Ritter, and N. Xu, “Scale for the Phase Diagram of Quantum Chromodynamics,” *Science*, vol. 332, pp. 1525–1528, 2011.
- [78] Z. Xu, C. Greiner, and H. Stoecker, “PQCD calculations of elliptic flow and shear viscosity at RHIC,” *Phys. Rev. Lett.*, vol. 101, p. 082302, 2008.
- [79] G. Ferini, M. Colonna, M. Di Toro, and V. Greco, “Scalings of Elliptic Flow for a Fluid at Finite Shear Viscosity,” *Phys. Lett. B*, vol. 670, pp. 325–329, 2009.
- [80] S. Plumari, A. Puglisi, M. Colonna, F. Scardina, and V. Greco, “Shear viscosity and chemical equilibration of the QGP,” *J. Phys. Conf. Ser.*, vol. 420, p. 012029, 2013.
- [81] M. Luzum and P. Romatschke, “Conformal Relativistic Viscous Hydrodynamics: Applications to RHIC results at $s(\text{NN})^{1/2} = 200\text{-GeV}$,” *Phys. Rev. C*, vol. 78, p. 034915, 2008, [Erratum: *Phys.Rev.C* 79, 039903 (2009)].
- [82] L. Adamczyk *et al.*, “Global Λ hyperon polarization in nuclear collisions: evidence for the most vortical fluid,” *Nature*, vol. 548, pp. 62–65, 2017.
- [83] M. S. Abdallah *et al.*, “Pattern of global spin alignment of ϕ and K^{*0} mesons in heavy-ion collisions,” *Nature*, vol. 614, no. 7947, pp. 244–248, 2023.
- [84] N. Cabibbo and G. Parisi, “Exponential Hadronic Spectrum and Quark Liberation,” *Phys. Lett. B*, vol. 59, pp. 67–69, 1975.
- [85] K. Fukushima and T. Hatsuda, “The phase diagram of dense QCD,” *Rept. Prog. Phys.*, vol. 74, p. 014001, 2011.
- [86] F. R. Brown, F. P. Butler, H. Chen, N. H. Christ, Z.-h. Dong, W. Schaffer, L. I. Unger, and A. Vaccarino, “On the existence of a phase transition for QCD with three light quarks,” *Phys. Rev. Lett.*, vol. 65, pp. 2491–2494, 1990.
- [87] Y. Aoki, G. Endrodi, Z. Fodor, S. D. Katz, and K. K. Szabo, “The Order of the quantum chromodynamics transition predicted by the standard model of particle physics,” *Nature*, vol. 443, pp. 675–678, 2006.
- [88] S. Ejiri, “Canonical partition function and finite density phase transition in lattice QCD,” *Phys. Rev. D*, vol. 78, p. 074507, 2008.

- [89] Y. Hatta and T. Ikeda, “Universality, the QCD critical / tricritical point and the quark number susceptibility,” *Phys. Rev. D*, vol. 67, p. 014028, 2003.
- [90] E. S. Bowman and J. I. Kapusta, “Critical Points in the Linear Sigma Model with Quarks,” *Phys. Rev. C*, vol. 79, p. 015202, 2009.
- [91] M. A. Stephanov, “QCD Phase Diagram and the Critical Point,” *Prog. Theor. Phys. Suppl.*, vol. 153, pp. 139–156, 2004.
- [92] K. Rajagopal and F. Wilczek, *The Condensed matter physics of QCD*, 11 2000, pp. 2061–2151.
- [93] A. Ghiorso, H. Grunder, W. Hartsough, G. Lambertson, E. Lofgren, K. Lou, R. Main, R. Mobley, R. Morgado, W. Salsig, and F. Selph, “The bevalac – an economical facility for very energetic heavy particle research,” *IEEE Transactions on Nuclear Science*, vol. 20, no. 3, pp. 155–158, 1973.
- [94] P. Braun-Munzinger, K. Redlich, and J. Stachel, “Particle production in heavy ion collisions,” pp. 491–599, 4 2003.
- [95] J. Adams *et al.*, “Multistrange baryon production in Au-Au collisions at $S(NN)^{1/2} = 130$ GeV,” *Phys. Rev. Lett.*, vol. 92, p. 182301, 2004.
- [96] O. Y. Barannikova, “Probing collision dynamics at RHIC,” in *17th International Conference on Ultra Relativistic Nucleus-Nucleus Collisions (Quark Matter 2004)*, 3 2004.
- [97] D. H. Rischke, “The Quark gluon plasma in equilibrium,” *Prog. Part. Nucl. Phys.*, vol. 52, pp. 197–296, 2004.
- [98] F. Karsch, “Lattice QCD at high temperature and density,” *Lect. Notes Phys.*, vol. 583, pp. 209–249, 2002.
- [99] N. Xu and M. Kaneta, “Hadron freezeout conditions in high-energy nuclear collisions,” *Nucl. Phys. A*, vol. 698, pp. 306–313, 2002.
- [100] E. Schnedermann, J. Sollfrank, and U. W. Heinz, “Thermal phenomenology of hadrons from 200-A/GeV S+S collisions,” *Phys. Rev. C*, vol. 48, pp. 2462–2475, 1993.
- [101] H. van Hecke, H. Sorge, and N. Xu, “Evidence of early multistrange hadron freezeout in high-energy nuclear collisions,” *Phys. Rev. Lett.*, vol. 81, pp. 5764–5767, 1998.
- [102] A. Shor, “PHI MESON PRODUCTION AS A PROBE OF THE QUARK GLUON PLASMA,” *Phys. Rev. Lett.*, vol. 54, pp. 1122–1125, 1985.
- [103] R. Vogt, *Ultrarelativistic heavy-ion collisions*. Amsterdam: Elsevier, 2007.
- [104] S. Mandelstam, “Determination of the pion-nucleon scattering amplitude from dispersion relations and unitarity. general theory,” *Phys. Rev.*, vol. 112, pp. 1344–1360, Nov 1958. [Online]. Available: <https://link.aps.org/doi/10.1103/PhysRev.112.1344>
- [105] W. Florkowski, *Phenomenology of Ultra-Relativistic Heavy-Ion Collisions*, 3 2010.
- [106] J. Rafelski and B. Muller, “Strangeness Production in the Quark - Gluon Plasma,” *Phys. Rev. Lett.*, vol. 48, p. 1066, 1982, [Erratum: *Phys.Rev.Lett.* 56, 2334 (1986)].
- [107] J. Rafelski and B. Müller, “Strangeness production in the quark-gluon plasma,” *Phys. Rev. Lett.*, vol. 56, pp. 2334–2334, May 1986. [Online]. Available: <https://link.aps.org/doi/10.1103/PhysRevLett.56.2334>

- [108] J. Adam *et al.*, “Enhanced production of multi-strange hadrons in high-multiplicity proton-proton collisions,” *Nature Phys.*, vol. 13, pp. 535–539, 2017.
- [109] T. Alber *et al.*, “Strange particle production in nuclear collisions at 200-GeV per nucleon,” *Z. Phys. C*, vol. 64, pp. 195–207, 1994.
- [110] P. Jones *et al.*, “Hadron yields and hadron spectra from the na49 experiment,” *Nuclear Physics A*, vol. 610, pp. 188–199, 1996, quark Matter '96. [Online]. Available: <https://www.sciencedirect.com/science/article/pii/S0375947496003545>
- [111] C. Adler *et al.*, “Kaon production and kaon to pion ratio in Au+Au collisions at $\sqrt{s_{NN}} = 130$ -GeV,” *Phys. Lett. B*, vol. 595, pp. 143–150, 2004.
- [112] M. Gyulassy and M. Plumer, “Jet Quenching in Dense Matter,” *Phys. Lett. B*, vol. 243, pp. 432–438, 1990.
- [113] B. Abelev *et al.*, “Transverse momentum distribution and nuclear modification factor of charged particles in p -Pb collisions at $\sqrt{s_{NN}} = 5.02$ TeV,” *Phys. Rev. Lett.*, vol. 110, no. 8, p. 082302, 2013.
- [114] T. Matsui and H. Satz, “ J/ψ Suppression by Quark-Gluon Plasma Formation,” *Phys. Lett. B*, vol. 178, pp. 416–422, 1986.
- [115] H. Satz, “Color Screening in $SU(N)$ Gauge Theory at Finite Temperature,” *Nucl. Phys. A*, vol. 418, pp. 447C–465C, 1984.
- [116] B. Alessandro *et al.*, “A New measurement of J/ψ suppression in Pb-Pb collisions at 158-GeV per nucleon,” *Eur. Phys. J. C*, vol. 39, pp. 335–345, 2005.
- [117] R. Arnaldi *et al.*, “ J/ψ production in Indium-Indium collisions at 158- GeV/nucleon,” *Conf. Proc. C*, vol. 060726, pp. 430–434, 2006.
- [118] A. Adare *et al.*, “ J/ψ production versus transverse momentum and rapidity in p^+p collisions at $\sqrt{s} = 200$ -GeV,” *Phys. Rev. Lett.*, vol. 98, p. 232002, 2007.
- [119] —, “ J/ψ Production in $\sqrt{s_{NN}} = 200$ -GeV Cu+Cu Collisions,” *Phys. Rev. Lett.*, vol. 101, p. 122301, 2008.
- [120] S. Voloshin and Y. Zhang, “Flow study in relativistic nuclear collisions by Fourier expansion of Azimuthal particle distributions,” *Z. Phys. C*, vol. 70, pp. 665–672, 1996.
- [121] M. Masera, G. Ortona, M. G. Poghosyan, and F. Prino, “Anisotropic transverse flow introduction in Monte Carlo generators for heavy ion collisions,” *Phys. Rev. C*, vol. 79, p. 064909, 2009.
- [122] D. Molnar and S. A. Voloshin, “Elliptic flow at large transverse momenta from quark coalescence,” *Phys. Rev. Lett.*, vol. 91, p. 092301, 2003.
- [123] R. J. Fries, B. Muller, C. Nonaka, and S. A. Bass, “Hadronization in heavy ion collisions: Recombination and fragmentation of partons,” *Phys. Rev. Lett.*, vol. 90, p. 202303, 2003.
- [124] S. P. M. Harrison and T. Roser, “THE RHIC ACCELERATOR,” *Annual Review of Nuclear and Particle Science*, vol. 52, pp. 425–469, 2002.
- [125] L. C. Bland, “Spin physics at RHIC,” *AIP Conf. Proc.*, vol. 675, no. 1, pp. 98–111, 2003.
- [126] D. B. Steski, J. Alessi, J. Benjamin, C. Carlson, M. Manni, P. Thieberger, and M. Wiplich, “Operation of the Relativistic Heavy Ion Collider Au- ion source,” *Rev. Sci. Instrum.*, vol. 73, pp. 797–799, 2002.

- [127] J. Alessi, E. Beebe, O. Gould, A. Kponou, R. Lockey, A. Pikin, D. Raparia, J. Ritter, and L. Snjdrstrup, “High performance ebis for rhic,” *Proceedings of the IEEE Particle Accelerator Conference*, pp. 3782 – 3785, 07 2007.
- [128] C. Gardner *et al.*, “Operation of the RHIC Injector Chain with Ions from EBIS,” in *6th International Particle Accelerator Conference*, 2015, p. THPF046.
- [129] M. Anerella *et al.*, “The RHIC magnet system,” *Nucl. Instrum. Meth. A*, vol. 499, pp. 280–315, 2003.
- [130] K. Adcox *et al.*, “Formation of dense partonic matter in relativistic nucleus-nucleus collisions at RHIC: Experimental evaluation by the PHENIX collaboration,” *Nucl. Phys. A*, vol. 757, pp. 184–283, 2005.
- [131] B. B. Back *et al.*, “The PHOBOS perspective on discoveries at RHIC,” *Nucl. Phys. A*, vol. 757, pp. 28–101, 2005.
- [132] I. Arsene *et al.*, “Quark gluon plasma and color glass condensate at RHIC? The Perspective from the BRAHMS experiment,” *Nucl. Phys. A*, vol. 757, pp. 1–27, 2005.
- [133] A. Adare *et al.*, “An Upgrade Proposal from the PHENIX Collaboration,” 1 2015.
- [134] F. Bergsma *et al.*, “The STAR detector magnet subsystem,” *Nucl. Instrum. Meth. A*, vol. 499, pp. 633–639, 2003.
- [135] 1996. [Online]. Available: <https://drupal.star.bnl.gov/STAR/starnotes/public/csn0121>
- [136] H. S. Matis, R. L. Brown, W. Christie, W. R. Edwards, R. Jared, B. Minor, and P. Salz, “Integration and conventional systems at STAR,” *Nucl. Instrum. Meth. A*, vol. 499, pp. 802–813, 2003.
- [137] M. Beddo *et al.*, “The STAR barrel electromagnetic calorimeter,” *Nucl. Instrum. Meth. A*, vol. 499, pp. 725–739, 2003.
- [138] C. E. Allgower *et al.*, “The STAR endcap electromagnetic calorimeter,” *Nucl. Instrum. Meth. A*, vol. 499, pp. 740–750, 2003.
- [139] J. M. Landgraf, M. J. LeVine, A. Ljubicic, D. Padrazo, J. M. Nelson, and M. W. Schulz, “An overview of the STAR DAQ system,” *Nucl. Instrum. Meth. A*, vol. 499, pp. 762–765, 2003.
- [140] B. Bonner, H. Chen, G. Eppley, F. Geurts, J. Lamas-Valverde, C. Li, W. Llope, T. Nussbaum, E. Platner, and J. Roberts, “A single time-of-flight tray based on multigap resistive plate chambers for the star experiment at rhic,” *Nuclear Instruments and Methods in Physics Research Section A: Accelerators, Spectrometers, Detectors and Associated Equipment*, vol. 508, no. 1, pp. 181–184, 2003.
- [141] W. J. Llope *et al.*, “The TOFp / pVPD time-of-flight system for STAR,” *Nucl. Instrum. Meth. A*, vol. 522, pp. 252–273, 2004.
- [142] W.-M. Y. et al”, “Review of particle physics,” *Journal of Physics G: Nuclear and Particle Physics*, vol. 33, no. 1, p. 1, jul 2006. [Online]. Available: <https://dx.doi.org/10.1088/0954-3899/33/1/001>
- [143] 2015. [Online]. Available: https://drupal.star.bnl.gov/STAR/system/files/TDRiTPCUpgrade_final.pdf

- [144] C. Adler, A. Denisov, E. Garcia, M. Murray, H. Strobele, and S. White, “The RHIC zero-degree calorimeters,” *Nucl. Instrum. Meth. A*, vol. 499, pp. 433–436, 2003.
- [145] A. J. Baltz, C. Chasman, and S. N. White, “Correlated forward - backward dissociation and neutron spectra as luminosity monitor in heavy ion colliders,” *Nucl. Instrum. Meth. A*, vol. 417, pp. 1–8, 1998.
- [146] 2003. [Online]. Available: <https://drupal.star.bnl.gov/STAR/files/ZDC-SMD.pdf>
- [147] S. C. C. A. Whitten, “The Beam-Beam Counter: A Local Polarimeter at STAR,” *AIP Conf. Proc.*, vol. 980 (1), pp. 390—396, 2008. [Online]. Available: <https://doi.org/10.1063/1.2888113>
- [148] L. Adamczyk *et al.*, “Inclusive charged hadron elliptic flow in Au + Au collisions at $\sqrt{s_{NN}} = 7.7 - 39$ GeV,” *Phys. Rev. C*, vol. 86, p. 054908, 2012.
- [149] L. Ruan *et al.*, “Perspectives of a Midrapidity Dimuon Program at RHIC: A Novel and Compact Muon Telescope Detector,” *J. Phys. G*, vol. 36, p. 095001, 2009.
- [150] L. C. Bland *et al.*, “Future of low-x forward physics at RHIC,” *Eur. Phys. J. C*, vol. 43, pp. 427–435, 2005.
- [151] S. STAR note, “Proposed Addition of a Shower Max Detector to the STAR Zero Degree Calorimeters.” [Online]. Available: <https://drupal.star.bnl.gov/STAR/starnotes/public/sn0448>
- [152] D. Kharzeev and M. Nardi, “Hadron production in nuclear collisions at RHIC and high density QCD,” *Phys. Lett. B*, vol. 507, pp. 121–128, 2001.
- [153] R. J. Glauber, “Lectures on Theoretical Physics,” In: W. E. Brittin and L. C. Dunham,” *Interscience*, vol. 1, p. 315, 1959.
- [154] B. B. Back *et al.*, “Collision geometry scaling of Au+Au pseudorapidity density from $s(NN)^{1/2} = 19.6$ -GeV to 200-GeV,” *Phys. Rev. C*, vol. 70, p. 021902, 2004.
- [155] S. Navas *et al.*, “Review of particle physics,” *Phys. Rev. D*, vol. 110, no. 3, p. 030001, 2024.
- [156] M. Shao, O. Y. Barannikova, X. Dong, Y. Fisyak, L. Ruan, P. Sorensen, and Z. Xu, “Extensive particle identification with TPC and TOF at the STAR experiment,” *Nucl. Instrum. Meth. A*, vol. 558, pp. 419–429, 2006.
- [157] L. Adamczyk *et al.*, “Probing parton dynamics of QCD matter with Ω and ϕ production,” *Phys. Rev. C*, vol. 93, no. 2, p. 021903, 2016.
- [158] V. Fine and P. Nevski, “Proc. chep 2000, 143,” 2000.
- [159] C. Tsallis, “Possible Generalization of Boltzmann-Gibbs Statistics,” *J. Statist. Phys.*, vol. 52, pp. 479–487, 1988.
- [160] M. A. Lisa *et al.*, “Femtoscopia in relativistic heavy ion collisions,” *Ann. Rev. Nucl. Part. Sci.*, vol. 55, pp. 357–402, 2005.
- [161] S. Dash, “Study of k^{*0} resonance production in relativistic heavy ion collision at rhic, phd thesis,” *HBNI*, 2010.
- [162] S. Singha, B. Mohanty, and Z.-W. Lin, “Studying re-scattering effect in heavy-ion collision through K^* production,” *Int. J. Mod. Phys. E*, vol. 24, no. 05, p. 1550041, 2015.

- [163] S. Wheaton and J. Cleymans, “THERMUS: A Thermal model package for ROOT,” *Comput. Phys. Commun.*, vol. 180, pp. 84–106, 2009.
- [164] S. A. Bass *et al.*, “Microscopic models for ultrarelativistic heavy ion collisions,” *Prog. Part. Nucl. Phys.*, vol. 41, pp. 255–369, 1998.
- [165] M. Bleicher *et al.*, “Relativistic hadron hadron collisions in the ultrarelativistic quantum molecular dynamics model,” *J. Phys. G*, vol. 25, pp. 1859–1896, 1999.
- [166] J. Weil *et al.*, “Particle production and equilibrium properties within a new hadron transport approach for heavy-ion collisions,” *Phys. Rev. C*, vol. 94, no. 5, p. 054905, 2016.
- [167] J. Steinheimer and M. Bleicher, “Sub-threshold ϕ and Ξ^- production by high mass resonances with UrQMD,” *J. Phys. G*, vol. 43, no. 1, p. 015104, 2016.
- [168] J. Adam, M. G. Cherney, J. D’Alesio, E. Dufresne, L. Holub, J. E. Seger, and D. Tlustý, “Upgrade of hardware controls for the star experiment at rhic,” *Nuclear Instruments and Methods in Physics Research Section A: Accelerators, Spectrometers, Detectors and Associated Equipment*, vol. 1013, p. 165644, 2021. [Online]. Available: <https://www.sciencedirect.com/science/article/pii/S016890022100629X>
- [169] R. Barlow, “Systematic errors: Facts and fictions,” pp. 134–144, 7 2002.
- [170] L. Adamczyk *et al.*, “Beam Energy Dependence of Jet-Quenching Effects in Au+Au Collisions at $\sqrt{s_{NN}} = 7.7, 11.5, 14.5, 19.6, 27, 39$, and 62.4 GeV,” *Phys. Rev. Lett.*, vol. 121, no. 3, p. 032301, 2018.
- [171] T. Parida, S. Chatterjee, and M. Nasim, “Effect of hadronic interaction on the flow of K^*0 ,” *Phys. Rev. C*, vol. 109, no. 4, p. 044905, 2024.
- [172] W. Reisdorf and H. G. Ritter, “COLLECTIVE FLOW IN HEAVY-ION COLLISIONS,” *Annual Review of Nuclear and Particle Science*, vol. 47, pp. 663–709, 1997.
- [173] H. Sorge, “Elliptical flow: A Signature for early pressure in ultrarelativistic nucleus-nucleus collisions,” *Phys. Rev. Lett.*, vol. 78, pp. 2309–2312, 1997.
- [174] J. P. W. Norbert Herrmann and T. Wienold, “COLLECTIVE FLOW IN HEAVY-ION COLLISIONS,” *Annual Review of Nuclear and Particle Science*, vol. 49, pp. 581–632, 1999.
- [175] P. Chung *et al.*, “Antiflow of $K0(s)$ mesons in 6-A-GeV Au + Au collisions,” *Phys. Rev. Lett.*, vol. 85, pp. 940–943, 2000.
- [176] ———, “Directed flow of Lambda hyperons in 2-AGeV to 6-AGeV Au+Au collisions,” *Phys. Rev. Lett.*, vol. 86, pp. 2533–2536, 2001.
- [177] J. Adams *et al.*, “Azimuthal anisotropy at RHIC: The First and fourth harmonics,” *Phys. Rev. Lett.*, vol. 92, p. 062301, 2004, [Erratum: *Phys.Rev.Lett.* 127, 069901 (2021)].
- [178] B. B. Back *et al.*, “Energy dependence of directed flow over a wide range of pseudorapidity in Au + Au collisions at RHIC,” *Phys. Rev. Lett.*, vol. 97, p. 012301, 2006.
- [179] B. Abelev *et al.*, “Directed Flow of Charged Particles at Midrapidity Relative to the Spectator Plane in Pb-Pb Collisions at $\sqrt{s_{NN}}=2.76$ TeV,” *Phys. Rev. Lett.*, vol. 111, no. 23, p. 232302, 2013.
- [180] P. Bozek and I. Wyskiel, “Directed flow in ultrarelativistic heavy-ion collisions,” *Phys. Rev. C*, vol. 81, p. 054902, 2010.

- [181] Y. Nara, H. Niemi, A. Ohnishi, and H. Stöcker, “Examination of directed flow as a signature of the softest point of the equation of state in QCD matter,” *Phys. Rev. C*, vol. 94, no. 3, p. 034906, 2016.
- [182] V. P. Konchakovski, W. Cassing, Y. B. Ivanov, and V. D. Toneev, “Examination of the directed flow puzzle in heavy-ion collisions,” *Phys. Rev. C*, vol. 90, no. 1, p. 014903, 2014.
- [183] L. Adamczyk *et al.*, “Beam-Energy Dependence of the Directed Flow of Protons, Antiprotons, and Pions in Au+Au Collisions,” *Phys. Rev. Lett.*, vol. 112, no. 16, p. 162301, 2014.
- [184] T. Parida and S. Chatterjee, “Baryon diffusion coefficient of the strongly interacting medium,” 5 2023.
- [185] D. E. Kharzeev, L. D. McLerran, and H. J. Warringa, “The Effects of topological charge change in heavy ion collisions: ‘Event by event P and CP violation’,” *Nucl. Phys. A*, vol. 803, pp. 227–253, 2008.
- [186] L. McLerran and V. Skokov, “Comments About the Electromagnetic Field in Heavy-Ion Collisions,” *Nucl. Phys. A*, vol. 929, pp. 184–190, 2014.
- [187] S. K. Das, S. Plumari, S. Chatterjee, J. Alam, F. Scardina, and V. Greco, “Directed Flow of Charm Quarks as a Witness of the Initial Strong Magnetic Field in Ultra-Relativistic Heavy Ion Collisions,” *Phys. Lett. B*, vol. 768, pp. 260–264, 2017.
- [188] U. Gürsoy, D. Kharzeev, E. Marcus, K. Rajagopal, and C. Shen, “Charge-dependent Flow Induced by Magnetic and Electric Fields in Heavy Ion Collisions,” *Phys. Rev. C*, vol. 98, no. 5, p. 055201, 2018.
- [189] J. Adam *et al.*, “First Observation of the Directed Flow of D^0 and \overline{D}^0 in Au+Au Collisions at $\sqrt{s_{NN}} = 200$ GeV,” *Phys. Rev. Lett.*, vol. 123, no. 16, p. 162301, 2019.
- [190] S. Acharya *et al.*, “Probing the effects of strong electromagnetic fields with charge-dependent directed flow in Pb-Pb collisions at the LHC,” *Phys. Rev. Lett.*, vol. 125, no. 2, p. 022301, 2020.
- [191] Y. Guo, F. Liu, and A. Tang, “Directed flow of transported and non-transported protons in Au+Au collisions from UrQMD model,” *Phys. Rev. C*, vol. 86, p. 044901, 2012.
- [192] “Electric charge and strangeness-dependent directed flow splitting of produced quarks in Au+Au collisions,” 4 2023.
- [193] T. Parida and S. Chatterjee, “Baryon inhomogeneities driven charge dependent directed flow in heavy ion collisions,” 5 2023.
- [194] J. T. Balewski *et al.*, “Total cross-section of the reaction $p p \rightarrow p K^+ \Lambda$ close to threshold,” *Phys. Lett. B*, vol. 420, pp. 211–216, 1998.
- [195] C. Zhou, J. Xu, X. Luo, and F. Liu, “Cumulants of event-by-event net-strangeness distributions in Au+Au collisions at $\sqrt{s_{NN}}=7.7$ -200 GeV from UrQMD model,” *Phys. Rev. C*, vol. 96, no. 1, p. 014909, 2017.
- [196] J. C. Dunlop, M. A. Lisa, and P. Sorensen, “Constituent quark scaling violation due to baryon number transport,” *Phys. Rev. C*, vol. 84, p. 044914, 2011.

- [197] A. Goudarzi, G. Wang, and H. Z. Huang, “Evidence of coalescence sum rule in elliptic flow of identified particles in high-energy heavy-ion collisions,” *Phys. Lett. B*, vol. 811, p. 135974, 2020.
- [198] G. Wang, “Directed flow of quarks from the RHIC Beam Energy Scan measured by STAR,” *Nucl. Phys. A*, vol. 982, pp. 415–418, 2019.